TAMPEREEN TEKNILLINEN YLIOPISTO
TAMPERE UNIVERSITY OF TECHNOLOGY

Ramakanth Neeli-Venkata

The Role of Nucleoid Exclusion in the Intracellular Spatial Organization of *Escherichia coli*

Julkaisu 1491 • Publication 1491

Tampere 2017

Tampereen teknillinen yliopisto. Julkaisu 1491
Tampere University of Technology. Publication 1491

Ramakanth Neeli-Venkata

The Role of Nucleoid Exclusion in the Intracellular Spatial Organization of *Escherichia coli*

Thesis for the degree of Doctor of Philosophy to be presented with due permission for public examination and criticism in Tietotalo Building, Auditorium TB109, at Tampere University of Technology, on the 10th of November 2017, at 12 noon.

Tampereen teknillinen yliopisto - Tampere University of Technology
Tampere 2017

Doctoral candidate:	Ramakanth Neeli-Venkata Faculty of Biomedical Sciences and Engineering Tampere University of Technology Finland
Supervisor:	Prof. Andre S. Ribeiro Faculty of Biomedical Sciences and Engineering Tampere University of Technology Finland
Instructor:	Emerita Prof. Ulla Ruotsalainen Laboratory of Signal Processing Tampere University of Technology Finland
Pre-examiners:	Prof. Paul Wiggins University of Washington United States of America
	Assist. Prof. Jaan Mannik University of Tennessee United States of America
Opponent:	Prof. Judy Armitage University of Oxford United Kingdom

ISBN 978-952-15-3990-9 (printed)
ISBN 978-952-15-4035-6 (PDF)
ISSN 1459-2045

Abstract

Not long ago, bacterial cells were regarded as organisms with hardly any internal organization, due to lack of visible physical compartments and, thus, proteins were believed to be distributed randomly. Since then, advances in microscopy, in *in vivo* protein labeling with fluorescent tags, and in image analysis techniques have enabled us to probe biological events at a single-cell, single-time moment, and single-molecule level. The results from these observations have led to a radical change in this view and, thus, revolutionized the field of bacterial cell biology. Namely, this novel source of information has made evident that proper bacterial functioning is not possible without a highly spatially organized, dynamic internal composition that depends on the deployment of functional proteins and other cellular components in specific locations, at specific moments.

The spatiotemporal organization of the functional proteins and other cellular components play a fundamental role in several key regulatory processes, such as transcription, translation and cell division. One class of proteins, termed as 'DNA-binding proteins', are associated with DNA replication and segregation. Not surprisingly, they preferentially locate at midcell, where the chromosomal DNA is condensed into a dynamic structure called 'nucleoid'. Another class of proteins, termed as 'polar proteins', are majorly involved in physiological behaviors such as chemotaxis, sugar uptake, motility and adhesion. In agreement, they are preferentially localized at the cell poles in the case of rod-shaped bacteria such as *E. coli*. Finally, there is a third class of proteins, called as 'cytoskeletal proteins', whose location differ widely during cell growth. For example, the Min system, a major cell division regulatory system, consisting of MinCDE proteins have a remarkable dynamic pattern inside the cell. These proteins localize for about half a minute in one cell half and then switch rapidly to the opposite half. This back and forth motion continues until the polymerization of the division protein FtsZ results in a ring-like structure at the cell center prior to cell division.

Cellular components, other than functional proteins, also exhibit a highly-organized spatial distribution. These components include plasmids, enzyme megacomplexes and unwanted protein aggregates. For example, protein aggregates, formed as a result of environment stress or errors in protein homeostasis, are generally sequestered into inclusion bodies (IBs) that localize at the cell poles. This process of polar localization is symmetric. However, following several cell division events, results in progeny cells containing the old pole having more aggregates than the new pole possessing progeny cells. Subsequent divisions lead to cell generations where some cells inherit more aggregates than others. Importantly, this was found to be positively correlated with increased division times, i.e., cellular aging. It is believed that such asymmetric partitioning of unwanted aggregates may be critical for the rejuvenation of bacterial populations. It is thus of major importance to understand the underlying mechanisms that are responsible for the above-described events.

In this thesis, using *Escherichia coli* as our model organism, we started by investigating and validating the hypothesis that the presence of the nucleoid at the midcell is responsible for the ability of this organism to segregate unwanted protein aggregates to the cell poles. We next investigated and characterized the robustness of these mechanisms to external perturbations and stressful environmental conditions. Afterwards, we hypothesized that the phenomenon of nucleoid exclusion should not be limited to protein aggregates alone but, instead, for physical reasons, it should influence any large macromolecule that is not affected by a transport or self-propelling mechanism (which is the case of all proteins in *E. coli*). Consequently, we hypothesized and subsequently proved that it should influence self-assembling proteins, such as the transmembrane Tsr chemoreceptors, which have a major role in bacterial chemotaxis. In addition, we also investigated to what extent cell-to-cell diversity in nucleoid sizes contributes to the cell-to-cell diversity in the spatial distribution of polar-localized proteins. For these studies, we made use of efficient fluorescent tags, *in vivo* single-cell, single-molecule time-lapse microscopy, tailored image and signal processing techniques and stochastic biophysical models.

Our results provide new perspectives regarding the role of the nucleoid in the spatial organization of protein aggregates as well as chemoreceptor clusters in *E. coli*. Interestingly, regarding the latter, nucleoid exclusion from midcell was shown not to be the sole phenomenon for the proper localization of Tsr protein clusters. However, it is expected to be the most robust, namely, in stressful environments or when the cell is subject to external perturbations, than the diffusion-and-capture mechanism mediated by the Tol-Pal complexes, as it does not require production of proteins or is under stringent control. Further, unlike the other mechanism, it is energy-free.

Given the rapid developments in single-cell biology techniques, particularly the emergence of super-resolution microscopy techniques, improved fluorescent probes, high-throughput and large-scale biochemical methods and theoretical tools, we expect several developments in the near future that will allow assessing further the role of the nucleoid as a ‘spatial organizer’ of the cellular architecture of *E. coli*.

Preface

This study was carried out at both the Biomeditech Institute and the Department of Signal processing of, respectively, the Faculty of Biomedical Sciences and Engineering and the Faculty of Computing and Electrical Engineering, both at Tampere University of Technology, under the supervision of Professor Andre S. Ribeiro.

First, I would like to express my sincere gratitude to my supervisor, Professor Andre S. Ribeiro for giving me this opportunity and for his persistent support, motivation and guidance during my doctoral studies. It was truly a pleasure working with him and an honor to be a member of his wonderful multidisciplinary group. Over the last few years, I have learned a lot, grown scientifically and prepared myself for future research. I would also like to express my sincere gratitude to Paul Wiggins and Jaan Mannik for the pre-examination of this thesis. Their insightful suggestions have helped to further improve this thesis.

Next, I would like to thank the TUT president's graduate programme for supporting my last 2 years of doctoral study and, in this regard, I sincerely thank my thesis instructor, Emerita Professor Ulla Ruotsalainen, not only for acting as a valuable instructor for my PhD dissertation, but also for supporting my application to this programme.

Also, I would like to thank all co-authors and current and past members of the Laboratory of Biosystem Dynamics. I especially thank Samuel Oliveira, Vinodh Kandavalli and Nadia Gonçalves for the valuable scientific discussions we had in the laboratory on the experimental technicalities, useful comments and advices related to my work, besides the entertainment. Those interactions were really helpful in making the thesis possible in its current form. I should also thank Jarno Mäkelä, Anantha-Barathi Muthukrishnan, Jerome Chandraseelan, Abhishekh Gupta, Jason Lloyd-Price, Sofia Startceva, Leonardo Martins, Antti Häkkinen, Huy Tran, Teppo Annila, Antti Martikainen, Marco Minoia, Cristina Palma and Mohammed Nasurudeen for the interesting discussions and contributions related to microscopy, experimental design and theoretical approaches that led to fulfilling the objectives in my thesis.

I sincerely thank all the personnel of the Biomeditech Institute and the Department of Signal Processing for assisting me and for creating an atmosphere that allowed me to focus on my work. In this regard, I would like to especially thank Virve Larmilla, Pirkko Ruotsalainen, Noora Rotola-Pukkila, Suvi Heinamaki, Annukka Viitanen, Anneli Lehtinen, Ulla Siltaloppi, Juha Peltonen, Kari Suomela, and Jari Yli-Hietanen for their constant support. I am also thankful to academic coordinators Elina Orava and Stefanie Kohlhoff and student assistant Minna Uusitalo for their help during my studies at TUT.

I also thank Professor Jose M. Fonseca, Universidade Nova de Lisboa, Portugal, for his support in the collaborative research work.

I would also like to thank my friends in Tampere for being supportive and helping me to stay focused during my doctoral study. In addition, I would like to thank all my friends in India. I cannot list all the names here, but you are always on my mind. My special thanks to Kishore Kumar and Suresh Tungala, who have been instrumental in making me realize my capabilities from the time I have known them. The support and encouragement you both have given during my PhD was worth more than I can express on this paper.

My deep and sincere gratitude to all my family members for their continuous and exceptional love, help and support. This thesis would not have been possible without your support. I would like to thank my parents Venkataiah Neeli and Chandrakala Neeli for allowing me to realize my own potential and encouraging me to follow my dreams. I am especially grateful to my elder brother, Srikanth Neeli, for inspiring me from the very beginning to aim for an academic career. I always knew that you believed in me and wanted the best for me. I also want to express gratitude to my three sisters and their families for offering unquantifiable love and taking care of me in many aspects. Also, I thank my sister-in-law and niece Sai Sahasra Neeli for their love and support. Additionally, I thank my in-laws for being affectionate and considerate.

Finally, special thanks to my wife, Ushakiran for all your love and support. You have entered in my life while I was shaping this thesis. I am looking forward to our lifelong journey.

Ramakanth Neeli-Venkata
Tampere, July 2017

Contents

List of Abbreviations

DAPI	4’, 6-diamidino-2-phenylindole
DNA	Deoxyribonucleic acid
FISH	Fluorescence *in-situ* hybridization
Fts	Filamentous temperature-sensitive gene
GFP	Green fluorescent protein
HILO	Highly inclined and laminated optical sheet
HupA	Protein HUα
IBs	Inclusion bodies
IbpA	Inclusion body protein A
MCP	Methyl-accepting chemotaxis proteins
NAPs	Nucleoid-associated proteins
ORF	Open reading frame
RNAp	RNA polymerase
RBS	Ribosome binding site
sHSPs	Small heat shock proteins
SSA	Stochastic Simulation Algorithm
SMC	Structural maintenance of chromosomes
TIRF	Total Internal Reflection Fluorescence
Tsr	Taxis to serine and repellants
YFP	Yellow fluorescent protein

List of Publications

This thesis is a compilation of the following publications. In the text, these are referred to as **Publication I, Publication II** and so on.

I. A. Gupta*, J. Lloyd-Price*, **R. Neeli-Venkata**, S.M.D. Oliveira, and A.S. Ribeiro, “*In vivo* kinetics of segregation and polar retention of MS2-GFP-RNA complexes in *Escherichia coli*”, *Biophysical Journal*, 106(9):1928-1937, 2014.

II. **R. Neeli-Venkata,** A. Martikainen*, N. Goncalves*, A. Gupta*, J.M. Fonseca and A.S. Ribeiro, “Robustness of the process of nucleoid exclusion of protein aggregates in *Escherichia coli*”, *Journal of Bacteriology,* 198:898-906, 2016.

III. S.M.D. Oliveira, **R. Neeli-Venkata**, N. Goncalves, J. A. Santinha, L. Martins, H. Tran, J. Mäkelä, A. Gupta, M. Barandas, A. Häkkinen, J. Lloyd-Price, J.M. Fonseca, and A.S. Ribeiro, “Increased cytoplasm viscosity hampers aggregate polar segregation in *Escherichia coli*”, *Molecular Microbiology*, 99(4), 686–699, 2016.

IV. **R. Neeli-Venkata**, S. Startceva, T. Annila, and A.S. Ribeiro, “Polar Localization of the Serine Chemoreceptor of *Escherichia coli* is Nucleoid Exclusion-Dependent”, *Biophysical Journal*, 111(11), 2512–2522, 2016.

The author of this thesis contributed to these publications as follows.

In **Publication I**, we studied the short and long term spatial distribution of large protein complexes in the cytoplasm of *Escherichia coli*, along with the kinetics that generates this distribution. We established that the preference for polar localization is an asymmetric process and then showed that this preference results from presence of the nucleoid at midcell that forces the MS2-GFP-RNA complexes to preferentially move in the poles direction when interacting with the nucleoid borders. The author of this thesis designed, performed, and interpreted all measurements. These were executed in synchrony with the theoretical models developed by other authors. In addition, the author actively participated in the writing of the manuscript, and was the main responsible for the writing of the sections of the manuscript associated with the experiments for this study. To the best of our knowledge, this was the first study to prove empirically that *E. coli* is able to generate heterogeneous distributions of protein complexes within its cytoplasm due to the presence of the nucleoid at midcell.

In **Publication II**, we investigated how robust is the process of nucleoid exclusion to differing medium richness and antibiotic stresses, as these are known to affect the nucleoid size. We found that the mechanisms of segregation and retention of protein aggregates in *E. coli* are robust, but not entirely immune to stress conditions that have tangible effect on the nucleoid sizes. The author of this thesis conceived the study with A.S. Ribeiro, designed and conducted all the experiments assisted by N. Goncalves, analyzed the results with A. Martikainen, A. Gupta and A.S. Ribeiro, and wrote the manuscript with A.S. Ribeiro.

In **Publication III**, we investigated the robustness of the process of nucleoid exclusion for a wide range of temperatures. From our studies, we found that, at lower-than-suboptimal temperatures, cells are no longer able to exclude unwanted protein aggregates to the poles. Importantly, we established that this is due to a much-increased cytoplasm viscosity, which weakens the anisotropy in the kinetics of the aggregates due to its interactions with the nucleoid. These findings contribute to the present understanding of *E. coli*'s internal organization and functioning, and its susceptibility to stressful conditions. For this work, the author of this thesis conceived and supervised all the experiments, analyzed all experimental results with S.M.D. Oliveira, and then actively participated in the writing of the manuscript sections associated with the experimental methods and results.

Finally, in **Publication IV**, from live time-lapse, single-cell microscopy measurements, we investigated the degree to which nucleoid exclusion enhances the segregation and retention of Tsr chemoreceptor clusters at the cell poles. Unlike the previous publications that focused on unwanted protein aggregates, Tsr clusters are known to play a key role in chemotaxis. We set out to show that *E. coli* uses the same means to place both types of protein clusters at the cell poles except that, in the latter, the process is further assisted by the presence of Tol-Pal complexes at the cell extremities. The author of this thesis conceived the study, and designed and performed all the experiments necessary to address the objective of this study. The experiments were designed in synchrony with the theoretical models developed by other authors. The author also assisted in the model design and, finally, analyzed the empirical and *in silico* results with the co-authors. The writing of the manuscript was mostly done by the author and A.S. Ribeiro. This was the first study to prove empirically that *E. coli* makes use of the presence of the nucleoid at midcell to 'engineer' its chemotaxis machinery.

Publication I has been used by A. Gupta in his PhD dissertation.

Publication III will be included in SMD Oliveira's PhD dissertation.

1. Introduction

1.1. Background and Motivation

In all living forms, from bacteria to mammals, the dynamic spatial organization of cellular components plays a fundamental role in crucial biological functions such as transcription, translation and cell division (Thanbichler 2010; Huh and Paulsson 2011a; Campos and Jacobs-Wagner 2013; Laloux and Jacobs-Wagner 2014; Weng and Xiao 2014; Castellana *et al.* 2016) This intricate organization consists of a specific localization of each cellular component at a specific time of the cell lifetime or at a specific condition, such as environmental stress. For example, the bacterial cytoskeletal protein FtsZ, which assembles into a cytokinetic Z ring at midcell just prior to cell division is dynamic during the course of cell cycle. Namely, they start at the cell poles as helical structures and then travel towards midcell prior to cell division (Erickson *et al.* 2010), where they condense into the Z ring, which dictates where the division point is formed, followed by constriction, resulting in two equal-sized daughter cells (Margolin 2005).

The spatial organization of proteins and other cellular components is critical for the bacterial physiology and their adaptability to diverse environments (Lindner *et al.* 2008; Winkler *et al.* 2010; Matsumoto *et al.* 2013). A specific organization of a given protein will favor a specific behavior, such as symmetric instead of asymmetric division, fast versus slow motility, active or inactive chemotaxis, etc. (Rudner and Losick 2010; Sourjik and Armitage 2010; Kruse 2012; Campos and Jacobs-Wagner 2013; Kysela *et al.* 2013; Jin *et al.* 2015). While there is much knowledge on the positioning of many bacterial proteins at specific times during the cell cycle (Shapiro *et al.* 2009; Campos and Jacobs-Wagner 2013; Loose and Mitchison 2014), much less is known on the cellular mechanisms that are responsible for these spatial organizations.

Unlike eukaryotes, bacteria lack organelles and membrane vesicles that facilitate the sorting and delivery of functional proteins to particular subcellular addresses with high precision. Because of this, bacteria were once viewed as an amorphous reaction vessel harboring a homogenous solution of proteins. The use of genetically encoded fluorescent reporters along with powerful cell imaging technologies over the past two decades, has changed this view radically. It is now accepted that a living bacterial cell is a complex entity; with an intricate subcellular architecture in which cellular components, much like in eukaryotic cells, get localize to particular sites in the cell, often in a dynamic manner (Rudner and Losick 2010). Thus, understanding the nature of mechanisms by which these cellular components localize to reach their proper destination inside the cell is a crucial question in present bacterial cell biology.

In this regard, e.g., several mechanisms have been proposed for how some macromolecules preferentially localize at the poles during the cell cycle as reviewed in (Laloux and Jacobs-Wagner

2014). One example is the diffusion-and-capture mechanism, associated for the recruitment of several polar localized proteins, e.g. the Tol-Pal complex mediates the polar localization of chemoreceptor clusters in *E. coli* (Santos *et al.* 2014). Another mechanism is nucleoid exclusion, a passive diffusion process that contributes to macromolecular crowding of, e.g. protein complexes, at the cell poles. Other mechanisms such as cell wall curvature, cell envelope affinity are reviewed in (Laloux and Jacobs-Wagner 2014).

In unicellular organisms, such as *Escherichia coli*, the genomic DNA is radially confined, condensed and packed within the cell cylinder as a single circular chromosome referred to as nucleoid (Wang *et al.* 2011). The structure of the nucleoid is very dynamic and sensitive to growth conditions and external perturbations. Meanwhile, the cytoplasm, a gel-like substance filling the rest of the interior of the cell, is more diffusive. Several studies have suggested that, regardless of its diffusive nature, the cytoplasm also possesses a highly crowded environment (Elowitz *et al.* 1999; Golding and Cox 2006). The presence of the nucleoid at mid-cell contributes to this crowding as it favors the association of macromolecules. Recent studies have shown that several cellular components, due to this macromolecular crowding, become prone to the volume exclusion effects caused by the presence of nucleoid at midcell (Straight *et al.* 2007; Winkler *et al.* 2010; Vecchiarelli *et al.* 2012; Reyes-Lamothe *et al.* 2014; Sanamrad *et al.* 2014).

One such cellular component in *E. coli* is the 'unwanted' or 'non-functional' proteins. At any moment there are many such proteins in the cell. Those not degraded by the cell (usually 20% of newly synthesized polypeptides are degraded (Goldberg 1972) tend to form aggregates. In stressful environments or following errors in protein homeostasis inside the cell, their numbers increase. It is yet debated how the aggregates are formed, with some evidence existing that it is an energy-dependent process (Hartl *et al.* 2011; Kim *et al.* 2013)

Recent studies have suggested that protein aggregates are segregated towards the poles (Lindner *et al.* 2008; Winkler *et al.* 2010) and, following a few cell division events, become asymmetrically distributed through the daughter cells of subsequent generations (Stewart *et al.* 2005; Lindner *et al.* 2008). Namely, after some generations, large amounts of these aggregates accumulate in the cells with older poles, when compared to those with new poles (Lindner *et al.* 2008). This accumulation of protein aggregates has been linked with reduced vitality, decreased growth rate thus contributing to cellular aging (Stewart *et al.* 2005; Lindner *et al.* 2008; Maisonneuve *et al.* 2008; Tyedmers *et al.* 2010). This observed phenomenon of cellular aging has led us to ask what mechanism is responsible for it. We speculated that the presence of the nucleoid at midcell could be playing a significant role.

Tsr, a major serine chemoreceptor protein involved in the process of chemotaxis, forms membrane clusters, preferentially at the cell poles using the mechanism of diffusion-and-capture (Laloux and Jacobs-Wagner 2014) aided by the presence of transmembrane Tol-Pal complex (Santos *et al.* 2014). A chimeric Tsr-Venus protein was used recently to study the kinetics of translation (Yu *et al.* 2006). While observing it at the microscope, we found that the long-term spatial distribution and kinetics of Tsr-Venus clusters could not be explained solely by a diffusion-and-capture mechanism made possible by Tol-Pal complexes at the cell poles. In particular, the clusters showed a clear tendency to move to the poles, and did so at a specific distance between the cell center and the cell extremities. Finally, the clusters exhibited a similar dynamics to that of other protein aggregates. Therefore, we again speculated that the presence of the nucleoid at midcell could be playing a significant role in its polar localization.

Given this, we made use of state-of-the-art methods and technologies in single-molecule fluorescence, live cell imaging, image analysis, and signal processing, to investigate the existence and then assess the robustness of the nucleoid exclusion phenomenon to environmental stresses and external perturbations at a single-cell level. In addition, we produced realistic models to test whether the nucleoid-exclusion mechanism could reproduce the experimental data. The models needed to mimic biological processes involving a small number of molecules and many events occurring in many cells for several generations. Because of this, the models were made according to the stochastic formulation of chemical kinetics. As such, we used stochastic simulators to efficiently simulate these models.

1.2. Thesis Objectives

This thesis focused on the study of the role of nucleoid exclusion on the intracellular spatial organization of *E. coli* cells. We established four primary objectives.

Our first objective was to study sources for the observed heterogeneity in the spatial distribution of large protein complexes, such as RNA molecules tagged with multiple MS2-GFP proteins. For that, we first studied the extent to which the nucleoid contributes to the heterogeneity of large biomolecules in the cytoplasm. For this, we measured the kinetics and long-term spatial distribution of fluorescent MS2-GFP-RNA complexes at the single-cell, single-molecule level in live *E. coli* cells subject to optimal and sub-optimal growth conditions. From the analysis of time-lapse microscopy images, we first characterized the spatiotemporal distributions of these specific complexes within the cells. It is well-established that aggregates preferentially locate at the cell poles (Lindner *et al.* 2008). Based on this, we investigated and identified the cause for this preference for localization at the cell poles from measurements and models. Also, we further assessed the robustness of this phenomenon in cells subject to sub-optimal temperature conditions. These goals were achieved in **Publication I**.

Second, our objective was to characterize the robustness of this newly identified phenomenon to various environmental stresses. These include media richness and antibiotic perturbations that are known to directly affect the nucleoid size (Cabrera *et al.* 2009; Hadizadeh Yazdi *et al.* 2012) and, thereby, it is reasonable to assume that they will alter the segregation and partitioning in division of the aggregates. For this, we studied the spatiotemporal distribution of protein aggregates in cells expressing a fluorescent YFP-tagged chaperone (IbpA-YFP), which identifies *in vivo* the location of protein aggregates, and HupA-mCherry, a fluorescent variant of a nucleoid-associated protein, which allows detecting the location and measure the dimensions of the nucleoid(s). From this data, we investigated through single-cell observations, if the identified mechanism is robust to varying media richness and antibiotic perturbations. These goals were achieved in **Publication II**.

Third, our objective was to determine the degree of functionality of this newly identified phenomenon in cells under various sub-optimal temperatures at which the cytoplasm properties are altered. These temperatures, in particular and in comparison to optimal conditions, are known to either enhance or diminish the metabolic activity of the cell, affecting the fluidity of the cytoplasm (Parry *et al.* 2014). As such, they are expected to cause perturbations to any diffusion-dependent cellular process. For this, we studied the spatiotemporal distribution of *E. coli* cells expressing the fluorescently-tagged chaperone (IbpA) protein aggregates, referred to here as 'natural' aggregates. We also employed cells expressing fluorescent MS2-GFP-RNA complexes, referred to here as 'synthetic' aggregates. We investigated how temperature affects the segregation and partitioning in division of these aggregates in *E. coli*, given the relative easiness with which they can be tracked from the images. These goals were achieved in **Publication III**.

Finally, based on the newly identified phenomenon, our objective was to study whether nucleoid exclusion affected other biomolecules (e.g. functional proteins), other than the segregation of unwanted protein aggregates. For that, we extended our studies to functional polar proteins, in particular, to chemoreceptor proteins, and studied whether the nucleoid was also involved in their preference for polar localization. For this, we studied the spatiotemporal distribution of fluorescent Tsr-Venus clusters and fluorescently tagged nucleoids, with the latter allowing the localization and dimension characterization of the nucleoid(s). It has recently been established that chemoreceptor proteins localize at the cell poles by a mechanism of 'diffusion-and-capture' (Greenfield *et al.* 2009; Laloux and Jacobs-Wagner 2014). We further investigated through single-cell observations, how our newly identified phenomenon acts in conjunction with this diffusion-and-capture mechanism in the polar localization of Tsr chemoreceptors. These goals were achieved in **Publication IV**.

1.3. Thesis Outline

This thesis is organized as follows: Chapter 2 introduces the biological background in detail, with special emphasis on nucleoid organization, followed by a brief description of transcription, translation and cell division. Also, the current knowledge on the spatial organization of various cellular components is discussed. Chapter 3 has a detailed view of experimental methods employed in the current study, focusing on fluorescent proteins, microscopy, experimental systems and stochastic models. Chapter 4 presents the computational tools used in this thesis, such as for cell segmentation, lineage construction, spots segmentation and nucleoid detection and segmentation. Finally, the conclusions and discussion are presented in Chapter 5.

2. Biological Background

This chapter gives an overview of the biological concepts, model organism, and cellular processes studied in this thesis. It includes a biological description of transcription, translation and cell division in *Escherichia coli* along with a more detailed view into the nucleoid's morphology and its organization, the cytoplasm properties, protein aggregates formation, and polar chemoreceptor clusters.

2.1. The Central Dogma of Molecular Biology

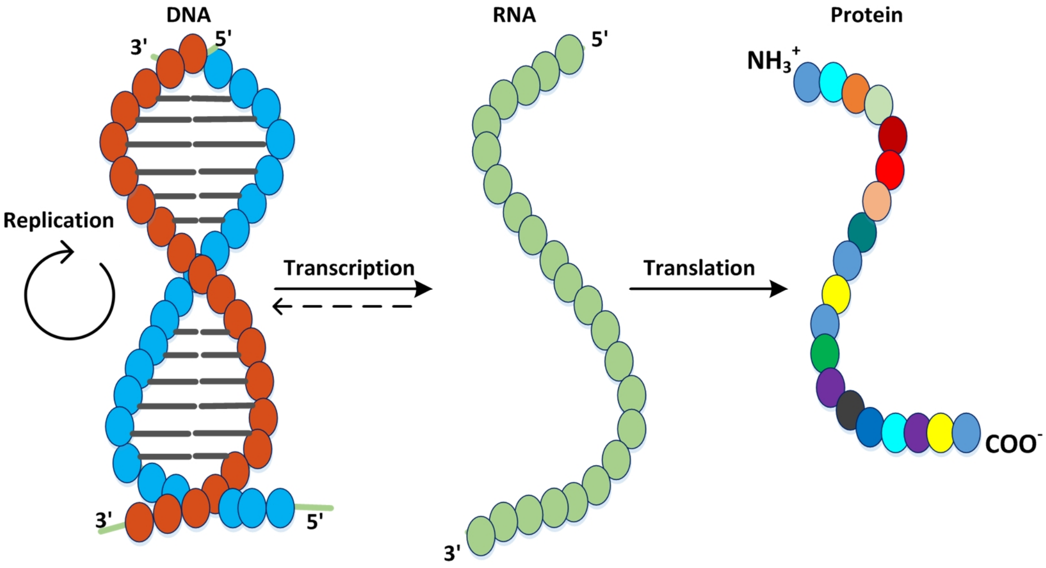

Figure 2.1: The central dogma of molecular biology. The information stored in the DNA can be transferred to mRNA by the process of transcription and then from mRNA to proteins by the process of translation. The information in the DNA can be replicated in the process of DNA replication. In special cases, information in the RNA can be transferred to the DNA in a process called reverse transcription (represented as dashed arrows).

The cell is rightfully called the 'building block of life'. Some organisms consist of a single cell, for example bacteria, while others consist of many cells, for example mammals. All of them need to survive, function and reproduce. The information on the basic machinery needed to achieve this is stored in its inherited genetic material, the DNA (deoxyribonucleic acid). The DNA does not encode proteins. Instead it encodes RNA (ribonucleic acid), which are used as an intermediary. The central dogma of molecular biology states how cells express their genetic information (present in the DNA sequentially) into proteins, by using RNA as an intermediary molecule (Figure 2.1). Therefore, the flow of genetic information in cells is always from DNA to RNA to protein (Crick 1970).

The DNA contains genes, each carrying specific biological information. A DNA molecule consists of two long polynucleotide chains made of nucleotide subunits. Each nucleotide is composed of a deoxyribose sugar, a nucleobase and a phosphate group. There are four nucleobases in a DNA molecule namely adenine (A), cytosine (C), guanine (G) and thymine (T). A always pairs with T, and G with C. The nucleotides are covalently linked together in a chain through sugars and phosphates, which form the backbone of alternating sugar-phosphates. Most DNA molecules exist as double-stranded helices, which are held together by hydrogen bonding between the nucleotides and noncovalent interactions between the nucleobases. The two strands are anti-parallel and complementary to each other with the same biological information on both the strands. DNA replicates in a highly coordinated fashion and accurately copies the information by enzymes called DNA-dependent DNA polymerases or reverse transcribes to DNA from RNA molecules by RNA-dependent DNA polymerases. In eukaryotes, the DNA is enclosed in membrane-bound nucleus, while in prokaryotes it is compacted into a structure called as ‘nucleoid’, which occupies a significant fraction of the cell volume (15% to 25%) (Churchward *et al.* 1981; Valkenburg and Woldringh 1984; Odijk 1998; Reyes-Lamothe *et al.* 2008; Klumpp *et al.* 2009; Vendeville *et al.* 2011).

RNA is the only macromolecule known to be involved in storage and transmission of information, regulation of gene expression and catalysis. Like the DNA, the RNA is a linear polymer made of four different nucleobases linked by phosphodiester bonds. Unlike the DNA, the RNA is single stranded and contains ribose instead of deoxyribose and nucleobase uracil (U) instead of thymine. Several kinds of RNA molecules are produced inside the cell. Messenger RNA (mRNA) carries information from DNA to ribosomes, the protein-making factories of the cell. Ribosomal RNA (rRNA) makes up the constituents of ribosomes and also catalyzes peptide bond formation. Transfer RNA (tRNA) reads information encoded in mRNA and transfers appropriate amino acid to a growing polypeptide chain. Small RNA (sRNA) regulates gene expression by binding to mRNA. Transfer-messenger RNA (tmRNA) binds to stalled ribosomes during translation, releases them and targets the incomplete polypeptides for degradation. RNA is transcribed by DNA-dependent RNA polymerases by copying the information from the template strand. Some viruses store their genetic information in RNA and they replicate this information using RNA-dependent RNA polymerases.

Proteins are the primary components of living organisms. Proteins are functional polymers of peptides, which are synthesized by the addition of amino acids while translating the information in the mRNA sequence. Proteins have a wide range of functionalities, such as gene expression regulation, environment sensing, interaction with cell membranes, binding to other macromolecules, transporting of signaling molecules, induction and catalyzes of biochemical reactions and providing structural support to the cell. Biologically occurring polypeptides differ widely in sizes and are composed of chains of characteristic amino acid molecules that are linked together by peptide bonds. A single peptide chain is derived from the condensation of amino acids and each amino acid consists of an α-carbon, an amino group, a carboxyl group and a side chain.

In a peptide, the amino acid residue at the end with a free amino group is known as N-terminal or amino-terminal residue, while the end with a free carboxyl group is known as C-terminal or carboxyl-terminal residue. Proteins are brought together as a three-dimensional conformation that is stabilized by noncovalent interactions. These conformations determine their functioning *in vivo*.

2.2. Biology of *Escherichia coli*

Escherichia coli (*E. coli)* is a gram-negative rod-shaped bacterium that was discovered by Theodor Escherich in 1886. A typical *E. coli* cell is 2 to 4µm long and 0.5 to 0.8 µm wide (Volkmer and Heinemann 2011) and normally lives in the gut of humans and other vertebrates. It is the most studied organism as a model system and has many useful characteristics. *E. coli* can be grown easily and are well adapted to the laboratory environments. They can be grown both in the presence and absence of oxygen. They have fast growth rates, with doubling time of 20 minutes in optimal conditions, i.e., at 37°C with Luria Broth (LB) as growth media.

E. coli genome can be easily manipulated and is also prone to evolve by mutations and genetic recombination. Genetic recombination involves transfer of genetic material. Genetic material can be transferred between *E. coli* cells either by cell-to-cell contact (conjugation), direct uptake of DNA from the medium and incorporation into the recipient chromosome (transformation) or by injection of foreign DNA by a bacteriophage virus (transduction) (Lehninger *et al.* 2000). *E. coli* use the flagella for locomotion and sense the environmental changes by chemotaxis. Most *E. coli* strains are harmless and play important role in nature and to mankind by preventing bacterial infections, aiding in metabolism and synthesis of vitamins.

The standard laboratory strain *E. coli* K-12 has a genome of approximately 4.6 million nucleotide pairs, containing 2584 clusters of genes called operons and 4300 protein-coding genes, which accounts for 88% of the whole genome (Lehninger *et al.* 2000).This genomic DNA is radially confined, condensed and packed within the cell cylinder as a single circular chromosome called the nucleoid (Wang *et al.* 2011). Additionally, *E. coli* also possess extra-chromosomal DNA, called plasmids that can exist and replicate independently of the chromosome, which carry genes that confer selective advantages to *E. coli* in the form of drug resistance, new metabolism capabilities, pathogenesis and colonization strategies (Pinto *et al.* 2012).

2.3. Nucleoid Organization and Partitioning

The *E. coli* nucleoid occupies approximately 75% of the cellular space in the cell cylinder (Fisher *et al.* 2013; Wang *et al.* 2013) (Figure 2.2). A single circular chromosome (nucleoid) in *E. coli*, if fully stretched out, would be >1mm in length, whereas the space occupied by the nucleoid is <1 µm in diameter (Wang *et al.* 2013). Packaging the chromosome into such small spaces must nonetheless conserve its functionality for a range of cellular processes: gene expression, DNA replication and its transfer into the daughter cells. This is made possible by the interplay of several proteins and mechanisms that operate together to allow the compaction of a circular chromosome by more than 1000-fold within the nucleoid, so as to fit inside the cell. These proteins and mechanisms include Nucleoid-associated proteins (NAPs), macromolecular crowding, DNA polymer dynamics, intranucleoid interactions and, DNA supercoiling (Odijk 1998; Travers and Muskhelishvili 2005; Skoko *et al.* 2006; Dillon and Dorman 2010; Wiggins *et al.* 2010; Pelletier *et al.* 2012). Computational modelling-based studies on chromosome organization in *E. coli* revealed that the compaction of the chromosome further requires the interplay of several regulatory interactions (Jun and Mulder 2006; Fritsche *et al.* 2012).

Despite the high degree of compaction in the nucleoid, the genome still remains accessible to essential biological processes, such as replication, transcription and translation. Various molecular and recombination-based methodologies have suggested the existence of an ordered and hierarchical compaction of nucleoid's DNA into smaller units called microdomains, which are further organized into higher-order structures called macrodomains (Boccard *et al.* 2005; Mercier *et al.* 2008; Wang *et al.* 2013; Song and Loparo 2015).

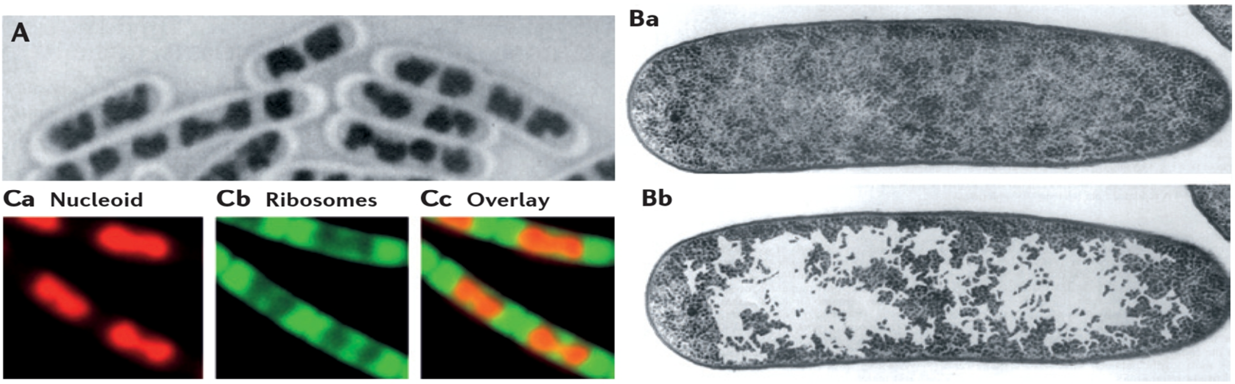

Figure 2.2: Example image of bacterial nucleoids. A) *Bacillus subtilis* nucleoid stained with Giemsa stain. B) The nucleoid of growing *Escherichia coli* in thin section. Panels (a) and (b) showing the same section; panel (b) showing ribosome-free spaces. C) (a) Nucleoid stained with DAPI, colored red, (b) GFP labeled ribosomes and (c) overlay of images (a) and (b). Reprinted with permission from Macmillan Publishers Ltd: (Nature Reviews Genetics) (Wang *et al*), copyright (2013).

2.3.1. Microdomains

The principal mechanism by which the bacterial chromosome is compacted is DNA supercoiling (Wang *et al.* 2013). The chromosome in *E. coli* is negatively supercoiled i.e., the 2 strands of DNA are maintained in an under-wind state because of the action of DNA gyrase, which introduces negative supercoils (Rovinskiy *et al.* 2012). This supercoiled form is relaxed by the action of DNA topoisomerases following DNA replication and transcription, to avoid tensions in the strands. The opposing activities of both of these enzymes maintain the superhelical form of the DNA (Champoux 2001). The action of supercoiling condenses the chromosome into independent domains called ‘microdomains’. These microdomains vary in size but, on average, are around 10 kb long (Postow 2004). Each of these microdomains are negatively supercoiled, topologically independent and insulated (Worcel and Burgi 1972). Thus, a 4.6-Million nucleotide genome is expected to have approximately 500 microdomains (Boccard *et al.* 2005). About half of these are present as branched intertwined structures called plectonemes, a form of supercoiled DNA (Rovinskiy *et al.* 2012).

The presence of microdomains provides several advantages to bacteria (Postow 2004). For example, lesions in the chromosome caused by DNA damage, repair processes, or replication, only relaxing a single domain without affecting the superhelicity of other DNA regions (Postow *et al.* 2001). In this way, the organization of the nucleoid into numerous small structured, supercoiled microdomains significantly contributes to the DNA’s overall compactness. These topological domains also contribute to the dynamic nature of the nucleoid. However, the *in vivo* compaction of the nucleoid is not static and depends on several factors, such as the richness of the nutrient medium, cell cycle stage and temperature.

2.3.2. Nucleoid-Associated Proteins

DNA Supercoiling alone does not account for the overall compaction exhibited by the bacterial chromosome (Dillon and Dorman 2010; Wang *et al.* 2013). Bacteria also possess proteins that associate with the chromosome and facilitate the compaction of chromosomal DNA, stabilizing the free supercoils that do not form plectonemes (Postow *et al.* 2001; Wang *et al.* 2013), thus playing a critical role as chromosomal architects. Approximately half of the chromosome is constrained by these small abundant DNA binding proteins (Dillon and Dorman 2010). These proteins have a functional analogy to histone proteins that are found in eukaryotes, involved in chromatin compaction (Wang *et al.* 2013). In bacteria, these proteins are called as nucleoid-associated proteins (NAPs).

In *Escherichia coli*, major NAPs include heat unstable proteins (HU), histone-like nucleoid-structuring proteins (H-NS), factor-for-inversion stimulation (Fis) and integration host factors (IHF) (Dillon and Dorman 2010; Wang *et al.* 2011). An exponentially growing *E. coli* contains 30000-55000 HU molecules, 20000 H-NS molecules, 60000 Fis molecules and 12000 IHF molecules (Azam *et al.* 1999). Fis, HU and IHF are major NAPs of the chromosome and are distributed throughout the *E. coli* nucleoid. In contrast, H-NS forms two compact clusters per chromosome and its deletion leads to substantial reorganization of the chromosome (Wang *et al.* 2011). It has also been shown that the composition of NAPs is dependent on the growth phase of the cell, with their relative levels differing in the exponential and stationary phases (Dillon and Dorman 2010).

In *E. coli*, NAPs have two major functions: chromosomal organization and gene regulation (Dillon and Dorman 2010; Wang *et al.* 2013). Each of these NAPs specifically binds up to hundreds of distinct sites distributed throughout the chromosome and facilitate chromosome compaction and organization by introducing bends in the DNA and by bridging chromosomal loci (Wang *et al.* 2013). Most NAPs can bend or wrap DNA, causing local deformation of the DNA backbone. Bending facilitates condensation of adjacent DNA segments, whereas bridging stabilizes DNA loops (Wang *et al.* 2011). Furthermore, because of the substantial nonspecific DNA-binding characteristic of cellular NAPs, most of them are bound to the chromosomal DNA with a coverage of roughly one NAP per 100 base pairs of DNA (Dillon and Dorman 2010; Wang *et al.* 2011).

HU protein has two subunits, HUα and HUβ that are 70% identical in amino acid sequence. In exponentially growing *E. coli*, HU exists as a mixture of hetero and homodimers (Claret and Rouviere-Yaniv 1997). HU proteins bind non-specifically to DNA and are distributed throughout the *E. coli* nucleoid (Figure 2.3) (Wang *et al.* 2011). HU is believed to primarily promote DNA compaction by bending (Swinger and Rice 2007). At low HU concentrations, HU-DNA interactions introduce flexible bends but at high HU concentrations they stiffen the DNA (van Noort *et al.* 2004). HU can also form multimers consisting of octameric units that stabilize or constrain supercoiled DNA. HU-induced flexibility facilitates DNA loop formation, which is important for both chromosome organization and gene regulation. HU influences the expression of wide range of genes in *E. coli* that have major role in central metabolism (Dillon and Dorman 2010). It also affects initiation of chromosome replication at the chromosomal origin. It is mostly expressed in the exponential phase of the growth (Azam *et al.* 1999).

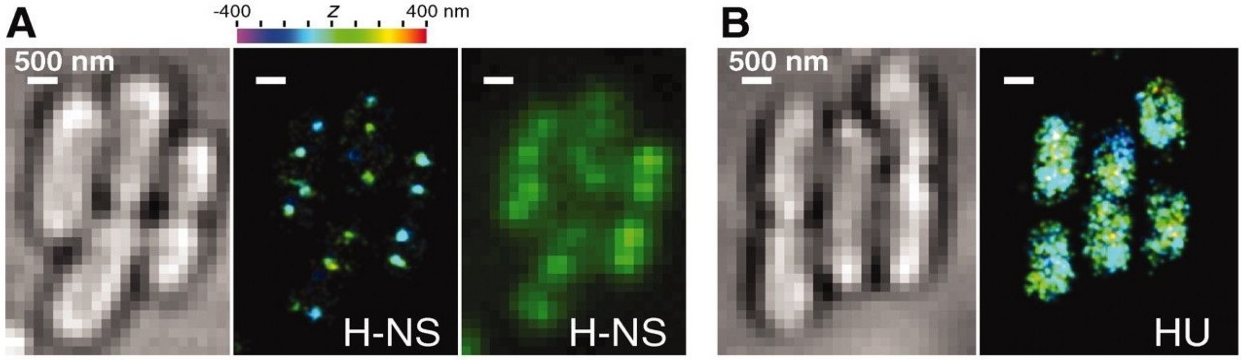

Figure 2.3: Super-resolution imaging of major nucleoid-associated proteins in live *E. coli* cells. A) Compact H-NS clusters in the nucleoid. The *E. coli* cells in bright-field image (left), expressing photoactivatable fluorescent protein mEos2 fused to H-NS (middle) and conventional fluorescent image of same cells (right). B) Scattered distribution of Nucleoid- Associated Protein, HU in the nucleoid. (Left) Bright-field image; (right) 3D STORM image of mEos2-labeled HU in the same cells. From (Wang *et al* 2011). Reprinted with permission from AAAS.

H-NS protein consists of two functionally different structural domains separated by a flexible linker: (i) a C-terminal DNA binding domain and (ii) a N-terminal domain that promotes dimerization and oligomerization (Dorman and Deighan 2003). In exponentially growing *E. coli*, H-NS exists as a hetero or homodimer. H-NS binds specifically to intertwined, supercoiled DNA duplexes and facilitate the formation of DNA-H-NS-DNA bridges which are approximately around 250 loci in the *E. coli* genome and are thought to reside at the center of the nucleoid (Figure

2.3) (Dorman and Kane 2009; Wang *et al.* 2011). This bridging allows H-NS to influence both the nucleoid structure, as well as gene expression simultaneously. It is believed that these bridges repress transcription and thus act as global transcriptional silencers (Dillon and Dorman 2010). H-NS are mostly expressed in the exponential phase of the growth (Azam *et al.* 1999).

The Fis protein is made of 4α-helices connected by β-hairpins (Skoko *et al.* 2006). It exists as a homodimer throughout the *E. coli* genome and binds to AT-rich binding sites, bending the DNA. Fis influences gene expression across the genome. It represses its own expression and also affects the initiation of chromosome replication at the chromosomal origin (Dillon and Dorman 2010). It is mostly expressed in the early exponential phase of the growth (Azam *et al.* 1999).

The IHF protein is related to HU at the level of the amino acid sequence and is composed of an α-subunit and a β-subunit. The IHF protein has a distinct mode of interaction with the DNA (Swinger and Rice 2007). The IHF exists as a heterodimer in *E. coli* and binds to well-conserved nucleotide sequences and introduces a U-turn into the DNA (Craig and Nash 1984). It influences gene expression and affects the initiation of chromosome replication at the chromosomal origin (Dillon and Dorman 2010). It is mostly expressed in the stationary phase (Azam *et al.* 1999).

In Publication **II, III and IV**, we made use of cells expressing nucleoid-associated protein, HU fused to fluorescent protein mCherry (HupA-mCherry), to conduct time-lapse microscopy of the nucleoid morphology and observe its dynamics to characterize the role of the nucleoid in the spatial organization of proteins complexes.

2.3.3. Macrodomains

Genetic experiments have revealed that the *E. coli* chromosome is further organized into distinguishable regions ranging in size from 800kb-1Mb and are referred to as macrodomains (Wang *et al.* 2013). In *E. coli*, four macrodomains have been identified (*ori*, left, right and *ter*) along with two non-structured regions (NS-left and NS-right) (Dorman 2013). The *ori* macrodomain consists of a region around the bidirectional chromosomal replication origin, *oriC* while the *ter* macrodomain is located at the opposite pole of the chromosome containing the terminus of DNA replication (Thanbichler *et al.* 2005; Dorman 2013). The remaining regions form the bulk of replichore arms.

The molecular mechanisms underlying the macrodomain organization is still unknown. However, recent evidence suggests that sequence-specific DNA binding proteins participate in this higher-order organization. For example, DNA binding protein MatP, binds to the sequence motif *matS* enriched in the *E. coli ter* macrodomain and plays a crucial role in the DNA bridging mechanism and condensation of the *ter* macrodomain (Dupaigne *et al.* 2012). Recent works on the localization of the nucleoid-associated protein H-NS and the DNA regions it interacts suggests that this DNA binding protein could impose a different type of organization on the *E. coli* chromosome (Wang *et al.* 2011). Specifically, this study revealed that H-NS forms 1-4 stable complexes at or near the nucleoid centre distributed across the four macrodomains along with two unstructured regions (Wang *et al.* 2011). The absence of H-NS in this regions thus leads to the reorganization of the chromosome, influencing the segregation of newly replicated sister chromosomes (Kaidow *et al.* 1995).

The macrodomains in the chromosome are organized in a pattern that are faithfully and robustly regenerated in daughter cells (Wang and Rudner 2014). This organization determines how the DNA replication machinery acts to ensure accurate chromosome segregation (Thanbichler *et al.* 2005).

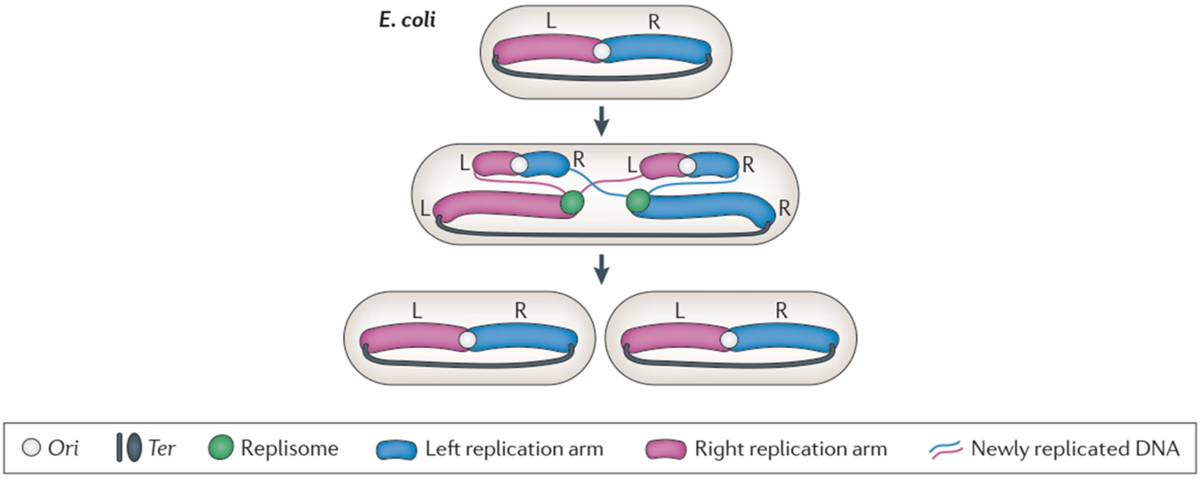

Figure 2.4: Representative image of the spatial organization of the chromosome(s) in *Escherichia coli*. The chromosome consists of four spatially organized regions (*ori*, left, right and *ter*). In *E. coli* a left-*ori*-right configuration is observed, with *ori* being centrally positioned at the mid-cell, while the left and right replichores flanking the origin in opposite cell halves. Reprinted with permission from Macmillan Publishers Ltd: (Nature Reviews Genetics) (Wang *et al*), copyright (2013).

Two distinct patterns of macrodomain organization have been reported so far, namely *ori*-*ter* and left-*ori*-right (Wang *et al.* 2013). In the *ori*-*ter* configuration, the origin is located at one end of the cell pole and the terminus at the other end of cell pole while both left and right macrodomains follow the longitudinal axis of the cell. This pattern is observed in Bacillus, Caulobacter species (Wang and Rudner 2014). In *E. coli* the left-*ori*-right configuration is observed, with *ori* being centrally positioned at mid-cell, while the left and right replichores flank the origin in opposite cell halves (Wang 2006) (Figure 2.4). This configuration is achieved by the concerted action of the chromosome partition protein complex MukBEF, which is involved in chromosome organization and segregation in *E. coli*, mediated by the SMC complexes (structural maintenance of chromosomes) (Rybenkov *et al.* 2014).

2.3.4. Chromosome Replication and Segregation

E. coli has a simple cell cycle, with replication and progressive segregation of the replicated chromosome completed before cell division (Nielsen *et al.* 2007). Unlike eukaryotes, chromosome replication and segregation in bacteria occur in a coordinated fashion, without a dedicated spindle-like apparatus (Thanbichler *et al.* 2005; Nielsen *et al.* 2006; Wang 2006). Briefly, the cell cycle in *E. coli* can be divided into three periods namely (i) the B period constituting the time between cell division and initiation of replication, (ii) the C period involving chromosome replication and (iii) the D period which is the time between the termination of replication and the completion of subsequent cell division (Wang and Levin 2009). When the cell's doubling time (Td) is shorter than the duration of its chromosome replication (C period), a new round of replication gets initiated before the previous round gets terminated. Thus newborn daughter cells inherit partially duplicated chromosomes. This phenomenon is referred to as multifork replication (Bates and Kleckner 2005; Wang *et al.* 2011).

Most importantly, *E. coli* and other bacteria are capable of multifork replication, i.e., maintaining multiple overlapping rounds of DNA synthesis before segregating the sister chromosomes (Youngren *et al.* 2014). Segregation of replicated chromosomes involves three discrete steps: separation of the newly replicated origins, bulk chromosome segregation and transport of replication termini at division septum (Figure 2.5)(Wang *et al.* 2013).

At the birth of the cell, chromosome replication initiates from a unique origin of replication site (*oriC*) near midcell, with the left and right chromosome arms in opposite cell halves, and proceeds bidirectionally to a terminus region (*ter*) on the opposite side of the circular DNA (Nielsen *et al.* 2007; Wang *et al.* 2011). To complete the circle, the terminus region spans the length of the cell to bridge the two arms (Wang *et al.* 2013). After the completion of replication, the newly replicated sister chromosomes are organized into a left-*ori*-right, left-*ori*-right configuration such that, upon cell division, the original organization is recapitulated in the daughter cells (Nielsen *et al.* 2006; Wang 2006).

After replication is completed, the segregation of replicated origins must be highly orchestrated such that the sister chromosomes rapidly move away from midcell. Different models and evidences have been proposed explaining the role of different mechanisms involved in chromosome segregation (Nielsen *et al.* 2006; Joshi *et al.* 2011; Badrinarayanan *et al.* 2012; Männik and Bailey 2015).

In one study, it has been suggested that, in *E. coli*, the chromosomal loci regions are extruded towards the cell poles as a result of intranucleoid pushing forces (Joshi *et al.* 2011). According to this model, the sister chromosomes' replicated origins undergo condensation and resolution from each other but remain cohesive at specific origin-proximal sites called snaps. The accumulation of intranucleoid pushing forces leads to the loss of cohesion, resulting in the extrusion of condensed origin regions towards opposite poles (Joshi *et al.* 2011).

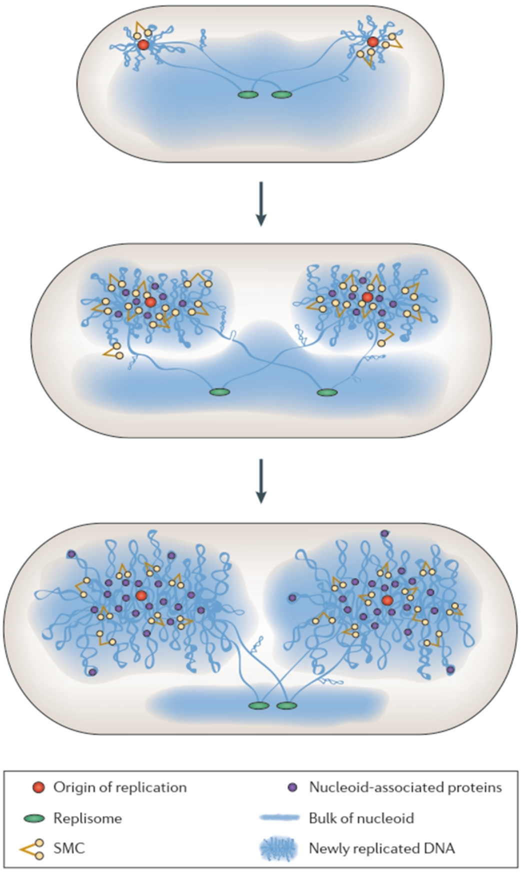

Figure 2.5: Schematic representation of chromosome segregation in *Escherichia coli*. The newly replicated sister loci are sequentially segregated and condensed by the coupled action of NAPs and SMC complexes, Interestingly, SMC and MukB complexes, responsible for a faithful segregation, are enriched at the origin of replication site in *E. coli*. Reprinted with permission from Macmillan Publishers Ltd: (Nature Reviews Genetics) (Wang *et al*), copyright (2013).

In another study, it is shown that the newly replicated chromosomal loci move subdiffusively through the viscoelastic cytoplasm (Weber *et al.* 2010). This study tracked fluorescently labeled chromosomal loci *in vivo* revealing that the subdiffusive motion may contribute to the maintenance of chromosome territories in *E. coli* (Weber *et al.* 2010).

Recent studies in *E. coli* have suggested the existence of molecular mechanisms mediated by the DNA binding protein SlmA and MinCDE system (Bernhardt and de Boer 2005; Wu and Errington 2012; Männik and Bailey 2015). Both these mechanisms directly regulate cell division by inhibiting polymerization of the cytokinetic ring protein, FtsZ in the vicinity of nucleoid and at the cell poles. These molecular mechanisms ensure faithful chromosome segregation by forcing cell division to occur at midcell (Di Ventura *et al.* 2013). Recent evidences also shows that, during rapid growth conditions, chromosomes segregate well before cell division, with replicated chromosomes coupled by a thin inter-daughter filament before completing segregation (Hadizadeh

Yazdi *et al.* 2012). Meanwhile, during slow growth, replicated chromosomes stay adjacent until cell division occurs (Hadizadeh Yazdi *et al.* 2012; Woldringh *et al.* 2015).

In *E. coli,* the complete chromosome segregation before cell division in *E. coli* involves the division-septum localized DNA translocase, FtsK (Steiner *et al.* 1999; Männik *et al.* 2017). Recent studies have shown that FtsK is involved in the ordered segregation of the replication terminus region (*ter*) of the *E.* coli chromosome (Stouf *et al.* 2013). Specifically, FtsK plays two essential roles in chromosome dimer resolution. First it ensures that the two *dif* sites of the dimeric chromosomes are brought together at the midcell region and next it is involved in resolving the catenanes (Peter *et al.* 1998), which are the interlocked rings of chromosomes and dimeric chromosomes (conjoined sisters formed in replication) (Steiner *et al.* 1999).

In **Publication IV**, measurements were conducted in cells lacking gene *mukB*, which leads to failures in chromosome segregation resulting in the formation of anucleate cells, so as to study the role of the nucleoid in the spatial organization of the chemotaxis protein, Tsr.

2.4. Gene Expression

Gene expression is the process by which the information encoded in the genetic material i.e., the nucleotide sequence of DNA, is read-out or expressed to direct protein synthesis and thus make a functional protein useful to the cell. This process uses RNA as an intermediary molecule and is comprised of two steps: transcription of a gene into a RNA followed by the RNA translation into a protein. Both of these steps are key to the central dogma of molecular biology (depicted in figure 2.1) (Crick 1970) as discussed previously. Gene expression can be regulated at many of the steps in the pathway from DNA to RNA to protein (Lehninger *et al.* 2000).

Structurally, each gene is composed of three components: a promoter, an operator(s) and a structural gene(s) (Alberts *et al.* 2002). The promoter is a region of DNA, upstream of the coding region of the structural gene, where RNA polymerase binds and initiates transcription (Figure 2.6). The operators are specific sites on the DNA, generally near to the promoter that are recognized by regulatory molecules that control the expression from the promoter. E.g. repressor molecules prevent access of RNA polymerase to the promoter, while activators enhance the RNA polymerase-promoter interaction (Alberts *et al.* 2002).

Structural genes in prokaryotes are clustered and regulated in operons. An operon is a set of genes that are controlled by a single promoter (Osbourn and Field 2009). Many prokaryotic mRNAs are polycistronic. I.e. a single RNA transcript encodes for more than one protein. These major principles of prokaryotic gene expression were first discovered by studies of Jacob and Monod of the lac operon, which controls the lactose metabolism in *E. coli* (Jacob and Monod 1961).

Transcription, the first step in gene expression, begins with the binding of RNA polymerase to the promoter of a gene and the subsequent copying of the genetic information stored in the coding region of the DNA molecule into a complementary strand of RNA called Messenger RNA (mRNA). The main enzyme involved in this process is the core RNA polymerase (RNAp). It is a large, enzyme complex with five core subunits ($\alpha_2 \beta\beta'\omega$) along with a sixth subunit called σ factor, which has variants designated by its size (molecular weight) (Lehninger *et al.* 2000). The core subunits are involved in a stable enzyme assembly, while the σ factor binds only transiently to the assembled core subunits and directs it to bind specific promoters (Murakami 2002). These six subunits constitute the RNA polymerase holoenzyme. The RNAp holoenzyme of *E.* coli thus exists in several forms, depending on the σ factor (Eσ) it is associated with. A typical *E.* coli cell contains 5000 RNAPs (Bakshi *et al.* 2012) that synthesize RNA at a rate of around 28 to 89 nucleotides per second (Vogel and Jensen 1994).

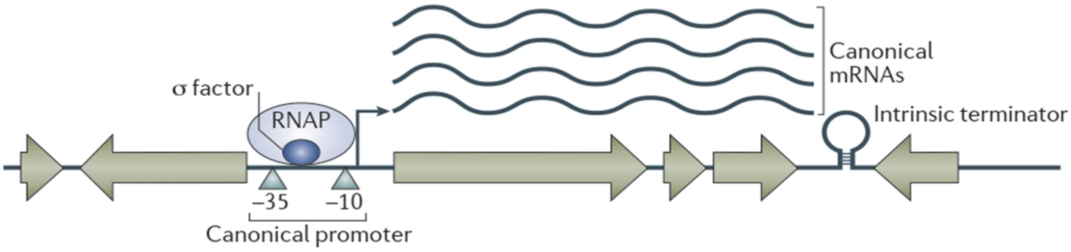

Figure 2.6: Genes in prokaryotes are organized as operons. The synthesis of mRNA is initiated by the recruitment of RNAp onto the promoter region and the subsequent formation of the transcription elongation complex, which produces mRNAs that terminate at a stem-loop structure, known as an intrinsic terminator. Reprinted with permission from Macmillan Publishers Ltd: (Nature Reviews Microbiology) (Wade et al), copyright (2014).

Briefly, bacterial transcription consists of three stages: initiation, elongation and termination (Wilson 2014). During initiation, the RNAp holoenzyme binds to a promoter, unwinds the double-stranded DNA and initiates transcription at the transcription start site (TSS) in the presence of ribonucleotide substrates as the precursors, as well as Mg^{2+}.

Next, in elongation, the RNAp holoenzyme in the transcription elongation complex undergoes a significant conformational change, as the σ factor is released from the complex. Addition of the new ribonucleotides to the growing mRNA transcript proceeds in single-nucleotide steps (Abbondanzieri *et al.* 2005), at about 40 ribonucleotides per second (Kennell and Riezman 1977) in the 5’ to 3’ direction.

Termination occurs when the RNAp reaches one or more termination signals present in the DNA template. *E. coli* has 2 classes of termination signals: termination factor Rho (ρ)-dependent and Rho (ρ)-independent signals. In the former, the helicase activity of Rho contributes in termination, while in the latter, the nascent transcript terminates by forming a destabilizing RNA hairpin loop without the involvement of the factor Rho (Lehninger *et al.* 2000).

Translation, the second step in gene expression, involves synthesis of a sequence of amino acids based on the information encoded in the mRNA. This information is read in triplets, called codons that are continuously stretched on an open reading frame (ORF). A codon is a triplet of nucleotides that codes for a specific amino acid. Translation occurs in such a way that these nucleotide triplets are read in a successive non-overlapping fashion. In bacteria, transcription is often coupled with translation and is carried out by catalytic machines called ribosomes.

The bacterial ribosome contains about 65% ribosomal RNAs (rRNAs) and 35% ribosomal proteins. A single bacterial ribosome consists of two unequal subunits with sedimentation coefficients of 50S and 30S and a combined sedimentation coefficient of 70S. Both the subunits consists of ribosomal proteins and at least one large rRNA. In the large 50S subunit, the 23S, 5S rRNAs and 33 proteins form the structural core and is involved in the catalysis of the peptide bond formation, while the small 30S subunit consists of a 16S rRNA and 21 proteins and is crucial for decoding the mRNA.

Each ribosome contains a mRNA channel, a mRNA decoding center, a peptide exit tunnel, a peptidyl transferase center (Kurkcuoglu *et al.* 2008) and three transfer RNA (tRNA) binding sites, known as the E site, the P site and the A site. Peptide bonds are formed in peptidyl transferase center, located at entrance of the peptide exit tunnel, which allows the synthesized peptide to pass through it and exit. The tRNA binding sites are located at interface between large and small ribosomal subunits. Each incoming tRNA lands into the A site upon entering the ribosome and gets translocated to the P site, followed by translocation to the E site, where it dissociates from the ribosome (Alberts *et al.* 2002). A typical *E. coli* cell contains 60000 ribosomes (Bakshi *et al.* 2012) that translate around 12-17 amino acids per second (Young and Bremer 1976).

The nascent mRNA produced from transcription possess a ribosome binding site (RBS) containing the consensus sequence called the Shine-Dalgarno sequence, located upstream of the initiation codon, AUG. The AUG initiation codon is recognized by a special initiator tRNA carrying N-formylmethionine (fMet). Briefly, bacterial translation consists of three stages: initiation, elongation and termination (Figure 2.7). During initiation, the RBS present on mRNA is recognized by 16S rRNA of the 30S subunit followed by the initiator fMet-tRNA base pairing with start codon, AUG at P site on ribosome, forming an 30S-RNA complex (Ramakrishnan 2002). Next, the large ribosome subunit attaches to this complex to form the initiation complex. During elongation, tRNAs carrying appropriate amino acids are then added to the initiation complex. Elongation in general consists of three steps: binding of an incoming appropriate amino acid possessing-tRNA, peptide bond formation and translocation. This step also requires elongation factors (EF-Tu, EF-Ts, and EF-G) and energy source, GTP. Termination occurs when a stop codon is encountered and translocated into the A site. Release factors (or) termination factors bind to the ribosome releasing both the ribosome and completed polypeptide chain.

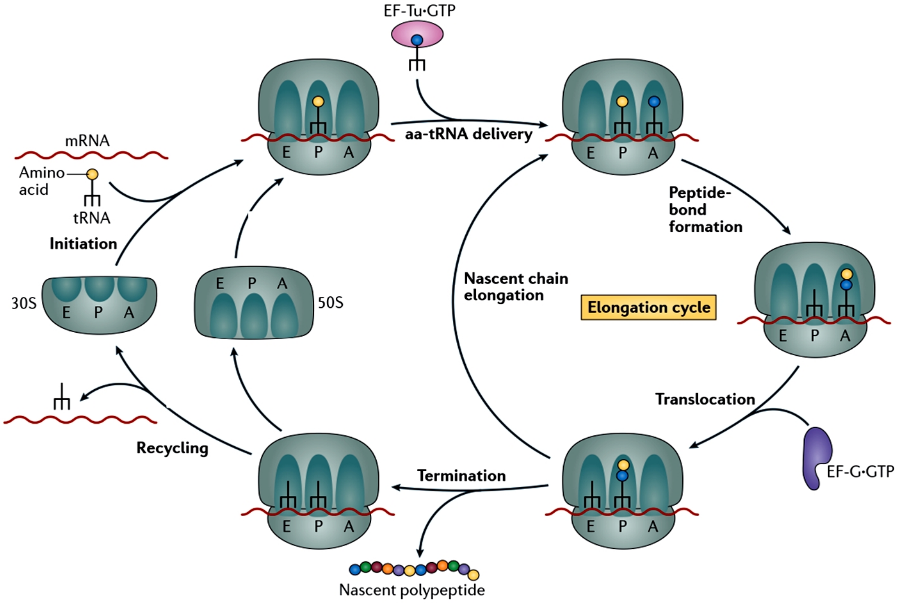

Figure 2.7: Translating an mRNA molecule. Translation initiation involves the assembly of 50S and 30S ribosomal subunits to form a functional 70S ribosome at the start codon, AUG present on the mRNA with the initiator tRNA positioned at the P-site of ribosome. The elongation cycle consists of 3 steps: (i) delivery of appropriate incoming aminoacylated-tRNA to the A-site of ribosome, mediated by the elongation factor EF-Tu. (ii) Peptide bond formation between the two amino acids bound by their tRNAs to the A and P-sites and (iii) translocation, the movement of the ribosome from one codon to the next towards the 3' end of the mRNA, catalyzed by EF-G. In termination, the presence of one of three termination codons in the mRNA triggers the dissociation of 70S ribosome, followed by the release of the polypeptide chain. Adapted with permission from Macmillan Publishers Ltd: (Nature Reviews Microbiology) (Wilson et al), copyright (2014).

2.5. Cell Division

Cytokinesis or cell division is a highly regulated process that is achieved by a complex macromolecular machine called the divisome (Errington *et al.* 2003; Harry *et al.* 2006). The event of cytokinesis results in the formation of two equal-sized daughter cells, each of which receiving a copy of the chromosome from the parent cell. Cell division requires accuracy in the timed positioning of cytokinetic proteins. *E. coli* cells, under optimal conditions of growth undergo three physiologically distinct events that lead to cell division: elongation, segregation and septation. During elongation, cells mostly stretch their length while also increasing their cellular mass by metabolizing nutrients. Next, in segregation, the chromosomal DNA replicates and the 2 resulting chromosomal copies are segregated to the opposite ends of the cell. Once segregation of the newly replicated chromosomes is complete, septation begins. Here, the cell constricts or splits in half, due to pinching of the cellular membrane (cytokinesis) followed by the synthesis of a new cell wall in the space in between, which defines the point of cell division.

The divisome complex contains at least 12 proteins (Vicente and Rico 2006; Adams and Errington 2009). These are cytoplasmic, inner membrane and periplasmic proteins that assemble into a ring at the point of division (division site) in a regulated, concerted manner (Goehring and Beckwith 2005; Vicente and Rico 2006). Recent studies using fluorescent microscopy/spectroscopy and mutant cells have shed light on how the assembly of these proteins at the division site takes place (Ma *et al.* 1996; Wang *et al.* 1998; Weiss 2004; Männik *et al.* 2012). In particular, conditional mutants unable to septate at nonpermissive conditions (usually high temperature) have been employed to identify genes involved in cell division. These temperature-sensitive genes were called *fts*, for filamentous temperature-sensitive genes, encoding for proteins such as FtsZ, FtsA, FtsI, FtsK, FtsL, FtsN, FtsQ, FtsW and ZipA, among others, assemble and form the divisome complex, which is essential for cytokinesis. The most important protein of the divisome is FtsZ. It is one of the well characterized and most thoroughly studied cell division protein known to initiate the polymerization of FtsZ filaments into the Z ring structure, underneath the cytoplasmic membrane at the division site (Bi and Lutkenhaus 1991; Ma *et al.* 1996; Ma and Margolin 1999; Yu and Margolin 1999).

E. coli cells have developed a number of molecular mechanisms to ensure that progeny are equally sized and that each receives an intact chromosome copy. These mechanisms include nucleoid occlusion (NO) and the Min system, depicted in (Figure 2.8). The concept of nucleoid occlusion (NO) emerged from the observation that the Z ring formation is hindered from the regions occupied by nucleoids (Hussain *et al.* 1987; Mulder and Woldringh 1989; Woldringh *et al.* 1990). Recent evidences have reported that the nucleoid occlusion protein, SlmA, a DNA-binding protein, influences the localization of the Z ring by inhibiting the formation of the Z ring over unsegregated nucleoids (Bernhardt and de Boer 2005; Tonthat *et al.* 2011). Specifically, SlmA binds to specific binding sites on the DNA as a dimer of dimers, which spread cooperatively on the DNA, forming a higher-order structure which captures FtsZ filaments that prevent the Z ring formation in that region (Tonthat *et al.* 2011, 2013).

Another important set of proteins known to play a key role in the divisome assembly in *E. coli* are the Min proteins, namely MinC, MinD and MinE, together referred as the ‘Min system’ (Yu and Margolin 1999; Huang *et al.* 2003; Kerr *et al.* 2006). These proteins exhibit remarkable oscillatory behavior, moving back and forth between the two poles, functioning as a geometric positioning system for the Z ring at midcell and preventing polar septation (Shapiro *et al.* 2009; Lutkenhaus *et al.* 2012). The typical oscillatory period under optimal conditions of growth ranges from 30 s to 1 min (Raskin and de Boer 1999). Of these three proteins, only MinD and MinE are necessary to set up the oscillations while MinC, binds to MinD and activates its inhibitory function preventing the polymerization of FtsZ subunits (Lutkenhaus 2007; Shen and Lutkenhaus 2010). Recent evidence shows that deletion of the Min system leads to defects in chromosome segregation, resulting in the formation of anucleate cells (Di Ventura *et al.* 2013).

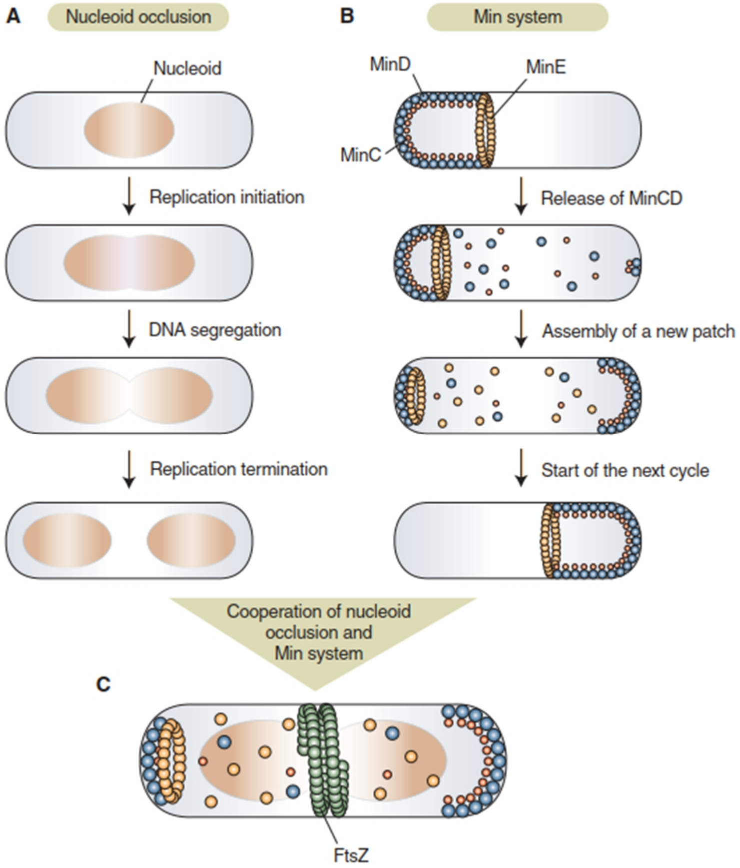

Figure 2.8: Schematic representation of the mechanisms controlling the divisome positioning and assembly. (A) Regulation of cell division by nucleoid occlusion. (B) Inhibition of polar cell-division events by the Min system. (C) Cooperation of nucleoid occlusion and Min systems targeting the FtsZ ring to the midcell. Reprinted from (Thanbichler 2009) with permission from the Cold Spring Harbor Perspectives in Biology.

Other recent studies have further shown evidences that the replication terminus region (*ter*) and the DNA translocase FtsK have important roles in coordinating the Z ring localization. Specifically, the replication terminus region forms a compact entity referred to as the *ter* macrodomain, which is organized by MatP proteins. MatP, like SlmA, is a DNA-binding protein with its binding sites distributed around the *dif* sequence located at the replication terminus region. It has been shown that terminus region in coordination with MatP proteins sequentially promote the assembly of Z ring in its immediate vicinity (Espéli *et al.* 2012). While the DNA translocase FtsK effectively translocates the chromosomal DNA and allows the divisome to actively rearrange chromosomal positioning (Männik and Bailey 2015). The present view is that all these mechanisms work in a coordinated fashion to achieve spatially accurate chromosome segregation and cell division processes.

2.6. Protein Aggregates and Cellular Aging

Proteins or polypeptides, the end products of translation by ribosomes, following their release into the cytoplasm undergo ‘folding’ into defined, unique three-dimensional structures. This step is required for attaining functionality (Stefani and Dobson 2003; Bartlett and Radford 2009). Evidences show that the native folding process of a protein is encoded in its amino acid sequence (Dobson 2001), with the vast majority of proteins being able to fold spontaneously inside the cells (Hartl and Hayer-Hartl 2002). However, a significant portion of them are not very efficient in this process, as they show some propensity to misfolding.

Commonly, misfolded proteins form aggregates that interfere with the normal functioning of the cell (Deuerling *et al.* 1999; Wickner 1999). To deal with this, bacteria have evolved robust protein quality control systems that are involved in the maintenance of the proteome homeostasis (proteostasis) (Hartl *et al.* 2011). In *E. coli*, proteostasis is achieved by an integrated network of several hundred proteins, including the well-known molecular chaperones and their regulators (Stefani and Dobson 2003). The chaperones function by assisting the *de novo* folding of newly synthesized proteins or refolding of misfolded proteins, while the regulators such as proteases degrade misfolded proteins. Proper protein folding is essential for cell survivability and is associated with a whole range of cellular processes, including transcription, cell division, chemotaxis, enzymatic activity, etc. (Hartl *et al.* 2011).

Molecular chaperones are classified into different groups, on the basis of their sequence homology. Most are stress or heat shock proteins (Hsps), i.e., their synthesis is induced under conditions of stress (e.g., heat shock, antibiotic perturbations, etc.) (Kim *et al.* 2013). The cytoplasm of *E. coli* possesses four major protein quality control systems, namely: (i) the GroEL-GroES chaperonin system, (ii) the DnaK-DnaJ chaperone system, (iii) the Ribosome-associated trigger factors (TF) and, (iv) the clpB-Proteasome system that deals with folding, refolding and degradation of nascent, newly synthesized polypeptides and misfolded proteins (Hartl and Hayer-Hartl 2002). Most of the chaperones are ATP regulated and function by recognizing the segments of exposed hydrophobic amino acid residues and bury them in the three-dimensional structure of the folded protein (Hartl *et al.* 2011). Despite the robustness of these systems, when perturbed by either mutations, post-translational modifications or severe stresses in the form of heat shock, antibiotic perturbations, or nutrient deprivation, among other, these quality control systems fail (Stefani and Dobson 2003; Tyedmers *et al.* 2010). These failures affect their refolding and degradation capacities, which creates an imbalance in protein homeostasis, leading to protein misfolding followed by protein aggregation (Tyedmers *et al.* 2010).

Interestingly, *E. coli* cells continuously degrade a fraction of proteins at all times, with approximately 20% of newly synthesized polypeptides being degraded (Goldberg 1972). While some degradation events are due to the detection of errors, this process also allows maintaining a continuous renewal of the composition of the functional proteome, so as to be responsive to a constantly changing environment. When the degradation rate increases, usually the process of protein aggregation becomes more prone to occur.

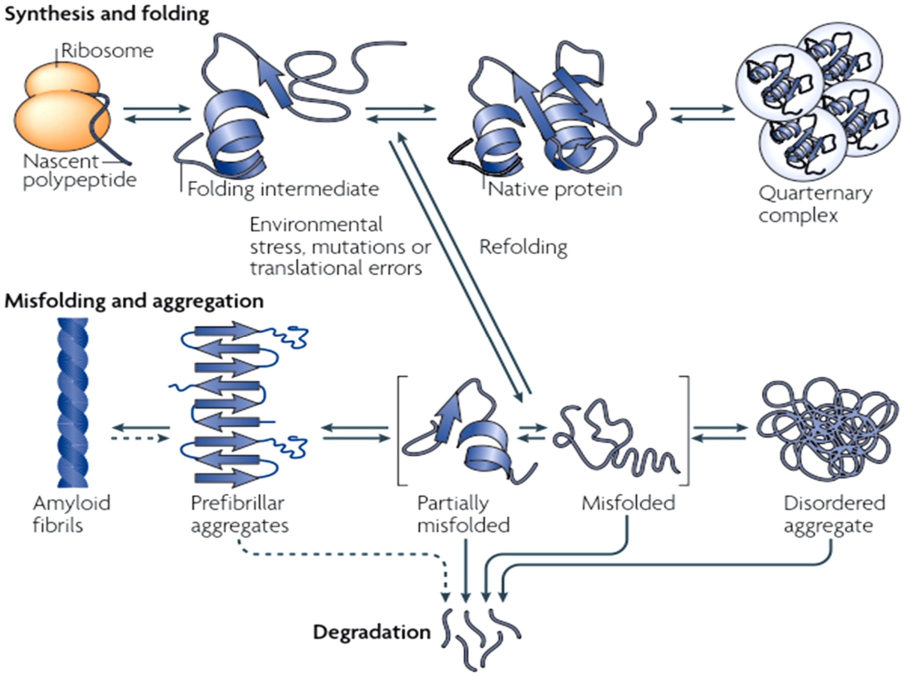

Figure 2.9: Schematic representation of protein aggregation. A Protein during and after its synthesis at the ribosome folds and attains a native structure. Cellular stresses, translational errors and mutations in the synthesized protein can cause protein misfolding. Once present, misfolded proteins can be refolded to the native state or be degraded by cellular proteolysis systems. Failures in the protein quality-control systems accelerates the accumulation of protein aggregates. Reprinted with permission from Macmillan Publishers Ltd: (Nature Reviews Molecular Cell Biology) (Tyedmers *et al*), copyright (2010).

Protein aggregation arises as a result of protein misfolding, typically by exposing the hydrophobic amino acid residues and the regions of the unstructured polypeptide backbone to the solvent, mediating aggregation in a concentration-dependent matter (Kim *et al.* 2013). This leads to clumping and accumulation of partially folded or misfolded proteins (Figure 2.9). Aggregate formation usually involves a slow nucleation step, during which a ‘seed’ is formed. A seed, which initially consists of a small number of molecules, eventually grows through monomer addition, thus forming larger aggregates by an energetically favorable process (Kim *et al.* 2013).

Protein aggregation leads to formation of either highly structured amyloid-fibril-like aggregates or amorphous aggregates. Most of the amyloid aggregates are compartmentalized into inclusions that help the cell to cope with an overload of misfolded proteins. These structures are called inclusion bodies (IBs) and are found mostly at the cell poles, functioning as an intracellular sink for cellular detoxification (Dougan *et al.* 2002; Stefani and Dobson 2003) (Figure 2.10). IBs serve as a parallel strategy employed by bacteria aimed at preserving the protein homeostasis by sequestering misfolded polypeptides into these structures (Bednarska *et al.* 2013). The presence of IBs has been directly associated with a decrease in the productivity and longevity of the cell (Ventura and Villaverde 2006). Most of the aggregates in IBs, once formed, have a tendency to remain insoluble, metabolically stable, and associated with small heat shock proteins (sHSPs), such as the inclusion body protein A (IbpA) and the inclusion body protein B (IbpB).

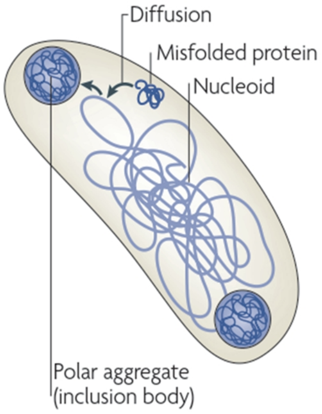

Figure 2.10: Inclusion Bodies (IBs) in bacteria. Misfolded proteins formed in the cell accumulate inside inclusion bodies when under different stressful conditions or following the heterogeneous expression of proteins. Most inclusion bodies are sequestered at the cell poles. Reprinted by permission from Macmillan Publishers Ltd: (Nature Reviews Molecular Cell Biology) (Tyedmers *et al*), copyright (2010).

The accumulation of protein aggregates inside the cell has consequences related to cellular aging (Lindner *et al.* 2008; Maisonneuve *et al.* 2008; Tyedmers *et al.* 2010). Aging, a fundamental characteristic of all living organisms can be defined as a progressive loss of functionality and increased vulnerability to death with time (Campisi 2013; López-Otín *et al.* 2013). Another worth mentioning definition is: “a persistent decline in the age-specific fitness of components of an organism due to internal physiological deterioration” (Rose *et al.* 2012).

Increasing evidences suggest that a process called ‘cellular senescence’ links numerous pathologies of aging (Campisi 2013). Senescence is a deterioration of functioning with age, manifested as a drop in survival and reproduction rates (Rose *et al.* 2012). It is previously believed that senescence occurred only in eukaryotes. Prokaryotes were believed to be immune due to their symmetrical division process.

However, recent studies have given us a new understanding of the process of aging in prokaryotes. Recent studies on *Escherichia coli* and *Caulobacter crescentus* provided substantial evidence that some bacteria species (if not all) do age at the single-cell level, and that only the cell lineage is immortal. Several experimental evidences suggest that the accumulation of protein aggregates is one of the major aging factors in bacteria (Ackermann *et al.* 2003; Stewart *et al.* 2005; Lindner *et al.* 2008). A recent study also reported that protein aggregation, an evolutionarily conserved process, is an active process of ‘defense against aging’ while also maintaining the protein homeostasis (Tyedmers *et al.* 2010).

In particular, it is now believed that there are deleterious effects of aging in bacteria and that, in order to cope with them, these organisms employ strategies that favor the rejuvenation process of some cells in the lineage at the expense of other cells of the same lineage. This was first observed in unicellular organisms that exhibit asymmetric cell division (e.g., *Caulobacter crescentus* and *Saccharomyces cerevisiae*). To study if such asymmetries exist in *E. coli* cells, whose division process is morphologically symmetric, Stewart and colleagues used automated time-lapse microscopy to track many generations of cells of several lineages. From the data, they demonstrated the existence of asymmetric partitioning of resources/damaged components between the offspring of division events. This resulted in offspring with functional asymmetries (Stewart *et al.* 2005). This strategy is bet hedging in that it favors one of the daughter cells, namely, the one with younger poles. Meanwhile, the daughter cell inheriting the older pole exhibits slower growth rate, decreased offspring production and increased incidence of death.

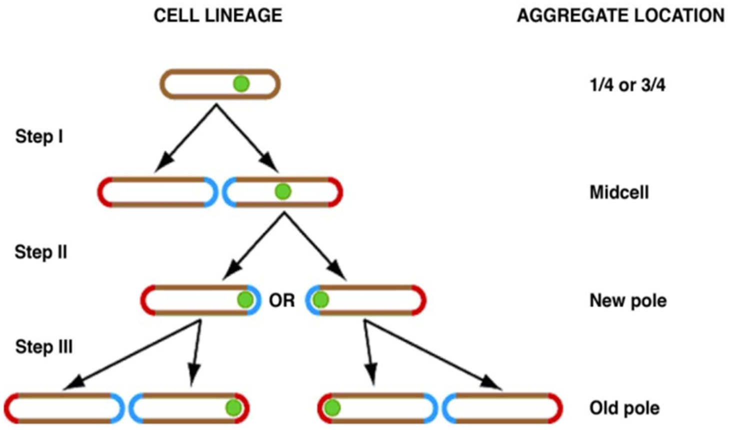

Figure 2.11: Schematic diagram of asymmetric segregation of protein aggregates to the old pole through cycles of cell division. Aggregates that are found concentrated at one-or three-quarter positions are found concentrated around the mid-cell after division (Step I). Aggregates at the mid-cell are subsequently located in the new pole, with equal probability to be in either of the two daughter cells (Step II). Those aggregates that are found in the new-pole of the cell, before division remain retained in the same pole and upon the subsequent cell division event, this pole becomes an old pole in the offspring cell (Step III). Aggregates are indicated by green dots. Red cell ends are old poles, and blue cell ends are new poles. Figure from (Lindner *et al.* 2008), Copyright (2008) National Academy of Sciences, U.S.A.

A subsequent study by Lindner and colleagues elucidated the molecular mechanisms for this functional asymmetry. Namely, it revealed that protein aggregates are segregated towards the poles (Lindner *et al.* 2008). When cell division occurs, it will generate daughter cells that have one pole (the newer) that is free of aggregates (Figure 2.11). In subsequent generations, aggregates become increasingly more heterogeneously distributed among the cell population. Finally, it was shown that the cells possessing a relatively old pole, with therefore high number of protein aggregates, also have a relatively decreased reproducing capacity (Figure 2.11). This asymmetric sequestration of protein aggregates at the population level, at the expense of aging individuals, allows the perpetuation of the population (Lindner *et al.* 2008).

Several others studies have also investigated the role of protein aggregates as well as of other mechanisms leading to cellular aging in bacteria (Ackermann *et al.* 2007; Erjavec *et al.* 2008; Lindner *et al.* 2008; Maisonneuve *et al.* 2008; Lindner and Demarez 2009; Sabate *et al.* 2010; Winkler *et al.* 2010; Baig *et al.* 2014), yeast (Coelho *et al.* 2014), and higher eukaryotes (Fuentealba *et al.* 2008; Youle and van der Bliek 2012).

In *E. coli*, the mechanisms responsible for the polar localization and subsequent asymmetric segregation have long been hypothesized to be associated with volume exclusion effects caused by the presence of the nucleoid at midcell (Lindner *et al.* 2008; Winkler *et al.* 2010; Coquel *et al.* 2013), particularly since the preferential polar aggregation and their retention at the cell pole appears to be an energy-independent process (Winkler *et al.* 2010; Coquel *et al.* 2013).

Recent studies have also investigated potential direct or indirect benefits of aging processes in bacteria. Growth arrest accompanying protein aggregation has been suggested to give temporary resistance to antibiotics (Leszczynska *et al.* 2013). This further suggests that protein aggregation is an evolvable phenomenon, rather than being an inevitable, physical process (Baig *et al.* 2014).

In **Publication I, II, III,** using novel methods of tracking protein aggregates and RNA-MS2-GFP complexes, we first investigate the underlying causes for the preferential polar localization of the proteins aggregates. Next, we investigate their long-term spatial distribution in *E. coli* as a function of the medium richness, and when subject to antibiotic stresses and sub-optimal temperatures, as these properties are known to affect the nucleoid morphology and the physical properties of the cytoplasm. Overall, these studies characterize the role of nucleoid exclusion in the spatial organization of protein aggregates, and its robustness to different stresses that *E. coli* encounters in its natural habitats.

2.7. Chemotaxis System and Chemoreceptor Protein Tsr

Escherichia coli cells are subject to fluctuations in their growth environments. To ensure optimum growth across these fluctuations, when not beneficial, they must be able to sense and then either avoid or adapt to these changes (Burkart *et al.* 1998; Jones and Armitage 2015). In general, the adaptation process consists of altering the patterns of gene expression and, ultimately, cellular behavior.

Following such environment cues, many bacteria are able to direct their movement towards a favorable direction, by a process known as taxis (for a review see, (Jones and Armitage 2015)). The movement is mediated by structures called as flagella, a fine thread like organelle extending outward from the membrane and cell wall. Flagella allow the bacteria to swim, move forward or change direction in response to varying environments (Berg and Turner 1993). In other words, bacteria in general, do not swim aimlessly. Instead, they direct their movement towards attractants such as sugars and amino acids, while avoiding harmful repellants such as phenols and bacterial wastes. This movement towards attractants and away from repellents is known as chemotaxis (Berg and Brown 1972).

A typical chemotactic response involves: detection of the attractant or repellent by the cell, integration and amplification of stimulus inputs, and generation of a coherent output signal that elicits an appropriate locomotor response by flagellar movement (Bren and Eisenbach 2000; Parkinson *et al.* 2005; Hazelbauer *et al.* 2008). To accomplish these tasks, bacteria evolved a remarkable chemotaxis system of signal transduction.

The chemotaxis system in *Escherichia coli* is one of the most thoroughly studied systems of signal transduction. *E. coli* senses amino acids serine, aspartate, and other attractant compounds with its transmembrane chemoreceptors, known as methyl-accepting chemotaxis proteins (MCPs) (Hazelbauer *et al.* 2008). MCPs are organized in trimers-of-dimers that form intercommunicating clusters, positioned primarily at the cell poles (Maddock and Shapiro 1993; Zhang *et al.* 2007; Greenfield *et al.* 2009).

E. coli has five MCPs: Tsr (Taxis to serine and repellents), Tar (Taxis to aspartate and repellents), Tap (Taxis to dipeptides), Trg (Taxis to ribose and galactose) and Aer (Taxis to oxygen) (Parkinson *et al.* 2005). All five receptors form ternary signaling complexes with CheW and CheA and are positioned at the cell poles (Lybarger and Maddock 2000). Tsr, one of the prominent and abundant chemoreceptors, existing roughly 3000 per cell, is a serine chemotaxis protein that mostly cluster at the cell poles (Zhang *et al.* 2007; Hazelbauer *et al.* 2008).

In *E. coli,* the MCPs cluster in membrane-associated patches (Hazelbauer *et al.* 2008). These patch of clusters are further stabilized by associating, forming ternary complexes with histidine autokinase, CheA and CheW proteins (Skidmore *et al.* 2000; Endres 2009). The purpose of clustering within these patches is thought to contribute to notable features of the chemotactic signaling system: high sensitivity, wide dynamic range, extensive cooperativity and precise adaptation (Hazelbauer *et al.* 2008).

Studies have suggested that the cluster formation occurs via an energy-free, self-assembly process known as stochastic nucleation (Wang *et al.* 2008; Greenfield *et al.* 2009). Recent cryo-electron microscopy and tomography techniques have imaged how these chemoreceptor signaling complexes cluster extensively in patches at the poles of *E. coli* (Figure 2.12) (Zhang *et al.* 2007; Hazelbauer *et al.* 2008). These patches are generally circular or ellipsoid and have varying sizes of ~200–400 nm in diameter. Interactions in these patches enable the chemoreceptors to control multiple kinases and other chemoreceptors present inside the cell (Hazelbauer *et al.* 2008).

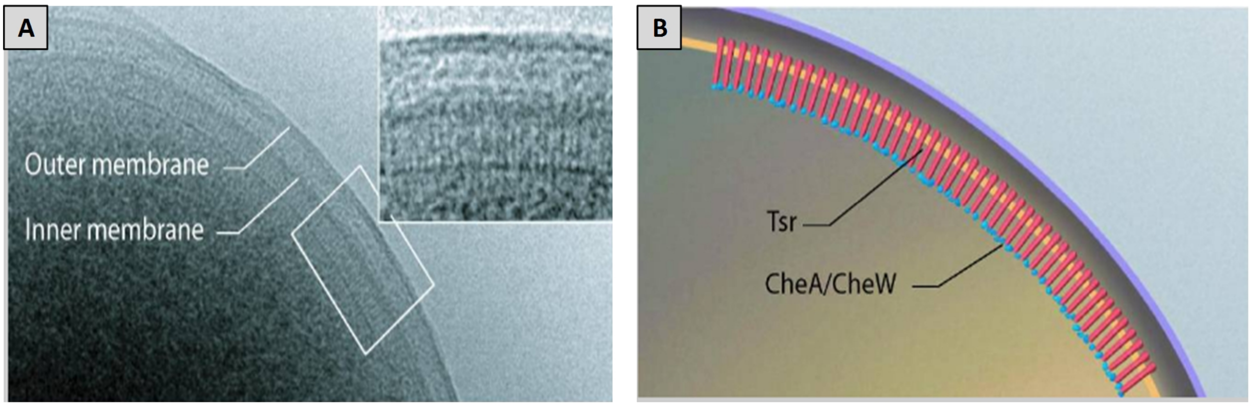

Figure 2.12: A patch of membrane-embedded chemoreceptors near the pole of an intact cell. (A) Low-dose electron microscopy (EM) cryo-projection image of the polar region in an *E. coli* cell, with the chemoreceptor array shown in greater detail in *Inset*. (B) Schematic representation of the cell polar region of *E. coli*, illustrating the assembly and orientation of the chemotaxis receptor array. Figure from (Zhang *et al.* 2007), Copyright (2007) National Academy of Sciences, U.S.A.

A variety of imaging studies have advanced our understanding on the spatial organization of chemoreceptor clusters at the cell poles (Kentner and Sourjik 2006; Thiem *et al.* 2007; Greenfield *et al.* 2009; Sourjik and Armitage 2010). Various mechanisms have been proposed by which this may occur, based on experimental evidences that support the claims. In one study, it has been suggested that the clusters first form at midcell by stochastic self-assembly (Greenfield *et al.* 2009), followed by attachment to cell membranes, and are then dragged to the poles by cell growth after a few rounds of cell division (Thiem *et al.* 2007). Another study suggested that newly produced chemoreceptor clusters diffuse freely in the cell membrane and that the pole curvature contributes to their localization, given the clusters ability and tendency to fit this curvature (Huang *et al.* 2006; Endres 2009; Draper and Liphardt 2017).

A recent study proposed the existence of a diffusion-and-capture mechanism being responsible for polar localization of chemoreceptor clusters (Shapiro *et al.* 2009; Laloux and Jacobs-Wagner 2014). According to these works, the newly produced chemoreceptor proteins diffuse in the cytoplasmic space until it encounters, and is captured by, a target protein to which they adhere, in this case is the membrane (Rudner *et al.* 2002; Laloux and Jacobs-Wagner 2014) (Figure 2.13 A). The study also hypothesized the possibility that diffusion-and-capture is a general feature of protein localization in most bacteria. The existence of a diffusion-and-capture mechanism is further supported by the observation that a fairly constant fraction (∼7%) of Tsr proteins exhibit free diffusion over the entire cell surface at any given time (Oh *et al.* 2014). Another recent study, supporting the existence of a diffusion-and-capture mechanism, has suggested that the chemoreceptor clusters interact with the components of Tol-Pal, a widely conserved protein complex of the cell envelope of gram-negative bacteria (Figure 2.13 B), making it responsible for capturing the clusters at the poles (Santos *et al.* 2014).

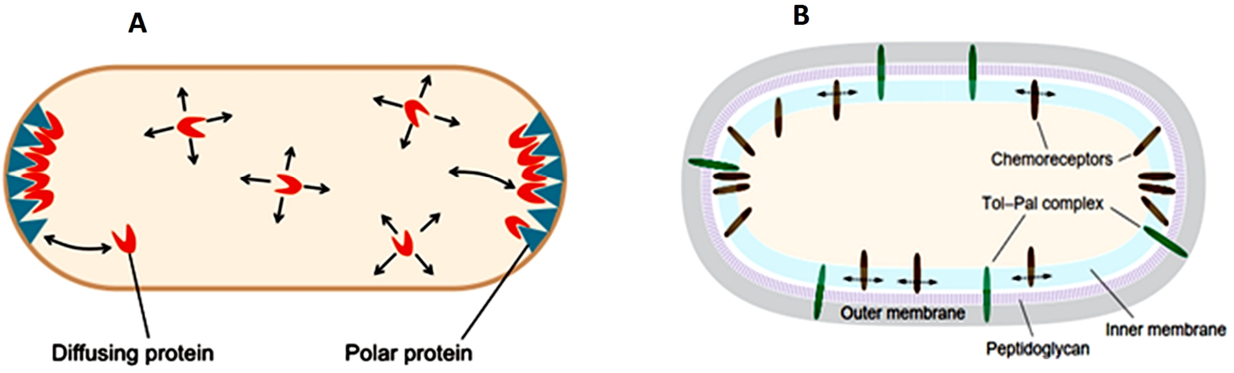

Figure 2.13: Schematic representation of the subcellular localization of chemoreceptor proteins (A) Chemoreceptor protein (e.g. Tsr chemoreceptors) diffusing in the cytoplasm, indicated by single arrows become trapped at the poles by a diffusion-and-capture mechanism due to the presence of intact Tol-Pal complexes. (B) The Tol-Pal complexes are spanned across the inner membrane, through periplasm to the outer membrane. Reprinted and adapted with permission from The Company of Biologists Ltd: (Journal of Cell Science) (Laloux *et al*), copyright (2014) and John Wiley & Sons Ltd, © 2014: Molecular Microbiology (Santos *et al*).

In **Publication IV,** we study whether nucleoid exclusion contributes to the segregation and retention of Tsr chemoreceptor clusters at the cell poles. Measurements were conducted using also cells lacking Tol-Pal components, in order to assess the contribution of the nucleoid in the intricate internal spatial organization of *E. coli* cells.

2.8. Effects of Growth Media and Antibiotics

E. coli cells vary significantly in growth rate, depending on the type and amount of nutrients in the growth media. For example, the doubling time of *E. coli* in optimal growth conditions (LB, 37°C) can be as short as 20 minutes. Meanwhile, the doubling times of *E. coli* in some poor media, such as minimal broth supplemented with glycerol as the carbon source, can reach approximately 110 minutes (Hadizadeh Yazdi *et al.* 2012). Many factors, such as the macromolecular composition, cell size, chromosome copy number, etc. are sensitive to growth rate (Tao *et al.* 1999; Dennis and Bremer 2008; Klumpp *et al.* 2009; Jin *et al.* 2013).

This acceleration/deceleration in growth rate is known to affect the process of transcription (Dennis and Bremer 2008; Lloyd-Price *et al.* 2016). For example, RNAp in nutrient-rich media is primarily allocated to the active transcription of the *rrn* operon, coding for rRNA and tRNA, which accelerates protein synthesis and growth rates (Jin *et al.* 2013). Meanwhile, in minimal medium, the distribution of RNAp on the chromosome differs, influencing the transcription of *rrn* operon (Jin *et al.* 2012).

Aside from gene expression dynamics, the nucleoid morphology in *E. coli* is also sensitive to the quality of the media. Experimental data show that there is a strong correlation between transcriptional activity and the dynamics of nucleoid structure (Dillon and Dorman 2010). Recent studies have shown that, when grown in rich media like LB media, the cells can contain between 4-8 chromosome equivalents, with the nucleoids being more compact and having well-defined edges (Hadizadeh Yazdi *et al.* 2012; Jin *et al.* 2013; Stracy *et al.* 2015). In contrast, under poor growth conditions, each cell contains only between 1-2 chromosomes, and the nucleoids are expanded, appearing more diffuse and having lesser defined edges (Hadizadeh Yazdi *et al.* 2012; Jin *et al.* 2013; Stracy *et al.* 2015). Additionally, when grown in rich media, the chromosome segregation occurs well before cell division, with the replicated chromatids being coupled by a thin inter-daughter filament before complete segregation, whereas during slow growth chromosomes stay adjacent until cell division occurs (Hadizadeh Yazdi *et al.* 2012). This suggests that media richness has more influence on the nucleoid compaction than the growth rate *per se.* It should be also noted that nucleoid-associated proteins (NAPs) involved in nucleoid compaction are sensitive to the growth phase of the cell, as their relative levels vary between exponential and stationary phases (Tao *et al.* 1999). Finally, it has also been reported that the time required to complete a single round of replication and subsequent chromosome segregation following cell division varies from ~70 to 150 min depending on the growth conditions (Jin *et al.* 2015).

Another set of substances known to affect the nucleoid morphology in *E. coli* cells are antibiotics. Antibiotics are chemical substances that kill or inhibit the growth of microorganisms. Some of them are known to inhibit transcription or translation, suggesting that both of these processes play an important role in the overall nucleoid morphology (Zimmerman and Murphy 2001; Cabrera *et al.* 2009; Bakshi *et al.* 2014; Sanamrad *et al.* 2014). Chloramphenicol, one of the most broad-spectrum and potent antibiotic, halts translation elongation by blocking access of charged tRNA to the ribosomal A site. This results in a lack of essential structural proteins, in this case NAPs, required to maintain the nucleoid's morphology, leading to nucleoid compaction (Zimmerman and Murphy 2001). Rifampin, another broad-spectrum and potent antibiotic, forms a very stable complex with the RNA polymerase and blocks transcription initiation (McClure and Cech 1978). Similar to the effect of chloramphenicol, blockage of transcription when treated with rifampin, also results in lack of essential structural proteins required to maintain the nucleoid's morphology, instead leading to nucleoid expansion (Cabrera *et al.* 2009). Both chloramphenicol and rifampin when added to the growth media enhance the compaction and expansion of nucleoids respectively.

Other antibiotics have different effects that, in the end, indirectly, also affect cellular processes such as protein aggregates formation, cell elongation etc. E.g., streptomycin is a potent aminoglycoside that targets ribosomes and causes translational errors (Sharma *et al.* 2007). This accelerates the appearance of protein aggregates inside the cell (Ling *et al.* 2012). Meanwhile, ampicillin, another broad-spectrum antibiotic, halts cell division by covalently binding to penicillin binding proteins (PBPs), which leads to cell elongation (Spratt 1975).

In **Publication II**, we study the robustness of the process of nucleoid exclusion of protein aggregates to differing media richness and antibiotic stresses that directly affect the nucleoid sizes, aggregates, and cell size. The measurements were conducted using HU protein fused to fluorescent protein mCherry that allows us to visualize the nucleoid morphology and dynamics over time.

2.9. Diffusive Nature of Bacterial Cytoplasm

The cytoplasm is a gel–like substance that fills the interior of the cell. It is composed of an aqueous solution, the cytosol, and a variety of suspended particles with specific functions. It is a highly concentrated solution containing macromolecules of different sizes ranging several orders of magnitude, from sub-nanometer (inorganic ions and metabolites) to nanometer (proteins) to tens and hundreds of nanometers (ribosomes, plasmids, enzymatic megacomplexes, granules) to micrometers (protein filaments and nucleoid). In a bacterial cell, all the contents of the cell are contained within the cytoplasm and surrounded by an intact cell membrane (Alberts *et al.* 2002). Unlike eukaryotes, bacteria do not possess defined pervasive cytoskeletal machinery that allow the movement of proteins from one location to another inside the cell. Therefore, in bacteria, diffusion is the most likely means of intracellular movement, molecular transport and cytoplasmic mixing (Elowitz *et al.* 1999; Parry *et al.* 2014).

Diffusion is the random movement of particles caused by thermal motion. A diffusion process depends on temperature, size of the particles and viscosity of the fluid. It is characterized by diffusion coefficients of the moving particle and its possible deviations from the ‘normal’ diffusive behavior. A diffusing particle can either have a normal symmetric random motion or an anomalous, sometimes asymmetric, diffusive motion. Both normal and anomalous diffusive motions have been reported in *E. coli* (Golding and Cox 2006; Niu and Yu 2008; English *et al.* 2009; Weber *et al.* 2010; Bakshi *et al.* 2011; Coquel *et al.* 2013).

The diffusion coefficient of a spherical particle in a solution is given by Stokes-Einstein equation:

$$D = \frac{kT}{6\pi\eta r}$$

where k is the Boltzmann constant, T is temperature, η is the dynamic viscosity of the medium and r is the radius of the particle. It has been reported that the viscosity of bacterial cytoplasm is up to 10 times higher than that of water, thus being of significance to the diffusion coefficients according to the Stokes-Einstein relationship (Puchkov 2013). Studies have also reported the experimental diffusion coefficients for various proteins (10-100 kDa) in the cytoplasm of *E. coli* and they ranged between 0.2 and 10 $\mu m^2 s^{-1}$ (Mika and Poolman 2011). For example, the diffusion coefficient of a green fluorescent protein (GFP) in the cytoplasm of a live *E. coli* cell is 6 to 8 $\mu m^2 s^{-1}$ (Elowitz *et al.* 1999; Konopka *et al.* 2006), while in solution it is 87 $\mu m^2 s^{-1}$ (Swaminathan *et al.* 1997).

Diffusion, as the primary method of intracellular protein movement in *E. coli*, is known to play a major role in controlling the rates of cellular processes (Parry *et al.* 2014). For example, it promotes a homogenous distribution of cytokinetic proteins involved in cell division and is involved in equal partitioning of cellular components between the daughter cells during division (Niu and Yu 2008; Huh and Paulsson 2011a). Interestingly, when ATP synthesis is inhibited, chromosomal loci, plasmids, protein filaments diffuse more slowly (Weber *et al.* 2012; Parry *et al.* 2014). This suggests that ATP-dependent enzymatic activity contributes to the diffusion of biomolecules in living cells (Parry *et al.* 2014).

Several recent studies have investigated the nature of the bacterial cytoplasm and suggest that it is diffusive in nature (Elowitz *et al.* 1999; Golding and Cox 2006), even though it displays properties characteristic of glass-forming liquids and cellular metabolic activity fluidizing it (Parry *et al.* 2014). In addition, it is also highly crowded (Elowitz *et al.* 1999; Golding and Cox 2006). Namely, the presence of cytoplasmic proteins, RNAs, ribosomes and other heterogeneous macromolecules appears to suffice to the emergence of 'macromolecular crowding' (Odijk 1998; Ellis 2001). This effect has been shown to facilitate the condensation of the bacterial nucleoid, influence the interactions between nucleoid and cytoplasm and affect the diffusion dynamics of particles inside the cell (Zimmerman and Murphy 1996; Ellis 2001).

Other interesting properties include the fact that the cytoplasm-nucleoid boundaries are dynamic in nature, with the cytoplasm being denser at the poles (e.g. ribosomes preferentially locate at these regions) (Bakshi *et al.* 2014; Sanamrad *et al.* 2014), probably due to higher entropic forces in the nucleoid-occupied regions of the cell (Mondal *et al.* 2011).

Osmotic upshift with osmolytes like sodium chloride in the growth medium also results in effects of increased macromolecular crowding in the cytoplasm (Konopka *et al.* 2009; Mika and Poolman 2011). Thus, it is crucial to understand the physical nature of the cytoplasm, since it defines the dynamics of intracellular processes and thus the cellular physiology. Recent methods that allow researchers to mechanically slow-down cytoplasmic diffusion to count single-molecule proteins *in vivo* (Okumus *et al.* 2016) will assist in these future efforts.

In **Publication III**, we study the functionality of nucleoid exclusion phenomenon under sub-optimal temperatures from microscopy images of individual *E. coli* cells with fluorescently tagged aggregates and nucleoids within. We characterize the aggregates diffusive properties at such sub-optimal temperatures.

2.10. Partitioning of Cellular Components

An aspect essential for normal cellular functioning in bacteria is the proper localization of newly replicated sister chromosomes during the division process, as this is required for a faithful inheritance of genetic material (Mulder and Woldringh 1989; Woldringh *et al.* 1994; Wang *et al.* 2005). Equally important is the proper partitioning of other cellular components, such as plasmids, protein complexes, and molecular machineries, such as RNA polymerases, ribosomes, etc.

This partitioning affects the daughter cells' growth rate (Klumpp and Hwa 2008, 2014; Bakshi *et al.* 2012), by dictating their internal composition (such as RNA and protein numbers (Huh and Paulsson 2011a, 2011b)), and thus the kinetics of processes such as transcription, translation and cell division (Woldringh 2002; Montero Llopis *et al.* 2010; Thanbichler 2010; Mondal *et al.* 2011; Chai *et al.* 2014; Castellana *et al.* 2016; Moffitt *et al.* 2016).

Previous studies on the internal spatial organization of protein aggregates have identified that *E. coli* lacks active diffusion processes and that the aggregates tend to locate at the cell poles (Figure 2.14). Consequently, they hypothesized that there is, an energy-free process, possibly volume exclusion caused by the nucleoid at midcell, responsible for this behavior (Winkler *et al.* 2010; Coquel *et al.* 2013).

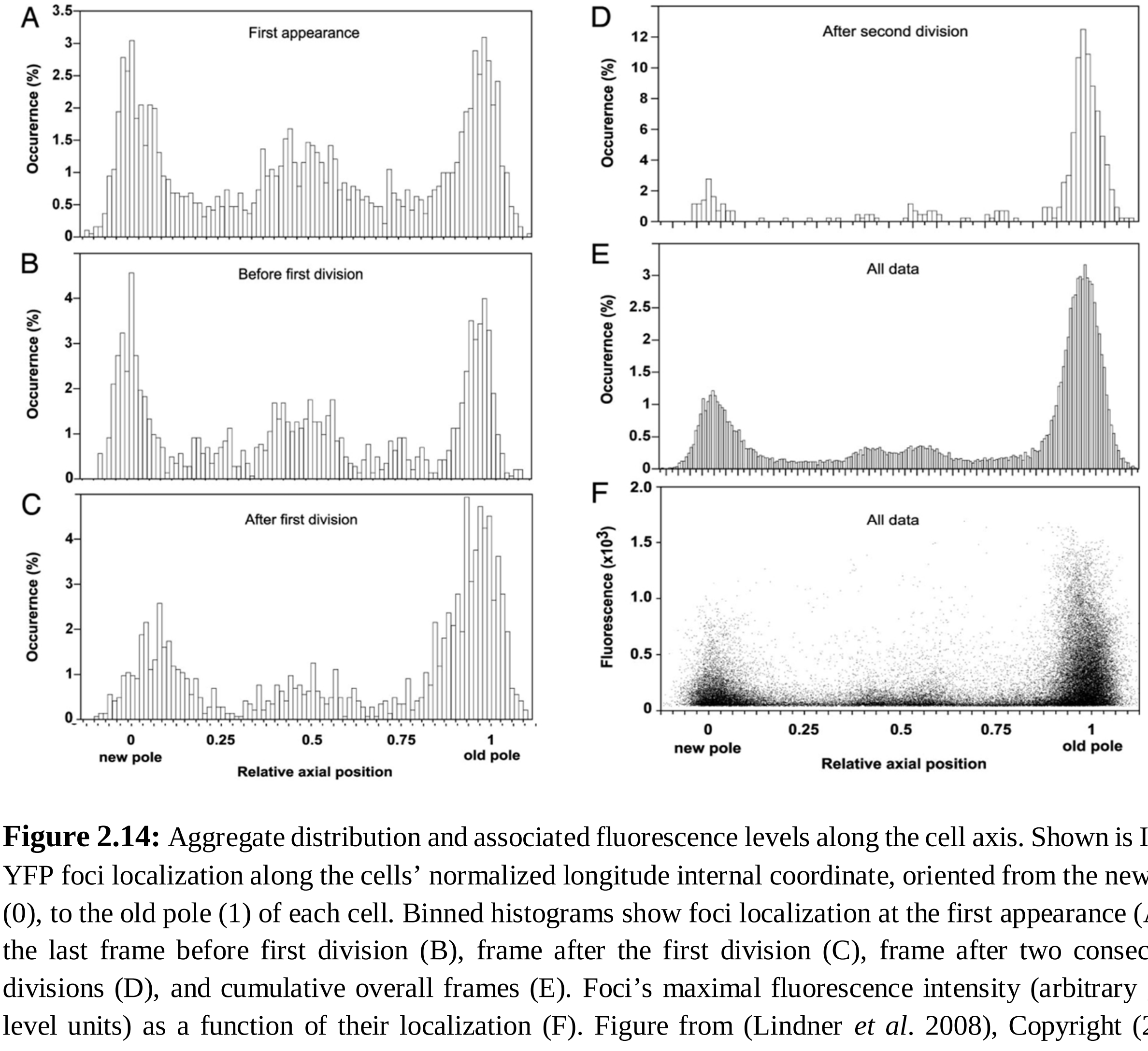

Figure 2.14: Aggregate distribution and associated fluorescence levels along the cell axis. Shown is IbpA-YFP foci localization along the cells' normalized longitude internal coordinate, oriented from the new pole (0), to the old pole (1) of each cell. Binned histograms show foci localization at the first appearance (A), at the last frame before first division (B), frame after the first division (C), frame after two consecutive divisions (D), and cumulative overall frames (E). Foci's maximal fluorescence intensity (arbitrary gray-level units) as a function of their localization (F). Figure from (Lindner *et al*. 2008), Copyright (2008) National Academy of Sciences, U.S.A.

Similar behaviors have been reported for other cellular components. For example, it has been established that plasmids are mainly located at the poles or in the cytosolic space between nucleoids (Erdmann *et al.* 1999; Ringgaard *et al.* 2011; Vecchiarelli *et al.* 2012; Reyes-Lamothe *et al.* 2014; Le Gall *et al.* 2016; Wang *et al.* 2016). Also, large protein complexes, such as the hybrid polyketide that assembles as an enzyme megacomplex (Straight *et al.* 2007), are segregated to the poles. Similarly, it was shown that the bound ribosomes (50S and 30S together) are excluded from the nucleoid, while the free ribosomal subunits are not (Bakshi *et al.* 2014; Sanamrad *et al.* 2014).

The preference for polar localization of the large protein aggregates, when combined with cell division, passively creates polar asymmetries. Subsequent cell division events generate diversity between cells, with a few cells of these subsequent generations carrying most protein aggregates, which appears to accelerate their aging process (Stewart *et al.* 2005; Lindner *et al.* 2008; Winkler *et al.* 2010). This was observed, for example, in the case of IbpA aggregates formed during a transient stress condition, which tend to accumulate at the cell poles and then, during cell division events, are partitioned into daughter cells which contain a new pole, free of aggregates, and an old pole, with the inherited aggregates. Following more divisions, the lineages will produce a few cells containing most aggregates, while most other cells are ‘rejuvenated’, in that they are free from aggregates (Stewart *et al.* 2005; Lindner *et al.* 2008).

The mechanisms responsible for the heterogeneous spatial organization of the cellular components in bacteria are not completely exploited. Recent studies proposed different mechanisms, e.g., diffusion and capture, membrane curvature of the pole of the cells, etc., as the possible mechanisms responsible for the preference for polar localization of many proteins and protein complexes inside the cell (Rudner and Losick 2010; Laloux and Jacobs-Wagner 2014; Draper and Liphardt 2017).

In this thesis, using efficient fluorescent probes, *in vivo* single-cell, single-molecule time-lapse microscopy, tailored image and signal processing techniques and stochastic biophysical models, we investigate the role of nucleoid exclusion from midcell in the preference for polar localization exhibited by both unwanted protein aggregates and the self-assembling, transmembrane Tsr chemoreceptor clusters responsible for chemotaxis. Further, we study the robustness of the underlying mechanisms to external perturbations and stressful conditions.

3. Single-Cell Methods for Localization Studies

This chapter provides an overview of the single-cell biology and fluorescence microscopy techniques employed in this thesis. These include the use of fluorescent probes for the detection and tracking of protein aggregates, of chemotaxis clusters, of the nucleoid. In addition, we describe the stochastic modelling techniques employed to produce models that accurately represent the systems studied.

3.1. Fluorescent Probes and Microscopy

Over the last few decades, the use of fluorescent molecules in biological research has been the primary choice of visual reporters in microscopy-based applications. The increased usage of both fluorescent dyes as well as genetically modified fluorescent proteins has revolutionized the field of cell biology.

Their increased usage over time is due to their versatility, sensitivity and quantitative capabilities. The use of fluorescent dyes for staining cells is already a standard practice in cell microscopy. Developments in this field during the past few decades has given the ability to image live cells with the development of biological fluorophores in the form of fluorescent proteins. The use of fluorescent proteins have enabled the visualization of cellular structures at an increased spatial resolution, when compared to standard dyes. This fluorescent protein labeling approach has advanced our understanding on the subcellular architecture and internal dynamics of the bacterial cell (Gahlmann and Moerner 2014). They also provided critical insights of various molecular processes in live cells, including at the sub-nano second time resolution.

In short, the use of fluorescent proteins for *in vivo* imaging has become an indispensable tool in many areas, ranging from the study of the complex behavior of single molecules, to the study of protein localization (Liu *et al.* 2015), and to the study of the dynamics of molecular processes, including quantitative studies of gene expression dynamics.

The revolution in biological imaging resulted from the discovery of the green fluorescent protein (GFP), isolated from the jellyfish *Aequorea victoria* (Shimomura *et al.* 1962), along with its gene fusion (Prasher *et al.* 1992; Tsien 1998) and its first application as fluorescence marker *in vivo* (Chalfie *et al.* 1994). Since then, several improved fluorescent protein variants have been developed using advanced genetic engineering techniques, leading to the rapid expansion of their usage, and their availability spanning the entire visible spectrum of light (Shaner *et al.* 2004; Day and Davidson 2009).

In addition, progresses over the two decades have improved several properties of these fluorescent proteins, such as enhancing their oligomerization, maturation and degradation, their folding, their brightness and their photostability (Shaner *et al.* 2005) (Figure 3.1). These improvements now allow performing multicolor imaging of nearly any set of proteins (Wu *et al.* 2015), characterize three-dimensional structures, and record dynamic processes in live cells.

Also, advances in the field led to the emergence of new spectral characteristics associated to these fluorescent proteins. One such characteristic is providing the fluorescent proteins with the means for controlled photoactivation and photoconversion (Day and Davidson 2009). Namely, these tailored fluorescent proteins can be switched on and off or be converted to a different emission wavelength upon irradiation with a specific wavelength of excited light (Lukyanov *et al.* 2005; Shaner *et al.* 2007). These capabilities have been exploited to produce many advanced imaging techniques in microscopy, e.g. in super-resolution microscopy (Huang *et al.* 2009), which enabled the visualization of cellular components with higher molecular resolution. It is to be noted that these advances were made possible through the development of not only the fluorescent probes, but also of the imaging optics.

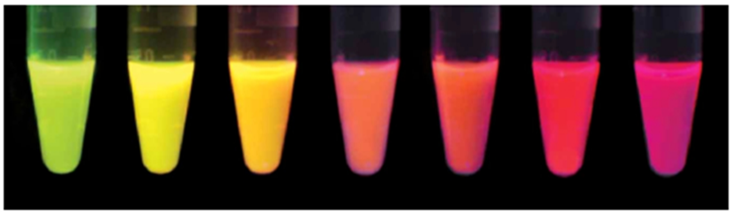

Figure 3.1: Purified fluorescent proteins derived from Discosoma sp. red fluorescent protein (from left to right, mHoneydew, mBanana, mOrange, tdTomato, mTangerine, mStrawberry, and mCherry). Reprinted from (Shaner *et al*, 2004) with permission from Nature Publishing Group.

In general, an ideal fluorescent protein employed for tagging a protein of interest for an imaging experiment should exhibit the following properties: enhanced brightness and photostability, as well as minimal crosstalk in its excitation and emission channels. Most importantly, it should confer zero toxicity and sufficient inertness when fused with the protein of interest, so as to not perturb the native functionality of the protein in the chosen system (Shaner *et al.* 2005). Drawbacks of many fluorescent proteins include blinking (intensity fluctuations) and limited photostability (Ha and Tinnefeld 2012). In addition, some fluorescent proteins artificially induce clustering under certain conditions, which may alter the native localization of the fused target proteins (Landgraf *et al.* 2012). The use of traditional fluorescent dyes in live cell imaging is limiting, as the dyes non-specifically bind and label the entire cell surface, impairing the cell growth (Pitchiaya *et al.* 2014). On the other hand, organic fluorophores, compared to fluorescent proteins and dyes, have a smaller size, and superior stability and enhanced brightness (Pitchiaya *et al.* 2014). Nevertheless, the use of fluorescent proteins for live-cell microscopy offers several advantages in terms of sensitivity and specificity, critical in studies of, among other, proteins spatial dynamics and organization.

In live cell microscopy, in order to detect the emitted fluorescence signal from fluorescent proteins accurately, the signal should be significantly brighter than the cellular background fluorescence, referred to as autofluorescence, which is a naturally-occurring phenomenon inherent to all living organisms (Andersson *et al.* 1998). To achieve this, first, the selection of a bright fluorophore that absorbs and emits light outside the spectrum of the autofluorescence is recommended (Ha and Tinnefeld 2012). Second, media and solvents exhibiting low autofluorescence should be selected. Third, the choice of light source, optics, illumination scheme, and spectral detectors contribute directly to signal-to-noise ratio and have to be optimized to minimize the autofluorescence in microscopy experiments.

The most commonly used illumination scheme in fluorescence microscopy is the conventional wide-field epifluorescence. In this microscopy, the incident lamp's excitation light excites an area of ~10 x 10 μm^2 of the sample (Lang *et al.* 2006; Webb and Brown 2012). The volume of the incident lamp illuminated on the sample is quite large, causing the out-of-focus fluorescent light also to contribute towards the background fluorescence intensity. The wide-field epifluorescence microscopy is recommended to be used in combination with strong fluorophores as the probe molecules (Lang *et al.* 2006). Epi-fluorescence microscopy is an important tool in bacterial studies as it enables the visualization of cellular components. For example, (nucleoid (Chazotte 2011), cell membrane (Lewenza *et al.* 2006)), specific molecules, e.g., RNA molecules (Golding and Cox 2004) and to assess the bacterial viability (Seo *et al.* 2010). However, it has severe limitations such as reduced image resolution, excess out-of-focus fluorescent light, and photobleaching of the sample (Sanderson *et al.* 2014).

A more efficient suppression of the excess out-of-focus light and enhanced image resolution is achieved by other methods such as Confocal Microscopy (Pawley 2006), Total Internal Reflection Fluorescence (TIRF) Microscopy (Axelrod 1981), and Highly Inclined and Laminated Optical sheet (HILO) Microscopy (Tokunaga *et al.* 2008). These methods were developed with the primary goal of rejecting the excess out-of-focus light during the imaging, which in turn is dependent on the illumination volume exposed onto the sample. Confocal microscopy is based on reducing the focal volume of the excitation light and, consequently, the out-of-focus light. This is achieved with a pinhole aperture that ensures that light reaching the detector comes only from the confocal plane of the sample (less than 1 μm^3) where the excitation light was focused on, rejecting the out-of-focus information (Figure 3.2) (Pawley 2006; Sanderson *et al.* 2014). However, the limiting factor with confocal microscopy is its slow point-scanning image acquisition, restricting the study of fast molecular dynamics inside the cell. The scan speed can be improved with setups, such as using spinning-disc confocal microscopy, which simultaneously illuminates multiple regions of the sample, minimizing the phototoxicity (Frigault *et al.* 2009).

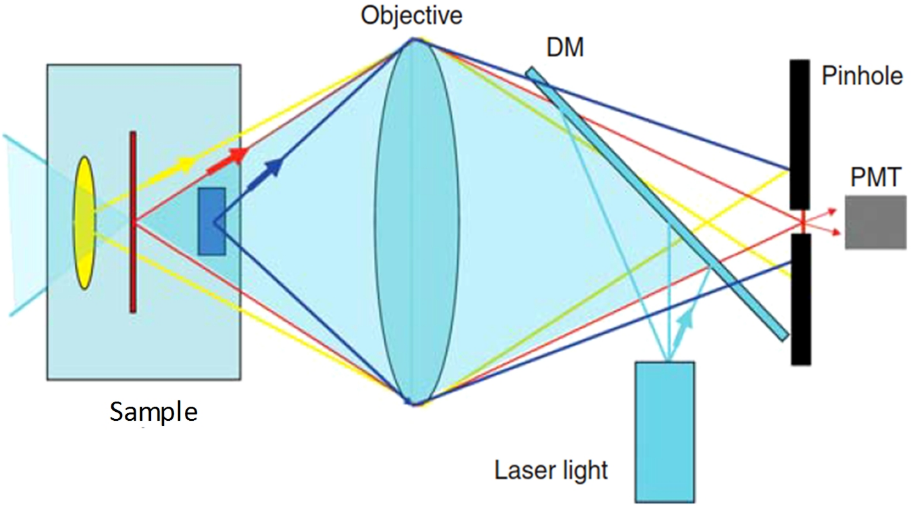

Figure 3.2: Principle of operation of a laser scanning confocal microscope. Laser light is focused on the sample by reflection from the dichroic mirror (DM) and the objective lens. The laser excites the fluorescence throughout the sample that passes through the DM and is focused onto the image plane. A pinhole only allows light from the confocal plane of the sample to reach the photomultiplier tube (PMT). Reprinted from (Sanderson *et al*, 2014) with permission from Cold Spring Harbor Laboratory Press.

TIRF microscopy offers better optical sectioning of the sample when compared to confocal microscopy. This is achieved by directing the excitation light through a coverglass towards a thin layer of aqueous sample, at a sufficiently shallow angle such that total internal reflection occurs because of the refractive index decrease at the glass/water interface (Sanderson *et al.* 2014). The light in total internal reflection creates a thin lamina of evanescent wave that penetrates this interface and decays exponentially with the distance from the interface. TIRF illuminates a region 50-200nm deep into the sample, smaller than the diffraction limit (Liu *et al.* 2015). Due to its restricted illumination range, TIRF based microscopy only probes molecules close to the coverglass surface, e.g. near the cell membrane. To selectively illuminate regions deeper than the TIRF range without significantly reducing the signal-to-noise ratio, HILO microscopy was developed (Tokunaga *et al.* 2008). In HILO microscopy, the incident angle at the coverglass-sample interface is slightly smaller than the critical angle. This creates a slightly inclined light sheet through the sample and just above the coverglass, resulting in minimal out-of-focus light.

Phase-contrast microscopy allows the visualization of high contrast images of transparent living organisms (Zernike 1942). Phase contrast microscopy employs an optical mechanism that converts slight differences in refractive index and cell density into easily detectable variations in light intensity, which can be visualized as differences in image contrast. Phase-contrast microscopy is especially useful for studying microbial cell size, shape, and motility. As such, it can be used, e.g., to study the proliferation of living cells. It can further be used to detect bacterial compartments, such as inclusion bodies (Lindner *et al.* 2008) and endospores inside the cell.

3.2. Imaging Nucleoid by Staining and Fluorescent Protein Tagging

The morphology of *E. coli* nucleoids is sensitive to the growth rate, the richness of the growth medium, and to the application of external perturbations such as nutrient-downshift or treatment with drugs (Zimmerman and Murphy 2001; Cabrera *et al.* 2009; Fisher *et al.* 2013; Jin *et al.* 2013). The use of basic DNA dyes, cell fixation and electron microscopy has allowed the conduction of research that revealed the irregular and dispersed morphologies that nucleoids exhibit (Robinow and Kellenberger 1994). However, it has been shown that nucleoid morphology is highly sensitive to the method of fixation (Kellenberger *et al.* 1992). Various technical advances in fluorescence-microscopy-based live-cell imaging and the emergence of fluorescent proteins/stains provide us nowadays with many means of visualization of nucleoids.

Several methods have been proposed to visualize *E. coli* nucleoids. An ideal fluorescent stain would permeate the cell membrane and provide bright, long-lasting fluorescence upon binding to the DNA without perturbing the cell functioning, growth or nucleoid morphology (Bakshi *et al.* 2014). The use of the popular fluorescent stain DAPI (4', 6-diamidino-2-phenylindole) has a long history and thus is considered as the traditional method to visualize nucleoids (Kapuscinski 1995). However, the presently available spectrum of fluorescent proteins for live-cell imaging offers multiple possibilities of monitoring time-dependent changes in nucleoid morphology, that are providing new insights in the organization and maintenance of the *E. coli* nucleoid during the cell cycle (Wu *et al.* 2015). The emergence of novel DNA dyes in recent years has further enabled us to perform time-lapse imaging of nucleoids without the need of cell fixation, as in case of DAPI (Bakshi *et al.* 2014).

DAPI is a popular DNA staining dye that is known to stain nucleoids by permeating the cell membrane and associating with A-T rich regions within the minor groove of double-stranded DNA with little or no cytoplasmic labeling (Kapuscinski 1995). DAPI can be used to stain both live and fixed cells. However, the efficient membrane permeabilization of the dye is visible only in fixed cells, making its usage more adaptable to these cells (Chazotte 2011). Cells stained with DAPI can be visualized by epifluorescence microscopy (Figure 3.3 A), with a mercury lamp and a DAPI filter set. The dye is excited in the near UV at ~350nm and emits at ~450nm. Despite its wide usage in imaging of the nucleoids, DAPI has many limitations. First, the concentrations of DAPI used for live-cell imaging is generally very high and, therefore, it can be toxic for growing cells (Zink *et al.* 2003). Finally, exposure of DAPI-stained cells to a UV lamp perturbs the nucleoid structure, causing the nucleoid morphology to appear expanded. These limitations make DAPI a non-ideal nucleoid stain.

Other DNA dyes for visualizing the nucleoid under a wide variety of conditions *in vivo* have been studied recently (Bakshi *et al.* 2014). SYTOX Orange, is one such dye, and it allows non-perturbative imaging of the nucleoid morphology at a single-cell level, without affecting the cell growth rate. The dye can be visualized using Confocal Laser Scanning Microscopy or HILO microscopy with a 543-nm laser illumination and a Texas Red filter (Figure 3.3 B). The quality of the images and the level of detail obtained with this dye are very similar to the images obtained when using HupA-mCherry (Bakshi *et al.* 2014). The nucleoids appear well distinguished, with little or no cytoplasmic labeling caused by the dye. Single-cell, time-lapse imaging of the nucleoids using a sensitive camera produces good quality images of nucleoids with minimal photobleaching, making this dye an excellent choice for studying the spatial distribution of nucleoids.

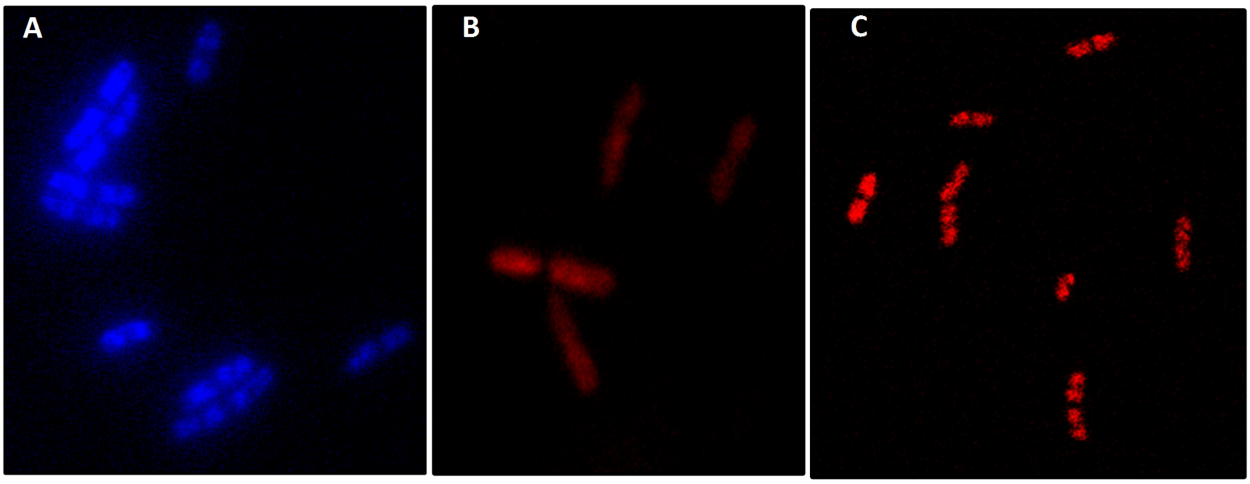

Figure 3.3: Fluorescence microscopy images of *E. coli* cells showing the nucleoid of each cell when visualized using fluorescent dyes (or) fluorescent proteins. (A) Epifluorescence imaging of DAPI stained nucleoids (B) HILO imaging of SYTOX-Orange stained nucleoids and, (C) Confocal imaging of HupA-mCherry tagged nucleoids.

Another approach to visualize the nucleoid morphology and study its dynamics over time *in vivo* is the use of Nucleoid Associated Proteins (NAPs). NAPs, when fused with efficient fluorescent proteins like YFP or mCherry, serve as an excellent marker for nucleoid visualization (Fisher *et al.* 2013). Protein HUα (HupA), encoded by *hupA* gene, is a subunit of nucleoid-associated proteins HU that serves as an excellent marker for fluorescent tagging of the nucleoid. The protein HU, when fused to GFP, was previously shown to colocalize with DAPI, suggesting that it is a natural tracer of DNA (Wery *et al.* 2001). Protein HupA, when fused with fast maturing fluorescent protein such as mCherry, can be used to study the spatial distribution of the nucleoids (Fisher *et al.* 2013) and also to understand the role of the nucleoid in the intracellular organization of proteins and other cellular components (Rudner and Losick 2010; Wang *et al.* 2013).

The chimeric gene *hupA-mCherry* can be engineered and inserted into the chromosome or, it can be cloned into a plasmid, which is then transformed into the host cell (Fisher *et al.* 2013). The fluorescently tagged nucleoids in individual cells can be visualized using Confocal Laser Scanning Microscopy or HILO microscopy when illuminated with a 543nm laser and HQ585/65 or Texas Red filter equipped in the microscope (Figure 3.3 C). The images obtained by confocal microscopy have higher contrast and a good level of detail, with well-separated nucleoids as discussed in (Fisher *et al.* 2013), while images obtained by HILO microscopy provide higher penetration into the sample without significantly compromising the signal-to-noise ratio. However, HU-based imaging strategies have some limitations in time-resolved studies. For example, in the transition from exponential growth to early stationary phase, the HupA protein is replaced with its structural homologs, such as Dps and IHF. This results in the decrease of fluorescence levels upon entry into stationary phase, making this fluorescently fused protein ideal only for studies of cells during exponential growth (Bakshi *et al.* 2014; Wu *et al.* 2015).

3.3. Single-Molecule Fluorescence Microscopy

Most of our current knowledge about the internal organization of bacteria comes from biophysical and fluorescent microscopy studies accumulated over the last few decades. These studies have significantly contributed to our understanding of the intracellular organization of bacteria, with advances in live-cell imaging methods and the subsequent developments in fluorescent fusion proteins, enabling us to probe biological events at the single-cell, single-molecule level. Such methods have facilitated our understanding of the internal organization of bacterial cells at an unprecedented level of sensitivity, specificity and spatial resolution.

Single-molecule studies, in particular, have gained much attention in the recent years as these are the unique method to monitor the *in vivo* spatial localization of several macromolecules, including RNA (Golding and Cox 2004; Nevo-Dinur *et al.* 2012; Pitchiaya *et al.* 2014), functional proteins (Betzig *et al.* 2006; Yu *et al.* 2006; Greenfield *et al.* 2009), as well as other cellular components such as protein aggregates (Winkler *et al.* 2010), plasmids (Reyes-Lamothe *et al.* 2014), RNA polymerases (Bakshi *et al.* 2012), ribosomal subunits (Mondal *et al.* 2011; Sanamrad *et al.* 2014), etc.. This is made possible by the usage of photoactivatable or photoconvertible fluorophores fused to target (Wang and Rudner 2014) and by limiting the expression of target fluorescent molecules to very low concentrations, in order to break the diffraction limit and distinguish each of them accurately (Pitchiaya *et al.* 2014). These two experimental approaches, along with the emergence of super-resolution imaging techniques, such as photoactivation localization microscopy (PALM) and stochastic optical reconstruction microscopy (STORM) which effectively breaks the diffraction limit barrier achieving a spatial resolution of up to 10nm, make up the multitude of single-molecule fluorescence microscopy techniques (Walter *et al.* 2008; Huang *et al.* 2009).

Recent works have proposed several methodologies to probe the localization of RNA as well as proteins with fluorescent probes *in vivo* (Yu *et al.* 2006; Raj and van Oudenaarden 2008; Nevo-Dinur *et al.* 2012; Pitchiaya *et al.* 2014; Moffitt *et al.* 2016). Protein localization studies, in general, require the fusion of the target protein with a fluorescent probe. The advent of single protein molecule tagging with fluorescent proteins has occurred in the past decade, aimed at achieving the real-time monitoring of protein production kinetics in live cells (Cai *et al.* 2006; Yu *et al.* 2006; Taniguchi *et al.* 2010). The fused fluorescent probe, because of its short maturation time, allows the detection of proteins with single- molecule sensitivity (Yu *et al.* 2006).

In the recent years, with the advent of new genomic techniques and several fluorescent proteins, single protein molecule studies have expanded its applicability and are being used to characterize the functioning of crucial cellular processes (Gahlmann and Moerner 2014; Stracy *et al.* 2015; Lee *et al.* 2016). Contrary to proteins, the method of RNA labeling can be divided into two categories, namely indirect and direct labeling schemes. The former employs the usage of sequence-complementary oligonucleotides or fluorophore-labeled RNA binding probes, which are associated to a specific RNA motif, e.g. in Fluorescence *in-situ* hybridization (FISH) (Femino *et al.* 1998; Raj and van Oudenaarden 2008; Pitchiaya *et al.* 2014). Conversely, direct labeling employs chemically reactive functional groups or structural motifs existing in the natural RNA for fluorophore conjugation (Pitchiaya *et al.* 2014). Currently, indirect labeling is becoming more predominant in single-molecule fluorescence microscopy.

One of the first methods developed to study the spatial localization of RNA molecules inside cells was FISH (Raj and van Oudenaarden 2008). This method is based on the partial permeabilization of cells and subsequent addition of fluorescently-labeled DNA probes that hybridize to complementary regions of the RNA molecule. A recent study, using FISH, demonstrated that the some of the RNA molecules of bacterial transcriptome are spatially organized and suggested that this organization is key into modulating the post-transcriptional fate of those RNAs in bacteria (Moffitt *et al.* 2016). Additionally, FISH is also used to characterize the expression levels of RNA *in vivo* (Pitchiaya *et al.* 2014). However, this methodology has the following limitations: long probes with poor cell membrane permeability, variability in fluorophores labeled to oligonucleotides, and low signal-to-noise ratio caused by the unbound and non-specifically bound probes (Pitchiaya *et al.* 2014). Several studies have been proposed to address these limitations that aim to improve cell permeability and minimize the impact of fluorescence mediated self-quenching exhibited by proximal probes (Femino *et al.* 1998; Raj and van Oudenaarden 2008).

3.3.1. MS2-GFP Tagging Method

Imaging of RNA *in vivo* can be achieved by employing RNA binding proteins, which when fused with fluorescent proteins, tag the RNA molecule upon its production. Currently, the use of MS2, a well-known protein-RNA tethering system, is one such *in vivo* method that allows the detection and tracking of single RNAs in living cells (Fusco *et al.* 2003; Golding and Cox 2004; Golding *et al.* 2005; Coulon *et al.* 2014). The usage of the MS2 system was pioneered by Singer and co-workers 15 years ago in *Saccharomyces cerevisiae* (Fusco *et al.* 2003) and only later it was adapted for use in *E.coli* (Golding and Cox 2004). The method is based on (i) fusing the target gene with multiple copies of an RNA motif, specifically in the untranslated region of the target gene encoding the target mRNA and (ii) fusing the RNA binding protein with a fluorescent reporter, so that when multiple fused proteins bind to the expressed RNA it appears as a bright “spot” under the fluorescence microscope. The DNA constructs employed for this method can be genetically engineered either into a plasmid and transformed into the host cell or can be integrated into the host chromosome.

The MS2 coat protein is derived from the native bacteriophage MS2, which binds to a unique 21nt genomic RNA of the phage that spontaneously adopts a stem-loop secondary structure (Keryer-Bibens *et al.* 2008) and aims at encapsulating the viral genome (Peabody 1993; Bertrand *et al.* 1998). This property of the MS2 coat protein was exploited and its fluorescent fusion proteins were constructed to tag the target RNA. Such RNAs are currently used to study cellular processes in different model organisms (Fusco *et al.* 2003; Golding *et al.* 2005). Two genetic constructs are necessary for this. The first construct carries the gene of interest fused with a tandem array of MS2 binding sites (BS), usually placed on a single copy plasmid (Golding *et al.* 2005; Muthukrishnan *et al.* 2012). The stability of this construct is increased by inserting random sequences between the successive MS2 binding sites. The second construct codes for the expression of RNA binding MS2 coat protein, dimerized and fused to the N terminus of GFPmut3, a GFP variant (MS2d-GFPmut3) and is placed on a high-copy plasmid (Golding *et al.* 2005) so that sufficient MS2d-GFP proteins are always available (Figure 3.4 A).

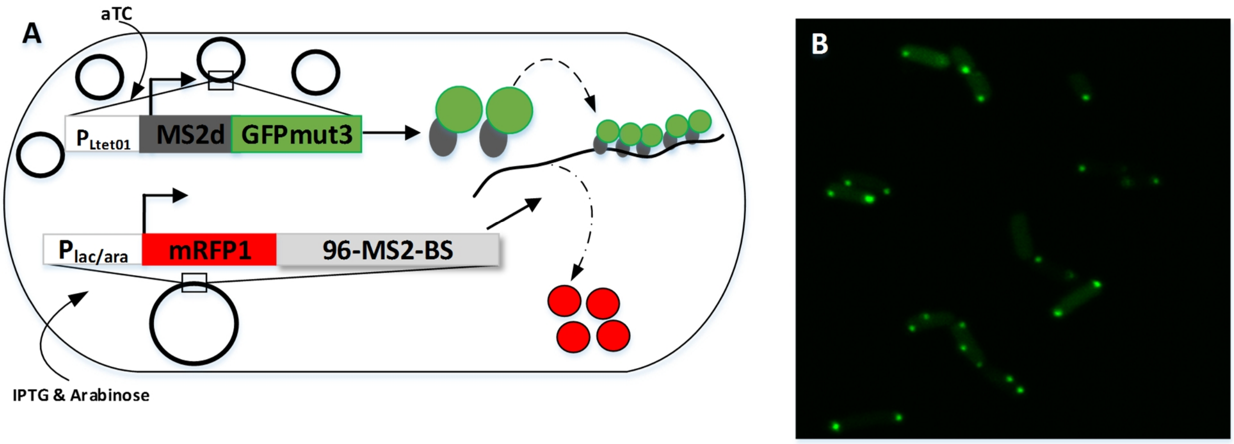

Figure 3.4: *in vivo* RNA detection with MS2-GFP method. (A) Schematic description of the MS2 based tagging system for RNA detection. Target RNA carrying 96 MS2 binding sites is produced from a regulatable promoter placed in a single copy F-plasmid (represented as big circle). MS2d-GFP molecules (green balls) are produced by a high-copy plasmid (represented as small circles). In the presence of inducers (aTC, IPTG and Arabinose), both the genetic constructs get co-expressed and the MS2d-GFP molecules bind to the target RNA. The target RNA also has a coding region for a red fluorescent protein, mRFP1 (represented as red balls). (B) Example image of *E.coli* cells expressing both target RNAs and MS2d-GFP proteins. Individual RNA molecules appear as a bright fluorescent spot when imaged under confocal laser scanning microscope. The uniform background of the cells is due to unbound MS2d-GFP diffusing inside the cell.

When imaging the cells under the fluorescence microscope, the reporter MS2d-GFP is extensively expressed in the cell prior to the activation of the target gene, so as to be able to detect any target RNA expressed. The consequent binding of multiple MS2d-GFP proteins to the same target RNA renders it much brightness than the fluorescence of the unbound MS2d-GFP that is freely diffusing in the cell (Figure 3.4 B) (Golding *et al.* 2005; Xie *et al.* 2008).

Under confocal laser scanning microscopy, the target RNA bound by multiple MS2d-GFP proteins can be detected as a distinct diffraction limited spot (referred in this thesis as MS2-GFP-RNA complex)(Figure 3.4 B) that moves slowly inside the cell (Golding and Cox 2004; Golding *et al.* 2005; Muthukrishnan *et al.* 2012). Given that the target RNA is wrapped by the MS2d-GFP proteins, which protects it from natural degradation (Fusco *et al.* 2003; Golding *et al.* 2005) or these fluorescent spots do not lose intensity over time (Tran *et al.* 2015), thus allowing to track single RNA molecules without the influence of photodegradation caused by laser illumination (Muthukrishnan *et al.* 2012).

The use of the MS2 tagging system in live-cell imaging has allowed to probe the patterns of RNA localization and *in vivo* detection of individual transcription events inside the cell with single-molecule sensitivity (Fusco *et al.* 2003; Golding *et al.* 2005). It should be noted that these studies are performed in live cells, unlike the traditional methods like FISH that require the fixation of the cells. However, this method also has some drawbacks that hinder its usage as a probe for RNA dynamics and localization studies. First, the MS2 tagging system can be used only to probe the target RNAs that are engineered to contain MS2 stem-loops. Second, an incomplete and heterogeneous binding of the fused MS2 proteins to the target RNA might affect its quantification, as fluorescence intensities fluctuate between tagged RNAs (Fusco *et al.* 2003; Wu *et al.* 2012). Lastly, the heterogeneous binding of fused MS2 proteins to target RNAs might affect the mobility, functioning, and/or localization of the tagged RNAs (Wu *et al.* 2012).

Aside from the MS2 tagging system, other viral protein-RNA tethering systems have recently been engineered for tagging RNA molecules, namely, the PP7 derived from the PP7 bacteriophage (Chao *et al.* 2008; Larson *et al.* 2011), and the λ_N peptide, derived from the lambda bacteriophage (Daigle and Ellenberg 2007; Lange *et al.* 2008). The protein-RNA tethering systems mentioned above are orthogonal to each other, i.e. the MS2 does not bind the PP7 binding site and the vice-versa (Chao *et al.* 2008; Lange *et al.* 2008). This property of orthogonal tethering can be exploited to simultaneously image up to three different RNA targets, or probe three different regions of a single RNA (Lange *et al.* 2008; Hocine *et al.* 2013).

In **Publication I and Publication III**, we made use of MS2-GFP tagging method, to study the kinetics and long-term spatial distribution of individual RNA molecules (tagged with multiple MS2-GFP proteins) at optimal and sub-optimal temperature conditions.

3.3.2. Tsr-Venus System

Visualization of individual protein in single, live cells is the ultimate sensitivity of quantifying gene expression or determining the localization of individual target proteins by tracking their movement *in vivo* (Larson *et al.* 2009). However, in addition to simply observing individual protein molecules, one must be able to record these stochastic events of protein production in the cell at any given time (Yu *et al.* 2006; Larson *et al.* 2009).

This was first reported in a study conducted by Yu and co-workers in *E. coli*. The authors made use of fast maturing fluorescent protein Venus, fused to the chemotaxis receptor protein, Tsr (Tsr-Venus) that anchors the membrane and cluster at the cell poles. The genetic constructs employed for this study are genetically engineered into the host chromosome. However, the coding gene Tsr, fused with fluorescent protein Venus, can also be maintained on a plasmid and transformed into the host cell.

Typically, the high diffusion rates of single protein molecules inside live cells renders their imaging very difficult. In this study, the approach used to overcome this problem was to use Tsr, since these proteins naturally localize at the membrane, and thus have a much reduced diffusion rate than proteins that diffuse in the cytoplasm (Yu *et al.* 2006). This single-protein detection has been achieved using a confocal microscope and a focused laser beam using short laser pulses that allow the shutter to remain open for longer periods of time, preventing significant diffusion of the fluorescent reporter (Xie *et al.* 2008).

Tsr, a well-studied methyl-accepting chemotaxis protein (MCP) containing two transmembrane domains, was fused to the N-terminus of the fluorescent protein Venus. The chimeric gene *tsr-venus* was then incorporated into the *E. coli* chromosome, replacing the native *lacZ* gene (Figure 3.5 A). The strain in this study is referred to as SX4 (Yu *et al.* 2006).

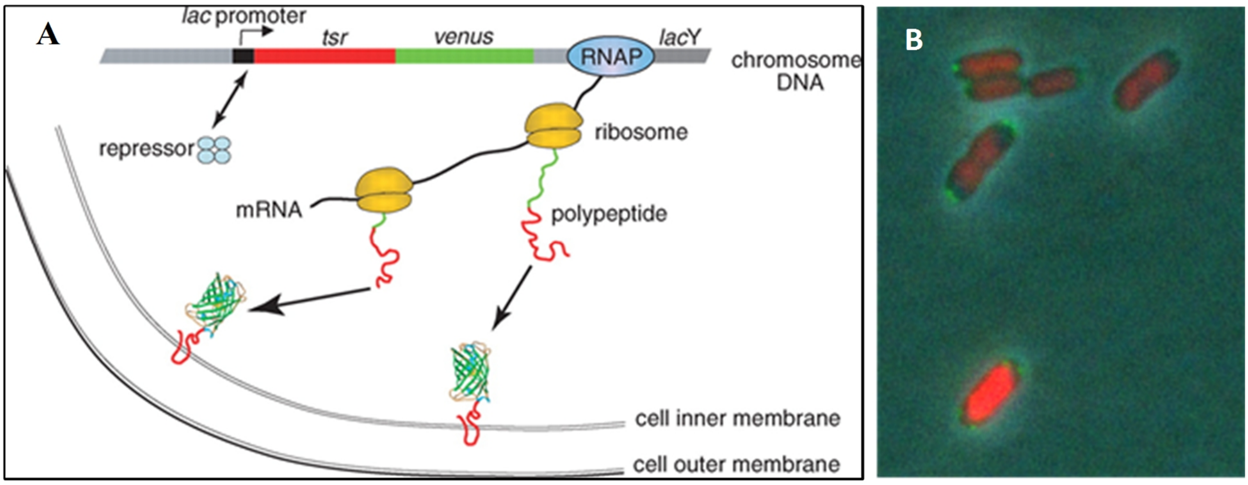

Figure 3.5: Experimental design for the visualization of fluorescent tagged chemoreceptor Tsr-Venus. (A) Schematic diagram of the chromosomally fused *tsr-venus* gene under the control of *lac* promoter. Transcription of one mRNA by an RNA polymerase, coupled with translation by ribosomes, results in the production of a few copies of protein molecules that attach onto the inner membrane. From (Yu *et al* 2006). Adapted and reprinted with permission from AAAS. (B) Example merged microscopy images of Tsr-Venus clusters (Green) and HupA-mCherry tagged nucleoids (Red), visualized by HILO imaging with an overlay of Phase contrast image.

It is noted that, because the *tsr* gene is highly expressed (Mowbray 1999), a small amount of exogenous Tsr-Venus produced by the artificial gene, is expected to pose minimal perturbation to the cell's normal functioning. This chimeric gene can also be maintained on a plasmid if needed. The expressed Tsr-Venus can be visualized using confocal microscopy or HILO microscopy and are easily visible as they form clusters at the cell poles (Figure 3.5 B).

In **Publication IV**, we made use of Tsr-Venus to study whether nucleoid exclusion plays a role in the polar localization of Tsr chemoreceptor protein clusters.

3.4. IbpA –YFP System

The *in vivo* detection of misfolded proteins (protein aggregates) at the single-cell level can be achieved by fusing a fluorescent protein to a gene encoding chaperones or small heat shock proteins (sHSP). The fluorescently tagged chaperones or sHSPs bind and directly interact with aggregating proteins and are known to increase cellular tolerance to stress conditions, by favoring protein aggregation. Inclusion body protein A (IbpA), is one such sHSP, ubiquitously present in *E. coli*'s inclusion bodies (IBs) (Thomas and Baneyx 1998). Also, it is a protein aggregation marker (Lindner *et al.* 2008), directing protein aggregates to specific cellular sites, here into the inclusion bodies (IBs). The genetic constructs employed for this study are genetically engineered into the host chromosome and the strain is referred to as MGAY (Lindner *et al.* 2008).

To determine the presence of protein aggregates and study their localization and spatial dynamics, Lindner and co-workers engineered a fluorescently labeled heat shock protein in an *E. coli* strain. To achieve this, the endogenous gene *ibpA* was replaced with its chromosomal gene fused to the yellow fluorescent protein (YFP) gene, making it *ibpA-yfp* (Lindner *et al.* 2008). The fluorescent IbpA-YFP, when visualized using confocal microscopy, are visible as fluorescent foci inside the cell, and were shown to faithfully identify the localization of aggregated proteins *in vivo* and to accumulate at the inclusion bodies (IBs) (Figure 3.6).

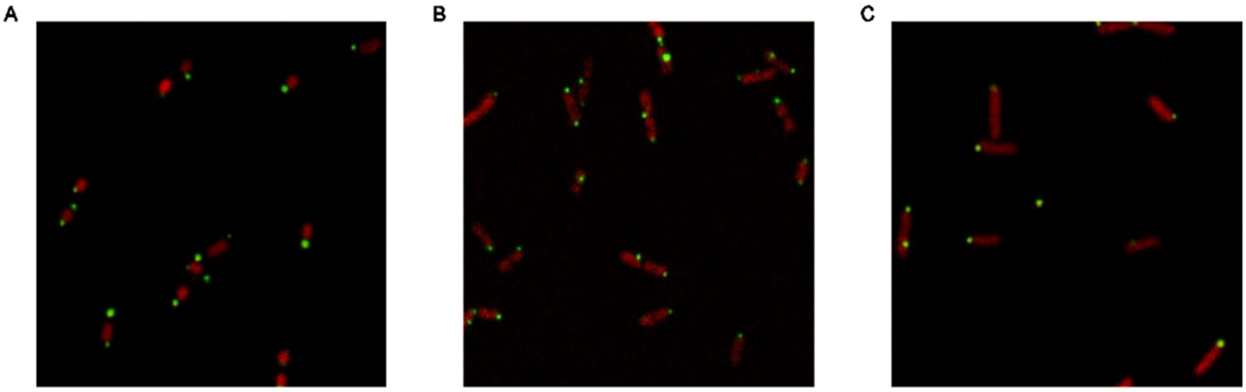

Figure 3.6: Example images of fluorescently tagged IbpA protein aggregates visible in green, while HupA-mCherry tagged nucleoids are visible in red. The example images result from merging the simultaneously obtained images from the red and green channels. Cell borders were detected from Phase Contrast images (not shown). Image obtained from **Publication II**.

Antibiotic streptomycin, known to target the ribosomes and cause translational errors (Sharma *et al.* 2007), accelerate the appearance of protein aggregates (Ling *et al.* 2012). This consequently leads to increased number of induced inclusion bodies, typically ranging from 1-5. These induced inclusion bodies were usually found to be located at the cellular poles, in mid or quarter-cell positions, presumably at the location of future septation sites independent of the presence of IbpA (Lindner *et al.* 2008). However, under native non-stressed conditions, no inclusion body could be visualized by the Phase Contrast Microscopy.

In **Publication II**, we made use of IbpA-YFP to characterize the robustness of nucleoid exclusion phenomenon to external perturbations and medium richness.

3.5. Stochastic Modelling

A biological model is simplified representation of a biological system that aims to assist in a better understanding of the system, by characterizing solely the relevant components of the biological phenomenon studied in that system. Once validated by comparison with empirical data, the model serves as a framework to test new hypotheses. Also, the model assists in the interpretation of additional empirical data, such as data on the system's behavior under new conditions. The usage of models has proven to be of use in providing key insights on biological phenomena and on the idealization of novel empirical tests.

A model representing a biological system should follow several criteria. For example, the resolution of the model (i.e. the level of detail of the modelling of the real system) should be identical to that of the empirical data used to generate it (e.g. there is little point in modelling all molecules in a cell, if the microscope used to test the validity of the model can only observe the cell borders). Similarly, models should be used to test hypotheses at the same level of resolution as the measurements. Also, the model should include all variables that may affect its behavior at its level of resolution, while, if possible, exclude those that do not.

3.5.1. Algorithms for Simulating Stochastic Reactive Systems

In agreement with the above criteria, as the measurement systems in the laboratory have moved away from standard techniques such as qPCR, Western Blot (as the ideal measurement techniques to obtain the mean values of protein and RNA numbers in cell populations), towards the single-cell microscopy (which provides either mean or absolute numbers of protein and RNA molecules in individuals), so have the modelling strategies of genetic circuits have moved from deterministic (see e.g. (Kauffman 1969; Monk 2003) to stochastic (for a review see e.g. (Ribeiro 2010).

Aside from revealing the stochastic nature of intracellular processes, the above-described advances in microscopy have also revealed the importance of the internal spatial organization of cells.

Following this, modelling strategies have and are currently being developed to cope with this aspect (see e.g. (Casanova *et al.* 2001; Andrews and Bray 2004).

One of the main reasons why deterministic and stochastic rate equations do not accurately predict cellular reactions is because they rely on bulk reactions that require millions of interactions between molecules. Also, while the deterministic prediction of the mean behavior of the system is adequate in some cases, it will not reflect the stochastic nature of the system, which is crucial in many biological systems, particularly those involving species that exist in very low copy numbers, such as transcription factors (Glick 1995; Fusco *et al.* 2003; Gordon *et al.* 2004; Taniguchi *et al.* 2010).

The most accurate method for simulating simple stochastic chemical reaction systems is the 'Stochastic Simulation Algorithm (SSA)' developed by D. Gillespie in 1976 and 1977 (Gillespie 1976, 1977). This algorithm, which consists of Monte Carlo simulations of the chemical master equation (CME), is suitable for spatially homogenous or well-stirred chemical systems. As such, it is rigorously based on the same microphysical principles that underlie the CME, which determines the probability that each chemical species has a specific concentration at a given time.

Shortly, the SSA has the following workflow: first, a thorough knowledge about the system should be gained. Namely, one needs to know the number of reactant molecules existing in the system at one point in time, and the reactions that can exist between these molecules, along with the respective rate constants. Given this information, first, at that point in time, we calculate the propensity of occurrence of each of the possible reactions based on the number of reactants and their rate constants. Next, we generate a random number that is used to select, as a function of these propensities, which of the possible reactions actually will occur next. Finally, we calculate the time for the occurrence of the next reaction, based on the propensities of each of the possible reactions. This value is randomly drawn from an exponential distribution, whose mean is equal to the mean time for the next reaction to occur.

3.5.2. Simulators of Stochastic Biological Processes

A simulator is a tool that can implement a model and simulate its dynamics. Here we consider simulators of bioprocesses at the molecular level that can include multi-delayed events, dynamic compartments and partitioning of molecules. The dynamics of the models is driven by the delayed SSA (Roussel and Zhu 2006), which able to handle reactions with multiple time delayed events. The first simulator developed for this purpose was SGNSim (Ribeiro and Lloyd-Price 2007).

Our studies require more complex components, than that of simple chemical reactive systems. Namely, it requires to know where are the molecules distributed in the space and what is the 'topology' of that space (e.g. it needs to consider if there are compartments in the space). Therefore, to implement our models, we made use of SGNS2, a development of SGNSIM, that can simulate multi-delayed stochastic reactions within a system of hierarchical, interlinked, and transient compartments (Lloyd-Price *et al.* 2012). Because of this, it can simulate a wide range of biological processes at the level of microscopy observations.

Specifically, SGNS2 was used, for example, to study partitioning of protein aggregates in cell division, known to have effects on cellular aging. The utility of SGNS2 is clearly demonstrated in (Gupta *et al.* 2015), where several models were constructed to demonstrated the findings. Of particular interest in this study is the model of biased partitioning of protein aggregates which have consequences of aging in *E. coli* leading to reduced cellular fitness (Stewart *et al.* 2005; Lindner *et al.* 2008). It is shown that, using SGNS2, the results of cell growth rate from simulations resembled to the one measured in (Stewart *et al.* 2005). Aside from studies on partitioning of protein aggregates, SGNS2 allows to simulate coupled transcription and translation elongation, cell perturbations, e.g. gene deletion, over-expression, copy and mutation, can be modeled as well, providing insights in gene expression studies (Mäkelä *et al.* 2011).

3.5.3. The Use of Compartments to Model Internal Cellular Organization

As noted, bacterial cells are not homogenous, having instead an intricate internal spatial organization (Alberts *et al.* 2002). This organization tangibly affects reactions' probabilities. Because of this, these cells' cytoplasm does not fulfill the criterion of homogenous system required for simple stochastic modelling.

Meanwhile, simulating explicitly the location of each molecule involved in, e.g., a genetic circuit, at each moment in time can rapidly become unfeasible computationally. To overcome this problem, and because it sufficed to accurately represent the phenomenon of nucleoid exclusion in our works, we made use of transient compartmentalization techniques (Lloyd-Price *et al.* 2012). Following the specificities of SGNS2, sub-compartments can be created, destroyed and divided at runtime inside a main compartment, and each is capable of containing subsets of the reactants in the cell. These reactants can be allowed (or not) to react inside the compartment, and to move between the sub-compartment and the cell cytoplasm (the 'main' compartment)

Sub-compartments contain a subset of the reactants in a simulation, which interact with the rest of the system. Each compartment is a well-mixed reactor and can have means of exchange of molecules with the main compartment. The compartments in SGNS2 simulator are organized in a hierarchical fashion, which implies that higher-level compartments always contain lower-level compartments.

In **Publication I**, to test whether the localized anisotropies of protein aggregates in directionality, given the homogeneity of their speeds, can generate the observed heterogeneity in their long-term spatial distributions, we constructed two one-dimensional models to simulate the diffusion of the complexes within the cell. While, in **Publication IV**, we made use of a spatial stochastic model of a cell that included a nucleoid as well as Tol-Pal complexes at the poles, to study the forces that drive the long-term spatial distribution of Tsr- Venus clusters.

4. Computational Tools for Image and Data Analysis

This chapter provides an overview of the computational tools used in the thesis for the analysis of microscopy images. These tools were used for cell segmentation, spot detection and tracking, and nucleoid detection from the microscope images.

4.1. Cell Segmentation and Lineage Construction

When conducting experiments involving different fluorescent probes and multimodal microscopy, robust image analysis and signal processing tools are needed for the accurate and unbiased extraction and quantification of the desired measure/variable of the study.

The first step in microscopy image analysis is cell segmentation, where cells are detected and segmented from the background. Next, in order to expand the analysis to time series, consecutive images need to be temporarily aligned, e.g. using cross-correlation. This alignment removes possible drifts in the image that may have occurred during the image acquisition process. Such drifts can occur for several reasons, e.g. temperature shift, media inflow etc. and, if ignored, will hamper the proper tracking of cells over time. Once individual cells are tracked, it is possible to construct cell lineages.

In order to perform multi-modal cell segmentation in individual images, we made use of the tailored software tool "MAMLE" (multi-resolution analysis and maximum likelihood estimation) (Chowdhury *et al.* 2013). It performs automatic segmentation of the cells, but then allows the results to be manually corrected, if necessary. The level of accuracy obtained by this tool is therefore very high, although laborious (Figure 4.1A).

Once individual images are segmented, in order to establish a temporal relationship between the cells of consecutive frames, we use the software tool "CellAging" (Häkkinen *et al.* 2013). The temporal relationships between cells from sequential frames are established as follows. A segment overlapping the most is associated with each segment in the next frame. If the association is 1-to-1, then the cell did not divide and it must be the same cell. If the association is 1-to-many, the cell divided. If the association is 0-to-1 or 1-to-0, there is no relationship.

All **Publications I-IV** made use of these two software tools to perform cell segmentation.

4.2. Fluorescent Spot Segmentation and Tracking

Both **Publication I** and **Publication III** requires segmentation of fluorescent MS2-GFP-RNA complexes and IbpA-YFP aggregates. These fluorescent spots are detected in each cell, at each frame of the time-lapse microscopy, using MAMLE (Chowdhury *et al.* 2013). The results of spot segmentation are illustrated in (Figure 4.1 B and C). Displacement vectors of these spots are obtained by determining their positions in the consecutive frames and subtracting the final and initial position **(**Figure 4.1 D).

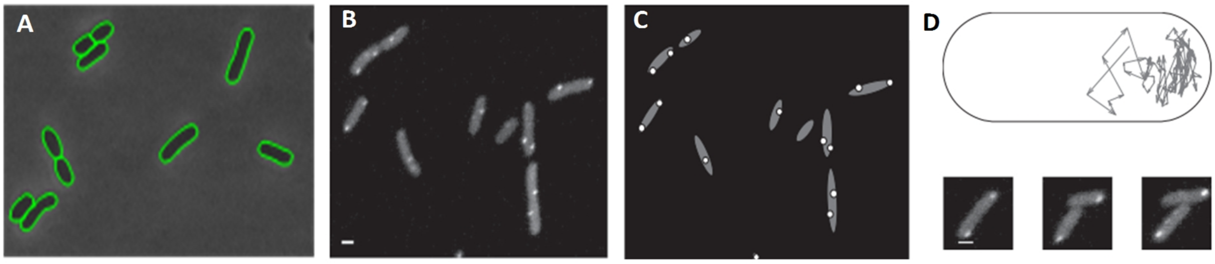

Figure 4.1: (A) Example image of cells using Phase Contrast Microscopy, and the results of cell segmentation (green curves). (B) Example image of cells with fluorescent MS2-GFP-RNA complexes within. (C) Segmentation results of the image in (B) with cells (gray) and complexes (white). (D) One example of extracted displacement vectors of a complex from its consecutive positions in the cell. Three images of the cell are shown below, taken at 40, 80, and 120 min (displacement vectors are from the upper cell). The contrast of these images were enhanced for easier visualization. Image adapted from **Publication I**.

In **Publication III**, we performed spot tracking using a semi-automatic method to quantify from the images the directionality and diffusion of spots, as assessed by the mean squared displacement (MSD). To determine the MSD, the tracking of spots must be accurate. To achieve this, first, spot segmentation is performed using MAMLE. An ID number is provided to the spot (automatically and then manually adjusted if needed) to identify it in each frame. Next, possible errors in the detection of the location of the spot are manually corrected. Afterwards, a displacement vector is automatically inserted, based on the shortest distance between the locations of the spot in consecutive frames.

For **Publication II**, detection of IbpA aggregates inside the cells was performed by defining them as connected components with each pixel having fluorescence intensity above a certain threshold. For this, it was assumed that the background pixel intensities follow a Gaussian distribution with the same median and upper quartile as the pixels inside the cell. A threshold was selected, such that the probability of mislabeling a pixel from this distribution is less than 0.005 for aggregates.

In **Publication IV**, we defined a ‘Tsr cluster’ (or ‘spot’) as a connected component with each pixel having a light intensity above a threshold. For this, Gaussian-based spot detection combined with an adaptive local threshold step is performed. It assumes that the background pixel intensities follow a Gaussian distribution (Annila *et al.* 2016). The threshold is then selected for each cell separately, based on the fitted distribution. From the segmented image, the number of clusters are counted and the area of each cluster is calculated, by counting the number of pixels within.

4.3. Nucleoid Detection and Segmentation Methods

For single time-point imaging, nucleoid (s) are visualized using either DAPI/ SYTOX dye staining or HupA-mCherry tagging. However for time-lapse imaging of nucleoids only HupA-mCherry tagging is used. The detection and segmentation in single time-point imaging is performed in each cell, while in the case of time-lapse imaging it is performed in each frame.

For **Publication I** and **Publication III**, we performed nucleoid detection. In **Publication I** the method used was based on the total fluorescence intensities of nucleoids along the major and minor cell axes. Then, the intensity distribution is fitted to a piecewise-constant probability density function. Meanwhile, in **Publication III**, we used a Gradient Path Labelling algorithm (Mora *et al.* 2011). This method starts by labeling each pixel based on its gradient azimuth and propagating these labels according to its gradient paths. Afterwards, a segmented image is obtained with the number of labels equaling the number of nucleoids (Figure 4.2 A).

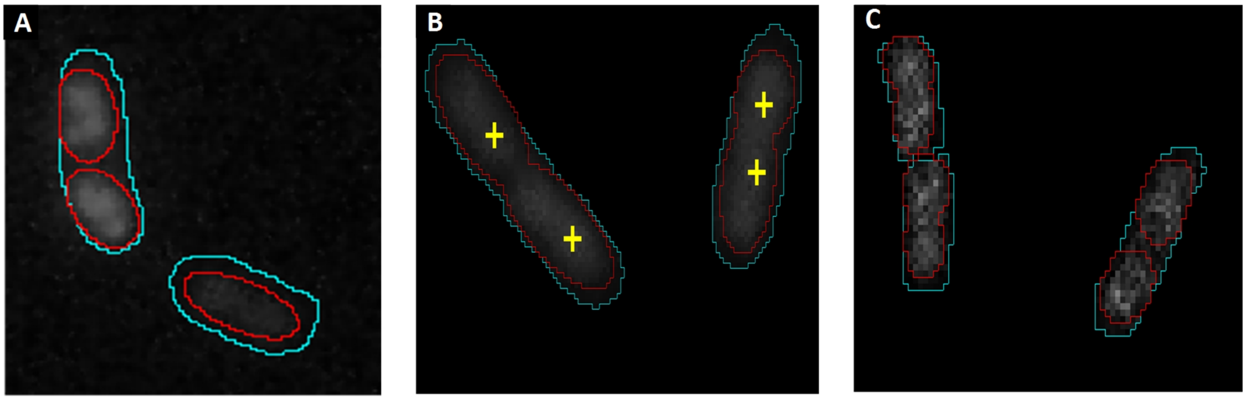

Figure 4.2: Segmentation results of nucleoids visualized using fluorescent dyes (or) fluorescent proteins by fitting the intensity distribution either to a piecewise-constant probability density function (A and B) or Gradient Path Labelling algorithm (C). Cell borders were detected from Phase Contrast images (not shown). Fitting of the segmented nucleoids outside of the cell borders are not considered.

Finally, in **Publication II** and **Publication IV**, the nucleoid detection method was based on the total fluorescence intensities and improved detection parameters. For each cell, the fluorescence levels are determined along the major cell axis of a background-corrected cell, followed by the summing of fluorescence intensities along its minor axis. For a given cell population, the cell lengths are normalized and the fluorescence intensities averaged over all the cells. This method can be used for images of DAPI/SYTOX Orange-stained and HupA-mCherry-tagged nucleoids. The boundaries of the nucleoid in each cell are detected by fitting a piecewise constant probability density function with three pieces to its fluorescence intensity distribution along the major cell axis by maximum likelihood (Figure 4.2 B and C).

5. Conclusions and Discussion

This thesis has studied the role of the nucleoid exclusion phenomenon in the internal organization of large protein aggregates and complexes within the bacterium *Escherichia coli*. For that, it made use of *in vivo* single-cell time-lapse microscopy measurements, fluorescent probes with single-molecule sensitivity, tailored image and signal processing techniques, and stochastic biophysical models. The four publications contribute to this by, first, presenting strong evidence that the presence of the nucleoid at midcell generates an anisotropy in the motions of the complexes that explains their heterogeneity in the bacterial cytoplasm (**Publication I**). Since protein aggregates tend to emerge in stress conditions, we next conducted a study to assess the robustness of this phenomenon in differing media richness and under antibiotics stresses known to affect nucleoid size (**Publication II**). Further, we assessed the effects of sub-optimal temperatures to this phenomenon, known to alter cells' metabolic activity and cytoplasm fluidity, which we hypothesized it would influence these diffusion-dependent processes (**Publication III**). Finally, we extended our studies to functional protein complexes, namely Tsr chemoreceptor clusters, and provided evidence that the phenomenon of nucleoid exclusion also contributes to their segregation and retention at the poles (**Publication IV**).

In **Publication I**, we investigated how *E. coli* cells are able to localize, in the long-term, protein complexes at the cell poles. We proposed that the nucleoid was as a major contributor to this heterogeneity of large biomolecules in the cytoplasm.

To prove this, we started by studying the long-term spatial distribution of biologically inert complexes, composed of RNA molecules tagged with multiple MS2-GFP proteins, in the cytoplasm of *E. coli* in optimal and sub-optimal temperature conditions. We observed that in both conditions the complexes exhibit preference for polar localization, but more so at optimal temperatures.

The choice of cell pole by the complexes was found to be a symmetric process in all the tested conditions. Meanwhile, as observed in previous studies (Stewart *et al.* 2005; Lindner *et al.* 2008), due to the robustness of retention at the poles, cell divisions introduce asymmetries in the numbers of these complexes between the old and the new poles of cells of subsequent generations and, after two generations, between sister cells.

We further studied the escape times of the complexes from the poles. While these were rare events, observation of many cells allowed establishing that they take longer, on average, to escape from the poles at low temperatures, as expected. More importantly, the standard deviations of escape times were similar to the means, which a characteristic of exponential distributions, implying that there is no energy-driven or diffusion-and-capture process in action to keep the complexes at the poles.

We next focused on the kinetics of the complexes by observing their positions between frames in cells with only one complex (so as to accurately determine the velocity vectors). We first studied whether the velocities of the complexes were position dependent, relative to the major cell axis. We found no such dependency. Also, we found little difference in these mean velocities between the two temperature conditions studied.

Finally, we studied local anisotropies along the major cell axis in the displacements of the complexes. We found only two such local anisotropies. One, negative, occurs at the cell extremities (as expected given the cell wall). The other, positive, occurs approximately midway between the cell center and the cell extremities. Interestingly, the degree of the positive anisotropy is equally strong to that of the negative anisotropy, explaining why the complexes accumulate at the cell poles.

Most relevantly, we next showed that the point where the positive anisotropy maximises coincides with the border of the nucleoid at midcell in both temperature conditions. We thus concluded that nucleoid exclusion is responsible for the complexes preference for polar localization. To gather additional proof, first, we observed the 10% longest cells (i.e. close to division and thus with two nucleoids) and compared the spatial distribution of the complexes with that of the general cell population. We found the complexes of these cells to be much closer to the cell extremities, as expected if their positioning is determined by nucleoid exclusion.

Additional support for our conclusions was provided by modeling. From the models, we showed that, in the absence of nucleoid exclusion from midcell, the retention at the poles is severely hampered, in that the spatial distribution of complexes becomes uniform throughout the cell. On the other hand, introduction of the anisotropy in the midpoint between poles and mid-cell generates a long-term spatial distribution of the complexes similar to the empirical data.

We thus conclude that the segregation of MS2-GFP RNA inert complexes to the cell poles is due to a volume exclusion phenomenon, caused by the presence of the nucleoid in the midcell region.

In **Publication II**, we assessed the robustness of the phenomenon of nucleoid exclusion to various external perturbations in the form of media richness and antibiotic stress that are known to affect the nucleoid sizes.

For this, we studied the spatiotemporal distribution of protein aggregates in cells expressing a fluorescent YFP-tagged chaperone (IbpA-YFP), which identifies *in vivo* the location of protein aggregates, and HupA-mCherry, a fluorescent variant of a nucleoid-associated protein, to detect the location and dimensions of nucleoid(s). Importantly, the tagged aggregates colocalize with inclusion bodies, which sequester them at the cell poles.

We show that the distribution of aggregates differed widely between the tested conditions, in agreement with the changes in the relative nucleoid size and a phenomena of nucleoid exclusion from midcell. Also, we found that this phenomenon of nucleoid exclusion is highly robust under varying environmental conditions, although it is not entirely immune to some stresses, leading to enhanced aggregate positioning at midcell.

Importantly, we observed that both increasing and decreasing the relative size of the nucleoid (compared to that of the control, optimal conditions) leads to an increase in the fraction of aggregates in the region between nucleoids the moment prior to cell division. This is particularly surprising for cells with large nucleoids. We speculate that increased nucleoid size, likely due to the reduction in the space available at the cell poles, thereby reducing the escape time from the poles.

The reduced degree of exclusion of aggregates from midcell for both larger and smaller nucleoids, likely affects the degree of asymmetries in the partitioning of aggregates between cells of future generations. We expect this to affect the aging process of lineages under stress conditions, where the cells tend to contain more than one aggregate (Lindner *et al.* 2008; Baig *et al.* 2014).

Finally, we report that, for the range of detectable aggregate sizes, no tangible differences exist between the spatial distributions of small and normal-sized aggregates irrespective of the nucleoid sizes. Nevertheless, we expect that below a certain aggregate size, nucleoid exclusion will lose much of its effectiveness, particularly given recent evidence that while translating ribosomes are excluded from the nucleoid, the ribosomal subunits are not (Sanamrad *et al.* 2014).

From these findings, we concluded that the phenomenon of nucleoid exclusion is most pronounced in cells with mid-sized nucleoids, partially losing its effectiveness under stressful conditions.

In **Publication III**, we study the functionality of the nucleoid exclusion phenomenon under sub-optimal temperatures, as these are known to alter the cytoplasm properties. For example, lower temperatures alters the cellular metabolic activity (Parry *et al.* 2014), which affects the fluidity of the cytoplasm and, therefore, the dynamics of diffusion-dependent cellular processes, such as nucleoid exclusion.

For this, we tracked ‘natural’ IbpA-YFP protein aggregates, which are accurate identifiers of the *in vivo* localization of natural protein aggregates that are known to be sequestered in inclusion bodies. We also observed ‘synthetic’ aggregates, consisting of the above RNA sequences bound by multiple MS2-GFP proteins that can be tracked individually. A tailored device was engineered that could allow imaging cells under microscopy at temperatures ranging from + 5ºC to + 50ºC.

Our main conclusion is that, at lower temperatures i.e. at 10ºC, the phenomenon of nucleoid exclusion is no longer able to, on average, cause aggregates to preferentially locate at the poles. Even at the single-cell level, we find that the aggregates positioning does not correlate with nucleoid size or positioning. This non-functionality is attributed to an alteration in the aggregates’ short-term behavior.

First, we report that the spatial distributions of both natural as well as synthetic aggregates change with temperature. Namely, the mean fraction of aggregates at the poles decreases with decreasing temperature, and we show that this cannot be explained by changes in the relative nucleoid length along the major cell axis. Further, the aggregates positioning becomes less correlated with the nucleoids size and location for decreasing temperatures, i.e., there is a reduction in the degree with which nucleoids affect aggregate positioning.

Second, we find that the relative concentration of aggregates in between nucleoids in cells near division is significantly higher at lower temperatures, again not due to changes in the relative nucleoid length along the major cell axis, but rather due to the homogenous distribution of the aggregates in the cytoplasm.

Third, strong anisotropies exhibited by the aggregates in the optimal growth conditions (37°C temperature) at the nucleoid borders and cell extremes, become weakened at lower temperatures due to enhanced cytoplasmic viscosity that renders the interactions between nucleoid and aggregates too infrequent and weak. Consequently, they no longer generate significant heterogeneities in the aggregate spatial distribution.

To validate these findings, we subject cells to osmotic stress. We observe that plasmolyzed cells formed as a result of this stress (Konopka *et al.* 2009) are unable to segregate aggregates to the poles, due to their much enhanced cytoplasmic viscosity. The similarity in aggregate behavior between low temperatures and osmotic stress suggests that, increase in cytoplasm viscosity will, in general, result in a decrease of aggregate preference for polar localization.

We conclude that the changes in aggregate spatial distribution in plasmolyzed cells and in cells subject to low temperatures are due to increased cytoplasm viscosity. Based on these compelling evidences, we conclude that the phenomenon of nucleoid exclusion of protein aggregates from midcell is not immune to stress conditions affecting the cytoplasm viscosity.

Finally, in **Publication IV**, we extended our studies to functional proteins known to exhibit preference for polar localization. In short, our findings show that the phenomenon of nucleoid exclusion is not confined to protein aggregates and complexes. Instead, it contributes to the establishment of the long-term spatial distribution of functional chemoreceptor clusters, such as those formed by Tsr, a major serine chemotactic protein involved in the process of chemotaxis.

For this, we made use of cells expressing both fluorescent Tsr-Venus clusters as well as fluorescently tagged nucleoids, so as to detect the nucleoid location and dimensions *in vivo*. This capability allowed us to demonstrate, the relationship, at the single-cell level, of the spatial distributions of clusters and nucleoids. The Venus protein used in this study, is a YFP variant that is derived from GFP and has a fast maturation time. This allowed real-time imaging by fluorescence microscopy.

First, we found that in cells with larger nucleoids, the Tsr clusters remain closer to the cell extremities in comparison to cells with smaller nucleoids, suggesting that existence of a volume exclusion caused by the nucleoid at midcell. Meanwhile, at the single-cell level, we found heterogeneities and asymmetries in the spatial distribution of Tsr clusters that are consistent with a nucleoid-exclusion phenomenon and cannot be explained solely by a diffusion-and-capture mechanism caused by Tol-Pal complexes at the poles.

Next, we made use of cells lacking the ability to express Tol-Pal proteins. We observed that, in the absence of Tol-Pal, the Tsr clusters still exhibit, albeit reduced, a preference for polar localization, indicating that the diffusion-and-capture mechanism made possible by Tol-Pal is not the only cause for the Tsr clusters' preference for polar localization in wild-type cells.

Interestingly, in the deletion mutants for Tol-Pal, it becomes visible that the distribution of Tsr clusters differs widely between cells with relatively small and large nucleoids, in a manner that is consistent with the existence of nucleoid exclusion from midcell. We also made use of cells without a nucleoid (anucleate cells). In these cells, the Tsr clusters are closer to midcell region, again as expected.

Overall, we found that the diffusion-and-capture by Tol-Pal complexes (Laloux and Jacobs-Wagner 2014; Santos *et al.* 2014) and the nucleoid exclusion from midcell have complementary effects on the spatial distribution of Tsr clusters. Additional support for this conclusion was provided by modeling. A stochastic model including nucleoid exclusion at midcell and diffusion-and-capture due to Tol-Pal at the poles is shown to exhibit a cluster's spatial dynamics that is consistent with the experimental data. Based on these evidences, we conclude that the phenomenon of nucleoid exclusion contributes to the preference of Tsr clusters for polar localization.

In this thesis, we investigated and validated the hypothesis that the presence of the nucleoid at midcell, due to its higher density than the cytoplasm (de Vries 2010; Wang *et al.* 2013; van den Berg *et al.* 2017), provides *E. coli* with the ability to segregate to the cell poles both unwanted protein aggregates as well as self-assembling, transmembrane Tsr chemoreceptors responsible for chemotaxis.

We believe that this 'mechanism' has three major advantages. First, it is an efficient, energy-free process contributing in the segregation of cellular components like protein aggregates and polar proteins. Second, it does not require stringent control (i.e., cell and nucleoid sizes, as well as cytoplasm properties are already under much regulation by *E. coli* for various reasons (van den Berg *et al.* 2017) and do not change rapidly when subject to mild, transient perturbations). Third, it is robust to most external perturbations and stressful conditions that we imposed in our studies. Namely, only under lower temperatures, due to the 'glassification' of the cytoplasm (Parry *et al.* 2014), and certain antibiotic stresses we did find its robustness to be partly hampered.

Overall, our results provide a new perspective regarding the role of the nucleoid in the spatial organization of the intracellular environment of *E. coli*. However, the possibility of existence of additional mechanisms complementing nucleoid exclusion remains ambiguous, and needs to be investigated on a case by case basis, as demonstrated by the behavior of Tsr complexes.

Also, given the importance of the nucleoid exclusion mechanism to multiple cellular processes, it will be important to find out how cells cope with transient changes in nucleoid structure and size and the role of these changes in cell physiology. The rapid development in single-cell biology techniques, particularly the emergence of super-resolution microscopy techniques, robust fluorescent probes, theoretical experiments and simulations, will assist these future efforts and studies of the role of the nucleoid as an ‘organizer’ of the internal architecture of *E. coli*.

Bibliography

Abbondanzieri, E. A., Greenleaf, W. J., Shaevitz, J. W., Landick, R. and Block, S. M. ‘‘Direct observation of base-pair stepping by RNA polymerase.’’ *Nature* 438.7067 (2005), pp. 460–5.

Ackermann, M., Schauerte, A., Stearns, S. C. and Jenal, U. ‘‘Experimental evolution of aging in a bacterium.’’ *BMC evolutionary biology* 7 (2007), p. 126.

Ackermann, M., Stearns, S. C. and Jenal, U. ‘‘Senescence in a bacterium with asymmetric division.’’ *Science* 300.5627 (2003), p. 1920.

Adams, D. W. and Errington, J. ‘‘Bacterial cell division: assembly, maintenance and disassembly of the Z ring.’’ *Nature reviews. Microbiology* 7.9 (2009), pp. 642–53.

Alberts, B., Johnson, A., Lewis, J., Raff, M., Roberts, K. and Walter, P. ‘*Molecular Biology of the Cell*’. Garland Science, USA (2002),.

Andersson, H., Baechi, T., Hoechl, M. and Richter, C. ‘‘Autofluorescence of living cells’’. *Journal of Microscopy* 191.1 (1998), pp. 1–7.

Andrews, S. S. and Bray, D. ‘‘Stochastic simulation of chemical reactions with spatial resolution and single molecule detail.’’ *Physical biology* 1.3–4 (2004), pp. 137–151.

Annila, T., Neeli-Venkata, R. and Ribeiro, A. S. ‘‘Robustness to Sub-optimal Temperatures of the Processes of Tsr Cluster Formation and Positioning in Escherichia Coli’’. in *Proceedings of the 9th International Joint Conference on Biomedical Engineering Systems and Technologies* (2016), pp. 137–141.

Axelrod, D. ‘‘Cell-substrate contacts illuminated by total internal reflection fluorescence.’’ *The Journal of cell biology* 89.1 (1981), pp. 141–5.

Azam, T. A. L. I., Iwata, A., Nishimura, A., Ueda, S., Ali Azam, T., Iwata, A., Nishimura, A., Ueda, S. and Ishihama, A. ‘‘Growth Phase-Dependent Variation in Protein Composition of the Escherichia coli Nucleoid’’. *Journal of Bacteriology* 181.20 (1999), pp. 6361–70.

Badrinarayanan, A., Lesterlin, C., Reyes-Lamothe, R. and Sherratt, D. ‘‘The Escherichia coli SMC complex, MukBEF, shapes nucleoid organization independently of DNA replication’’. *Journal of Bacteriology* 194.17 (2012), pp. 4669–4676.

Baig, U. I., Bhadbhade, B. J., Mariyam, D. and Watve, M. G. ‘‘Protein aggregation in E. coli : short term and long term effects of nutrient density.’’ *PloS one* 9.9 (2014), p. e107445.

Bakshi, S., Bratton, B. P. and Weisshaar, J. C. ‘‘Subdiffraction-limit study of Kaede diffusion and spatial distribution in live Escherichia coli’’. *Biophysical Journal* 101.10 (2011), pp. 2535–2544.

Bakshi, S., Choi, H., Mondal, J. and Weisshaar, J. C. ‘‘Time-dependent effects of transcription- and translation-halting drugs on the spatial distributions of the Escherichia coli chromosome and ribosomes.’’ *Molecular microbiology* 94.4 (2014), pp. 871–87.

Bakshi, S., Choi, H., Rangarajan, N., Barns, K. J., Bratton, B. P. and Weisshaar, J. C.

‘‘Nonperturbative imaging of nucleoid morphology in live bacterial cells during an antimicrobial peptide attack.’’ *Applied and environmental microbiology* 80.16 (2014), pp. 4977–86.

Bakshi, S., Siryaporn, A., Goulian, M. and Weisshaar, J. C. ‘‘Superresolution imaging of ribosomes and RNA polymerase in live Escherichia coli cells’’. *Molecular Microbiology* 85.1 (2012), pp. 21–38.

Bartlett, A. I. and Radford, S. E. ‘‘An expanding arsenal of experimental methods yields an explosion of insights into protein folding mechanisms.’’ *Nature structural & molecular biology* 16.6 (2009), pp. 582–8.

Bates, D. and Kleckner, N. ‘‘Chromosome and replisome dynamics in E. coli: Loss of sister cohesion triggers global chromosome movement and mediates chromosome segregation’’. *Cell* 121.6 (2005), pp. 899–911.

Bednarska, N. G., Schymkowitz, J., Rousseau, F. and Van Eldere, J. ‘‘Protein aggregation in bacteria: the thin boundary between functionality and toxicity.’’ *Microbiology* 159.9 (2013), pp. 1795–806.

Berg, H. C. and Brown, D. A. ‘‘Chemotaxis in Escherichia coli analysed by three-dimensional tracking.’’ *Nature* 239.5374 (1972), pp. 500–4.

Berg, H. C. and Turner, L. ‘‘Torque generated by the flagellar motor of Escherichia coli’’. *Biophysical Journal* 65.5 (1993), pp. 2201–2216.

van den Berg, J., Boersma, A. J. and Poolman, B. ‘‘Microorganisms maintain crowding homeostasis.’’ *Nature reviews. Microbiology* 15 (2017), pp. 309–318.

Bernhardt, T. G. and de Boer, P. A. J. ‘‘SlmA, a nucleoid-associated, FtsZ binding protein required for blocking septal ring assembly over Chromosomes in E. coli.’’ *Molecular cell* 18.5 (2005), pp. 555–564.

Bertrand, E., Chartrand, P., Schaefer, M., Shenoy, S. M., Singer, R. H. and Long, R. M. ‘‘Localization of ASH1 mRNA Particles in Living Yeast’’. *Molecular Cell* 2.4 (1998), pp. 437–445.

Betzig, E., Patterson, G. H., Sougrat, R., Lindwasser, O. W., Olenych, S., Bonifacino, J. S., Davidson, M. W., Lippincott-Schwartz, J. and Hess, H. F. ‘‘Imaging intracellular fluorescent proteins at nanometer resolution.’’ *Science* 313.5793 (2006), pp. 1642–5.

Bi, E. and Lutkenhaus, J. ‘‘FtsZ ring structure associated with division in Escherichia coli’’. *Nature* 354.6349 (1991), pp. 161–164.

Boccard, F., Esnault, E. and Valens, M. ‘‘Spatial arrangement and macrodomain organization of bacterial chromosomes.’’ *Molecular microbiology* 57.1 (2005), pp. 9–16.

Bren, A. and Eisenbach, M. ‘‘How Signals Are Heard during Bacterial Chemotaxis : Protein-Protein Interactions in Sensory Signal Propagation’’. *Journal of Bacteriology* 182.24 (2000), pp. 6865–6873.

Burkart, M., Toguchi, A. and Harshey, R. M. ‘‘The chemotaxis system, but not chemotaxis, is essential for swarming motility in Escherichia coli.’’ *Proceedings of the National Academy of Sciences of the United States of America* 95.5 (1998), pp. 2568–2573.

Cabrera, J. E., Cagliero, C., Quan, S., Squires, C. L., Ding, J. J. and Jin, D. J. ‘‘Active transcription of rRNA operons condenses the nucleoid in Escherichia coli: examining the effect of transcription on nucleoid structure in the absence of transertion.’’ *Journal of Bacteriology* 191.13 (2009), pp. 4180–4185.

Cai, L., Friedman, N. and Xie, X. S. ‘‘Stochastic protein expression in individual cells at the single molecule level.’’ *Nature* 440.7082 (2006), pp. 358–362.

Campisi, J. ‘‘Aging, cellular senescence, and cancer.’’ *Annual review of physiology* 75 (2013), pp. 685–705.

Campos, M. and Jacobs-Wagner, C. ‘‘Cellular organization of the transfer of genetic information’’. *Current Opinion in Microbiology* 16.2 (2013), pp. 171–176.

Casanova, H., Bartol, T. M., Stiles, J. and Berman, F. ‘‘Distributing MCell simulations on the grid’’. *International Journal of High Performance Computing Applications* 15.3 (2001), pp. 243–257.

Castellana, M., Hsin-Jung Li, S. and Wingreen, N. S. ‘‘Spatial organization of bacterial transcription and translation.’’ *Proceedings of the National Academy of Sciences of the United States of America* 113.33 (2016), pp. 9286–91.

Chai, Q., Singh, B., Peisker, K., Metzendorf, N., Ge, X., Dasgupta, S. and Sanyal, S. ‘‘Organization of ribosomes and nucleoids in Escherichia coli cells during growth and in quiescence.’’ *The Journal of biological chemistry* 289.16 (2014), pp. 11342–52.

Chalfie, M., Tu, Y., Euskirchen, G., Ward, W. W. and Prasher, D. C. ‘‘Green fluorescent protein as a marker for gene expression.’’ *Science* 263.5148 (1994), pp. 802–5.

Champoux, J. J. ‘‘DNA topoisomerases: structure, function, and mechanism.’’ *Annual review of biochemistry* 70 (2001), pp. 369–413.

Chao, J. A., Patskovsky, Y., Almo, S. C. and Singer, R. H. ‘‘Structural basis for the coevolution of a viral RNA–protein complex’’. *Nature Structural & Molecular Biology* 15.1 (2008), pp. 103–105.

Chazotte, B. ‘‘Labeling nuclear DNA using DAPI’’. *Cold Spring Harbor Protocols* 6.1 (2011), pp. 80–82.

Chowdhury, S., Kandhavelu, M., Yli-Harja, O. and Ribeiro, A. S. ‘‘Cell segmentation by multi-resolution analysis and maximum likelihood estimation (MAMLE).’’ *BMC bioinformatics* 14 Suppl 1.Suppl 10 (2013), p. S8.

Churchward, G., Estiva, E. and Bremer, H. ‘‘Growth rate-dependent control of chromosome replication initiation in Escherichia coli’’. *Journal of Bacteriology* 145.3 (1981), pp. 1232–1238.

Claret, L. and Rouviere-Yaniv, J. ‘‘Variation in HU composition during growth of Escherichia coli: the heterodimer is required for long term survival.’’ *Journal of molecular biology* 273.1 (1997), pp. 93–104.

Coelho, M., Lade, S. J., Alberti, S., Gross, T. and Tolić, I. M. ‘‘Fusion of Protein Aggregates Facilitates Asymmetric Damage Segregation’’. *PLoS Biology* 12.6 (2014), p. e1001886.

Coquel, A.-S. S., Jacob, J.-P. P., Primet, M., Demarez, A., Dimiccoli, M., Julou, T., Moisan, L., Lindner, A. B. and Berry, H. ‘‘Localization of protein aggregation in Escherichia coli is governed by diffusion and nucleoid macromolecular crowding effect.’’ *PLoS computational biology* 9.4 (2013), p. e1003038.

Coulon, A., Ferguson, M. L., De Turris, V., Palangat, M., Chow, C. C. and Larson, D. R. ‘‘Kinetic competition during the transcription cycle results in stochastic RNA processing’’. *eLife* 3 (2014), pp. 1–22.

Craig, N. L. and Nash, H. A. ‘‘E. coli integration host factor binds to specific sites in DNA.’’ *Cell* 39.3 (1984), pp. 707–16.

Crick, F. ‘‘Central dogma of molecular biology.’’ *Nature* 227.5258 (1970), pp. 561–3.

Daigle, N. and Ellenberg, J. ‘‘λN-GFP: an RNA reporter system for live-cell imaging.’’ *Nature methods* 4.8 (2007), pp. 633–636.

Day, R. N. and Davidson, M. W. ‘‘The fluorescent protein palette: tools for cellular imaging.’’ *Chemical Society reviews* 38.10 (2009), pp. 2887–921.

Dennis, P. P. and Bremer, H. ‘‘Modulation of Chemical Composition and Other Parameters of the Cell at Different Exponential Growth Rates’’. *EcoSal Plus* 3.1 (2008), pp. 765–77.

Deuerling, E., Schulze-Specking, A., Tomoyasu, T., Mogk, A. and Bukau, B. ‘‘Trigger factor and DnaK cooperate in folding of newly synthesized proteins.’’ *Nature* 400.6745 (1999), pp. 693–6.

Dillon, S. C. and Dorman, C. J. ‘‘Bacterial nucleoid-associated proteins, nucleoid structure and gene expression.’’ *Nature reviews. Microbiology* 8.3 (2010), pp. 185–95.

Dobson, C. M. ‘‘The structural basis of protein folding and its links with human disease.’’ *Philosophical transactions of the Royal Society of London. Series B, Biological sciences* 356.1406 (2001), pp. 133–45.

Dorman, C. J. ‘‘Genome architecture and global gene regulation in bacteria: making progress towards a unified model?’’ *Nature reviews. Microbiology* 11.5 (2013), pp. 349–55.

Dorman, C. J. and Deighan, P. ‘‘Regulation of gene expression by histone-like proteins in bacteria’’. *Current Opinion in Genetics & Development* 13.2 (2003), pp. 179–184.

Dorman, C. J. and Kane, K. A. ‘‘DNA bridging and antibridging: a role for bacterial nucleoid-associated proteins in regulating the expression of laterally acquired genes.’’ *FEMS microbiology reviews* 33.3 (2009), pp. 587–92.

Dougan, D. A., Mogk, A., Zeth, K., Turgay, K. and Bukau, B. ‘‘AAA+ proteins and substrate recognition, it all depends on their partner in crime.'' *FEBS letters* 529.1 (2002), pp. 6–10.

Draper, W. and Liphardt, J. ''Origins of chemoreceptor curvature sorting in Escherichia coli''. *Nature Communications* 8 (2017), p. 14838.

Dupaigne, P., Tonthat, N. K., Espeli, O., Whitfill, T., Boccard, F. and Schumacher, M. A. ''Molecular Basis for a Protein-Mediated DNA-Bridging Mechanism that Functions in Condensation of the E. coli Chromosome''. *Molecular Cell* 48.4 (2012), pp. 560–571.

Ellis, R. J. ''Macromolecular crowding: obvious but underappreciated.'' *Trends in biochemical sciences* 26.10 (2001), pp. 597–604.

Elowitz, M. B., Surette, M. G., Wolf, P. E., Stock, J. B. and Leibler, S. ''Protein mobility in the cytoplasm of Escherichia coli''. *Journal of Bacteriology* 181.1 (1999), pp. 197–203.

Endres, R. G. ''Polar chemoreceptor clustering by coupled trimers of dimers.'' *Biophysical journal* 96.2 (2009), pp. 453–63.

English, B., Sanamrad, A., Tankov, S., Hauryliuk, V. and Elf, J. ''Tracking of individual freely diffusing fluorescent protein molecules in the bacterial cytoplasm''. *arXiv.org* (2009), p. 30.

Erdmann, N., Petroff, T. and Funnell, B. E. ''Intracellular localization of P1 ParB protein depends on ParA and parS.'' *Proceedings of the National Academy of Sciences of the United States of America* 96.26 (1999), pp. 14905–10.

Erickson, H. P., Anderson, D. E. and Osawa, M. ''FtsZ in Bacterial Cytokinesis: Cytoskeleton and Force Generator All in One''. *Microbiology and Molecular Biology Reviews* 74.4 (2010), pp. 504–528.

Erjavec, N., Cvijovic, M., Klipp, E. and Nyström, T. ''Selective benefits of damage partitioning in unicellular systems and its effects on aging.'' *Proceedings of the National Academy of Sciences of the United States of America* 105.48 (2008), pp. 18764–9.

Errington, J., Daniel, R. A. and Scheffers, D.-J. ''Cytokinesis in bacteria.'' *Microbiology and molecular biology reviews* 67.1 (2003), pp. 52–65.

Espéli, O., Borne, R., Dupaigne, P., Thiel, A., Gigant, E., Mercier, R. and Boccard, F. ''A MatP-divisome interaction coordinates chromosome segregation with cell division in E. coli.'' *The EMBO journal* 31.14 (2012), pp. 3198–211.

Femino, A. M., Fay, F. S., Fogarty, K. and Singer, R. H. ''Visualization of single RNA transcripts in situ.'' *Science* 280.5363 (1998), pp. 585–590.

Fisher, J. K., Bourniquel, A., Witz, G., Weiner, B., Prentiss, M. and Kleckner, N. ''Four-dimensional imaging of E. coli nucleoid organization and dynamics in living cells''. *Cell* 153.4 (2013), pp. 882–895.

Frigault, M. M., Lacoste, J., Swift, J. L. and Brown, C. M. ''Live-cell microscopy - tips and tools.'' *Journal of cell science* 122.6 (2009), pp. 753–67.

Fritsche, M., Li, S., Heermann, D. W. and Wiggins, P. A. ''A model for Escherichia coli chromosome packaging supports transcription factor-induced DNA domain formation.'' *Nucleic Acids Research* 40.3 (2012), pp. 972–980.

Fuentealba, L. C., Eivers, E., Geissert, D., Taelman, V. and De Robertis, E. M. ''Asymmetric mitosis: Unequal segregation of proteins destined for degradation.'' *Proceedings of the National Academy of Sciences of the United States of America* 105.22 (2008), pp. 7732–7.

Fusco, D., Accornero, N., Lavoie, B., Shenoy, S. M., Blanchard, J. M., Singer, R. H. and Bertrand, E. ''Single mRNA molecules demonstrate probabilistic movement in living mammalian cells.'' *Current biology* 13.2 (2003), pp. 161–7.

Gahlmann, A. and Moerner, W. E. ''Exploring bacterial cell biology with single-molecule tracking and super-resolution imaging.'' *Nature reviews. Microbiology* 12.1 (2014), pp. 9–22.

Le Gall, A., Cattoni, D. I., Guilhas, B., Mathieu-Demazière, C., Oudjedi, L., Fiche, J.-B., Rech, J., Abrahamsson, S., Murray, H., Bouet, J. and Nollmann, M. ''Bacterial partition complexes segregate within the volume of the nucleoid''. *Nature Communications* in press.May (2016), pp. 1–10.

Gillespie, D. T. ''A general method for numerically simulation the stochastic time evolution of coupled chemical reactions''. *Journal of Computational Physics* (1976), pp. 403–434.

Gillespie, D. T. ''Concerning the validity of the stochastic approach to chemical kinetics''. *Journal of Statistical Physics* 16.3 (1977), pp. 311–318.

Glick, B. R. ''Metabolic load and heterogenous gene expression''. *Biotechnology Advances* 13.2 (1995), pp. 247–261.

Goehring, N. W. and Beckwith, J. ''Diverse paths to midcell: assembly of the bacterial cell division machinery.'' *Current biology* 15.13 (2005), pp. 514–26.

Goldberg, A. L. ''Degradation of abnormal proteins in Escherichia coli (protein breakdown-protein structure-mistranslation-amino acid analogs-puromycin).'' *Proceedings of the National Academy of Sciences of the United States of America* 69.2 (1972), pp. 422–6.

Golding, I. and Cox, E. C. ''RNA dynamics in live Escherichia coli cells.'' *Proceedings of the National Academy of Sciences of the United States of America* 101.31 (2004), pp. 11310–11315.

Golding, I. and Cox, E. C. ''Physical nature of bacterial cytoplasm''. *Physical Review Letters* 96.9 (2006), pp. 1–4.

Golding, I., Paulsson, J., Zawilski, S. M. and Cox, E. C. ''Real-time kinetics of gene activity in individual bacteria''. *Cell* 123.6 (2005), pp. 1025–1036.

Gordon, S., Rech, J., Lane, D. and Wright, A. ''Kinetics of plasmid segregation in Escherichia coli.'' *Molecular microbiology* 51.2 (2004), pp. 461–9.

Greenfield, D., McEvoy, A. L., Shroff, H., Crooks, G. E., Wingreen, N. S., Betzig, E. and Liphardt, J. ''Self-organization of the Escherichia coli chemotaxis network imaged with super-resolution light microscopy.'' *PLoS biology* 7.6 (2009), p. e1000137.

Gupta, A., Lloyd-Price, J. and Ribeiro, A. S. ‘‘In silico analysis of division times of Escherichia coli populations as a function of the partitioning scheme of non-functional proteins’’. *In Silico Biology* 12.1,2 (2015), pp. 9–21.

Ha, T. and Tinnefeld, P. ‘‘Photophysics of Fluorescence Probes for Single Molecule Biophysics and Super-Resolution Imaging’’. *Annual Review of Physical Chemistry* 63.2 (2012), pp. 595–617.

Hadizadeh Yazdi, N., Guet, C. C., Johnson, R. C. and Marko, J. F. ‘‘Variation of the folding and dynamics of the Escherichia coli chromosome with growth conditions.’’ *Molecular microbiology* 86.6 (2012), pp. 1318–33.

Harry, E., Monahan, L. and Thompson, L. ‘‘Bacterial cell division: the mechanism and its precison.’’ *International review of cytology* 253.6 (2006), pp. 27–94.

Hartl, F. U., Bracher, A. and Hayer-Hartl, M. ‘‘Molecular chaperones in protein folding and proteostasis’’. *Nature* 475.7356 (2011), pp. 324–332.

Hartl, F. U. and Hayer-Hartl, M. ‘‘Molecular chaperones in the cytosol: from nascent chain to folded protein.’’ *Science* 295.5561 (2002), pp. 1852–8.

Hazelbauer, G. L., Falke, J. J. and Parkinson, J. S. ‘‘Bacterial chemoreceptors: high-performance signaling in networked arrays’’. *Trends in Biochemical Sciences* 33.1 (2008), pp. 9–19.

Hocine, S., Raymond, P., Zenklusen, D., Chao, J. a and Singer, R. H. ‘‘Single-molecule analysis of gene expression using two-color RNA labeling in live yeast.’’ *Nature methods* 10.2 (2013), pp. 119–21.

Huang, B., Bates, M. and Zhuang, X. ‘‘Super-Resolution Fluorescence Microscopy’’. *Annual Review of Biochemistry* 78.1 (2009), pp. 993–1016.

Huang, K. C., Meir, Y. and Wingreen, N. S. ‘‘Dynamic structures in Escherichia coli: spontaneous formation of MinE rings and MinD polar zones.’’ *Proceedings of the National Academy of Sciences of the United States of America* 100.22 (2003), pp. 12724–8.

Huang, K. C., Mukhopadhyay, R. and Wingreen, N. S. ‘‘A curvature-mediated mechanism for localization of lipids to bacterial poles’’. *PLoS Computational Biology* 2.11 (2006), pp. 1357–1364.

Huh, D. and Paulsson, J. ‘‘Non-genetic heterogeneity from stochastic partitioning at cell division’’. *Nature Genetics* 43.2 (2011a), pp. 95–100.

Huh, D. and Paulsson, J. ‘‘Random partitioning of molecules at cell division.’’ *Proceedings of the National Academy of Sciences of the United States of America* 108.36 (2011b), pp. 15004–9.

Hussain, K., Begg, K. J., Salmond, G. P. C. and Donachie, W. D. ‘‘ParD: a new gene coding for a protein required for chromosome partitioning and septum localization in Escherichia coli’’. *Molecular Microbiology* 1.3 (1987), pp. 73–81.

Häkkinen, A., Muthukrishnan, A.-B. B., Mora, A., Fonseca, J. M. and Ribeiro, A. S. ‘‘CellAging: a tool to study segregation and partitioning in division in cell lineages of Escherichia coli.’’

Bioinformatics 29.13 (2013), pp. 1708–9.

Jacob, F. and Monod, J. ‘‘Genetic regulatory mechanisms in the synthesis of proteins.’’ *Journal of molecular biology* 3 (1961), pp. 318–56.

Jin, D., Cagliero, C. and Zhou, Y. ‘‘Growth rate regulation in Escherichia coli’’. *FEMS microbiology* 36.2 (2012), pp. 269–87.

Jin, D. J., Cagliero, C., Martin, C. M., Izard, J. and Zhou, Y. N. ‘‘The dynamic nature and territory of transcriptional machinery in the bacterial chromosome’’. *Frontiers in Microbiology* 497.6 (2015), pp. 1–14.

Jin, D. J. D., Cagliero, C. and Zhou, Y. Y. N. ‘‘Role of RNA polymerase and transcription in the organization of the bacterial nucleoid’’. *Chemical reviews* 113.11 (2013), pp. 8662–82.

Jones, C. W. and Armitage, J. P. ‘‘Positioning of bacterial chemoreceptors’’. *Trends in Microbiology* 23.5 (2015), pp. 247–256.

Joshi, M. C., Bourniquel, A., Fisher, J., Ho, B. T., Magnan, D., Kleckner, N. and Bates, D. ‘‘Escherichia coli sister chromosome separation includes an abrupt global transition with concomitant release of late-splitting intersister snaps.’’ *Proceedings of the National Academy of Sciences of the United States of America* 108.7 (2011), pp. 2765–70.

Jun, S. and Mulder, B. ‘‘Entropy-driven spatial organization of highly confined polymers: Lessons for the bacterial chromosome’’. *Proceedings of the National Academy of Sciences of the United States of America* 103.33 (2006), pp. 12388–12393.

Kaidow, A., Wachi, M., Nakamura, J., Magae, J. and Nagai, K. ‘‘Anucleate cell production by Escherichia coli Δhns mutant lacking a histone-like protein, H-NS’’. *Journal of Bacteriology* 177.12 (1995), pp. 3589–3592.

Kapuscinski, J. ‘‘DAPI: a DNA-specific fluorescent probe.’’ *Biotechnic & histochemistry* 70.5 (1995), pp. 220–33.

Kauffman, S. A. ‘‘Metabolic stability and epigenesis in randomly constructed genetic nets.’’ *Journal of theoretical biology* 22.3 (1969), pp. 437–467.

Kellenberger, E., Johansen, R., Maeder, M., Bohrmann, B., Stauffer, E. and Villiger, W. ‘‘Artefacts and morphological changes during chemical fixation’’. *Journal of Microscopy* 168.2 (1992), pp. 181–201.

Kennell, D. and Riezman, H. ‘‘Transcription and translation initiation frequencies of the Escherichia coli lac operon’’. *Journal of Molecular Biology* 114.1 (1977), pp. 1–21.

Kentner, D. and Sourjik, V. ‘‘Spatial organization of the bacterial chemotaxis system’’. *Current Opinion in Microbiology* 9.6 (2006), pp. 619–624.

Kerr, R. a, Levine, H., Sejnowski, T. J. and Rappel, W.-J. ‘‘Division accuracy in a stochastic model of Min oscillations in Escherichia coli.’’ *Proceedings of the National Academy of Sciences of the United States of America* 103.2 (2006), pp. 347–52.

Keryer-Bibens, C., Barreau, C. and Osborne, H. B. ‘‘Tethering of proteins to RNAs by bacteriophage proteins.’’ *Biology of the cell* 100.2 (2008), pp. 125–138.

Kim, Y. E., Hipp, M. S., Bracher, A., Hayer-Hartl, M. and Ulrich Hartl, F. ‘‘Molecular Chaperone Functions in Protein Folding and Proteostasis’’. *Annual Review of Biochemistry* 82.1 (2013), pp. 323–355.

Klumpp, S. and Hwa, T. ‘‘Growth-rate-dependent partitioning of RNA polymerases in bacteria.’’ *Proceedings of the National Academy of Sciences of the United States of America* 105.51 (2008), pp. 20245–50.

Klumpp, S. and Hwa, T. ‘‘Bacterial growth: global effects on gene expression, growth feedback and proteome partition.’’ *Current opinion in biotechnology* 28 (2014), pp. 96–102.

Klumpp, S., Zhang, Z. and Hwa, T. ‘‘Growth rate-dependent global effects on gene expression in bacteria.’’ *Cell* 139.7 (2009), pp. 1366–75.

Konopka, M. C., Shkel, I. A., Cayley, S., Record, M. T. and Weisshaar, J. C. ‘‘Crowding and confinement effects on protein diffusion in vivo’’. *Journal of Bacteriology* 188.17 (2006), pp. 6115–6123.

Konopka, M. C., Sochacki, K. A., Bratton, B. P., Shkel, I. A., Record, M. T. and Weisshaar, J. C. ‘‘Cytoplasmic protein mobility in osmotically stressed Escherichia coli.’’ *Journal of Bacteriology* 191.1 (2009), pp. 231–7.

Kruse, K. ‘‘Bacterial organization in space and time’’. *Comprehensive Biophysics* 7 (2012), pp. 208–221.

Kurkcuoglu, O., Doruker, P., Sen, T. Z., Kloczkowski, A. and Jernigan, R. L. ‘‘The ribosome structure controls and directs mRNA entry, translocation and exit dynamics.’’ *Physical biology* 5.4 (2008), p. 46005.

Kysela, D. T. D., Brown, P. J. B. P., Huang, K. C. and Brun, Y. V ‘‘Biological consequences and advantages of asymmetric bacterial growth’’. *Annual review of microbiology* 67 (2013), pp. 417–435.

Laloux, G. and Jacobs-Wagner, C. ‘‘How do bacteria localize proteins to the cell pole?’’ *Journal of cell science* 127.1 (2014), pp. 11–9.

Landgraf, D., Okumus, B., Chien, P., Baker, T. a and Paulsson, J. ‘‘Segregation of molecules at cell division reveals native protein localization’’. *Nature methods* 9.5 (2012), pp. 480–482.

Lang, E., Baier, J. and Köhler, J. ‘‘Epifluorescence, confocal and total internal reflection microscopy for single-molecule experiments: A quantitative comparison’’. *Journal of Microscopy* 222.2 (2006), pp. 118–123.

Lange, S., Katayama, Y., Schmid, M., Burkacky, O., Brauchle, C., Lamb D.C., D. C. and Jansen, R. P. ‘‘Simultaneous transport of different localized mRNA species revealed by live-cell imaging’’. *Traffic* 9.8 (2008), pp. 1256–1267.

Larson, D. R., Singer, R. H. and Zenklusen, D. ‘‘A single molecule view of gene expression’’. *Trends in Cell Biology* 19.11 (2009), pp. 630–637.

Larson, D. R., Zenklusen, D., Wu, B., Chao, J. a and Singer, R. H. ‘‘Real-time observation of transcription initiation and elongation on an endogenous yeast gene.’’ *Science* 332.6028 (2011), pp. 475–478.

Lee, T. K., Meng, K., Shi, H. and Huang, K. C. ‘‘Single-molecule imaging reveals modulation of cell wall synthesis dynamics in live bacterial cells’’. *Nature Communications* 7 (2016), p. 13170.

Lehninger, A. L., Nelson, D. L. and Cox, M. M. ‘*Lehninger principles of biochemistry.* 6th edn’. NewYork: Worth Publishers (2000),.

Leszczynska, D., Matuszewska, E., Kuczynska-Wisnik, D., Furmanek-Blaszk, B. and Laskowska, E. ‘‘The Formation of Persister Cells in Stationary-Phase Cultures of Escherichia Coli Is Associated with the Aggregation of Endogenous Proteins’’. *PLoS ONE* 8.1 (2013),.

Lewenza, S., Vidal-Ingigliardi, D. and Pugsley, A. P. ‘‘Direct visualization of red fluorescent lipoproteins indicates conservation of the membrane sorting rules in the family Enterobacteriaceae’’. *Journal of Bacteriology* 188.10 (2006), pp. 3516–3524.

Lindner, A. B. and Demarez, A. ‘‘Protein aggregation as a paradigm of aging.’’ *Biochimica et biophysica acta* 1790.10 (2009), pp. 980–96.

Lindner, A. B., Madden, R., Demarez, A., Stewart, E. J. and Taddei, F. ‘‘Asymmetric segregation of protein aggregates is associated with cellular aging and rejuvenation’’. *Proceedings of the National Academy of Sciences of the United States of America* 105.8 (2008), pp. 3076–3081.

Ling, J., Cho, C., Guo, L.-T., Aerni, H. R., Rinehart, J. and Söll, D. ‘‘Protein aggregation caused by aminoglycoside action is prevented by a hydrogen peroxide scavenger.’’ *Molecular cell* 48.5 (2012), pp. 713–22.

Liu, Z., Lavis, L. D. and Betzig, E. ‘‘Imaging Live-Cell Dynamics and Structure at the Single-Molecule Level’’. *Molecular Cell* 58.4 (2015), p. 644.

Lloyd-Price, J., Gupta, A. and Ribeiro, A. S. ‘‘SGNS2: a compartmentalized stochastic chemical kinetics simulator for dynamic cell populations’’. *Bioinformatics* 28.22 (2012), pp. 3004–3005.

Lloyd-Price, J., Startceva, S., Kandavalli, V., Chandraseelan, J. G., Goncalves, N., Oliveira, S. M. D., Häkkinen, A. and Ribeiro, A. S. ‘‘Dissecting the stochastic transcription initiation process in live Escherichia coli.’’ *DNA Research* 23.3 (2016), pp. 203–14.

Loose, M. and Mitchison, T. J. ‘‘The bacterial cell division proteins FtsA and FtsZ self-organize into dynamic cytoskeletal patterns.’’ *Nature cell biology* 16.1 (2014), pp. 38–46.

López-Otín, C., Blasco, M. A., Partridge, L., Serrano, M. and Kroemer, G. ‘‘The hallmarks of aging.’’ *Cell* 153.6 (2013), pp. 1194–217.

Lukyanov, K. a, Chudakov, D. M., Lukyanov, S. and Verkhusha, V. V ‘‘Innovation: Photoactivatable fluorescent proteins.’’ *Nature reviews. Molecular cell biology* 6.11 (2005), pp.

885–891.

Lutkenhaus, J. ‘‘Assembly dynamics of the bacterial MinCDE system and spatial regulation of the Z ring’’. *Annual review of biochemistry* 76 (2007), pp. 539–562.

Lutkenhaus, J., Pichoff, S. and Du, S. ‘‘Bacterial cytokinesis: From Z ring to divisome’’. *Cytoskeleton* 69.10 (2012), pp. 778–790.

Lybarger, S. R. and Maddock, J. R. ‘‘Differences in the polar clustering of the high- and low-abundance chemoreceptors of Escherichia coli.’’ *Proceedings of the National Academy of Sciences of the United States of America* 97.14 (2000), pp. 8057–62.

Ma, X., Ehrhardt, D. W. and Margolin, W. ‘‘Colocalization of cell division proteins FtsZ and FtsA to cytoskeletal structures in living Escherichia coli cells by using green fluorescent protein.’’ *Proceedings of the National Academy of Sciences of the United States of America* 93.23 (1996), pp. 12998–3003.

Ma, X. and Margolin, W. ‘‘Genetic and functional analyses of the conserved C-terminal core domain of Escherichia coli FtsZ’’. *Journal of Bacteriology* 181.24 (1999), pp. 7531–7544.

Maddock, J. R. and Shapiro, L. ‘‘Polar location of the chemoreceptor complex in the Escherichia coli cell.’’ *Science* 259.5102 (1993), pp. 1717–23.

Maisonneuve, E., Ezraty, B. and Dukan, S. ‘‘Protein aggregates: an aging factor involved in cell death.’’ *Journal of Bacteriology* 190.18 (2008), pp. 6070–5.

Margolin, W. ‘‘FtsZ and the division of prokaryotic cells and organelles’’. *Nature Reviews Molecular Cell Biology* 6.11 (2005), pp. 862–871.

Matsumoto, Y., Murakami, Y., Tsuru, S., Ying, B. and Yomo, T. ‘‘Growth rate-coordinated transcriptome reorganization in bacteria.’’ *BMC genomics* 14.1 (2013), p. 808.

McClure, W. R. and Cech, C. L. ‘‘On the mechanism of rifampicin inhibition of RNA synthesis.’’ *The Journal of biological chemistry* 253.24 (1978), pp. 8949–56.

Mercier, R., Petit, M.-A., Schbath, S., Robin, S., El Karoui, M., Boccard, F. and Espéli, O. ‘‘The MatP/matS site-specific system organizes the terminus region of the E. coli chromosome into a macrodomain.’’ *Cell* 135.3 (2008), pp. 475–85.

Mika, J. T. and Poolman, B. ‘‘Macromolecule diffusion and confinement in prokaryotic cells’’. *Current Opinion in Biotechnology* 22.1 (2011), pp. 117–126.

Moffitt, J. R., Pandey, S., Boettiger, A. N., Wang, S. and Zhuang, X. ‘‘Spatial organization shapes the turnover of a bacterial transcriptome’’. *eLife* 5 (2016), pp. 1–22.

Mondal, J., Bratton, B. P., Li, Y., Yethiraj, A. and Weisshaar, J. C. ‘‘Entropy-based mechanism of ribosome-nucleoid segregation in E. coli Cells’’. *Biophysical Journal* 100.11 (2011), pp. 2605–13.

Monk, N. A. M. ‘‘Oscillatory expression of Hes1, p53, and NF-kB driven by transcriptional time delays’’. *Current Biology* 13.16 (2003), pp. 1409–1413.

Montero Llopis, P., Jackson, A. F., Sliusarenko, O., Surovtsev, I., Heinritz, J., Emonet, T. and Jacobs-Wagner, C. ‘‘Spatial organization of the flow of genetic information in bacteria’’. *Nature* 466.7302 (2010), pp. 77–81.

Mora, A. D., Vieira, P. M., Manivannan, A. and Fonseca, J. M. ‘‘Automated drusen detection in retinal images using analytical modelling algorithms’’. *BioMedical Engineering OnLine* 10.1 (2011), p. 59.

Mowbray, S. L. ‘‘Bacterial chemoreceptors: recent progress in structure and function’’. *Molecules and Cells* 9.2 (1999), pp. 115–118.

Mulder, E. and Woldringh, C. L. ‘‘Actively replicating nucleoids influence positioning of division sites in Escherichia coli filaments forming cells lacking DNA.’’ *Journal of Bacteriology* 171.8 (1989), pp. 4303–4314.

Murakami, K. S. ‘‘Structural Basis of Transcription Initiation: An RNA Polymerase Holoenzyme-DNA Complex’’. *Science* 296.5571 (2002), pp. 1285–1290.

Muthukrishnan, A.-B. B., Kandhavelu, M., Lloyd-Price, J., Kudasov, F., Chowdhury, S., Yli-Harja, O. and Ribeiro, A. S. ‘‘Dynamics of transcription driven by the tetA promoter, one event at a time, in live Escherichia coli cells.’’ *Nucleic acids research* 40.17 (2012), pp. 8472–83.

Mäkelä, J., Lloyd-Price, J., Yli-Harja, O. and Ribeiro, A. S. ‘‘Stochastic sequence-level model of coupled transcription and translation in prokaryotes.’’ *BMC bioinformatics* 12.1 (2011), p. 121.

Männik, J. and Bailey, M. W. ‘‘Spatial coordination between chromosomes and cell division proteins in Escherichia coli.’’ *Frontiers in microbiology* 6 (2015), p. 306.

Männik, J., Bailey, M. W., O’Neill, J. C. and Männik, J. ‘‘Kinetics of large-scale chromosomal movement during asymmetric cell division in Escherichia coli’’. *PLOS Genetics* 13.2 (2017), p. e1006638.

Männik, J., Wu, F., Hol, F. J. H., Bisicchia, P., Sherratt, D. J., Keymer, J. E. and Dekker, C. ‘‘Robustness and accuracy of cell division in Escherichia coli in diverse cell shapes.’’ *Proceedings of the National Academy of Sciences of the United States of America* 109.18 (2012), pp. 6957–62.

Nevo-Dinur, K., Govindarajan, S. and Amster-Choder, O. ‘‘Subcellular localization of RNA and proteins in prokaryotes’’. *Trends in Genetics* 28.7 (2012), pp. 314–322.

Nielsen, H. J., Ottesen, J. R., Youngren, B., Austin, S. J. and Hansen, F. G. ‘‘The Escherichia coli chromosome is organized with the left and right chromosome arms in separate cell halves.’’ *Molecular microbiology* 62.2 (2006), pp. 331–8.

Nielsen, H. J., Youngren, B., Hansen, F. G. and Austin, S. ‘‘Dynamics of Escherichia coli chromosome segregation during multifork replication.’’ *Journal of Bacteriology* 189.23 (2007), pp. 8660–6.

Niu, L. and Yu, J. ‘‘Investigating intracellular dynamics of FtsZ cytoskeleton with photoactivation single-molecule tracking’’. *Biophysical journal* 95.4 (2008), pp. 2009–2016.

van Noort, J., Verbrugge, S., Goosen, N., Dekker, C. and Dame, R. T. ‘‘Dual architectural roles of HU: formation of flexible hinges and rigid filaments.’’ *Proceedings of the National Academy of Sciences of the United States of America* 101.18 (2004), pp. 6969–74.

Odijk, T. ‘‘Osmotic compaction of supercoiled DNA into a bacterial nucleoid’’. *Biophysical Chemistry* 73.1–2 (1998), pp. 23–29.

Oh, D., Yu, Y., Lee, H., Wanner, B. L. and Ritchie, K. ‘‘Dynamics of the serine chemoreceptor in the Escherichia coli inner membrane: a high-speed single-molecule tracking study.’’ *Biophysical journal* 106.1 (2014), pp. 145–53.

Okumus, B., Landgraf, D., Lai, G. C., Bakhsi, S., Arias-Castro, J. C., Yildiz, S., Huh, D., Fernandez-Lopez, R., Peterson, C. N., Toprak, E., El Karoui, M. and Paulsson, J. ‘‘Mechanical slowing-down of cytoplasmic diffusion allows in vivo counting of proteins in individual cells’’. *Nature Communications* 7 (2016), p. 11641.

Osbourn, A. E. and Field, B. ‘‘Operons’’. *Cellular and Molecular Life Sciences* 66.23 (2009), pp. 3755–3775.

Parkinson, J. S., Ames, P. and Studdert, C. A. ‘‘Collaborative signaling by bacterial chemoreceptors.’’ *Current opinion in microbiology* 8.2 (2005), pp. 116–21.

Parry, B. R., Surovtsev, I. V., Cabeen, M. T., O’Hern, C. S., Dufresne, E. R., Jacobs-Wagner, C., Jabobs-Wagner. Christine and Jacobs-Wagner, C. ‘‘The bacterial cytoplasm has glass-like properties and is fluidized by metabolic activity.’’ *Cell* 156.1–2 (2014), pp. 183–94.

Pawley, J. B. ‘*Handbook of Biological Confocal Microscopy*. 3rd edn’. Berlin: Springer (2006),.

Peabody, D. S. ‘‘The RNA binding site of bacteriophage MS2 coat protein.’’ *The EMBO journal* 12.2 (1993), pp. 595–600.

Pelletier, J., Halvorsen, K., Ha, B.-Y., Paparcone, R., Sandler, S. J., Woldringh, C. L., Wong, W. P. and Jun, S. ‘‘Physical manipulation of the Escherichia coli chromosome reveals its soft nature.’’ *Proceedings of the National Academy of Sciences of the United States of America* 109.40 (2012), pp. 2649–56.

Peter, B. J., Ullsperger, C., Hiasa, H., Marians, K. J. and Cozzarelli, N. R. ‘‘The structure of supercoiled intermediates in DNA replication.’’ *Cell* 94.6 (1998), pp. 819–27.

Pinto, U. M., Pappas, K. M. and Winans, S. C. ‘‘The ABCs of plasmid replication and segregation.’’ *Nature reviews. Microbiology* 10.11 (2012), pp. 755–65.

Pitchiaya, S., Heinicke, L. A., Custer, T. C. and Walter, N. G. ‘‘Single molecule fluorescence approaches shed light on intracellular RNAs’’. *Chemical Reviews* 114.6 (2014), pp. 3224–3265.

Postow, L. ‘‘Topological domain structure of the Escherichia coli chromosome’’. *Genes & Development* 18.14 (2004), pp. 1766–1779.

Postow, L., Crisona, N. J., Peter, B. J., Hardy, C. D. and Cozzarelli, N. R. ‘‘Topological challenges to DNA replication: conformations at the fork.’’ *Proceedings of the National Academy of Sciences* *of the United States of America* 98.15 (2001), pp. 8219–26.

Prasher, D. C., Eckenrode, V. K., Ward, W. W., Prendergast, F. G. and Cormier, M. J. ‘‘Primary structure of the Aequorea victoria green-fluorescent protein’’. *Gene* 111.2 (1992), pp. 229–233.

Puchkov, E. O. ‘‘Intracellular viscosity: Methods of measurement and role in metabolism’’. *Biochemistry (Moscow) Supplement Series A: Membrane and Cell Biology* 7.4 (2013), pp. 270–279.

Raj, A. and van Oudenaarden, A. ‘‘Nature, Nurture, or Chance: Stochastic Gene Expression and Its Consequences’’. *Cell* 135.2 (2008), pp. 216–226.

Ramakrishnan, V. ‘‘Ribosome structure and the mechanism of translation.’’ *Cell* 108.4 (2002), pp. 557–72.

Raskin, D. M. and de Boer, P. A. ‘‘Rapid pole-to-pole oscillation of a protein required for directing division to the middle of Escherichia coli.’’ *Proceedings of the National Academy of Sciences of the United States of America* 96.9 (1999), pp. 4971–6.

Reyes-Lamothe, R., Tran, T., Meas, D., Lee, L., Li, A. M., Sherratt, D. J. and Tolmasky, M. E. ‘‘High-copy bacterial plasmids diffuse in the nucleoid-free space, replicate stochastically and are randomly partitioned at cell division.’’ *Nucleic acids research* 42.2 (2014), pp. 1042–51.

Reyes-Lamothe, R., Wang, X. and Sherratt, D. ‘‘Escherichia coli and its chromosome.’’ *Trends in microbiology* 16.5 (2008), pp. 238–45.

Ribeiro, A. S. ‘‘Stochastic and delayed stochastic models of gene expression and regulation’’. *Mathematical Biosciences* 223.1 (2010), pp. 1–11.

Ribeiro, A. S. and Lloyd-Price, J. ‘‘SGN Sim, a Stochastic Genetic Networks Simulator’’. *Bioinformatics* 23.6 (2007), pp. 777–779.

Ringgaard, S., Schirner, K., Davis, B. M. and Waldor, M. K. ‘‘A family of ParA-like ATPases promotes cell pole maturation by facilitating polar localization of chemotaxis proteins’’. *Genes & Development* 25.14 (2011), pp. 1544–1555.

Robinow, C. and Kellenberger, E. ‘‘The bacterial nucleoid revisited.’’ *Microbiological reviews* 58.2 (1994), pp. 211–32.

Rose, M. R., Flatt, T., Graves, J. L., Greer, L. F., Martinez, D. E., Matos, M., Mueller, L. D., Shmookler Reis, R. J. and Shahrestani, P. ‘‘What is Aging?’’ *Frontiers in genetics* 3.July (2012), p. 134.

Roussel, M. R. and Zhu, R. ‘‘Validation of an algorithm for delay stochastic simulation of transcription and translation in prokaryotic gene expression.’’ *Physical biology* 3.4 (2006), pp. 274–84.

Rovinskiy, N., Agbleke, A. A., Chesnokova, O., Pang, Z. and Higgins, N. P. ‘‘Rates of gyrase supercoiling and transcription elongation control supercoil density in a bacterial chromosome.’’ *PLoS genetics* 8.8 (2012), p. e1002845.

Rudner, D. Z. and Losick, R. ‘‘Protein subcellular localization in bacteria.’’ *Cold Spring Harbor perspectives in biology* (2010), pp. 1–14.

Rudner, D. Z., Pan, Q. and Losick, R. M. ‘‘Evidence that subcellular localization of a bacterial membrane protein is achieved by diffusion and capture.’’ *Proceedings of the National Academy of Sciences of the United States of America* 99.13 (2002), pp. 8701–6.

Rybenkov, V. V., Herrera, V., Petrushenko, Z. M. and Zhao, H. ‘‘MukBEF, a chromosomal organizer.’’ *Journal of molecular microbiology and biotechnology* 24.5–6 (2014), pp. 371–83.

Sabate, R., de Groot, N. S. and Ventura, S. ‘‘Protein folding and aggregation in bacteria.’’ *Cellular and molecular life sciences* 67.16 (2010), pp. 2695–715.

Sanamrad, A., Persson, F., Lundius, E. G., Fange, D., Gynnå, A. H. and Elf, J. ‘‘Single-particle tracking reveals that free ribosomal subunits are not excluded from the Escherichia coli nucleoid.’’ *Proceedings of the National Academy of Sciences of the United States of America* 111.31 (2014), pp. 11413–8.

Sanderson, M. J., Smith, I., Parker, I. and Bootman, M. D. ‘‘Fluorescence Microscopy’’. *Cold Spring Harbor Protocols* .10 (2014), pp. 1042–1065.

Santos, T. M. A., Lin, T. Y., Rajendran, M., Anderson, S. M. and Weibel, D. B. ‘‘Polar localization of Escherichia coli chemoreceptors requires an intact Tol-Pal complex’’. *Molecular Microbiology* 92.5 (2014), pp. 985–1004.

Seo, E.-Y., Ahn, T.-S. and Zo, Y.-G. ‘‘Agreement, precision, and accuracy of epifluorescence microscopy methods for enumeration of total bacterial numbers.’’ *Applied and environmental microbiology* 76.6 (2010), pp. 1981–91.

Shaner, N. C., Campbell, R. E., Steinbach, P. A., Giepmans, B. N. G., Palmer, A. E. and Tsien, R. Y. ‘‘Improved monomeric red, orange and yellow fluorescent proteins derived from Discosoma sp. red fluorescent protein.’’ *Nature biotechnology* 22.12 (2004), pp. 1567–72.

Shaner, N. C., Patterson, G. H. and Davidson, M. W. ‘‘Advances in fluorescent protein technology.’’ *Journal of cell science* 120.24 (2007), pp. 4247–60.

Shaner, N. C., Steinbach, P. A. and Tsien, R. Y. ‘‘A guide to choosing fluorescent proteins.’’ *Nature methods* 2.12 (2005), pp. 905–909.

Shapiro, L., McAdams, H. H. and Losick, R. ‘‘Why and how bacteria localize proteins’’. *Science* 326.5957 (2009), pp. 1225–1228.

Sharma, D., Cukras, A. R., Rogers, E. J., Southworth, D. R. and Green, R. ‘‘Mutational analysis of S12 protein and implications for the accuracy of decoding by the ribosome.’’ *Journal of molecular biology* 374.4 (2007), pp. 1065–76.

Shen, B. and Lutkenhaus, J. ‘‘Examination of the interaction between FtsZ and MinCN in E. coli suggests how MinC disrupts Z rings’’. *Molecular Microbiology* 75.5 (2010), pp. 1285–1298.

Shimomura, O., H. Johnson, F. and Saiga, Y. ‘‘Extraction, Purification and Properties of Aequorin, a Bioluminescent Protein from the Luminous Hydromedusan, Aequorea''. *Journal of Cellular Physiology* 1353.165 (1962), pp. 223–239.

Skidmore, J. M., Ellefson, D. D., McNamara, B. P., Couto, M. M., Wolfe, A. J. and Maddock, J. R. ''Polar clustering of the chemoreceptor complex in Escherichia coli occurs in the absence of complete CheA function.'' *Journal of Bacteriology* 182.4 (2000), pp. 967–73.

Skoko, D., Yoo, D., Bai, H., Schnurr, B., Yan, J., McLeod, S. M., Marko, J. F. and Johnson, R. C. ''Mechanism of Chromosome Compaction and Looping by the Escherichia coli Nucleoid Protein Fis''. *Journal of Molecular Biology* 364.4 (2006), pp. 777–798.

Song, D. and Loparo, J. J. ''Building bridges within the bacterial chromosome.'' *Trends in genetics* 31.3 (2015), pp. 164–73.

Sourjik, V. and Armitage, J. P. ''Spatial organization in bacterial chemotaxis''. *The EMBO Journal* 29.16 (2010), pp. 2724–2733.

Spratt, B. G. ''Distinct penicillin binding proteins involved in the division, elongation, and shape of Escherichia coli K12.'' *Proceedings of the National Academy of Sciences of the United States of America* 72.8 (1975), pp. 2999–3003.

Stefani, M. and Dobson, C. M. ''Protein aggregation and aggregate toxicity: new insights into protein folding, misfolding diseases and biological evolution.'' *Journal of molecular medicine* 81.11 (2003), pp. 678–99.

Steiner, W., Liu, G., Donachie, W. D. and Kuempel, P. ''The cytoplasmic domain of FtsK protein is required for resolution of chromosome dimers.'' *Molecular microbiology* 31.2 (1999), pp. 579–83.

Stewart, E. J., Madden, R., Paul, G. and Taddei, F. ''Aging and death in an organism that reproduces by morphologically symmetric division.'' *PLoS biology* 3.2 (2005), p. e45.

Stouf, M., Meile, J.-C. and Cornet, F. ''FtsK actively segregates sister chromosomes in Escherichia coli''. *Proceedings of the National Academy of Sciences of the United States of America* 110.27 (2013), pp. 11157–11162.

Stracy, M., Lesterlin, C., Garza de Leon, F., Uphoff, S., Zawadzki, P. and Kapanidis, A. N. ''Live-cell superresolution microscopy reveals the organization of RNA polymerase in the bacterial nucleoid''. *Proceedings of the National Academy of Sciences of the United States of America* 112.32 (2015), p. 201507592.

Straight, P. D., Fischbach, M. A., Walsh, C. T., Rudner, D. Z. and Kolter, R. ''A singular enzymatic megacomplex from Bacillus subtilis.'' *Proceedings of the National Academy of Sciences of the United States of America* 104.1 (2007), pp. 305–10.

Swaminathan, R., Hoang, C. P. and Verkman, A. S. ''Photobleaching recovery and anisotropy decay of green fluorescent protein GFP-S65T in solution and cells: cytoplasmic viscosity probed by green fluorescent protein translational and rotational diffusion.'' *Biophysical journal* 72.4 (1997), pp. 1900–7.

Swinger, K. K. and Rice, P. A. ‘‘Structure-based analysis of HU-DNA binding.’’ *Journal of molecular biology* 365.4 (2007), pp. 1005–16.

Taniguchi, Y., Choi, P. J., Li, G.-W. W., Chen, H., Babu, M., Hearn, J., Emili, A. and Xie, X. S. ‘‘Quantifying E. coli Proteome and Transcriptome with Single-Molecule Sensitivity in Single Cells’’. *Science* 329.5991 (2010), pp. 533–538.

Tao, H., Bausch, C., Richmond, C., Blattner, F. R. and Conway, T. ‘‘Functional genomics: expression analysis of Escherichia coli growing on minimal and rich media.’’ *Journal of Bacteriology* 181.20 (1999), pp. 6425–40.

Thanbichler, M. ‘‘Synchronization of chromosome dynamics and cell division in bacteria.’’ *Cold Spring Harbor perspectives in biology* 2.1 (2010), pp. 1–15.

Thanbichler, M., Viollier, P. H. and Shapiro, L. ‘‘The structure and function of the bacterial chromosome.’’ *Current opinion in genetics & development* 15.2 (2005), pp. 153–62.

Thiem, S., Kentner, D. and Sourjik, V. ‘‘Positioning of chemosensory clusters in E. coli and its relation to cell division.’’ *The EMBO journal* 26.6 (2007), pp. 1615–1623.

Thomas, J. G. and Baneyx, F. ‘‘Roles of the Escherichia coli small heat shock proteins Ibpa and ibpb in thermal stress management: Comparison with Clpa, Clpb, and HtpG in vivo’’. *Journal of Bacteriology* 180.19 (1998), pp. 5165–5172.

Tokunaga, M., Imamoto, N. and Sakata-Sogawa, K. ‘‘Highly inclined thin illumination enables clear single-molecule imaging in cells’’. *Nature Methods* 5.2 (2008), pp. 159–161.

Tonthat, N. K., Arold, S. T., Pickering, B. F., Van Dyke, M. W., Liang, S., Lu, Y., Beuria, T. K., Margolin, W. and Schumacher, M. A. ‘‘Molecular mechanism by which the nucleoid occlusion factor, SlmA, keeps cytokinesis in check.’’ *The EMBO journal* 30.1 (2011), pp. 154–64.

Tonthat, N. K., Milam, S. L., Chinnam, N., Whitfill, T., Margolin, W. and Schumacher, M. A. ‘‘SlmA forms a higher-order structure on DNA that inhibits cytokinetic Z-ring formation over the nucleoid.’’ *Proceedings of the National Academy of Sciences of the United States of America* 110.26 (2013), pp. 10586–91.

Tran, H., Oliveira, S. M. D., Goncalves, N. and Ribeiro, A. S. ‘‘Kinetics of the cellular intake of a gene expression inducer at high concentrations’’. *Molecular Biosystems* 11.9 (2015), pp. 2579–2587.

Travers, A. and Muskhelishvili, G. ‘‘DNA supercoiling - a global transcriptional regulator for enterobacterial growth?’’ *Nature reviews. Microbiology* 3.2 (2005), pp. 157–69.

Tsien, R. Y. ‘‘The green fluorescent protein’’. *Annual Review Biochemistry* 67 (1998), pp. 509–544.

Tyedmers, J., Mogk, A. and Bukau, B. ‘‘Cellular strategies for controlling protein aggregation.’’ *Nature reviews. Molecular cell biology* 11.11 (2010), pp. 777–88.

Valkenburg, J. A. C. and Woldringh, C. L. ‘‘Phase separation between nucleoid and cytoplasm in

Escherichia coli as defined by immersive refractometry’’. *Journal of Bacteriology* 160.3 (1984), pp. 1151–1157.

Vecchiarelli, A. G., Mizuuchi, K. and Funnell, B. E. ‘‘Surfing biological surfaces: exploiting the nucleoid for partition and transport in bacteria.’’ *Molecular microbiology* 86.3 (2012), pp. 513–23.

Vendeville, A., Larivière, D. and Fourmentin, E. ‘‘An inventory of the bacterial macromolecular components and their spatial organization’’. *FEMS Microbiology Reviews* 35.2 (2011), pp. 395–414.

Di Ventura, B., Knecht, B., Andreas, H., Godinez, W. J., Fritsche, M., Rohr, K., Nickel, W., Heermann, D. W. and Sourjik, V. ‘‘Chromosome segregation by the Escherichia coli Min system.’’ *Molecular systems biology* 9.686 (2013), p. 686.

Ventura, S. and Villaverde, A. ‘‘Protein quality in bacterial inclusion bodies’’. *Trends in Biotechnology* 24.4 (2006), pp. 179–185.

Vicente, M. and Rico, A. I. ‘‘The order of the ring: assembly of Escherichia coli cell division components.’’ *Molecular microbiology* 61.1 (2006), pp. 5–8.

Vogel, U. and Jensen, K. F. ‘‘The RNA chain elongation rate in Escherichia coli depends on the growth rate.’’ *Journal of Bacteriology* 176.10 (1994), pp. 2807–13.

Volkmer, B. and Heinemann, M. ‘‘Condition-dependent cell volume and concentration of Escherichia coli to facilitate data conversion for systems biology modeling.’’ *PloS one* 6.7 (2011), p. e23126.

de Vries, R. ‘‘DNA condensation in bacteria: Interplay between macromolecular crowding and nucleoid proteins’’. *Biochimie* 92.12 (2010), pp. 1715–21.

Walter, N. G., Huang, C.-Y., Manzo, A. J. and Sobhy, M. a ‘‘Do-it-yourself guide: how to use the modern single-molecule toolkit.’’ *Nature methods* 5.6 (2008), pp. 475–489.

Wang, H., Wingreen, N. S. and Mukhopadhyay, R. ‘‘Self-organized periodicity of protein clusters in growing bacteria.’’ *Physical review letters* 101.21 (2008), p. 218101.

Wang, J. D. and Levin, P. A. ‘‘Metabolism, cell growth and the bacterial cell cycle.’’ *Nature reviews. Microbiology* 7.11 (2009), pp. 822–7.

Wang, L., Khattar, M. K., Donachie, W. D. and Lutkenhaus, J. ‘‘FtsI and FtsW are localized to the septum in Escherichia coli.’’ *Journal of Bacteriology* 180.11 (1998), pp. 2810–6.

Wang, W., Li, G.-W., Chen, C., Xie, X. S. and Zhuang, X. ‘‘Chromosome organization by a nucleoid-associated protein in live bacteria.’’ *Science* 333.6048 (2011), pp. 1445–9.

Wang, X. ‘‘The two Escherichia coli chromosome arms locate to separate cell halves’’. *Genes & Development* 20.13 (2006), pp. 1727–1731.

Wang, X., Lesterlin, C., Reyes-Lamothe, R., Ball, G. and Sherratt, D. J. ‘‘Replication and segregation of an Escherichia coli chromosome with two replication origins.’’ *Proceedings of the*

National Academy of Sciences of the United States of America 108.26 (2011), pp. E243-50.

Wang, X., Llopis, P. M., Rudner, D. Z., Montero Llopis, P. and Rudner, D. Z. ‘‘Organization and segregation of bacterial chromosomes.’’ *Nature reviews. Genetics* 14.3 (2013), pp. 191–203.

Wang, X., Possoz, C. and Sherratt, D. J. ‘‘Dancing around the divisome: Asymmetric chromosome segregation in Escherichia coli’’. *Genes and Development* 19.19 (2005), pp. 2367–2377.

Wang, X. and Rudner, D. Z. ‘‘Spatial organization of bacterial chromosomes.’’ *Current opinion in microbiology* 22 (2014), pp. 66–72.

Wang, Y., Penkul, P. and Milstein, J. N. ‘‘Quantitative Localization Microscopy Reveals a Novel Organization of a High-Copy Number Plasmid’’. *Biophysical Journal* 111.3 (2016), pp. 467–479.

Webb, D. J. and Brown, C. M. ‘‘Epi-Fluorescence Microscopy’’. in *Cell imaging techniques* (2012), pp. 29–59.

Weber, S. C., Spakowitz, A. J. and Theriot, J. A. ‘‘Bacterial chromosomal loci move subdiffusively through a viscoelastic cytoplasm.’’ *Physical review letters* 104.23 (2010), pp. 1–4.

Weber, S. C., Spakowitz, A. J. and Theriot, J. A. ‘‘Nonthermal ATP-dependent fluctuations contribute to the in vivo motion of chromosomal loci.’’ *Proceedings of the National Academy of Sciences of the United States of America* 109.19 (2012), pp. 7338–43.

Weiss, D. S. ‘‘Bacterial cell division and the septal ring.’’ *Molecular microbiology* 54.3 (2004), pp. 588–97.

Weng, X. and Xiao, J. ‘‘Spatial organization of transcription in bacterial cells’’. *Trends in Genetics* 30.7 (2014), pp. 287–297.

Wery, M., Woldringh, C. L. and Rouviere-Yaniv, J. ‘‘HU-GFP and DAPI co-localize on the Escherichia coli nucleoid.’’ *Biochimie* 83.2 (2001), pp. 193–200.

Wickner, S. ‘‘Posttranslational Quality Control: Folding, Refolding, and Degrading Proteins’’. *Science* 286.5446 (1999), pp. 1888–1893.

Wiggins, P. A., Cheveralls, K. C., Martin, J. S., Lintner, R. and Kondev, J. ‘‘Strong intranucleoid interactions organize the Escherichia coli chromosome into a nucleoid filament.’’ *Proceedings of the National Academy of Sciences of the United States of America* 107.11 (2010), pp. 4991–5.

Wilson, D. N. ‘‘Ribosome-targeting antibiotics and mechanisms of bacterial resistance’’. *Nature reviews. Microbiology* 12.1 (2014), pp. 35–48.

Winkler, J., Seybert, A., König, L., Pruggnaller, S., Haselmann, U., Sourjik, V., Weiss, M., Frangakis, A. S., Mogk, A. and Bukau, B. ‘‘Quantitative and spatio-temporal features of protein aggregation in Escherichia coli and consequences on protein quality control and cellular ageing.’’ *The EMBO journal* 29.5 (2010), pp. 910–23.

Woldringh, C. L. ‘‘The role of co-transcriptional translation and protein translocation (transertion) in bacterial chromosome segregation’’. *Molecular Microbiology* 45.1 (2002), pp. 17–29.

Woldringh, C. L., Hansen, F. G., Vischer, N. O. E. and Atlung, T. ‘‘Segregation of chromosome arms in growing and non-growing Escherichia coli cells.’’ *Frontiers in microbiology* 6 (2015), p. 448.

Woldringh, C. L., Mulder, E., Valkenburg, J. A., Wientjes, F. B., Zaritsky, A. and Nanninga, N. ‘‘Role of the nucleoid in the toporegulation of division.’’ *Research in microbiology* 141.1 (1990), pp. 39–49.

Woldringh, C. L., Zaritsky, A. and Grover, N. B. ‘‘Nucleoid pertitioning and the division plane in Escherichia coli’’. *Journal of Bacteriology* 176.19 (1994), pp. 6030–6038.

Worcel, A. and Burgi, E. ‘‘On the structure of the folded chromosome of Escherichia coli.’’ *Journal of molecular biology* 71.2 (1972), pp. 127–47.

Wu, B., Chao, J. A. and Singer, R. H. ‘‘Fluorescence fluctuation spectroscopy enables quantitative imaging of single mRNAs in living cells’’. *Biophysical Journal* 102.12 (2012), pp. 2936–2944.

Wu, F., Van Rijn, E., Van Schie, B. G. C., Keymer, J. E. and Dekker, C. ‘‘Multi-color imaging of the bacterial nucleoid and division proteins with blue, orange, and near-infrared fluorescent proteins’’. *Frontiers in Microbiology* 6 (2015), pp. 1–15.

Wu, L. J. and Errington, J. ‘‘Nucleoid occlusion and bacterial cell division.’’ *Nature reviews. Microbiology* 10.1 (2012), pp. 8–12.

Xie, X. S., Choi, P. J., Li, G. W., Lee, N. K. and Lia, G. ‘‘Single-molecule approach to molecular biology in living bacterial cells’’. *Annual Review of Biophysics* 37 (2008), pp. 417–444.

Youle, R. J. and van der Bliek, A. M. ‘‘Mitochondrial fission, fusion, and stress.’’ *Science* 337.6098 (2012), pp. 1062–5.

Young, R. and Bremer, H. ‘‘Polypeptide-chain-elongation rate in Escherichia coli B/r as a function of growth rate.’’ *The Biochemical journal* 160.2 (1976), pp. 185–94.

Youngren, B., Nielsen, H. J., Jun, S. and Austin, S. ‘‘The multifork Escherichia coli chromosome is a self-duplicating and self-segregating thermodynamic ring polymer.’’ *Genes & development* 28.1 (2014), pp. 71–84.

Yu, J., Xiao, J., Ren, X., Lao, K. and Xie, X. S. ‘‘Probing gene expression in live cells, one protein molecule at a time.’’ *Science* 311.5767 (2006), pp. 1600–3.

Yu, X. C. and Margolin, W. ‘‘FtsZ ring clusters in min and partition mutants: role of both the Min system and the nucleoid in regulating FtsZ ring localization.’’ *Molecular microbiology* 32.2 (1999), pp. 315–26.

Zernike, F. ‘‘Phase contrast, a new method for the microscopic observation of transparent objects’’. *Physica* 9.10 (1942), pp. 974–986.

Zhang, P., Khursigara, C. M., Hartnell, L. M. and Subramaniam, S. ‘‘Direct visualization of Escherichia coli chemotaxis receptor arrays using cryo-electron microscopy.’’ *Proceedings of the National Academy of Sciences of the United States of America* 104.10 (2007), pp. 3777–81.

Zimmerman, S. B. and Murphy, L. D. ‘‘Macromolecular crowding and the mandatory condensation of DNA in bacteria.’’ *FEBS letters* 390.3 (1996), pp. 245–8.

Zimmerman, S. B. and Murphy, L. D. ‘‘Release of Compact Nucleoids with Characteristic Shapes from Escherichia coli’’. *Journal of Bacteriology* 183.17 (2001), pp. 5041–5049.

Zink, D., Sadoni, N. and Stelzer, E. ‘‘Visualizing chromatin and chromosomes in living cells’’. *Methods* 29.1 (2003), pp. 42–50.

Publications

Publication I

A. Gupta*, J. Lloyd-Price*, R. Neeli-Venkata, S.M.D. Oliveira, and A.S. Ribeiro, "*In vivo* kinetics of segregation and polar retention of MS2-GFP-RNA complexes in *Escherichia coli*", *Biophysical Journal*, 106(9):1928-1937, 2014.

Biophysical Journal Volume 106 May 2014 1928–1937

In Vivo Kinetics of Segregation and Polar Retention of MS2-GFP-RNA Complexes in *Escherichia coli*

Abhishekh Gupta, Jason Lloyd-Price, Ramakanth Neeli-Venkata, Samuel M. D. Oliveira, and Andre S. Ribeiro*
Laboratory of Biosystem Dynamics, Department of Signal Processing, Tampere University of Technology, Tampere, Finland

ABSTRACT The cytoplasm of *Escherichia coli* is a crowded, heterogeneous environment. From single cell live imaging, we investigated the spatial kinetics and heterogeneities of synthetic RNA-protein complexes. First, although their known tendency to accumulate at the cell poles does not appear to introduce asymmetries between older and newer cell poles within a cell lifetime, these emerge with cell divisions. This suggests strong polar retention of the complexes, which we verified in their history of positions and mean escape time from the poles. Next, we show that the polar retention relies on anisotropies in the displacement distribution in the region between midcell and poles, whereas the speed is homogeneous along the major cell axis. Afterward, we establish that these regions are at the border of the nucleoid and shift outward with cell growth, due to the nucleoid's replication. Overall, the spatiotemporal kinetics of the complexes, which is robust to suboptimal temperatures, suggests that nucleoid occlusion is a source of dynamic heterogeneities of macromolecules in *E. coli* that ultimately generate phenotypic differences between sister cells.

INTRODUCTION

Even single-celled organisms, such as *Escherichia coli*, possess a far from random internal organization. Proteins involved in chemotaxis are preferentially located at the cellular poles (1–4), whereas proteins (e.g., RNA polymerases) and transcription factors involved in gene expression mostly locate within a structure known as the nucleoid that, before its replication, is generally located in the central region of the cell (5–9).

At least some of the heterogeneities in the cytoplasm of *E. coli* cells influence their functioning. One example is that cells inheriting the older pole of the mother cell exhibit diminished growth rate (10), which suggests that some contents in the older pole are harmful, and exist in smaller amounts in the newer pole. Subsequent studies hypothesized that one possibly harmful component inherited with the older pole is protein aggregates (10–14).

It is well known that *E. coli* cells, apart from the nucleoid, lack internal organelles (15). They also lack transport mechanisms for proteins (12,15). Thus, the generation and maintenance of most heterogeneity are likely based on the physical properties of the cells, namely, the presence of the nucleoid at midcell (16) and the shape of the cell (17), and on the physical properties of the components (18).

Recently, to study the nature of the cytoplasm of *E. coli*, Golding and Cox (15,19) used live cell microscopy and a synthetic RNA coding for multiple binding sites for a synthetic protein MS2-GFP, based on the MS2 capsid protein (20). By tracking the MS2-GFP tagged RNA molecules, they observed that, at short timescales, their motion was subdiffusive with an exponent that is robust to physiological changes, such as the disruption of cytoskeletal elements (15). In addition, they showed that, at long timescales, these complexes tend to localize at the cell poles. It was hypothesized that this was due to hydrodynamic coupling between the complexes and the cell walls of the poles (19).

Here, using the same approach as in (15), we further investigate the behavior of these large, inert complexes within the cytoplasm of *E. coli*. We choose to use this complex because of its long lifetime (19) (longer than 2 h) and its robustness to photobleaching (21). Furthermore, the individual MS2-GFP proteins are known to distribute uniformly within the cell (22), whereas the motion of the complexes appears to be dominated by physical interactions (15). This provides strong evidence that there are no significant biological interactions between the MS2-GFP proteins or between the MS2-GFP-tagged RNA and other components of the cytoplasm.

From the analysis of time series images of cells expressing MS2-GFP and the target RNA, we address the following questions. Is the accumulation of these complexes at the cell poles a symmetric process? Do cell divisions introduce asymmetries in their numbers in older and newer cell poles, as in the case of unwanted protein aggregates (11)? Are they retained at the poles, and if so, for how long? What heterogeneities and anisotropies in their motion exist along the major cell axis? Does their spatial distribution change in the course of a cell's lifetime? Finally, we investigate to what extent the nucleoid is involved in the observed behavior of these complexes.

MATERIALS AND METHODS

Chemicals

Bacterial cell cultures were grown in lysogeny broth (LB) media. The chemical components of LB (Tryptone, Yeast extract, and NaCl) were purchased

---

Submitted February 10, 2014, and accepted for publication March 28, 2014.

*Correspondence: andre.ribeiro@tut.fi

Abhishekh Gupta and Jason Lloyd-Price contributed equally to this work.

0006-3495/14/05/1928/10 $2.00

http://dx.doi.org/10.1016/j.bpj.2014.03.035

from LabM (Topley House, Bury, Lancashire, UK) and the antibiotics from Sigma-Aldrich (St. Louis, MO). Isopropyl β-D-1-thiogalactopyranoside (IPTG) and anhydrotetracycline (aTc) used for induction of the target genes are from Sigma-Aldrich. Agarose (Sigma-Aldrich) was used for microscope slide gel preparation for cell imaging. 4′,6-diamidino-2-phenylindole (DAPI) from Sigma-Aldrich was used to stain cell nucleoids.

Cells and plasmids

Experiments were conducted in *E. coli* strain DH5α-PRO, generously provided by I. Golding (Baylor College of Medicine, Houston, TX), which contains two constructs: i), PROTET-K133 carrying $P_{LtetO-1}$-*MS2d-GFP* (19), and ii), a pIG-BAC ($P_{lac/ara-1}$-*mRFP1-MS2-96bs*) vector, carrying a 96 MS2 binding site array under the control of $P_{lac/ara-1}$ (19).

Induction of production of fluorescent complexes

The dimeric MS2 fused to green fluorescent protein (GFP) (MS2-GFP fusion protein) used as a detection tag (19) is expressed from a medium-copy vector under the control of the $P_{LtetO-1}$ promoter (23), which is regulated by the tetracycline repressor. The RNA target for MS2-GFP is located on a single-copy F-based vector, and is controlled by the $P_{lac/ara-1}$ promoter (23). For our measurements, precultures were diluted from the overnight culture to an OD_{600} of 0.1, in fresh LB media supplemented with the appropriate antibiotics and kept at 24°C or 37°C at 250 RPM in a shaker for ~2 h at 24°C or ~1.5 h at 37°C until they reached an $OD_{600} \approx 0.5$. At this point, cells were induced with 50 ng/ml of aTc and 0.1% L-arabinose for 45 min, at which point the OD_{600} was ~0.8. Induction of the target RNA production was then completed by adding 1 mM IPTG and cells were incubated for 5 min before preparation of the microscope slide. We note that this induction procedure is necessary for cells to have sufficient numbers of MS2-GFP to detect the target RNA and to achieve full induction of the target gene during the microscopy measurements (24,25).

Imaging

After induction of the target gene, a few microliters of culture were placed on a microscope slide between a coverslip and a 0.8% agarose gel pad set with the LB media, followed by the assembly of a thermal imaging chamber (Bioptechs, FCS2) set at the appropriate temperature. Cells were visualized by fluorescence microscopy using a Nikon Eclipse (TE2000-U, Nikon, Tokyo, Japan) inverted microscope with a C1 confocal laser scanning system using a 100× Apo TIRF (1.49 NA, oil) objective. GFP fluorescence was measured using a 488 nm laser (Melles-Griot) and a 515/30 nm detection filter. Images of cells were taken from each slide by the Nikon software EZ-C1, starting ~10 min after induction of the target gene, 1/min, for 2 h. The pixel dwell was 1.33 μs, resulting in a line scanning time of ~1.4 ms; this is significantly faster than the diffusion speed of the MS2-GFP-RNA particles (see (15)), and should therefore not introduce any time-averaging artifacts.

Imaging of nucleoids

DAPI stains nucleoids specifically, with little or no cytoplasmic labeling (26). Precultures were grown for ~3 h with the same previous protocol (but without inducing the target or reporter genes). After reaching an $OD_{600} \approx 0.8$, cells were centrifuged and suspended in phosphate buffered saline (PBS). For live cell nucleoid staining, DAPI (2 μg/ml) was added to the cells suspended in PBS and incubated for 20 min in the dark. Cells were then washed twice with PBS, and placed on a 1% agarose gel pad prepared with LB. The cells were simultaneously observed by epifluorescence microscopy, using a mercury lamp with a DAPI filter, and by phase contrast microscopy. DAPI is excited at 359 nm and emits at 461 nm. Images were acquired with Nikon software NIS-Elements. Cells in phase contrast images were segmented using the software MAMLE (27). The background of the images obtained by epifluorescence microscopy was removed by subtracting a cubic polynomial surface, fitted to the image by L1-norm minimization (i.e., minimizing the absolute difference between the surface and the image; see, e.g. (28)). The fluorescence intensities in each cell were then extracted. See Fig. 6, which shows the fluorescence intensities were projected along the major axis of the cell.

Detection of cells and individual complexes within from the images

Cells were detected from the images by a semiautomatic method as in (22). First, the time series images from confocal microscopy were aligned, so that the cells stayed in the same position throughout the time series. Next, a mask was manually drawn over the region that each cell occupied during the time series. When a cell divided, separate masks were drawn in the frame where the division was first observed, to represent daughter cells after division. After thresholding the fluorescence distribution within each mask to enforce a uniform fluorescence within the cell, principal component analysis was used to obtain, at each frame, the position, dimension, and orientation of the cell inside each mask.

To construct cell lineages, we automatically assigned a parent to each cell in each frame, as the cell in the previous frame with the nearest centroid. This was done after transforming the previous frame's cell centroids by the inverse of the transform that maps a unit circle to the cell's ellipse, to avoid incorrectly assigning adjacent cells as parents. When two cells are assigned the same parent, a division is assumed to have occurred. We verified the efficiency of this method by inspection, and found the rate of error to be negligible.

Next, we detected fluorescent MS2-GFP-RNA complexes in each cell, at each frame, as in (22). We segmented the fluorescent complexes automatically inside each mask with the kernel density estimation (KDE) method for spot detection (29). This method measures the local smoothness of the image, and determines spot locations by designating areas with low smoothness as spots. We used a Gaussian kernel as in (22). Cell background corrected complex intensities were then calculated by subtracting the mean cell background intensity multiplied by the area of the complex from the total fluorescence intensity of the complex.

For cells containing only one complex, once the complexes were detected at each time point, we obtained displacement vectors from their positions in consecutive frames. In Fig. 1, we show an example image of cells (Fig. 1 *A*), along with the segmented cells and detected complexes within (Fig. 1 *B*), and an example of the extracted displacement vectors of a complex from its positions at consecutive frames (Fig. 1 *C*).

By inspection, we observed that the spot detection is reliable. Although we are unable to determine the precision with exactness, as it depends on many variables including noise in the image, we can estimate a conservative upper bound for the error. Assuming that the method of detection is perfect, the discrete nature of the pixels implies that the error in the estimate of the spot's position is up to $2^{-1/2}$ pixels. If the spot detection, e.g., misidentifies pixels at the borders of spots, in the worst case scenario, it would misidentify all pixels only on one side of the spot. This could introduce a further $2^{-1/2}$ error into the estimation of the spot's position. Given this, the error in the estimate of the spot position should have an upper bound of $\sqrt{2}$ pixels, or ~0.17 μm. As several rare events are required to produce this error, the real expected error is considerably lower. Nevertheless, even this upper bound is much smaller than the cell length (2–4 μm), rendering this error negligible.

Models of long-term spatial distributions of large molecules in the cytoplasm of *E. coli*

A cell is modeled as a one-dimensional space, which is divided into N homogeneous subvolumes. The motion of the complexes is modeled by

FIGURE 1 (*A*) Example image of cells with fluorescent MS2-GFP-RNA complexes within. (*B*) Segmentation and principal component analysis results of the image in (*A*) with cells (*gray*) and complexes (*white*). (*C*) One example of the extracted displacement vectors of a complex from its consecutive positions in the cell. Three images of the cell are shown below, taken at 40, 80, and 120 min (displacement vectors are from the upper cell). Scale bars are 1 μm. The contrast of these images was enhanced for easier visualization.

unimolecular reactions following the reaction-diffusion master equation (30). The propensities in the reaction-diffusion master equation are functions of the position of the subvolume, and are presented in the Supporting Material. Three models were implemented: one without internal heterogeneities or anisotropies, one with heterogeneities, and one with anisotropies. Also in the Supporting Material, we present the methods used to analyze the results of the models.

RESULTS

Spatial distribution of the complexes

To study the spatial distribution of the complexes, we imaged cells for 2 h following the induction of the target RNA and tagging MS2-GFP proteins (see Methods). Images were taken once per minute, in optimal and suboptimal growth conditions (LB media, 37°C and 24°C, respectively). An example image is shown in Fig. 1 *A*. During this period, cells grew, divided, and produced MS2-GFP-RNA complexes, which moved within the cytoplasm of the cells and were partitioned in cell divisions.

In general, these complexes are first observed at midcell (where the F-plasmid carrying the target gene is located (31)) and then travel toward the cell extremes, where they tend to remain (19). To study whether the side to which they travel is a symmetric (i.e., unbiased) process with respect to the age of the cell halves, we observed this process in cells that initially contained no complexes and that were born during the measurement period (107 cells at 37°C and 156 cells at 24°C), so that the older half of each cell could be identified. In these cells, at each time moment, we identified the locations of fluorescent complexes along the major axis of the cell (positions are normalized by half the length of the major axis), and determined the background-corrected fluorescence intensity of each. Colocalized complexes will, approximately, exhibit a fluorescence intensity that is the sum of the intensity of its component complexes (25). For each condition, we summed the intensities of the complexes at each location along the major axis of the cell, over all time points and cells, thus obtaining the spatiotemporal distribution of the complexes. We used KDE (32) with a Gaussian kernel to perform this sum, resulting in a smooth distribution (Fig. 2 *A*). We note that we did not separate cells of different sizes when obtaining this distribution. Given the time length of the measurements and the fact that most cells divided during this period, the resulting distribution and all conclusions drawn from it should be considered to be the average behavior over the cell cycle.

From the distribution for each condition, we computed the fraction of complexes in the older half. We found this fraction to be 0.46 at 37°C and 0.47 at 24°C, which are both statistically indistinguishable from the expected fraction assuming an unbiased partitioning of complexes (p-values of the binomial test with N equal to the number of observed cells were larger than 0.2, and it is usually accepted that, for p-values smaller than 0.01, the null hypothesis is rejected). We therefore find no evidence that

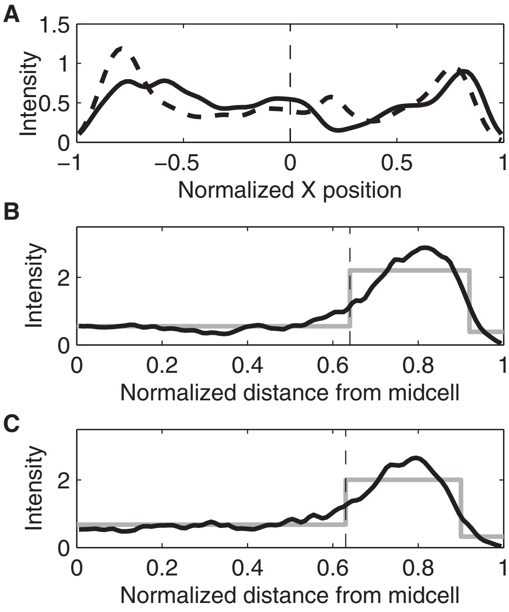

FIGURE 2 KDE of spatial distributions of the fluorescence intensity (in arbitrary units) of complexes along the major axis of the cells (bandwidths 0.05). All cells were born during the measurement period. (*A*) Data from all cells that inherited no complexes but produced one or more. The old pole is at +1 and the new pole is at −1. Data are from 107 cells at 37°C (*solid line*) and 156 cells at 24°C (*dashed line*). The dashed vertical line represents the cell center. (*B* and *C*) Data from all cells (*black line*). Complex positions were normalized by half the cell length and mirrored about the cell center. Also shown is the fit of a piecewise constant probability density function by maximum likelihood (*gray line*). The vertical dashed line represents the detected separation points between the midcell and poles. Measurements are from (*B*) 531 cells at 37°C, with separation point at 0.64 and (*C*) 372 cells at 24°C, with separation point at 0.61.

the complexes are asymmetrically distributed between the older and newer halves of the cell before division events.

Also from Fig. 2 *A*, in both conditions, the complexes were preferentially located close to the cell extremes (i.e., at the polar regions) for most of the measurement period, as reported in (25). To quantify the degree of polarization of the complexes, one needs to formally define such polar regions, along the major axis of the cells. We did this from a functional perspective, i.e., based on the heterogeneities of the spatial distributions of the complexes visible in Fig. 2 *A*. Given the symmetry in these distributions between the old and new halves of the cells, from here onward, we folded the spatial distribution around 0, and summed the intensities from both halves. As such, it is possible to include all cells born during the measurements in this analysis. The resulting distributions of each condition are shown in Fig. 2, *B* and *C*.

To distinguish the functional regions in each condition, we fitted a piecewise constant probability density function with three pieces to each intensity distribution by maximum likelihood (*gray line* in Fig. 2, *B* and *C*). The separation points between the regions from the fit were found to be at 0.64 for 37°C and at 0.61 for 24°C.

Based on this separation between poles and midcell regions, we calculated the concentration of complexes at the poles and at midcell, in each condition, to assess the degree of polarization of the complexes. In this case, concentrations >1 indicate that the complexes are located in this region beyond what would be expected from a uniform distribution. This concentration was found to be 1.72 at 37°C and 1.45 at 24°C.

From this separation, we also determined whether cell divisions introduced biases in the numbers of complexes at the old and new poles in subsequent generations. In the measurements conducted at 37°C, sufficient divisions occurred in the 2 h measurement period of to assess this. From these, we selected cells that inherited one complex but produced none during their lifetime (111 cells), to ensure that the complexes analyzed are only inherited ones. During the lifetime of these cells, the old pole contained 65% of the complexes located in a pole. The p-value that this fraction arises from an unbiased binomial distribution with the number of trials equal to the number of cells is 0.004, from which we conclude there is a significant bias that favors the old pole.

As a control, similar experiments were performed in minimal media (M63) at 37°C (for details, see the Supporting Material). The results (Fig. S1 and Fig. S2) are qualitatively the same as in LB media. Specifically, the complexes accumulated at the poles, in well-defined regions. Furthermore, cell divisions introduced asymmetries between the numbers of complexes at the old and new poles of the daughter cells. These asymmetries following divisions are possible if, to some extent, the complexes are retained at the pole where they are inherited (otherwise, the bias would be rapidly lost).

Retention of complexes at the poles

To study the retention of the complexes at the poles, for each condition, we selected cells that contained at most one complex throughout their lifetime (either inherited or produced), so that they could be reliably tracked. We recorded the position along the major axis where the complex was first observed within a polar region, as previously defined, and the complex's final position, i.e., either before division or at the end of the measurement period. This information is presented in Fig. 3. In general, a complex's final position is within the polar region to which it first traveled to, as expected from a strong polar retention. However, in a few cases, the opposite occurs, which shows that complexes can move across the entire major cell axis (as reported in (19)). This indicates that there is a degree of leakiness, or noise, in the retention at the poles.

To quantify the strength of polar retention, we measured the escape times of the complexes from the poles, in each condition (mean values in Table 1). Note that, on some (rare) occasions, the complexes appeared to leave the pole for only one time moment, and then promptly returned. We did not count these cases as escapes. Furthermore, when complexes did not leave the pole until the end of the measurement period or until a division event, we consider that they remained at the pole only until the next time

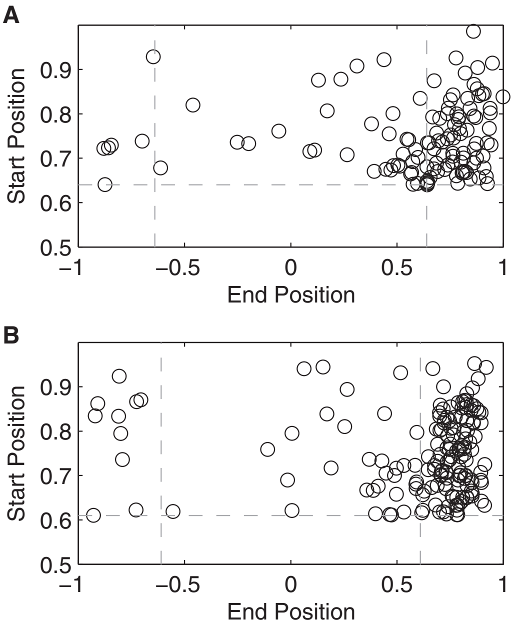

FIGURE 3 Relationship between the position along the major axis where each complex was last observed and the absolute position where it was first observed at a pole. Here, an end position of +1 indicates that the complex remained at the same pole as it was first observed, whereas −1 indicates that it traveled to the other pole. The horizontal and vertical dashed lines represent the detected separation between the midcell and poles from Fig. 2, *B* and *C*. All cells were born during the measurement period and contained only one complex during their lifetime. Measurements are from (*A*) 160 cells at 37°C and (*B*) 198 cells at 24°C.

TABLE 1 Mean and standard deviations of escape times of complexes from the poles, in each condition

T (°C)	No. cells	Mean division time (min)	Escape times (min)	p-value of *t*-test
37	160	63	14.8 ± 19.3	0.062
24	198	91	18.0 ± 18.4	

Also shown is the number of cells observed, their mean division time, and the *p*-value of the *t*-test with the hypothesis that the mean escape times are identical in both conditions.

moment. Thus, the measured mean escape times are underestimates of the real escape times.

From Table 1, within the range tested, we find no evidence that temperature affects the mean escape time from the poles. Furthermore, in both temperature conditions, the standard deviations of escape times were similar to the means, a characteristic of exponential distributions, which is the expected solution of, e.g., a barrier crossing problem or of a particle trying to escape from a region through small passages (33).

Spatial dynamics of complexes

To better understand how the complexes are retained at the poles, from cells containing at most one complex during their lifetime, we obtained their displacement vectors along the major cell axis between frames. These inform on the directionality of a complex between consecutive images (assessed by the sign of the displacement vector). In addition, they inform on the speed at which the complexes are able to move along the major cell axis during the intervals between consecutive images (assessed by the magnitude of the displacement vector). Cell growth between consecutive frames was accounted for by projecting the origin of each displacement vector into the cell space in the following frame, before calculating the magnitude and direction.

First, for each condition, we extracted the speeds from the displacement vectors going toward a pole and going toward the midcell, as a function of their point of origin. For this, we defined a sliding window with a width of 0.1 cell lengths and determined which displacement vectors originated within that window and their direction.

At midcell, the mean speed of complexes going toward a pole (0.13 μm/min at 37°C and 0.14 μm/min at 24°C) was statistically indistinguishable from the mean speed of those going toward midcell (0.12 μm/min at 37°C and 0.14 μm/min at 24°C) (*p*-values of the *t*-tests >0.4). At the poles, in both temperature conditions, the mean speed of complexes going toward a pole (~0.07 μm/min) and toward midcell (~0.11 μm/min) was distinguishable, in a statistical sense (*p*-values of the *t*-tests <0.01). This difference is visible in Fig. 4, for both conditions. The decrease in mean speed as the complexes approach the cell extremes is expected, given the proximity to the cell wall.

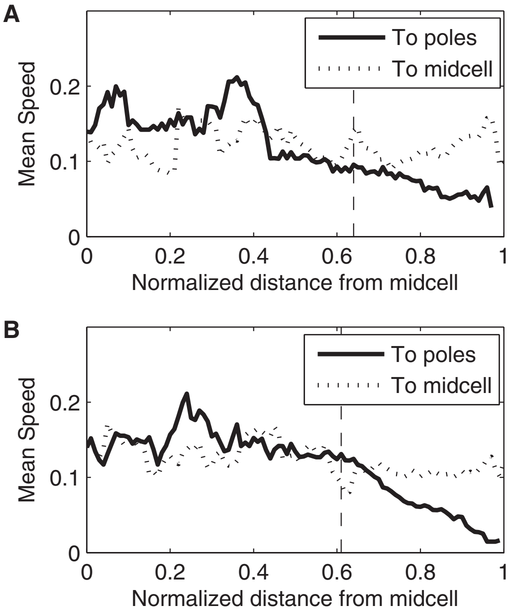

FIGURE 4 Mean speed (μm/min) of the displacement vectors directed toward the poles and toward midcell along the major cell axis. The mean speeds were calculated from the displacement vectors originating within a window extending 0.05 normalized cell lengths around that point. The dashed vertical lines represent the functional separation between midcell and poles (obtained from Fig. 2, *B* and *C*). All cells were born during the measurement period and contained one complex in their lifetime. Measurements are from (*A*) 49 cells at 37°C and (*B*) 101 cells at 24°C.

Relevantly, the mean speed of the vectors going toward the cell center of complexes at the poles and at midcell is indistinguishable in a statistical sense, in both temperature conditions (*p*-values of the *t*-tests >0.01). Given that the mean speeds at midcell of complexes traveling toward poles and toward midcell are also indistinguishable (see above), we conclude that the speed of complexes is fairly homogenous throughout the major cell axis, except for the complexes traveling toward a pole that are already near the cell extreme (which, therefore exhibit lower mean speed).

We next analyzed the directionality of the displacement vectors. Using the same sliding window as before, we counted the number of displacement vectors originated in the window, which were directed toward the midcell and toward the poles. In Fig. 5, we show the difference between these two numbers along the major cell axis. In both conditions, a characteristic spatial heterogeneity is observable. At midcell, the complexes have equal probability of moving in either direction, whereas at the poles, there are local biases in the directionality of the displacement vectors. In particular, if close to the cell extremes, the complexes tend to move inward, toward the midcell. Meanwhile, if they are close to the border between midcell and the pole (as defined from the spatial distributions of complexes shown in Fig. 2, *B* and *C*), the opposite occurs. As a result, once reaching a pole, the complexes tend to remain there.

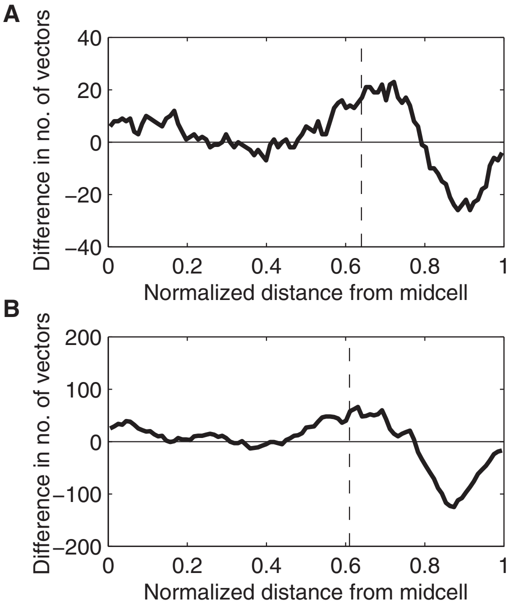

FIGURE 5 Difference between the numbers of displacement vectors that are directed toward the poles and toward the midcell along the major cell axis. The differences were calculated from the displacement vectors originating within a window extending 0.05 normalized cell lengths around that point. The dashed vertical lines represent the functional separation between midcell and poles (obtained from Fig. 2, *B* and *C*). All cells were born during the measurement period and contained one complex in their lifetime. Measurements are from (*A*) 49 cells at 37°C and (*B*) 101 cells at 24°C.

It is noted that although the anisotropic displacement distribution at the extremes of the cell is expected from the geometry of the cell wall at the poles, the source of the opposite anisotropy in the transition between midcell and poles is less clear. Its existence suggests that the motion of the complexes going from poles to midcell is, to a degree, obstructed. This effect is possible if the complexes are encountering a more dense structure that hampers their entrance into that region.

Relevantly, the location of the anisotropy, namely, 0.64 at 37°C and 0.61 at 24°C, is in agreement with previous measurements of the nucleoid size in *E. coli* cells grown in LB media at 37°C (e.g., its length relative to the major axis length is 0.53 ± 0.05 in wild-type DJ2599 cells (34)). We thus hypothesized that the nucleoid is involved in this phenomenon, and measured its length in the cells of the strain used here, in the same conditions as above.

Spatial distribution of nucleoids

To test whether the regions of anisotropies of the displacement distributions along the major cell axis are consistent with the borders of the nucleoid, we measured the nucleoid size (see Methods) from 220 cells at 37°C and 143 cells at 24°C (see example, Fig. 6, *A* and *B*). The intensity of the DAPI signal, summed along the minor axis for each position along the major axis of the cells, and summed over all cells, is shown in Fig. 6, *C* and *D*.

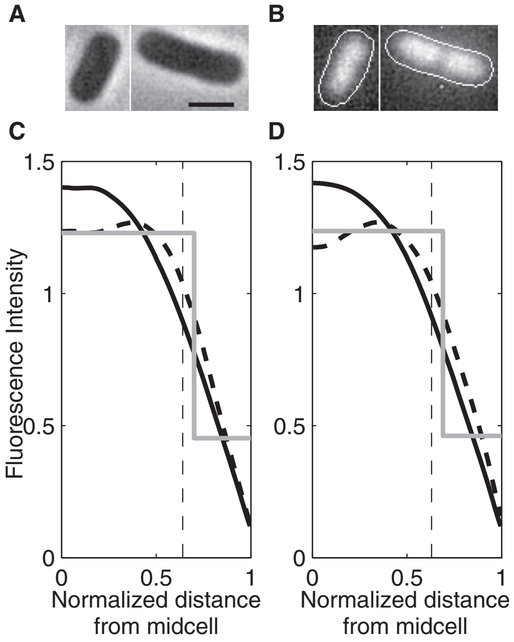

FIGURE 6 (*A*) Example phase contrast images of cells and (*B*) corresponding background-subtracted epifluorescence with the nucleoids stained by DAPI, and the detected cell contours superimposed (contrast enhanced for easier visualization in both *A* and *B*). Scale bar is 1 μm. The two bottom figures (*C*) and (*D*) show the spatial distributions of the fluorescence intensity (in arbitrary units) of the DAPI signal along the major cell axis (*black line*) and the fit of a piecewise constant probability density function by maximum likelihood (*gray line*). The vertical dashed lines represent the detected separation between midcell and poles (from Fig. 2, *B* and *C*). Also shown is the fluorescence distribution from the 10% longest cells in each condition (*dashed line*). Measurements are from (*C*) 220 cells at 37°C and (*D*) 143 cells at 24°C.

To determine the edge of the nucleoid, we fitted a piecewise constant probability density function with two pieces to the intensity distribution by maximum likelihood. We found the separation point to be at 0.69 in both conditions. This is close to the measured separation points between the midcell region, which the complexes avoid, and the poles, where they accumulate (0.61 and 0.64 at 24°C and 37°C, respectively, see Fig. 2, *B* and *C*). The slightly larger size of the nucleoid may be due to DAPI being an intercalating dye (26). Note that the nucleoid size was not altered by the differences in temperature. This is in agreement with the lack of differences in the width of the polar regions where the complexes tend to accumulate in the two temperature conditions.

If the heterogeneities in the spatial distribution of the complexes depend on the positioning of the nucleoid(s), as these results suggest, the replication of the nucleoid before cell division should then affect this distribution. To determine this, we first selected the 10% longest cells detected in the DAPI measurements and searched for differences in their spatial distribution of fluorescence intensities, when compared to the total population. Results in Fig. 6, *C* and *D*, confirm the existence of differences, as the region occupied by the nucleoids along the major cell axis is relatively wider in these cells. Note also a decrease in fluorescence intensity, precisely at midcell, as expected if several of these cells contain two nucleoids.

Next, we studied the spatial distribution of the complexes in the 10% longest cells as extracted from the time series measurements of the complexes' positions and kinetics (from the same data used in Fig. 2, *B* and *C*). If the nucleoid(s) affect the spatial distribution of complexes, in these cells one can expect the complexes to accumulate relatively closer to the poles. Fig. 7 shows that this is the case both at 37°C and 24°C, thus providing supporting evidence that the nucleoid(s) influence(s) the complexes' preferential positioning.

As a side note, we did not find evidence for cells with more than two nucleoids at any stage of their lifetime (see, e.g., that Fig. 6, *C* and *D* do not show evidence for more than two lobes). This could be due to the strain used (DH5α-PRO divides slower than wild-type *E. coli* (35)) along with the measurement conditions. In addition, we found no significant accumulation of complexes at the center in the longer cells (i.e., in between the two nucleoids). This is likely due to the very small number of complexes (~1 to 3 per cell before division). Furthermore, many are created before nucleoid partitioning and thus simply remain at the poles as the nucleoid divides.

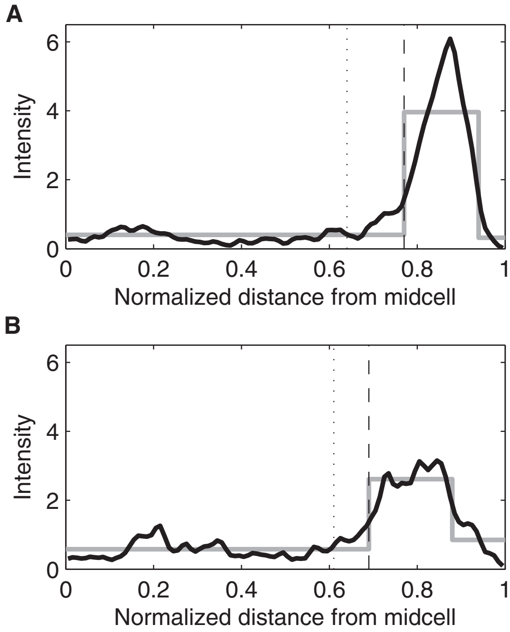

FIGURE 7 KDE of the spatial distribution of the fluorescence intensity (in arbitrary units) of complexes along the major axis of the cells, extracted from all time points when the cells were among the 10% longest cells (*black line*, bandwidth 0.05). All cells were born during the measurement period. The dashed vertical line represents the detected separation point for (*A*) 531 cells at 37°C and (*B*) 372 cells at 24°C, both grown in LB media.

Finally, because we observed several complexes traveling from one pole to the other, it is of interest to ask whether they do so by traveling through the nucleoid or around it. To address this, we obtained the KDE of the two-dimensional distributions of complexes from all time points in both temperature conditions (Fig. S3, *A* and *B*). From the figures, it is visible that the complexes tend to avoid the nucleoid region both axially and radially, concentrating at midcell close to the cell walls (despite the greater width in the center of the bacteria, at $Y = 0$). From this, we conclude that the complexes tend to go around the nucleoid, when traveling through the midcell region. Relevantly, this result is in agreement with both the homogeneity in the distributions of speeds along the major axis of the cells as well as with the localized anisotropies between midcell and poles.

Models of the spatial kinetics of complexes

To test whether the localized anisotropies in directionality, given the homogeneity of the speeds, can generate the observed heterogeneity in the long-term spatial distributions of the complexes, we constructed two one-dimensional models to simulate the diffusion of the complexes within the cell. Both models contain spherical cell caps and their effects. Meanwhile, in one model, we also introduced a localized anisotropy (see Fig. 8, *A* and *B*; for a complete description of the models see the Supporting Material).

Given that the mean speeds of the complexes (see Fig. 4) are sufficiently large to allow them to travel from one pole to the other within the cell's lifetime (more than once), we assume that the initial positions of the complexes do not have a significant effect on their long-term spatial distribution, and thus this information is not included in the models. Additionally, for both models, we set N, the number of subvolumes in the cell, to 100, and D, the diffusion coefficient, to 1.43×10^{-2} μm^2/min (measured from the displacement distribution depicted in Fig. 4 *B*), which we normalized by half the mean cell length (~1 μm), in agreement with previous measurements (15).

Next, for each model, we varied all parameters and, for each set of values, obtained the distribution of complex positions that would be observed at infinite time. We then selected the set of parameters whose resulting distribution best fit the measured distribution of complex positions at each time point (Fig. 2, *B* and *C*). This fitting was done to the distribution obtained from the measurements at 24°C (from which we extracted more data points), using the earth-mover's measure of distance between distributions (36,37), which measures the amount of work required to make two distributions identical (see methods in the Supporting Material). Similar parameter values were obtained when fitting to the measurements at 37°C.

The results from the two models, each using the best-fit parameter values, are shown in Fig. 8. The propensities of the two models are shown in Fig. 8, *A* and *B*. From Fig. 8,

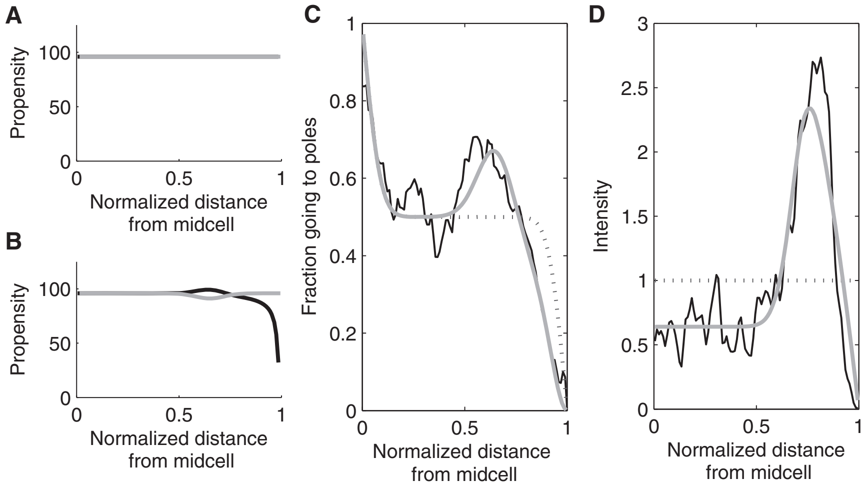

FIGURE 8 (*A*) Propensities $\overrightarrow{a}(x) = \overleftarrow{a}(x)$ (*gray line*) of the best-fitting model without a nucleoid ($B = 1$). (*B*) Propensities $\overrightarrow{a}(x)$ (*black line*) and $\overleftarrow{a}(x)$ (*gray line*) of the best-fitting model with a nucleoid ($B = 0.46$, $\mu = 0.65$, $\sigma = 0.07$, and $h = 0.05$). (*C*) Measured fraction of displacement vectors originating within a window extending 0.05 normalized cell lengths around that point which are directed toward the pole (*black line*), model prediction without (*dashed line*), and with (*gray line*) a nucleoid. Note that the dashed line is superimposed by the gray line in the left side of the graph. (*D*) Measured spatial distribution of fluorescence intensities of complexes (*black line*) model prediction without (*dashed line*) and with (*gray line*) a nucleoid.

C and *D*, the model without the anisotropy fails to reproduce the displacement distribution (Fig. 8 *C*), and the consequent heterogeneity in the spatial distribution of complexes that favors their presence at the poles (Fig. 8 *D*). Meanwhile, the other model captures both of these properties of the dynamics of the complexes with significant accuracy.

DISCUSSION

We studied the kinetics and spatial distribution of biologically inert complexes, composed of RNA molecules tagged with multiple MS2-GFP proteins, in the cytoplasm of *E. coli* cells. The advantages of using these complexes are that their numbers can be controlled by regulating the activity of the target gene, both the target gene and the tagging MS2-GFP molecules are functional in a wide range of environmental conditions including stresses, and the complexes formed have a long lifetime (38,39). This last advantage ensures that we can observe how they are partitioned in division and thus, how they become distributed across cell lineages.

We found that their previously reported tendency to travel toward the poles (19) is a symmetric process in the conditions tested, in that equal numbers of newly produced complexes travel toward the old and the new pole of the cells. Once reaching the poles, they are robustly retained there. Because of this, cell divisions introduce asymmetries in their numbers between the old and new poles of cells of subsequent generations, and after two generations, between sister cells.

There are two possible mechanisms by which the complexes could accumulate at the cell poles, without a transport mechanism. Either their speed distribution is heterogeneous along the major cell axis (i.e., slower at the poles, see Fig. S4), or there is an excluded volume effect at midcell. We found that the retention is solely based on the latter. First, we showed that the speed distribution is homogenous, which rejects the first mechanism. Next, we showed that there is a strong anisotropy in the displacement distribution at approximately half way between the cell extremes and the center, where the motion of the complexes toward midcell is, to a great extent, obstructed. This is consistent with volume exclusion effects due to the presence of the nucleoid.

The existence of the anisotropy and the absence of heterogeneity in the speeds suggest that to go from one pole to the other, the complexes go around the nucleoid. The overall two-dimensional distributions of positions occupied by complexes throughout their lifetimes supported this hypothesis, as they showed that the complexes avoid the nucleoid, both axially and radially. Meanwhile, the escape times of these complexes from the poles were found to be approximately equal to a third of the cell's lifetime and to follow exponential distributions. This implies that the escape from the pole is a Poisson process, which is consistent with the behavior of a particle trying to escape from a region through a small passage (33).

To further support the hypothesis that the polar retention is primarily driven by the nucleoid positioning, we tested whether there is an agreement between the location of the nucleoid and where the movement of complexes is obstructed. We found that the region where the complexes are retained agrees with the region where the nucleoid ends. In addition, we observed that in the longest cells, where the nucleoid(s) occupy a relatively wider region (due to nucleoid replication), the complexes occupy a relatively smaller region at the poles. Additional support was provided by modeling. From the models, in the absence the nucleoid's effects, namely, in the absence of the anisotropy in the region between poles and midcell, the retention at the poles was severely hampered. Introducing anisotropy in the velocity distribution resulted in an accurate long-term spatial distribution.

The size of the region occupied by the nucleoid(s) during the cell lifetime was found to be robust for optimal and sub-optimal temperatures. This explains the robustness of the width of the region where the complexes accumulated, in the range of temperatures tested here. In the future, measurements in wider temperature ranges may help to establish if the retention at the poles is affected, as the number of genes transcribed changes, altering the nucleoid size (40).

It is known that, when in exponential growth phase, some cells can contain more than two nucleoids. Although we did not observe this here (perhaps due to the strain used), if these nucleoids become widely spread across the major cell axis long enough, the regions in between the nucleoids may become regions of accumulation of complexes, until multiple cell division events separate the nucleoids. Future research may determine whether this occurs and to what extent.

Finally, by using the methodology employed here on other *E. coli* strains, it should be possible to determine whether our observations are representative of the behavior of wild-type *E. coli*. Given the physical nature of the underlying processes suggested by our results, we expect this to be the case. In this regard, it is worth noting that the long-term spatial distribution of the complexes observed here is strikingly similar to other protein complexes in *E. coli*. In particular, their accumulation at the poles of the cells is similar to aggregate processing chaperones (11) and ribosomes (9). Furthermore, clusters of Tsr proteins, involved in chemotaxis, are known to accumulate at the poles (4,41), although the mechanisms by which these heterogeneities are achieved remain unknown. Future research may establish if all these processes in *E. coli* are regulated by the same means.

SUPPORTING MATERIAL

Four figures and supporting data are available at http://www.biophysj.org/biophysj/supplemental/S0006-3495(14)00336-1.

This work was supported by the Finnish Funding Agency for Technology and Innovation (S.O., R.N.V., A.S.R.), the Academy of Finland (A.S.R.), the Portuguese Foundation for Science and Technology (A.S.R.), the Tampere Doctoral Programme in Information Science and Engineering (A.G.), and the TUT President's graduate programme (J.L.P.). The funders had no role in study design, data collection and analysis, decision to publish, or preparation of the manuscript.

REFERENCES

1. Sourjik, V., and H. C. Berg. 2004. Functional interactions between receptors in bacterial chemotaxis. *Nature.* 428:437–441.
2. Wadhams, G. H., and J. P. Armitage. 2004. Making sense of it all: bacterial chemotaxis. *Nat. Rev. Mol. Cell Biol.* 5:1024–1037.
3. Parkinson, J. S., P. Ames, and C. A. Studdert. 2005. Collaborative signaling by bacterial chemoreceptors. *Curr. Opin. Microbiol.* 8:116–121.
4. Zhang, P., C. M. Khursigara, ..., S. Subramaniam. 2007. Direct visualization of *Escherichia coli* chemotaxis receptor arrays using cryo-electron microscopy. *Proc. Natl. Acad. Sci. USA.* 104:3777–3781.
5. Kuhlman, T. E., and E. C. Cox. 2012. Gene location and DNA density determine transcription factor distributions in *Escherichia coli*. *Mol. Syst. Biol.* 8:610.
6. Montero Llopis, P., A. F. Jackson, ..., C. Jacobs-Wagner. 2010. Spatial organization of the flow of genetic information in bacteria. *Nature.* 466:77–81.
7. Jin, D. J., C. Cagliero, and Y. N. Zhou. 2012. Growth rate regulation in *Escherichia coli*. *FEMS Microbiol. Rev.* 36:269–287.
8. Bratton, B. P., R. A. Mooney, and J. C. Weisshaar. 2011. Spatial distribution and diffusive motion of RNA polymerase in live *Escherichia coli*. *J. Bacteriol.* 193:5138–5146.
9. Bakshi, S., A. Siryaporn, ..., J. C. Weisshaar. 2012. Superresolution imaging of ribosomes and RNA polymerase in live *Escherichia coli* cells. *Mol. Microbiol.* 85:21–38.
10. Stewart, E. J., R. Madden, G. Paul, and F. Taddei. 2005. Aging and death in an organism that reproduces by morphologically symmetric division. *PLoS Biol.* 3:0295–0300.
11. Lindner, A. B., R. Madden, ..., F. Taddei. 2008. Asymmetric segregation of protein aggregates is associated with cellular aging and rejuvenation. *Proc. Natl. Acad. Sci. USA.* 105:3076–3081.
12. Winkler, J., A. Seybert, ..., B. Bukau. 2010. Quantitative and spatio-temporal features of protein aggregation in *Escherichia coli* and consequences on protein quality control and cellular ageing. *EMBO J.* 29:910–923.
13. Ebersbach, G., A. Briegel, ..., C. Jacobs-Wagner. 2009. A multimeric pole-organizing protein critical for chromosome attachment, division and protein localization in *Caulobacter*. *Cell.* 134:956–968.
14. Maisonneuve, E., B. Ezraty, and S. Dukan. 2008. Protein aggregates: an aging factor involved in cell death. *J. Bacteriol.* 190:6070–6075.
15. Golding, I., and E. C. Cox. 2006. Physical nature of bacterial cytoplasm. *Phys. Rev. Lett.* 96:098102.
16. Fisher, J. K., A. Bourniquel, ..., N. Kleckner. 2013. Four-dimensional imaging of *E. coli* nucleoid organization and dynamics in living cells. *Cell.* 153:882–895.
17. Coquel, A.-S., J.-P. Jacob, ..., H. Berry. 2013. Localization of protein aggregation in *Escherichia coli* is governed by diffusion and nucleoid macromolecular crowding effect. *PLOS Comput. Biol.* 9:e1003038.
18. Mondal, J., B. P. Bratton, ..., J. C. Weisshaar. 2011. Entropy-based mechanism of ribosome-nucleoid segregation in *E. coli* cells. *Biophys. J.* 100:2605–2613.
19. Golding, I., and E. C. Cox. 2004. RNA dynamics in live *Escherichia coli* cells. *Proc. Natl. Acad. Sci. USA.* 101:11310–11315.
20. Peabody, D. S. 1993. The RNA binding site of bacteriophage MS2 coat protein. *EMBO J.* 12:595–600.
21. Kandhavelu, M., A. Häkkinen, ..., A. S. Ribeiro. 2012. Single-molecule dynamics of transcription of the lar promoter. *Phys. Biol.* 9:026004.
22. Kandhavelu, M., J. Lloyd-Price, ..., A. S. Ribeiro. 2012. Regulation of mean and noise of the in vivo kinetics of transcription under the control of the lac/ara-1 promoter. *FEBS Lett.* 586:3870–3875.
23. Lutz, R., and H. Bujard. 1997. Independent and tight regulation of transcriptional units in *Escherichia coli* via the LacR/O, the TetR/O and AraC/I1-I2 regulatory elements. *Nucleic Acids Res.* 25:1203–1210.
24. Mäkelä, J., M. Kandhavelu, ..., A. S. Ribeiro. 2013. In vivo single-molecule kinetics of activation and subsequent activity of the arabinose promoter. *Nucleic Acids Res.* 41:6544–6552.
25. Golding, I., J. Paulsson, ..., E. C. Cox. 2005. Real-time kinetics of gene activity in individual bacteria. *Cell.* 123:1025–1036.
26. Kapuscinski, J. 1995. DAPI: a DNA-specific fluorescent probe. *Biotech. Histochem.* 70:220–233.
27. Chowdhury, S., M. Kandhavelu, ..., A. S. Ribeiro. 2013. Cell segmentation by multi-resolution analysis and maximum likelihood estimation (MAMLE). *BMC Bioinformatics.* 14 (*Suppl 10*):S8.
28. Portnoy, S., and R. Koenker. 1997. The Gaussian hare and the Laplacian tortoise: computability of squared-error versus absolute-error estimators. *Stat. Sci.* 12:279–300.
29. Ruusuvuori, P., T. Aijö, ..., O. Yli-Harja. 2010. Evaluation of methods for detection of fluorescence labeled subcellular objects in microscope images. *BMC Bioinformatics.* 11:248.

30. Gardiner, C. W., K. J. McNeil, …, I. S. Matheson. 1976. Correlations in Stochastic theories of chemical reactions. *J. Stat. Phys.* 14:307.
31. Gordon, S., J. Rech, …, A. Wright. 2004. Kinetics of plasmid segregation in *Escherichia coli*. *Mol. Microbiol.* 51:461–469.
32. Silverman, B. W. 1986. Density Estimation for Statistics and Data Analysis. Chapman and Hall, London, UK.
33. Chandrasekhar, S. 1943. Stochastic problems in physics and astronomy. *Rev. Mod. Phys.* 15:1–89.
34. Cabrera, J. E., C. Cagliero, …, D. J. Jin. 2009. Active transcription of rRNA operons condenses the nucleoid in *Escherichia coli*: examining the effect of transcription on nucleoid structure in the absence of transertion. *J. Bacteriol.* 191:4180–4185.
35. Jung, S.-C., C. L. Smith, …, Y. S. Jin. 2010. Restoration of growth phenotypes of *Escherichia coli* DH5alpha in minimal media through reversal of a point mutation in *purB*. *Appl. Environ. Microbiol.* 76:6307–6309.
36. Rubner, Y., C. Tomasi, and L. J. Guibas. 2000. The earth mover's distance as a metric for image retrieval. *Int. J. Comput. Vis.* 40:99–121.
37. Dobrushin, R. L. 1970. Prescribing a system of random variables by conditional distributions. *Theory Probab. Appl.* 15:458–486.
38. Lloyd-Price, J., M. Lehtivaara, …, A. S. Ribeiro. 2012. Probabilistic RNA partitioning generates transient increases in the normalized variance of RNA numbers in synchronized populations of *Escherichia coli*. *Mol. Biosyst.* 8:565–571.
39. Muthukrishnan, A.-B., M. Kandhavelu, …, A. S. Ribeiro. 2012. Dynamics of transcription driven by the tetA promoter, one event at a time, in live *Escherichia coli* cells. *Nucleic Acids Res.* 40:8472–8483.
40. Tao, H., C. Bausch, …, T. Conway. 1999. Functional genomics: expression analysis of *Escherichia coli* growing on minimal and rich media. *J. Bacteriol.* 181:6425–6440.
41. Yu, J., J. Xiao, …, X. S. Xie. 2006. Probing gene expression in live cells, one protein molecule at a time. *Science.* 311:1600–1603.

Supporting Material for "*In vivo* kinetics of segregation and polar retention of MS2-GFP-RNA complexes in *Escherichia coli*"

Abhishekh Gupta[†,‡], Jason Lloyd-Price[†,‡], Ramakanth NeeliVenkata[†], Samuel M.D. Oliveira[†],
and Andre S. Ribeiro[†]

† Laboratory of Biosystem Dynamics, Department of Signal Processing, Tampere University of Technology, FI-33101 Tampere, Finland.

‡ Equal contributions

Measurements in M63 Media

We imaged cells grown in M63 media at 37°C for 2 hours, following induction of the target RNA and of the tagging MS2-GFP proteins (one hour before), using the same experimental and analysis protocols as in the experiments in LB described in the main text. The spatial distribution of newly-produced complexes, corresponding to Fig. 2 *A* in the main text for LB, is presented in Fig. S1.

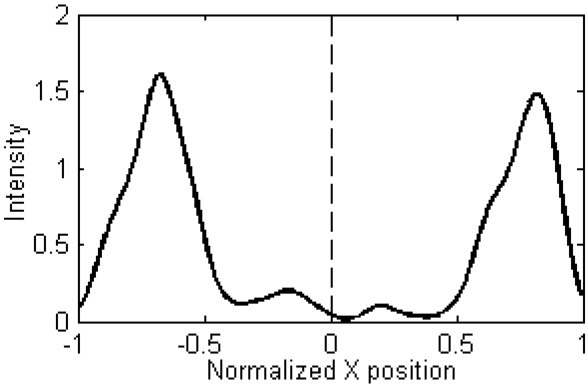

FIGURE S1 KDE of the spatial distribution of the fluorescence intensity (in arbitrary units) of complexes along the major axis of the cells, extracted from all cells and time points (*black line*, bandwidth 0.05). Data is extracted from cells that inherited no complexes but produced one or more. The old pole is at +1 and the new pole is at -1. All cells were born during the measurement period. The dashed vertical line represents the cell center. Measurements are from 63 cells grown in M63 media at 37°C. The fraction of complexes observed in the older half of the cells was 0.45 which is statistically indistinguishable from an unbiased partitioning of complexes (p-value of the binomial test with *N* equal to the number of observed cells is 0.45).

The folded, spatial distribution of all complexes, corresponding to Figs. 2, *B* and *C* in the main text for LB, is presented in Fig. S2. Also shown are the results from the 'region detection' method.

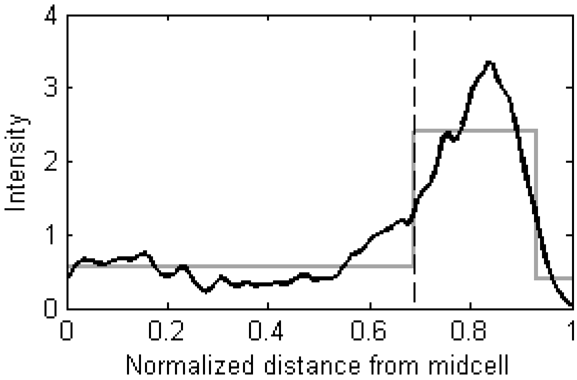

FIGURE S2 KDE of the spatial distribution of the fluorescence intensity (in arbitrary units) of complexes along the major axis of the cells, extracted from all cells and time points (*black line*, bandwidth 0.05). Complex positions were normalized by half the cell length. Also shown is the fit to a piecewise-constant probability density function by maximum likelihood (*gray line*). All cells were born during the measurement period. The vertical dashed lines represent the detected separation points between the midcell and poles. Measurements are from 221 cells grown in M63 media at 37°C, with separation point detected at 0.69.

2D Spatial distribution of complexes

We obtained the KDE of the 2D distributions of complexes from all time points in both temperature conditions. Results are shown in Figs. S3, *A* and *B*, for cells at 37°C and 24°C in LB, respectively.

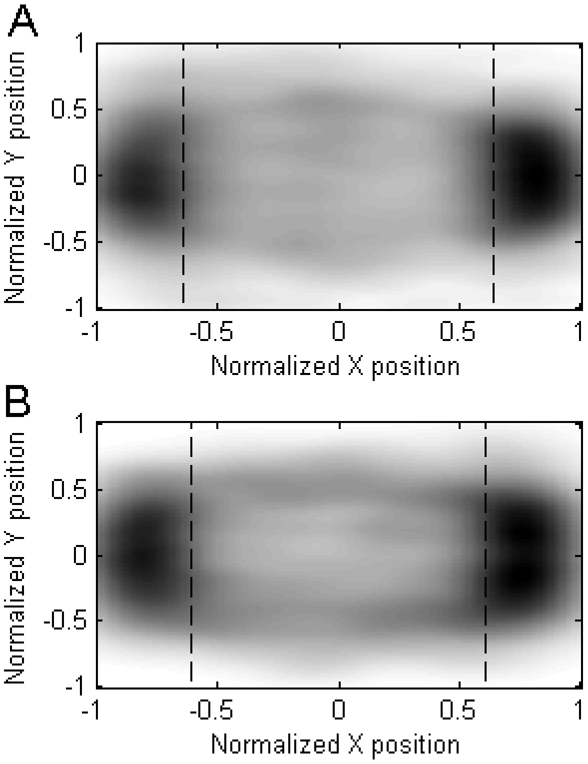

FIGURE S3 KDE of the 2D spatial distributions of complexes from all time points. All cells were born during the measurement period. Measurements are from (*A*) 531 cells at 37°C and (*B*) 372 cells at 24°C, both grown in LB media. Separation points (obtained from Figs. 2, *B* and *C*) are also shown.

Models of long-term spatial distributions of large molecules in the cytoplasm of *E. coli*

A cell is modeled as a 1-dimensional space, which is divided into N homogeneous sub-volumes, indexed from $[1, N]$. The motion of the complexes is modeled along the major cell axis by unimolecular reactions following the Reaction-Diffusion Master Equation (1). Collisions between complexes are not modelled. We define $\vec{a}(x)$ as the propensity of the forward reaction (modeling the motion of a complex from position x to position x+1) and $\overleftarrow{a}(x)$ as the propensity of the reverse reaction (from x to x-1).

These two propensities account for the combined effects of the cell geometry (rod shape and pole caps) and of the nucleoid on the displacements of the complexes. Let $\mathbf{P}(t)$ be the N-by-1 vector describing the probability of observing a complex in each sub-volume at time t. $\mathbf{P}(t)$ therefore evolves according to the following master equation, in matrix-vector form:

$$\frac{d\mathbf{P}(t)}{dt} = \mathbf{AP}(t)$$

where

$$\mathbf{A} = \begin{bmatrix} -\vec{a}(1) & \overleftarrow{a}(2) & 0 & & 0 & 0 \\ \vec{a}(1) & -\overleftarrow{a}(2)-\vec{a}(2) & \overleftarrow{a}(3) & \cdots & 0 & 0 \\ 0 & \vec{a}(2) & -\overleftarrow{a}(3)-\vec{a}(3) & & 0 & 0 \\ & \vdots & & \ddots & & \vdots \\ 0 & 0 & 0 & & -\overleftarrow{a}(N-1)-\vec{a}(N-1) & \overleftarrow{a}(N) \\ 0 & 0 & 0 & \cdots & \vec{a}(N-1) & -\overleftarrow{a}(N) \end{bmatrix}$$

Since a complex can travel from any sub-volume in the cell to any other sub-volume, given enough time, the system is ergodic. Therefore, as $t \to \infty$, $\mathbf{P}(t)$ will converge to a unique solution, $\mathbf{P}_\infty$. This solution can be found by solving the linear system of equations $\mathbf{0} = \mathbf{AP}_\infty$, with the constraint that the total probability must sum to 1. As this is the long-term spatial distribution of the complexes predicted by the model, this was the distribution we fit to the measurements.

In a model not accounting for the caps of the cells, the propensities of the forward and reverse diffusion reactions would be proportional to the diffusion constant of the complexes, *D*:

$$\vec{a}(x) = \overleftarrow{a}(x) = \frac{N^2 D}{2}$$

To account for the rod shape, i.e. a cylinder capped with two half-spheres, the length of the cell was parameterized by $B \in [0,1]$, the normalized distance from midcell at which the cap begins. The forward propensities were attenuated by $\phi(x)$, the ratio between the areas of the cross sections of the cell (denoted $S(x)$) at adjacent positions. As such, $\overleftarrow{a}(x)$ remains the same and $\vec{a}(x)$ becomes:

$$\vec{a}(x) = \frac{N^2 D}{2}\phi(x)$$

where

$$\phi(x) = \frac{S(x+1)}{S(x)}$$

$$S(x) = \begin{cases} \pi, & c(x) < B \\ \pi\left[1 - \left(\dfrac{c(x)-B}{1-B}\right)^2\right], & c(x) \geq B \end{cases}$$

$$c(x) = \frac{x-0.5}{N}$$

Here, $c(x)$ translates the index of a sub-volume into the normalized distance from the midcell to the center of the sub-volume. In this case, $B = 1$ recovers the cylindrical cell from above, and $B = 0$ produces a spherical cell.

The effects of a nucleoid are introduced in the above model by adding a Gaussian function to $\vec{a}(x)$ while subtracting it from $\overleftarrow{a}(x)$. This anisotropy was parameterized with center $\mu \in [0,1]$, standard deviation σ, and height h. Specifically:

$$\vec{a}(x) = \frac{N^2 D}{2}\left[\phi(x) + h \cdot \exp\left\{-\frac{(c(x)-\mu)^2}{2\sigma^2}\right\}\right]$$

$$\overleftarrow{a}(x) = \frac{N^2 D}{2}\left[1 - h \cdot \exp\left\{-\frac{(c(x)-\mu)^2}{2\sigma^2}\right\}\right]$$

To fit the models to the measurements, we use the Earth-Mover's metric (2), otherwise known as the first Wasserstein metric (3), defined as:

$$W(F,G) = \int_{-\infty}^{\infty} |F(x) - G(x)|\,dx$$

where F and G are the cumulative distribution functions of the model and the measurements.

To obtain the fraction of complexes moving towards the pole from sub-volume x, we first initialized the model with all probability in sub-volume x, denoted $\mathbf{P}^x(0)$, and numerically integrated the system over one minute using the Matlab function `ode23s` to obtain the probability distribution at $t = 1$, $\mathbf{P}^x(1)$. This fraction was then calculated as:

$$\frac{1}{2}\mathbf{P}_x^x(1) + \sum_{i=x+1}^{N}\mathbf{P}_i^x(1)$$

Spatial distribution without anisotropy

We constructed a 1-dimensional model with the forward and backwards propensities of diffusion events set to be equal, and inversely proportional to the observed spatial distribution (results in Fig. S4). When both propensities are equal, the probability that a complex will travel in one direction is 0.5, and thus there is no velocity anisotropy. When the propensities are inversely proportional to the observed distribution, in the long term, the complexes tend to linger in the areas where they were observed with high probability. Thus, the long-term spatial distribution is exactly as observed (the lines are indistinguishable in Fig. S4 *B*), while producing a negligible anisotropy in the predicted displacement distribution (Fig. S4 *A*).

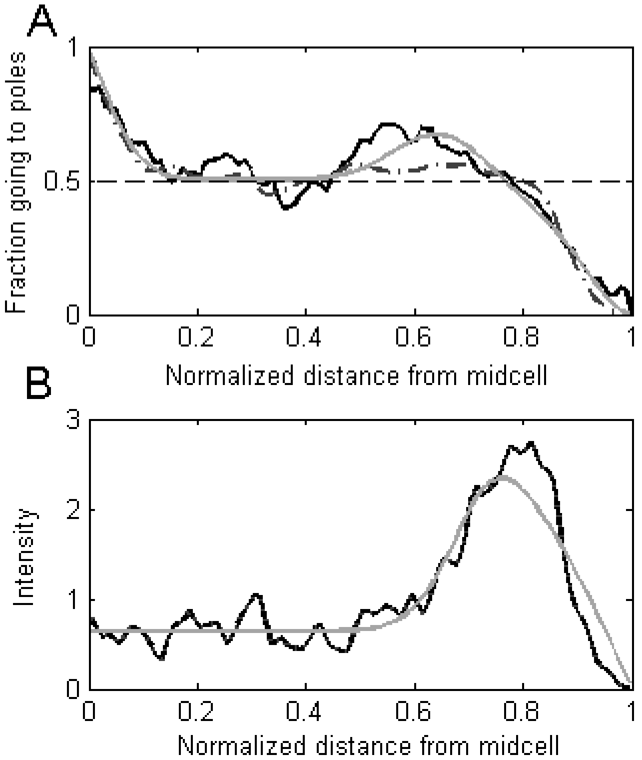

FIGURE S4 (*A*) Predicted fraction of complexes travelling towards the pole from each position along the major axis. (*B*) Long-term spatial distribution of complexes. Results are from a model with a localized anisotropy as in Fig. 8 (*gray lines*), a model with heterogeneous speeds (*dashed lines*), and the measurements at 24°C (*black lines*). Note that the dashed line in (*B*) is superimposed by the black line.

SUPPORTING REFERENCES

1. Gardiner, C.W., K.J. McNeil, D.F. Walls, and I.S. Matheson. 1976. Correlations in Stochastic Theories of Chemical Reactions. *J. Statiscal Phys.* 14: 307.

2. Rubner, Y., C. Tomasi, and L.J. Guibas. 2000. The Earth Mover’s Distance as a Metric for Image Retrieval. *Int. J. Comput. Vis.* 40: 99–121.

3. Dobrushin, R.L. 1970. Prescribing a system of random variables by conditional distributions. *Theory Probab. Its Appl.* 15: 458.

Publication II

R. Neeli-Venkata**,** A. Martikainen*, N. Goncalves*, A. Gupta*, J.M. Fonseca and A.S. Ribeiro, "Robustness of the process of nucleoid exclusion of protein aggregates in *Escherichia coli*", *Journal of Bacteriology*, 198:898-906, 2016.

AMERICAN SOCIETY FOR MICROBIOLOGY Journal of Bacteriology

Robustness of the Process of Nucleoid Exclusion of Protein Aggregates in *Escherichia coli*

Ramakanth Neeli-Venkata,[a] Antti Martikainen,[a] Abhishekh Gupta,[a] Nadia Gonçalves,[a] Jose Fonseca,[b] Andre S. Ribeiro[a]

Laboratory of Biosystem Dynamics, Department of Signal Processing, Tampere University of Technology, Tampere, Finland[a]; UNINOVA, Instituto de Desenvolvimento de Novas Tecnologias, Campus FCT-UNL, Caparica, Portugal[b]

ABSTRACT

Escherichia coli **segregates protein aggregates to the poles by nucleoid exclusion. Combined with cell divisions, this generates heterogeneous aggregate distributions in subsequent cell generations. We studied the robustness of this process with differing medium richness and antibiotics stress, which affect nucleoid size, using multimodal, time-lapse microscopy of live cells expressing both a fluorescently tagged chaperone (IbpA), which identifies *in vivo* the location of aggregates, and HupA-mCherry, a fluorescent variant of a nucleoid-associated protein. We find that the relative sizes of the nucleoid's major and minor axes change widely, in a positively correlated fashion, with medium richness and antibiotic stress. The aggregate's distribution along the major cell axis also changes between conditions and in agreement with the nucleoid exclusion phenomenon. Consequently, the fraction of aggregates at the midcell region prior to cell division differs between conditions, which will affect the degree of asymmetries in the partitioning of aggregates between cells of future generations. Finally, from the location of the peak of anisotropy in the aggregate displacement distribution, the nucleoid relative size, and the spatiotemporal aggregate distribution, we find that the exclusion of detectable aggregates from midcell is most pronounced in cells with mid-sized nucleoids, which are most common under optimal conditions. We conclude that the aggregate management mechanisms of *E. coli* are significantly robust but are not immune to stresses due to the tangible effect that these have on nucleoid size.**

IMPORTANCE

Escherichia coli **segregates protein aggregates to the poles by nucleoid exclusion. From live single-cell microscopy studies of the robustness of this process to various stresses known to affect nucleoid size, we find that nucleoid size and aggregate preferential locations change concordantly between conditions. Also, the degree of influence of the nucleoid on aggregate positioning differs between conditions, causing aggregate numbers at midcell to differ in cell division events, which will affect the degree of asymmetries in the partitioning of aggregates between cells of future generations. Finally, we find that aggregate segregation to the cell poles is most pronounced in cells with mid-sized nucleoids. We conclude that the energy-free process of the midcell exclusion of aggregates partially loses effectiveness under stressful conditions.**

Aging can be defined as a progressive loss of functionality and increased death incidence with time. Even simpler organisms, such as *Escherichia coli*, are not exempted (1). While under optimal conditions most *E. coli* cells in a population appear to perpetuate by dividing into genetically identical, functional cells, there are a few individuals that exhibit reduced or no reproductive capability (1, 2). As in other organisms (3, 4), the reduced vitality of those individuals appears to be linked to the excessive accumulation of nonfunctional proteins (5).

E. coli has evolved a complex machinery to enhance protein functionality. Chaperones, e.g., GroEL and DnaK (6), catalyze the proper folding of stable proteins, preventing aggregation, and assist in the rescue of misfolded ones (7). When these mechanisms fail, the protease machinery can target some misfolded proteins for degradation (8, 9). Likely due to this and perhaps to ensure the existence of raw material for novel proteins, *E. coli* degrades certain fractions of proteins at all times (10, 11). Finally, when protein degradation is impaired, *E. coli* cells are able to aggregate the misfolded proteins, making use of the exposed hydrophobic surfaces of the misfolded proteins that can interact with one another (12, 13). Recent evidence suggests that the aggregation process is not energy free (14); thus, it likely is essential for proper cell functioning. Interestingly, this process exhibits similarities to events in eukaryotic cells, whose malfunctioning has been linked to diseases such as Huntington's, Alzheimer's, and Parkinson's (15).

Active protein aggregation in bacteria is common in stressful environments (2, 5, 14, 16) and likely minimizes the harmful effects of nonfunctional proteins. However, the accumulation of such aggregates also interferes with cellular functioning, thereby compromising cellular fitness (2, 5). Importantly, these aggregates are passively segregated to the poles by an energy-free volume exclusion mechanism, made possible by the presence of the nucleoid at the midcell region (16, 17), similar to the processes of the polar segregation of plasmids (18, 19) and other large complexes

Received 15 October 2015 **Accepted** 22 December 2015

Accepted manuscript posted online 4 January 2016

Citation Neeli-Venkata R, Martikainen A, Gupta A, Gonçalves N, Fonseca J, Ribeiro AS. 2016. Robustness of the process of nucleoid exclusion of protein aggregates in *Escherichia coli*. J Bacteriol 198:898–906. doi:10.1128/JB.00848-15.

Editor: V. J. DiRita, Michigan State University

Address correspondence to Andre S. Ribeiro, andre.ribeiro@tut.fi.

A.M., A.G., and N.G. contributed equally.

Supplemental material for this article may be found at http://dx.doi.org/10.1128/JB.00848-15.

(20, 21). Consequently, division events will generate daughter cells that have at least one (the newer) pole free of aggregates (5). In subsequent generations, aggregates become heterogeneously distributed among the cell population, and those cells with more aggregates exhibit diminished growth rate, while their sister cells remain functional (5). Relevantly, this process is present not only under stressed conditions but also under nonstressed conditions, albeit at a lower rate (5).

A recent study (21) tracked synthetic, stable, fluorescent aggregates across a few cell generations and showed that, under optimal growth conditions, aggregates are excluded from midcell (unbiasedly) to the older and newer cell poles and then are tightly retained there, exhibiting escape times of (at least) the same order of magnitude as the cell division time. As in the case of natural aggregates (5, 16, 17), their retention is caused by nucleoid occlusion. This can be demonstrated by the fact that, rather than exhibiting reduced velocities at the poles, the aggregates exhibit only a strong anisotropy in their displacement distribution that occurs at the nucleoid borders and is similar in intensity to the anisotropy at the cell extremities but opposite in direction (21). Further, as the nucleoid replicates and the two sister nucleoids move to the focal points of the cell, the peaks of anisotropy "follow" the nucleoids' repositioning, and new aggregates now also accumulate between the two sister nucleoids (21). Finally, another recent work (17) showed that the kinetics of aggregates is always purely diffusive, in agreement with the absence of active transport mechanisms.

The nucleoid is usually at midcell, has an ellipsoidal shape, and is confined within the cell cylinder (22). Among other things, it contains DNA, RNA, and nucleoid-associated proteins (NAPs), which are involved in its structural organization. Major NAPs include H-NS, HU, Fis, IHF, and StpA. The dimeric histone-like protein HU, highly abundant and involved in DNA compaction (23), can be used to assess the nucleoid's morphology and positioning *in vivo* when fused with mCherry (22).

The morphology of the nucleoid is sensitive to medium composition and antibiotic stresses (24–27). One such stress-inducing antibiotic is chloramphenicol, which halts translation elongation by blocking access of charged tRNA to the ribosomal A site (28), leading to nucleoid compaction (25). Meanwhile, another antibiotic, rifampin, blocks transcription initiation by binding to RNA polymerases (29), leading to nucleoid expansion (27). Meanwhile, medium richness affects the nucleoid size by affecting the cell growth rate (30, 31). For example, in minimal M63 glycerol medium, nucleoids are relatively larger than in lysogeny broth (LB) medium (32). Nucleoids also are relatively larger in terrific broth (TB) medium (considered to be a rich medium), perhaps due to the absence of important, unidentified nutrients that are present in LB medium (33).

Even though such stress-induced changes in nucleoid morphology do not suffice to affect the degree of exclusion of aggregates from inside the nucleoid, they likely alter the efficiency with which aggregates are excluded from midcell and retained at the poles, including during cell division. Importantly, if a large number of cells of a population contain more than 1 aggregate (e.g., when cells are subject to heat shock [16], various natural antibiotics such as streptomycin [5], conditions leading to enhanced gene expression rates [34], etc.), the locations of the aggregates the moment prior to division will affect the distribution of aggregate numbers in cells of future generations (35, 36). Consequently, in enhanced aggregate production conditions, changes in nucleoid morphology could affect the generation of asymmetries in numbers of aggregates in cells of future generations (1, 5, 27, 37).

Here, we use single-cell, time-lapse, multimodal fluorescence microscopy to investigate how medium richness and antibiotic stresses affect the nucleoid size and positioning and, in doing so, affect the long-term spatial distribution of protein aggregates in *E. coli*. For this, we also investigate whether the aggregate dynamics, within the range of visibility, differs with aggregate size. Measurements were conducted using the *E. coli* MGAY strain expressing IbpA-yellow fluorescent protein (YFP) (5) and harboring the plasmid expressing the nucleoid-tagging protein HupA-mCherry (22), whose expression is controlled by a constitutive promoter. We selected IbpA-YFP, since it has been shown to be an accurate identifier of the *in vivo* localization of aggregated proteins (5). Meanwhile, HupA-mCherry was selected for the reasons mentioned above.

MATERIALS AND METHODS

Chemicals. Components of lysogeny broth (LB), terrific broth (TB), and M63 minimal medium for *E. coli* cultures, 4′, 6-diamidino-2-phenylindole (DAPI), formaldehyde, and the agarose for the microscopic slide gel preparations were purchased from Sigma-Aldrich. Amino acids and vitamins were purchased from Gibco.

Bacterial strains and plasmids. The *Escherichia coli* MG1655 (MGAY) strain carrying the *ibpA-yfp* sequence in the chromosome under the control of the endogenous chromosomal *ibpA* promoter was used for all measurements (a kind gift from Ariel Lindner, Paris Descartes University, France). This strain was modified by us so as to also harbor a plasmid expressing HupA-mCherry (a nucleoid-tagging protein) under the control of a constitutive promoter with ampicillin resistance (a kind gift from Nancy Kleckner, Harvard University). This original form of the plasmid was modified by removing TetR-mVenus and the promoter controlling its expression, since it would interfere with our measurements of IbpA-YFP. We refer to this strain as MGAY-HupA-mCherry.

Growth conditions. We used a rich medium (TB), an optimal medium (LB), and a poor medium (M63 with glycerol as the carbon source), in accordance with the definitions of medium richness in references 30 to 32. The composition of the LB medium was 10 g liter^{-1} tryptone, 5 g liter^{-1} yeast extract, and 5 g liter^{-1} NaCl. The composition of the TB medium was 12 g liter^{-1} tryptone, 24 g liter^{-1} yeast extract, 0.4% glycerol, and TB salts (KH_2PO_4 and K_2HPO_4). The M63 medium was prepared using M63 salts supplemented with 0.4% glycerol and 20% Casamino Acids. MGAY and MGAY-HupA-mCherry cells were grown overnight from single colonies at 37°C with vigorous shaking (250 rpm) in the respective medium. For the latter, we supplemented the medium with 50 μg ml^{-1} ampicillin.

Growth rate measurements. Growth rates were measured at 37°C in the appropriate medium (without antibiotics) using a spectrophotometer (Ultrospec 10; GE Health Care). The cultures were grown overnight with continuous shaking. Overnight cultures next were diluted into fresh medium to an optical density at 600 nm (OD_{600}) of 0.05, and we recorded the OD_{600} values every 30 min up to 4 h to obtain growth curves for each medium condition in the presence and absence of streptomycin. Results are shown in Fig. S1 in the supplemental material. In all cases, streptomycin negatively affects the growth rates (very mildly in TB medium). Note that the live cell imaging is made during the first hour after adding streptomycin (see below), during which the growth rates are still positive under all conditions.

Cell growth and induction of protein aggregates. Overnight cultures were diluted (1:200) into fresh medium supplemented with antibiotics and incubated at 37°C, with shaking until reaching an OD_{600} of 0.3. At this stage, to induce the protein aggregates, cells were incubated with streptomycin (10 μg ml^{-1}) 30 min before placing them on the slide. The cells then were centrifuged and supernatant was discarded. From these, 4 μl of cells was placed on a 1% agarose gel pad prepared in the respective medium for image acquisition.

Nucleoid perturbation by antibiotics. In some cases, we used chloramphenicol and rifampin to alter the relative size of nucleoids in the cells. Chloramphenicol inhibits translation, which leads to nucleoid condensation (25, 27). Rifampin inhibits transcription, which results in nucleoid expansion (26, 27). Chloramphenicol (100 μg ml^{-1}) and rifampin (100 μg ml^{-1} dissolved in dimethyl sulfoxide [DMSO]) were added after aggregate induction. We observed that at these concentrations, both antibiotics reduce the cell growth significantly but do not halt it completely.

Nucleoid visualization by HupA-mCherry tagging and by DAPI staining. HupA-mCherry (22) is constitutively expressed from a plasmid (MGAY-HupA-mCherry strain); thus, no activation procedure is required.

DAPI stains nucleoids specifically with little or no cytoplasmic labeling by binding to A-T-rich regions of the DNA (38). Following the induction of the production of IbpA-tagged aggregates, cells were fixed with 3.7% formaldehyde in phosphate-buffered saline (PBS) for 30 min and then washed with PBS to remove excess formaldehyde. The pellets were suspended in PBS, and DAPI (2 μg $\cdot$ ml^{-1}) was added to this suspension. After being incubated for 20 min in the dark, cells were centrifuged and washed twice with PBS to remove excess DAPI. Cells then were resuspended in PBS, and 8-μl aliquots of these samples were placed on 1% agarose gel pads prepared in appropriate media for microscopy observation. DAPI measurements were performed on the original MGAY strain.

It has been reported that DAPI causes nucleoid expansion (39). However, this is not expected to affect our conclusions, as we only use these data to compare nucleoid sizes between conditions in order to validate (at a qualitative level) the comparative analysis performed by HupA-mCherry tagging.

Microscopy. We used multimodal time-lapse microscopy for the visualization of cells and fluorescence within both IbpA-YFP aggregates and DAPI-stained or HupA-mCherry-tagged nucleoids.

We conducted measurements of IbpA aggregates and DAPI-stained nucleoids (MGAY strain) at a single time point. Similar measurements of IbpA aggregates and HupA-mCherry-tagged nucleoids (MGAY-HupA-mCherry strain) at a single moment in time also were performed. For cells with DAPI-stained nucleoids, images were taken 1 h after aggregate induction. For cells with HupA-mCherry-tagged nucleoids, images were taken 30 min after aggregate induction.

We also performed time-lapse measurements of IbpA aggregates and HupA-mCherry-tagged nucleoids in individual cells (MGAY-HupA-mCherry strain). For this, streptomycin-induced cells were placed on a microscope slide between a coverslip and appropriate media on an agarose gel pad containing streptomycin (10 μg ml^{-1}). When antibiotics were applied, the agarose gel pad also was supplied with appropriate antibiotics along with streptomycin. During image acquisition, the slide was kept in a temperature-controlled chamber (FCS2; Bioptechs) at 37°C. Image acquisition began once the slide reached the appropriate temperature (which takes 3 to 5 min).

Images of cells were captured every 1 min for 1 h. Phase-contrast images were captured every 5 min for cell segmentation. The software for image acquisition was NIS Elements (Nikon). Cells were visualized using a Nikon Eclipse (Ti-E) inverted microscope with a 100× (1.49-numeric-aperture) objective. Phase-contrast images were acquired using a charge-coupled display camera (DS-Fi2; Nikon). Confocal microscopy was used to detect IbpA-YFP aggregates (488-nm laser; Melles-Griot HQ514/30; Nikon) and HupA-mCherry-tagged nucleoids (543-nm HeNe laser; Melles-Griot HQ585/65; Nikon). Epifluorescence microscopy with a mercury lamp was used to detect DAPI-stained nucleoids (DAPI filter block; Nikon).

Image analysis. Analysis of the time-lapse microscopy images was performed as described in reference 21, using a semiautomated method (40) augmented with an automatic presegmentation step of cell borders in the phase-contrast images using the software MAMLE (41). We performed manual correction of these results when needed, using the software CellAging (40), to obtain precise masks of the region each cell occupies at each time point and precise detection of division events. The masks next were manually aligned to the corresponding confocal images based on the information from the red channel (see Fig. S2 in the supplemental material). For additional details along with information on how the data extraction from the images was performed, please see the supplemental material.

Tests of statistical significance. Distributions of results from sets of individual cells were compared by tests of statistical significance, such as the Kolmogorov-Smirnov test. All conclusions of differences between conditions are based on these tests.

RESULTS

Functionality of the process of polar retention of protein aggregates under different conditions. To study the spatiotemporal distribution of protein aggregates, we performed multimodal, time-lapse microscopy of live MGAY-HupA-mCherry cells expressing a YFP-tagged chaperone (IbpA), which identifies *in vivo* the location of protein aggregates, and HupA-mCherry, a fluorescent variant of a nucleoid-associated protein, to detect the location and dimensions of the nucleoid(s) (see Fig. S7 to S9 in the supplemental material). We also observed cell borders by phase-contrast microscopy. In all cases, cells first were grown overnight in the appropriate medium (LB, M63, or TB). The next day, their precultures were grown in the appropriate media and then were incubated with streptomycin (10 μg ml^{-1}) for 30 min to induce aggregate production. If appropriate, they then were subjected to chloramphenicol or rifampin for 30 additional minutes. Finally, cells were placed under the microscope and imaged once while being kept under the appropriate conditions (Materials and Methods). Overall, we imaged cells under 9 conditions (see Table S1 in the supplemental material), differing in medium (M63, LB, or TB) and/or antibiotic stress (chloramphenicol, rifampin, or no antibiotic), for the reasons described in the Introduction. The condition LB with no antibiotics is considered the control.

From the images, after selecting cells with 1 nucleoid only (see Materials and Methods), we extracted from each cell, at each time point, the center position and the size of the nucleoid as well as the position of each aggregate along the major and minor cell axes, regardless of its location in the cell (see Table S1 in the supplemental material). We next folded the two halves of a cell on top of each other and then normalized the size, with 0 being the cell center and +1 the pole extremities. From there, we obtained distributions of the relative nucleoid size along the major axis and of the relative positioning of aggregates (see Fig. S3 and S4). These are in agreement with the absolute measures of size and positioning of nucleoids and aggregates, respectively, shown in Table S1 in the supplemental material.

In Tables S2 and S3 in the supplemental material, we show the results of Kolmogorov-Smirnov (KS) tests of comparison between pairs of conditions of the distribution of relative nucleoid sizes along the major cell axis and of the distribution of aggregate location along the major cell axis, respectively. In these, as well as in subsequent tests, we consider that for P values smaller than 0.05, the null hypothesis that the two sets of data are from the same distribution can be rejected. In this case, we only compared conditions that differ in one variable from the control. From the P values shown in Table S2, we conclude that the relative nucleoid size differs significantly between all pairs of conditions differing in medium richness or in antibiotic stress.

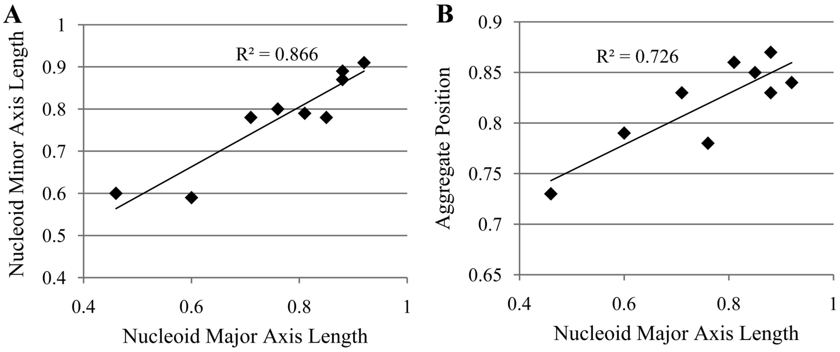

FIG 1 (A) Scatter plot between the relative major axis length and minor axis length of nucleoids under different conditions. (B) Scatter plot between the relative major axis length of nucleoid and the relative position of aggregates along the cell major axis under different conditions. In both panels, the values of the coefficient of determination (R^2) of the fit also are shown.

As shown in Fig. 1A, we find that the changes in nucleoid relative size along the minor and major axes with changing conditions are heavily positively correlated (Pearson correlation of 0.9 with a *P* value smaller than 10^{-3} in a *t* test with the null hypothesis that the data are uncorrelated), indicating that the increase in size in one direction is not made at the cost of size reduction in the other direction (i.e., changes in nucleoid size appear to be due to similar radial and axial changes). Regarding the measurements of relative nucleoid size along the major cell axis, qualitatively similar results (see Table S4 in the supplemental material) were attained when assessing the nucleoid size by DAPI staining (usually, the nucleoid appeared to be approximately 10% to 15% larger when measured by HupA-mCherry tagging than when measured by DAPI staining). Furthermore, the mean relative nucleoid size of cells grown in LB medium without streptomycin was found to be similar to the control condition with streptomycin (LB, no antibiotic), which implies that streptomycin, on its own, does not affect the relative nucleoid size significantly (see Table S4).

Meanwhile, from Fig. S3 and Table S3 in the supplemental material, we conclude that the distribution of aggregates along the major cell axis also differs significantly between any pair of conditions differing in medium richness or antibiotic stress. Further, one invariably observes that under the conditions where the mean relative nucleoid size is larger, the aggregates preferentially locate closer to the pole, in agreement with the existence of (at least partial) volume exclusion under all conditions. This is confirmed by the results depicted in Fig. 1B, showing the correlation between aggregate positioning (i.e., distance from cell center) and nucleoid size.

Finally, it is noted that changing both medium richness and antibiotic stress causes combined effects on nucleoids that are at least as strong as the strongest individual change and that the mean positioning of the aggregates changes accordingly, in agreement with the existence of nucleoid occlusion and consequent midcell exclusion.

Robustness of the process of retention of protein aggregates under different conditions. To assess if the changes in nucleoid size affect the efficiency with which aggregates are excluded from midcell, we obtained for each condition the correlation between the positions of aggregates and nucleoids in individual cells during their lifetimes. Results are shown in Table 1. Also shown is the *P* value of statistical significance of the correlation from a *t* test with the null hypothesis that the data are uncorrelated.

From Table 1, the positioning of aggregates and nucleoid centers along the major cell axis is negatively correlated under most conditions (except in cells in LB medium with chloramphenicol, which, on average, have the smallest relative nucleoid of all). Also, in general, the correlation strength increases with nucleoid size. This negative correlation (statistically significant under all conditions) is a result of the fact that in most cells where the nucleoid is off-centered, i.e., biasedly positioned toward one side, the aggregates preferentially locate on the opposite side (as expected from volume exclusion).

Meanwhile, under the conditions where the relative nucleoid size is smallest, the correlation becomes positive (while remaining statistically significant). This suggests that asymmetric positioning by such nucleoids, due to their reduced size, no longer causes tangible asymmetries in the positioning of aggregates by the two poles. The statistically significant positive correlation likely is also a result of volume exclusion caused by the nucleoid at midcell. While the nucleoid is not large enough in these cells to define to which side the aggregates preferentially locate, it is still able, when it moves along the major cell axis, to cause aggregates to move accordingly in a positively correlated fashion. Interestingly, such positive correlations between nucleoid and aggregate motions are easily detected in cells under all conditions, provided that we fold the major cell axis so as to remove the influence of asymmetries in nucleoid positioning (see Table S5 in the supplemental material).

TABLE 1 Correlation between relative positions along the major cell axis of the nucleoid center and of individual aggregates[a]

Condition	Correlation	*P* value
M63, Chlor	−0.2	$<10^{-5}$
M63, no AB	−0.2	$<10^{-5}$
M63, Rif	−0.2	$<10^{-5}$
LB, Chlor	+0.1	$<10^{-5}$
LB, no AB	−0.1	0.02
LB, Rif	−0.2	$<10^{-5}$
TB, Chlor	−0.3	$<10^{-5}$
TB, no AB	−0.4	$<10^{-5}$
TB, Rif	−0.3	$<10^{-5}$

[a] For each condition, the correlation between the relative positions in individual cells of the nucleoid center and of the aggregates along the major cell axis is shown. Also shown are the *P* values of statistical significance of the correlation from a *t* test with the null hypothesis that the data are uncorrelated. Chlor, chloramphenicol; Rif, rifampin; no AB, no antibiotic.

TABLE 2 Fraction of aggregates located between the centers of the nucleoids in cells with two nucleoids the moment prior to division[a]

Condition	No. of aggregates	Fraction of aggregates between nucleoids (10^{-1})	Expected fraction if uniformly distributed	Distance between nucleoid centers along major axis	*P* value
LB, Chlor	5,027	2.8	0.5	1.0 ± 0.1	$<10^{-3}$
LB, no AB	3,492	3.2	0.5	1.0 ± 0.1	
LB, Rif	604	2.7	0.5	1.0 ± 0.1	$<10^{-2}$
TB, no AB	1,434	2.7	0.5	1.1 ± 0.1	$<10^{-3}$
M63, no AB	1,527	3.6	0.5	1.1 ± 0.1	$<10^{-2}$

[a] Shown are the total number of aggregates, the mean fraction of aggregates between the centers of the two nucleoids in each cell, the expected fraction if the aggregates were distributed uniformly along the major cell axis, and the distances (means and standard deviations) along the major cell axis between the nucleoid centers (normalized by half the cell length). Also shown are the *P* values for the fractions of aggregates between nucleoids in cells in LB medium and no antibiotic and cells under other conditions from the same binomial distribution. Cell size along the major axis is normalized to equal 2. Finally, we performed statistical tests of comparison to determine whether the distributions of aggregate numbers found between the centers of the nucleoids differ between conditions. Results are shown in Table S6 in the supplemental material.

Effects in the process of partitioning of aggregates in cell division. From previous works (1, 5, 21, 42) it is expected that, in cells with more than one aggregate, the preference for polar localization of the aggregates will generate asymmetries in aggregate numbers between sister cells of future generations. Meanwhile, the presence of aggregates between nucleoids during cell division will result in decreased asymmetries in aggregate numbers between sister cells (35, 36).

Thus, we assessed whether, in the moment prior to cell division, the numbers of aggregates located between the two nucleoid centers differ significantly between conditions. For that, we obtained the fraction of aggregates located between nucleoid centers in cells the moment before division was detected and assessed if, between conditions, the differences in the fraction of aggregates between nucleoid centers are significant by performing a binomial test with the null hypothesis that the two sets of data are generated from an equal distribution. Further, we calculated the fraction of aggregates that would be expected to be in the region between nucleoids if the aggregates distributed uniformly along the major cell axis, accounting for the relative size of this region. Results are shown in Table 2.

From Table 2 and from Table S6 in the supplemental material, regarding the fraction of aggregates between nucleoids in cells the moment prior to cell division, all conditions differ significantly from the control (LB with no antibiotics), although not always between them. In TB medium this fraction is smaller, while the relative nucleoid size along the major cell axis is larger (in agreement with the results reported in reference 33). Meanwhile, in M63 medium this fraction is larger, while the relative nucleoid size also is larger. Further, the presence of chloramphenicol or rifampin also decreases this fraction, but while chloramphenicol decreases the relative nucleoid size, rifampin increases it.

Given these results, we conclude that both increasing and decreasing the relative size of the nucleoid (compared to that of the control) leads to an increase in the fraction of aggregates in the region between nucleoids the moment prior to cell division. Nevertheless, it is worth noting that under no condition is the retention of aggregates at the poles absent, given that the fraction of aggregates found between nucleoids is always much smaller than that expected by chance. While the observation that smaller nucleoids lead to a decrease in the ability to segregate to and then retain aggregates at the poles might have been expected, it can be argued that the weaker retention of aggregates at the poles in cells with the largest nucleoids was less expected. In the next section, we investigate this further by grouping individual cells according to their relative nucleoid size rather than the experimental conditions and studying the dynamics of individual aggregates in each group of cells.

Dynamics of the aggregates as a function of nucleoid size. From the results described above, it is apparent that there is a wide cell-to-cell variability in some of the properties studied, even between cells under the same conditions. Thus, in order to study how the changes in nucleoid size affect the dynamics of aggregates, we gathered data from all conditions and partitioned the cells into quartiles based on their relative nucleoid sizes (Fig. 2). Table 3 shows the fraction of cells from each condition that belongs to each quartile. Not surprisingly, cells under different conditions contribute differently, in numbers, to the various quartiles. Nevertheless, under all conditions there are at least a few cells in each of the quartiles.

We next compared the spatial distributions and dynamics of

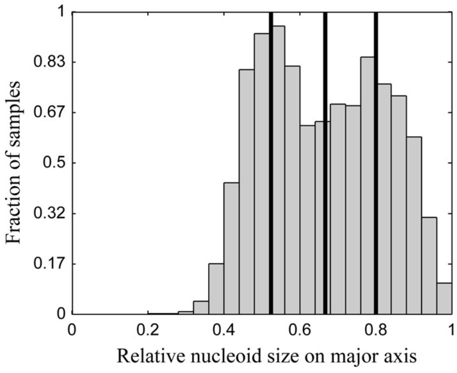

FIG 2 Distribution of relative nucleoid sizes. The distribution of relative nucleoid sizes obtained from cells under all conditions described in Table 1 are shown. The black lines separate the quartiles of relative nucleoid size.

TABLE 3 Fraction of cells in each quartile of nucleoid size[a]

	Fraction of cells in indicated quartile			
Condition	1st	2nd	3rd	4th
LB, Chlor	0.6	0.4	0.0	2.7×10^{-4}
LB, no AB	0.1	0.3	0.3	0.2
LB, Rif	3×10^{-3}	0.1	0.3	0.6
TB, no AB	0.0	0.1	0.3	0.5
M63, no AB	5×10^{-3}	0.1	0.2	0.7

[a] Fraction of cells from each condition whose relative nucleoid size belongs to each of the quartiles in the distribution shown in Fig. 2.

TABLE 4 Aggregate positioning and dynamics along the major cell axis in cells having different quartiles of nucleoid size[a]

Quartile	No. of aggregates	Fraction of aggregates in poles	Relative nucleoid size along: Major axis	Relative nucleoid size along: Minor axis	Peak location along major axis of anisotropy curve (10^{-1})
1st	2,404	0.9	0.5 ± 0.0	0.6 ± 0.1	(~0.03)
2nd	2,681	0.9	0.6 ± 0.0	0.7 ± 0.1	7.1
3rd	2,104	0.7	0.7 ± 0.0	0.8 ± 0.1	7.4
4th	2,147	0.4	0.9 ± 0.0	0.9 ± 0.1	7.7

[a] The table shows the number of aggregates analyzed in cells of each quartile, the fraction of aggregates at the poles, the relative nucleoid size (means and standard deviations) along the major and minor axes, and the location of the positive maximum peak of anisotropy along the major cell axis. The total number of cells observed was 2,138.

aggregates of cells in different quartiles of nucleoid size. First, we investigated whether the location of the nucleoid borders along the major cell axis is related to the position along the same axis of the local maxima of positive anisotropy in the motion of the aggregates, which is responsible for their accumulation at the poles (21). Anisotropy curves extracted from the motion of aggregates in cells of each quartile are shown in Fig. S5 in the supplemental material. From these, we extracted the location on the major cell axis where the maximum peak of positive anisotropy occurs (Table 4). Also in Table 4 are the number of aggregates analyzed per quartile, fraction of aggregates at the poles, and means and standard deviations of the relative nucleoid sizes along the major and minor axes.

First, as shown in Table 4, the fraction of aggregates in the poles differs between quartiles. This was expected given, among other things, the definition of pole and the differences in relative pole size. More importantly, the location of the peak of positive anisotropy (see Fig. S5 in the supplemental material) follows the same trend as that of the relative position of the nucleoid borders. Namely, as the latter become relatively closer to the cell extremities, so do the positive peaks of anisotropy.

Nevertheless, it is worth noting that while for cells of the 2nd quartile the peak of anisotropy is closer to the cell extremity than the nucleoid border, for cells of the 3rd quartile the peak of anisotropy and the nucleoid border match in position, and for cells of the 4th quartile the peak of anisotropy is closer to the cell center than to the nucleoid border. We hypothesize that this reflects the increasing space constraints, which in cells of the 4th quartile may force aggregates to move more often into the midcell region while not necessarily entering the nucleoid *per se*.

Also, interestingly, we were unable to find a clear anisotropy peak in cells of the 1st quartile. We hypothesize that the relatively smaller nucleoid of these cells causes the retention of aggregates at the poles by nucleoid exclusion to be weaker. Further, the fraction of events between consecutive microscopy frames that correspond to encounters between an aggregate and the nucleoid become rarer (due to reduced relative nucleoid size). This is in agreement with the above-described observation that, under conditions where cells have relatively smaller nucleoids, the aggregates more likely locate between nucleoids prior to division.

We next studied the extent to which the retention of aggregates at the poles differs between cells of different quartiles. In Fig. 3, we show the distribution of locations of aggregates along the major cell axis (from all time points) in cells of each quartile (top row). Also shown (bottom row) is their location along the major and minor cell axes along with the mean position of the nucleoid border (vertical line).

Finally, in Table S7 in the supplemental material, we present the results of KS tests of comparison between the distributions of aggregate positioning along the major cell axis from cells of different quartiles. The results show that all pairs of distributions differ in a statistical sense.

Figure 3 (bottom) suggests that in cells with the smallest nucleoids (1st quartile), there is little interaction between aggregates and nucleoids, as aggregates rarely locate close to the nucleoid borders or at midcell. Meanwhile, in the cells with the largest

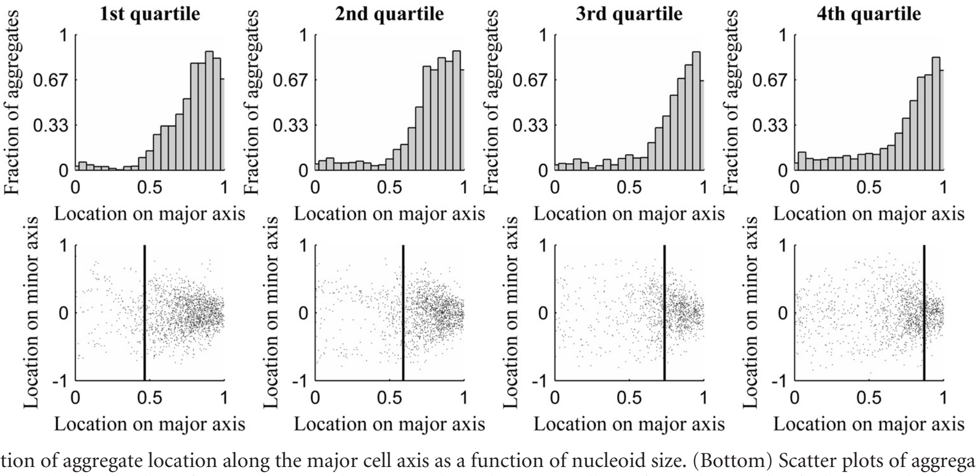

FIG 3 (Top) Distribution of aggregate location along the major cell axis as a function of nucleoid size. (Bottom) Scatter plots of aggregate locations along the major and minor cell axes. (Top) Number of aggregates in each position along the major cell axis for each quartile of relative nucleoid size. (Bottom) Positions occupied by aggregates along the major and minor axes, along with the mean relative position of the nucleoid border for each quartile of relative nucleoid size.

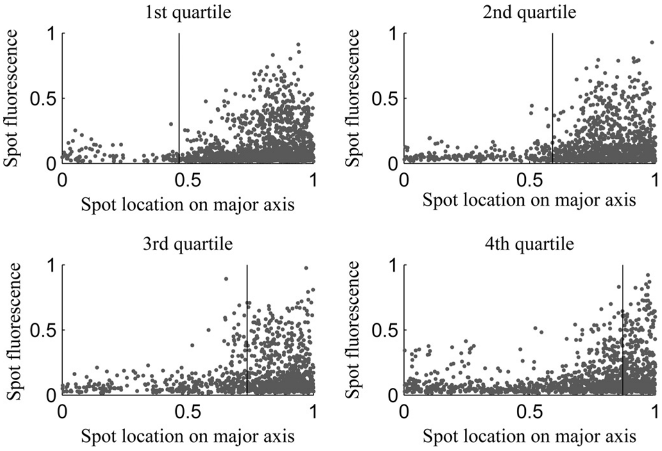

FIG 4 Individual aggregate intensity versus location along the major cell axes for cells of each quartile. Shown are all positions occupied by aggregates during a cell's lifetime along with the mean relative position of the nucleoid border in cells of each of the quartiles along the major axis (vertical line).

nucleoids (4th quartile), the aggregates often are found at midcell. This is in agreement with the observation in the previous section of a decrease in retention of aggregates outside the midcell region in cells with larger nucleoids. It is also in agreement with the relationship between the positioning along the major cell axis of the nucleoid size and the peak of positive anisotropy as a function of nucleoid size. Given this, we conclude that the segregation and retention of (visually detectable) aggregates at the poles is most pronounced in cells with mid-sized nucleoids.

Degree of nucleoid exclusion as a function of aggregate size. The conclusions described above were obtained from the analysis of the behavior of detectable aggregates as a function of nucleoid size. However, the degree of aggregate exclusion from midcell also may differ significantly as a function of aggregate size within the range of visibility. Thus, we investigated the location of aggregates along the major cell axis as a function of their size (as measured by their fluorescence intensity) for cells from each quartile of nucleoid size (Fig. 4).

From Fig. 4, we extracted for each set of cells the 10% and 25% smallest aggregates (as measured by their fluorescence intensity) and their location along the major cell axis. We obtained the fraction of these that is excluded from midcell. Results are shown in Table 5. Also shown is the fraction of aggregates that would be expected to be excluded from midcell if the aggregates distributed uniformly along the major cell axis and accounting for the relative size of the midcell region.

From Table 5, the spatial distributions of aggregates along the major cell axis do not differ significantly with aggregate size for any of the quartiles of relative nucleoid size. As such, we conclude that, for the range of aggregate sizes that we can detect, there is no significant difference in their degree of exclusion from midcell.

DISCUSSION

Based on previous studies that identified nucleoid exclusion as the mechanism responsible for the segregation and subsequent retention of protein aggregates at the cell poles in *E. coli* (21), and given the knowledge that the relative size of nucleoids is sensitive to environmental conditions, we observed cells where both the nucleoid and protein aggregates are made visible by fluorescent tagging to study how robust, under different medium and stress conditions, is the process of the accumulation of aggregates at the poles due to nucleoid occlusion.

We found it to be highly robust under changing conditions, although it was not entirely immune. In particular, while the distribution of aggregates differed widely between conditions, in agreement with the wide changes in relative nucleoid size, under no conditions, even when combining changes in medium richness with antibiotic stresses (which caused, in several cases, combined effects on the relative nucleoid size), was the retention of aggregates at the poles completely hampered (although partial loss of retention strength was observed).

The exclusion of aggregates from the space between the replicated nucleoids in cells close to division is what causes the aggregates to be asymmetrically distributed in the daughter cells (i.e., most will be at the old pole) (5). We observed that for distinct reasons, both increasing as well as decreasing the relative nucleoid size reduced the degree of exclusion of aggregates from midcell, which is likely to affect the degree of asymmetries in the partitioning of aggregates between cells of future generations and, thus, the aging process of lineages under stress conditions, where cells tend to contain more than one aggregate. Reduced nucleoid size obviously hampers the retention of aggregates at the poles both prior to and after nucleoid partitioning. Meanwhile, increased nucleoid size, perhaps due to increasing the space constraints at the poles, seems to cause aggregates to locate in the relatively enlarged midcell region more often, again both prior to and after nucleoid partitioning. Future studies may reveal whether the aggregates enter the midcell region by penetrating an enlarged and perhaps less dense nucleoid or by moving into the regions between the inner cell walls and the nucleoid borders. The use of synthetic aggregates of known, regulated sizes (21) may help answer this question.

It is worth mentioning a previous work which showed that, in *E. coli* cells under suboptimal conditions, the morphological asymmetries in cell division are larger (37) because the mean distance between the nucleoids of cells close to division is wider. Such higher asymmetry was shown to have negative functional conse-

TABLE 5 Aggregate positioning along the major cell axis in cells of different quartiles of nucleoid size[a]

Quartile	Relative nucleoid size along major axis	Fraction of aggregates at poles	Fraction of 25% smallest aggregates at poles	Fraction of 10% smallest aggregates at poles	Expected fraction at poles if uniformly distributed
1st	0.5	0.9	0.9	0.9	0.5
2nd	0.6	0.9	0.9	0.9	0.4
3rd	0.7	0.7	0.7	0.7	0.3
4th	0.9	0.4	0.4	0.4	0.1

[a] Shown are the relative nucleoid size along the major cell axis, the mean fraction of aggregates excluded from midcell (i.e., at the poles), the mean fraction of the 25% and of the 10% smallest aggregates excluded from midcell, and the expected fraction if the aggregates were distributed uniformly along the major cell axis.

quences, namely, slower mean division times (37). It is interesting to hypothesize that the preferential absence of aggregates from the midcell region also contributes to the symmetry in division by maintaining the space between the nucleoids, where the division septum is to form, free from obstructing objects. Future research should be able to address this issue.

Also of interest, we expect that the fraction of time that a cell has two nucleoids will affect the fraction of aggregates that are at midcell the moment division occurs. This fraction of time is highly dependent on environmental conditions, and one could argue that it at least partially explains the observed differences in the fraction of aggregates at midcell prior to division between the conditions. However, given the lack of evidence that the rate of aggregate formation changes during the cell cycle, and since this preferential appearance at midcell in the presence of two nucleoids is possible only if there is a nucleoid exclusion mechanism (or else the aggregates would distribute homogenously), it is reasonable to assume that the nucleoid size is, at least partially, also affecting the fraction of aggregates at midcell prior to division. This assumption is further supported by the existence of the clear positive peaks in the anisotropy curves (precisely at the borders of the nucleoids) that show that aggregates move significantly between frames and are excluded from midcell precisely where the nucleoid borders are located. Given this, we argue that the differences between the fractions of aggregates at midcell prior to cell division between the conditions tested are created by both the differences in the ability of the nucleoids (of different relative sizes) to retain the aggregates at midcell and poles and the differences in the mean fraction of time that cells have two nucleoids under the various conditions.

Finally, we also investigated the degree to which the effects of nucleoid exclusion are aggregate size dependent. For the range of aggregate sizes detectable from the images, we were unable to find tangible differences between the spatial distributions of small- and normal-sized aggregates regardless of the nucleoid size. Nevertheless, we expect that below a certain aggregate size (beyond our detection range), nucleoid exclusion will lose much of its effectiveness, particularly given recent evidence that while ribosomes are excluded from the nucleoid, ribosomal subunits are not (43). In this regard, recent studies provided evidence that the aggregation of nonfunctional proteins is an active process (14). Besides benefits such as reducing the possibility of harmful interactions between nonfunctional proteins and other cellular components, active aggregation should guarantee efficient, energy-free nucleoid occlusion by contributing aggregates to reach sufficient sizes so as to be excluded from the midcell region.

In conclusion, our results suggest that within the set of conditions studied, while being a robust process under changing conditions, the exclusion from midcell of aggregates (large enough to be detected by the methods employed here) is, on average, more efficient in cells with mid-sized nucleoids, which are the most common ones under optimal growth conditions. This optimality of mid-sized nucleoids undoubtedly is aggregate size dependent, but it should be tangibly perturbed only if there are major failures in the active aggregation process.

ACKNOWLEDGMENTS

The work was supported by the Academy of Finland (257603; A.S.R.), the Portuguese Foundation for Science and Technology (PTDC/BBB-MET/1084/2012; J.M.F. and A.S.R.), and the Finnish Cultural Foundation (A.G.).

The funders had no role in study design, data collection and analysis, decision to publish, or preparation of the manuscript.

FUNDING INFORMATION

Portuguese Foundation for Science and Technology provided funding to Jose Fonseca under grant number PTDC/BBB-MET/1084/2012. Academy of Finland | Biotieteiden ja Ympäristön Tutkimuksen Toimikunta (Forskningsrådet för Biovetenskap och Miljö) provided funding to Andre S. Ribeiro under grant number 257603.

REFERENCES

1. **Stewart EJ, Madden R, Paul G, Taddei F.** 2005. Aging and death in an organism that reproduces by morphologically symmetric division. PLoS Biol **3:**e45. http://dx.doi.org/10.1371/journal.pbio.0030045.
2. **Maisonneuve E, Ezraty B, Dukan S.** 2008. Protein aggregates: an aging factor involved in cell death. J Bacteriol **190:**6070–6075. http://dx.doi.org/10.1128/JB.00736-08.
3. **Nyström T, Liu B.** 2014. The mystery of aging and rejuvenation—a budding topic. Curr Opin Microbiol **18:**61–67. http://dx.doi.org/10.1016/j.mib.2014.02.003.
4. **Soti C, Csermely P.** 2003. Aging and molecular chaperones. Exp Gerontol **38:**1037–1040. http://dx.doi.org/10.1016/S0531-5565(03)00185-2.
5. **Lindner AB, Madden R, Demarez A, Stewart EJ, Taddei F.** 2008. Asymmetric segregation of protein aggregates is associated with cellular aging and rejuvenation. Proc Natl Acad Sci U S A **105:**3076–3081. http://dx.doi.org/10.1073/pnas.0708931105.
6. **Deuerling E, Schulze-Specking A, Tomoyasu T, Mogk A, Bukau B.** 1999. Trigger factor and DnaK cooperate in folding of newly synthesized proteins. Nature **400:**693–696. http://dx.doi.org/10.1038/23301.
7. **Wickner S, Maurizi M, Gottesman S.** 1999. Posttranslational quality control: folding, refolding, and degrading proteins. Science **286:**1888–1893. http://dx.doi.org/10.1126/science.286.5446.1888.
8. **Mandelstam J.** 1960. The intracellular turnover of protein and nucleic acids and its role in biochemical differentiation. Bacteriol Rev **24:**289–308.
9. **Goldberg AL.** 2003. Protein degradation and protection against misfolded or damaged proteins. Nature **426:**895–899. http://dx.doi.org/10.1038/nature02263.
10. **Goldberg AL.** 1972. Degradation of abnormal proteins in Escherichia coli. Proc Natl Acad Sci U S A **69:**422–426. http://dx.doi.org/10.1073/pnas.69.2.422.
11. **Willetts N.** 1967. Intracellular protein breakdown in non-growing cells of Escherichia coli. Biochem J 453–461.
12. **Tyedmers J, Mogk A, Bukau B.** 2010. Cellular strategies for controlling protein aggregation. Nat Rev Mol Cell Biol **11:**777–788. http://dx.doi.org/10.1038/nrm2993.
13. **Sabate R, de Groot NS, Ventura S.** 2010. Protein folding and aggregation in bacteria. Cell Mol Life Sci **67:**2695–2715. http://dx.doi.org/10.1007/s00018-010-0344-4.
14. **Govers SK, Dutré P, Aertsen A.** 2014. In vivo disassembly and reassembly of protein aggregates in Escherichia coli. J Bacteriol **196:**2325–2332. http://dx.doi.org/10.1128/JB.01549-14.
15. **Dobson CM.** 2001. The structural basis of protein folding and its links with human disease. Philos Trans R Soc Lond B Biol Sci **356:**133–145. http://dx.doi.org/10.1098/rstb.2000.0758.
16. **Winkler J, Seybert A, König L, Pruggnaller S, Haselmann U, Sourjik V, Weiss M, Frangakis AS, Mogk A, Bukau B.** 2010. Quantitative and spatio-temporal features of protein aggregation in Escherichia coli and consequences on protein quality control and cellular ageing. EMBO J **29:**910–923. http://dx.doi.org/10.1038/emboj.2009.412.
17. **Coquel A-S, Jacob J-P, Primet M, Demarez A, Dimiccoli M, Julou T, Moisan L, Lindner AB, Berry H.** 2013. Localization of protein aggregation in Escherichia coli is governed by diffusion and nucleoid macromolecular crowding effect. PLoS Comput Biol **9:**e1003038. http://dx.doi.org/10.1371/journal.pcbi.1003038.
18. **Reyes-Lamothe R, Tran T, Meas D, Lee L, Li AM, Sherratt DJ, Tolmasky ME.** 2014. High-copy bacterial plasmids diffuse in the nucleoid-free space, replicate stochastically and are randomly partitioned at cell division. Nucleic Acids Res **42:**1042–1051. http://dx.doi.org/10.1093/nar/gkt918.

19. **Vecchiarelli AG, Mizuuchi K, Funnell BE.** 2012. Surfing biological surfaces: exploiting the nucleoid for partition and transport in bacteria. Mol Microbiol **86:**513–523. http://dx.doi.org/10.1111/mmi.12017.
20. **Straight PD, Fischbach MA, Walsh CT, Rudner DZ, Kolter R.** 2007. A singular enzymatic megacomplex from Bacillus subtilis. Proc Natl Acad Sci U S A **104:**305–310. http://dx.doi.org/10.1073/pnas.0609073103.
21. **Gupta A, Lloyd-Price J, Neeli-Venkata R, Oliveira SMD, Ribeiro AS.** 2014. In vivo kinetics of segregation and polar retention of MS2-GFP-RNA complexes in Escherichia coli. Biophys J **106:**1928–1937. http://dx.doi.org/10.1016/j.bpj.2014.03.035.
22. **Fisher JK, Bourniquel A, Witz G, Weiner B, Prentiss M, Kleckner N.** 2013. Four-dimensional imaging of E. coli nucleoid organization and dynamics in living cells. Cell **153:**882–895. http://dx.doi.org/10.1016/j.cell.2013.04.006.
23. **Dillon SC, Dorman CJ.** 2010. Bacterial nucleoid-associated proteins, nucleoid structure and gene expression. Nat Rev Microbiol **8:**185–195. http://dx.doi.org/10.1038/nrmicro2261.
24. **Cabrera JE, Cagliero C, Quan S, Squires CL, Jin DJ.** 2009. Active transcription of rRNA operons condenses the nucleoid in Escherichia coli: examining the effect of transcription on nucleoid structure in the absence of transertion. J Bacteriol **191:**4180–4185. http://dx.doi.org/10.1128/JB.01707-08.
25. **Van Helvoort JM, Kool J, Woldringh CL.** 1996. Chloramphenicol causes fusion of separated nucleoids in Escherichia coli K-12 cells and filaments. J Bacteriol **178:**4289–4293.
26. **Chai Q, Singh B, Peisker K, Metzendorf N, Ge X, Dasgupta S, Sanyal S.** 2014. Organization of ribosomes and nucleoids in Escherichia coli cells during growth and in quiescence. J Biol Chem **289:**11342–11352. http://dx.doi.org/10.1074/jbc.M114.557348.
27. **Sun Q, Margolin W.** 2004. Effects of perturbing nucleoid structure on nucleoid occlusion-mediated toporegulation of FtsZ ring assembly. J Bacteriol **186:**3951–3959. http://dx.doi.org/10.1128/JB.186.12.3951-3959.2004.
28. **Weber MJ, DeMoss JA.** 1966. The inhibition by chloramphenicol of nascent protein formation. Proc Natl Acad Sci U S A **407:**1224–1230.
29. **McClure WR, Cech CL.** 1978. On the mechanism of rifampicin inhibition of RNA synthesis. J Biol Chem **253:**8949–8956.
30. **Tao H, Bausch C, Richmond C.** 1999. Functional genomics: expression analysis of Escherichia coli growing on minimal and rich media. J Bacteriol **181:**6425–6440.
31. **Cabrera JE, Jin DJ.** 2003. The distribution of RNA polymerase in Escherichia coli is dynamic and sensitive to environmental cues. Mol Microbiol **50:**1493–1505. http://dx.doi.org/10.1046/j.1365-2958.2003.03805.x.
32. **Hadizadeh Yazdi N, Guet CC, Johnson RC, Marko JF.** 2012. Variation of the folding and dynamics of the Escherichia coli chromosome with growth conditions. Mol Microbiol **86:**1318–1333. http://dx.doi.org/10.1111/mmi.12071.
33. **Jin DJ, Cagliero C, Zhou YN.** 2013. Role of RNA polymerase and transcription in the organization of the bacterial nucleoid. Chem Rev **113:**8662–8682. http://dx.doi.org/10.1021/cr4001429.
34. **Carrio MM, Corchero JL, Villaverde A.** 1998. Dynamics of in vivo protein aggregation: building inclusion bodies in recombinant bacteria. FEMS Microbiol Lett **169:**9–15.
35. **Huh D, Paulsson J.** 2011. Random partitioning of molecules at cell division. Proc Natl Acad Sci U S A **108:**15004–15009. http://dx.doi.org/10.1073/pnas.1013171108.
36. **Gupta A, Lloyd-Price J, Ribeiro AS.** 2015. In silico analysis of division times of Escherichia coli populations as a function of the partitioning scheme of non-functional proteins. In Silico Biol **12:**9–21. http://dx.doi.org/10.3233/ISB-140462.
37. **Gupta A, Lloyd-Price J, Oliveira SMD, Yli-Harja O, Muthukrishnan AB, Ribeiro AS.** 2014. Robustness of the division symmetry in Escherichia coli and functional consequences of symmetry breaking. Phys Biol **11:**066005. http://dx.doi.org/10.1088/1478-3975/11/6/066005.
38. **Chazotte B.** 2011. Labeling nuclear DNA using DAPI. Cold Spring Harb Protoc **1:**80–82.
39. **Bakshi S, Choi H, Rangarajan N, Barns KJ, Bratton BP, Weisshaar JC.** 2014. Nonperturbative imaging of nucleoid morphology in live bacterial cells during an antimicrobial peptide attack. Appl Environ Microbiol **80:**4977–4986. http://dx.doi.org/10.1128/AEM.00989-14.
40. **Hakkinen A, Muthukrishnan AB, Mora A, Fonseca JM, Ribeiro AS.** 2013. CellAging: a tool to study segregation and partitioning in division in cell lineages of Escherichia coli. Bioinformatics **29:**1708–1709. http://dx.doi.org/10.1093/bioinformatics/btt194.
41. **Chowdhury S, Kandhavelu M, Yli-Harja O, Ribeiro AS.** 2013. Cell segmentation by multi-resolution analysis and maximum likelihood estimation (MAMLE). BMC Bioinformatics **14**(Suppl 1)**:**S8.
42. **Lloyd-Price J, Häkkinen A.** 2012. Asymmetric disposal of individual protein aggregates in Escherichia coli, one aggregate at a time. J Bacteriol **194:**1747–1752. http://dx.doi.org/10.1128/JB.06500-11.
43. **Sanamrad A, Persson F, Lundius EG, Fange D, Gynnå AH, Elf J.** 2014. Single-particle tracking reveals that free ribosomal subunits are not excluded from the Escherichia coli nucleoid. Proc Natl Acad Sci U S A **111:**11413–11418. http://dx.doi.org/10.1073/pnas.1411558111.

Supplement for “Robustness of the process of nucleoid exclusion of protein aggregates in *Escherichia coli*” by R. Neeli-Venkata et al.

1. Supplementary Figures

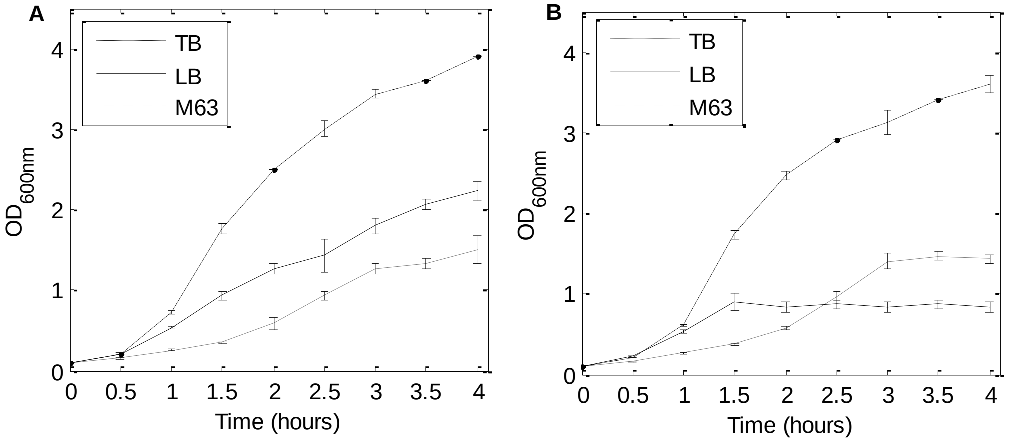

Supplementary Figure S1: Growth curves in different media. (A) Cells were grown at 37 °C, 250 rpm. No streptomycin was added. The growth was followed for 4 hours with the OD being measured every 30 minutes. The mean values and standard deviation bars are from three independent experiments. (B) Cells were grown at 37 °C, 250 rpm. Streptomycin (10µg ml^{-1}) was added in the early logarithmic phase and cell growth was followed for 4 hours with the OD being measured every 30 minutes. Mean values and standard deviation bars are from three independent experiments.

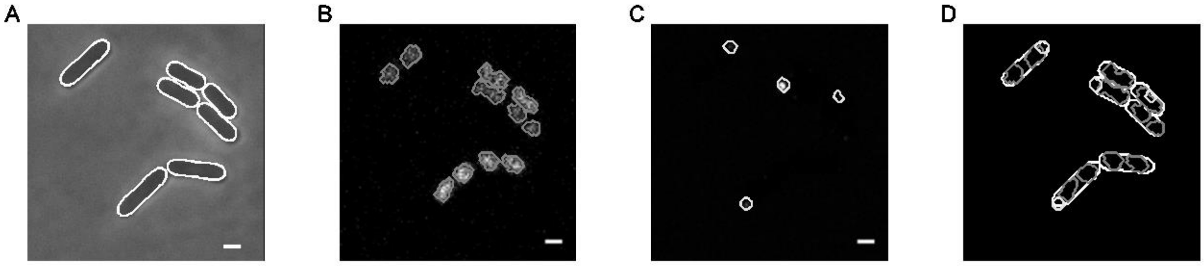

Supplementary Figure S2: Images of *E. coli* cells, protein aggregates and nucleoids. (A) Example image of cells visualized by Phase-Contrast microscopy along with the cell contours (white lines) automatically detected by the software MAMLE (41) and manually corrected using the software ‘CellAging’(40). (B) Confocal image of HupA-mCherry tagged nucleoids of the same cells as in (A). Results from the segmentation of the nucleoids (grey lines) using a low pass filter are also shown. (C) Confocal images of IbpA-YFP aggregates of the cells in (A). Segmentation results for the aggregates (white lines) are also shown. (D) Image resulting from the alignment of the three images (A-C) and the merging of their segmentation results. Scale bars are 1 µm. In the confocal images, the contrast was enhanced for easier visualization and, in (B) the effects of crosstalk between the green and red channels were removed by subtraction.

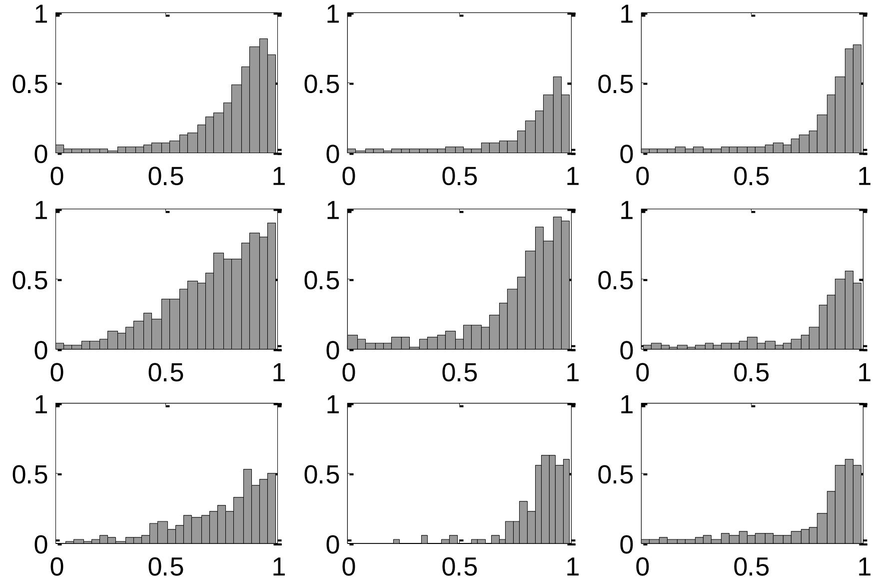

Supplementary Figure S3: Histograms of the relative positions of aggregates along the major cell axis in different conditions: Distributions of relative position of aggregates along the major cell axis for cells grown in M63 media (top row), LB media (middle row), and TB media (bottom row). Cells are also subjected to chloramphenicol (left column), no antibiotics (middle column) and rifampicin (right column).

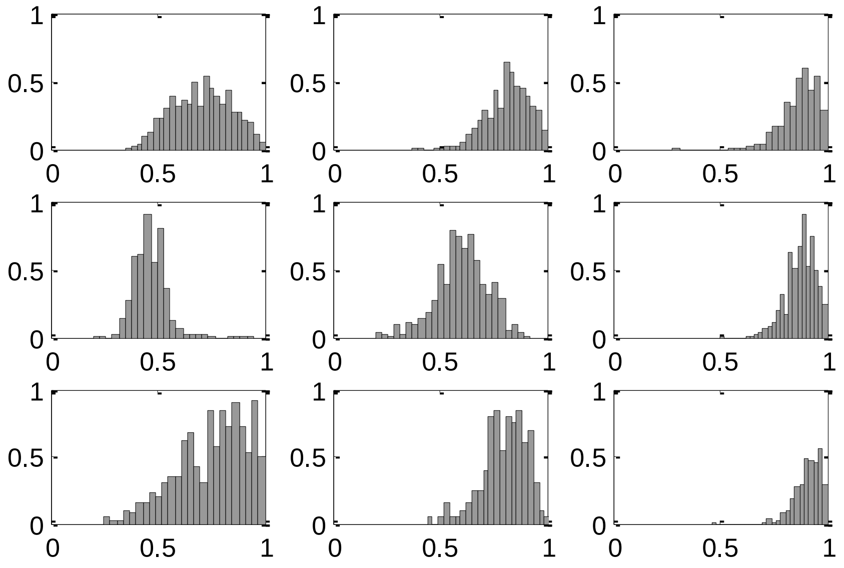

Supplementary Figure S4: Histograms of the relative nucleoid lengths along the major cell axis in different conditions: Distributions of the relative nucleoid length along the major cell axis for cells grown in M63 media (top row), LB media (middle row), and TB media (bottom row). Cells are also subjected to chloramphenicol (left column), no antibiotics (middle column) and rifampicin (right column).

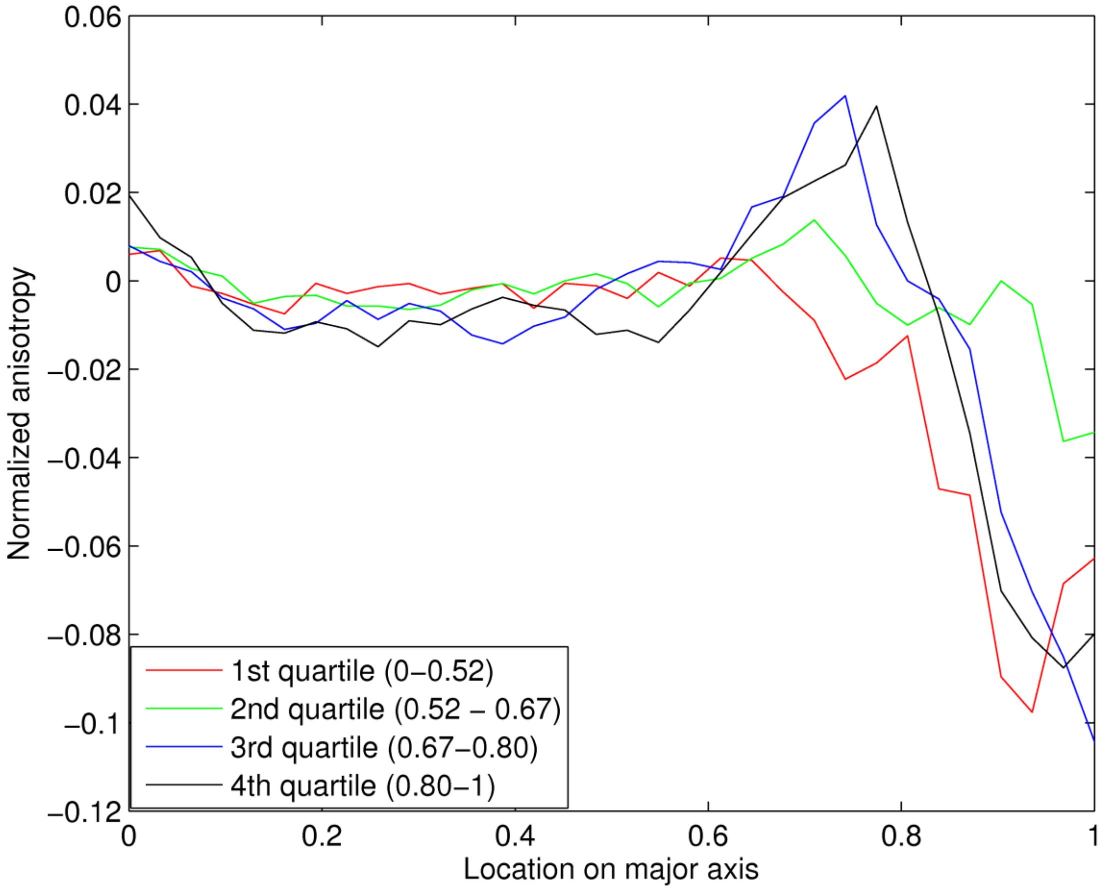

Supplementary Figure S5: Anisotropy curves of aggregates in cells in different quartiles of nucleoid size. Difference between the numbers of displacement vectors that are directed toward the poles and toward the midcell along the major cell axis. The differences were calculated from the displacement vectors originating within a window extending 0.05 normalized cell lengths around that point. The analysis was performed solely during periods of time when only one nucleoid and only one aggregate were detected in the cell to allow precise determination of the motion vectors. The number of cells contributing to this data was 2138.

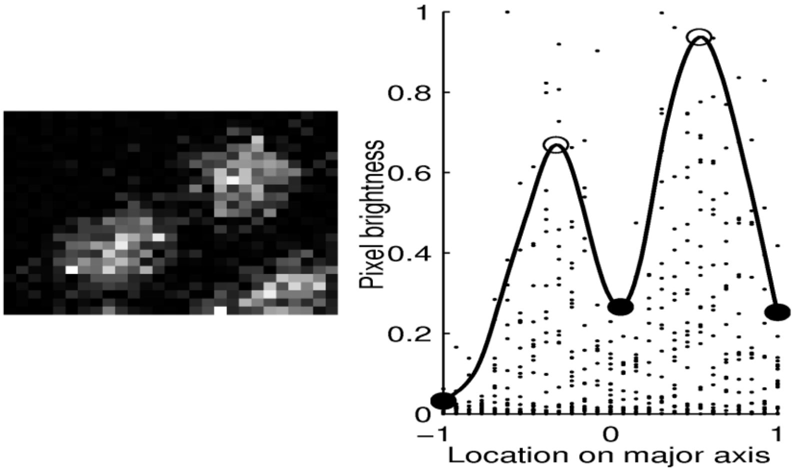

Supplementary Figure S6: Illustration of cell feature extraction for cell classification. The left image shows the two nucleoids of a single cell (the nucleoid of another cell also appears in the bottom right corner). The right image shows a scatter plot of the normalized pixel intensity values along the major axis of the cell with two nucleoids. The curve indicates the Gaussian KDE for the intensity using smoothing factor equal to 0.1. Open circles indicate local maxima while filled circles indicate local minima of the KDE, which are used for the classification. Location of zero indicates the cell center and locations 1 and -1 indicate the cell extremities along the major axis (the signs were selected arbitrarily).

2. Supplementary Tables

Supplementary Table S1: Absolute positioning of aggregates along the major cell axis and absolute nucleoid size. For each condition, described in the first column, it is shown the mean and standard deviation of the location of the aggregates along the major cell axis. Also shown are the mean and standard deviation of the major and minor axes of the nucleoid. “Chlor.” stands for chloramphenicol, “Rif.” stands for rifampicin, and “no AB” stands for “no antibiotic”. In all conditions, standard errors of the mean were < 0.3.

Condition	No. cells	Absolute aggregate positioning along major cell axis (pixels)	Absolute nucleoid size along major cell axis (pixels)	Absolute nucleoid size along minor cell axis (pixels)	Absolute major cell axis length (pixels)
M63, Chlor.	3898	17.9±6.3	15.9±5.7	9.5±3.8	22.3±5.7
M63, no AB	1879	19.3±6.4	19.5±5.5	10.4±4.8	23.7±5.3
M63, Rif.	2299	18.4±6.7	19.7±5.6	10.7±4.3	22.4±5.5
LB, Chlor.	1180	17.8±6.3	11.5±3.1	8.6±1.9	24.9±5.3
LB, no AB	743	15.9±6.4	12.5±4.4	7.6±3.0	20.7±5.8
LB, Rif.	617	22.9±8.2	24.9±6.3	12.4±4.4	28.3±6.8
TB, Chlor.	520	18.8±6.7	18.8±6.0	11.7±4.0	24.8±5.7
TB, no AB	460	24.2±6.4	22.7±5.8	14.5±3.0	28.7±6.2
TB, Rif.	820	25.1±9.5	28.8±6.8	15.6±5.5	31.6±7.1

Supplementary Table S2: Statistical KS tests of comparison of the distribution of relative nucleoid sizes along the major cell axis between pairs of conditions. Comparison of distributions of relative nucleoid sizes along the major cell axis between pairs of conditions that differ in one variable from the control (in presence or absence of antibiotic, or in media richness). For p-values smaller than 0.05, the null hypothesis that the two sets of data are from the same distribution can be rejected. “Chlor.” stands for chloramphenicol, “Rif.” stands for rifampicin, and “no AB” stands for “no antibiotic”.

	LB, no AB	LB, Rif.	TB, no AB	M63, no AB
LB, Chlor.	$< 10^{-5}$	0	$< 10^{-5}$	0

LB, no AB	-	$< 10^{-5}$	$< 10^{-5}$	$< 10^{-5}$
LB, Rif.	-	-	$< 10^{-5}$	$< 10^{-5}$
TB, no AB	-	-	-	$< 10^{-5}$
M63, no AB	-	-	-	-

Supplementary Table S3: Statistical KS tests of comparison of the distribution of aggregates location along the major cell axis between pairs of conditions. Comparison of distributions of aggregate locations along the major cell axis between pairs of conditions that differ in one variable from the control (presence or absence of antibiotic, or media richness). For p-values smaller than 0.05, the null hypothesis that the two sets of data are from the same distribution can be rejected. “Chlor.” stands for chloramphenicol, “Rif.” stands for rifampicin, and “no AB” stands for “no antibiotic”.

	LB, no AB	**LB, Rif.**	**TB, no AB**	**M63, no AB**
LB, Chlor.	$< 10^{-5}$	$< 10^{-5}$	$< 10^{-5}$	$< 10^{-5}$
LB, no AB	-	$< 10^{-5}$	$< 10^{-5}$	$< 10^{-5}$
LB, Rif.	-	-	$< 10^{-5}$	$< 10^{-4}$
TB, no AB	-	-	-	$< 10^{-5}$
M63, no AB	-	-	-	-

Supplementary Table S4: Relative nucleoid size along the major cell axis as measured by DAPI staining. The size of the major cell axis was normalized to equal 1. “Chlor.” stands for chloramphenicol, “Rif.” stands for rifampicin, “no Strep” stands for “no streptomycin”, and “no AB” stands for “no antibiotic”.

Condition	**Relative nucleoid size along major cell axis ($\times 10^{-1}$)**
M63, no AB	7.2
LB, no AB	6.9
TB, no AB	7.5
LB, Chlor.	5.6
LB, Rif.	7.7
LB, no AB no Strep.	6.6

Supplementary Table S5: Correlation between the relative nucleoid center location and the relative aggregate location at the functional pole region. Also shown is the p-value of statistical significance of the correlation from a t-test with the null hypothesis that the data are uncorrelated. “Chlor.” stands for chloramphenicol, “Rif.” stands for rifampicin, and “no AB” stands for “no antibiotic”.

Condition	Pearson correlation	p-value
M63, Chlor.	0.3	$< 10^{-4}$
M63, no AB	0.3	$< 10^{-4}$
M63, Rif.	0.2	$< 10^{-4}$
LB, Chlor.	0.6	$< 10^{-4}$
LB, no AB	0.4	$< 10^{-4}$
LB, Rif.	0.3	$< 10^{-4}$
TB, Chlor.	0.3	$< 10^{-4}$
TB, no AB	0.4	$< 10^{-4}$
TB, Rif.	0.2	$< 10^{-4}$

Supplementary Table S6: Statistical KS tests of comparison between pairs of conditions of the numbers of aggregates found in between the centers of the nucleoids of cells the moment prior to cell division. Comparison of the distributions of numbers of aggregates located in between the two nucleoids center in different conditions. For p-values smaller than 0.05 the null hypothesis that the two sets of data are from the same distribution can be rejected. “Chlor.” stands for chloramphenicol, “Rif.” stands for rifampicin, and “no AB” stands for “no antibiotic”.

	LB, Chlor.	**LB, no AB**	**LB, Rif.**	**TB, no AB**	**M63, no AB**
LB, Chlor.	-	$< 10^{-4}$	0.6	0.8	$< 10^{-4}$
LB, no AB	-	-	$< 10^{-2}$	$< 10^{-3}$	$< 10^{-2}$
LB, Rif.	-	-	-	0.7	$< 10^{-4}$
TB, no AB	-	-	-	-	$< 10^{-4}$
M63, no AB	-	-	-	-	-

Supplementary Table S7: Statistical KS tests of comparison between the distribution of aggregates positioning along the major cell axis from cells of different quartiles. Comparison of the distribution of numbers of aggregates' location along the major cell axis of cells placed in different quartiles. For p-values smaller than 0.05 the null hypothesis that the two sets of data are from the same distribution can be rejected.

	1st Q	**2nd Q**	**3rd Q**	**4th Q**
1st Q	-	$< 10^{-4}$	$< 10^{-4}$	$< 10^{-4}$
2nd Q	-	-	$< 10^{-2}$	$< 10^{-4}$
3rd Q	-	-	-	$< 10^{-4}$
4th Q	-	-	-	-

3. Image Analysis

Prior to the analysis of the data, in order to reduce crosstalk from the green to the red channel, the intensity values of the confocal green channel (used to detect aggregates) were subtracted from the red channel (used to detect nucleoids), as the emission spectrum of IbpA-YFP overlaps slightly with the pass band of the microscope filter for the red channel. We observed by inspection that, due to the much smaller size of the aggregates relative to the nucleoids, this step does not affect significantly the measurements of nucleoids from the resulting images.

We then performed data extraction from the images. First, the size of the cells was measured by determining the orientation of the cell inside the mask, using principal component analysis, and then measuring the dimensions for the smallest bounding box for the mask with the same orientation as the cell.

Next, nucleoids and IbpA aggregates were detected inside the cells by defining them as connected components with each pixel having fluorescence intensity above a certain threshold. For this, it was assumed that the background pixel intensities follow a Gaussian distribution with the same median and upper quartile as the pixels inside the cell. A threshold was selected such that the probability of mislabeling a pixel from this distribution was less than 0.005 for aggregates and less than 0.01 for nucleoids. For nucleoids, a low pass filter was used to obtain a smoothly connected nucleoid area. The number of nucleoids in each cell was determined by classifying the segmented images (see Supplementary Material section ‘Nucleoid Classifier’). The dimensions of nucleoids were measured identically as the dimensions of cells.

The analysis of images of cells with DAPI-stained nucleoids was performed similarly. Background from the epifluorescence images was removed by subtracting a cubic polynomial surface, fitted to the image by L1-norm minimization as in (21). The size for the nucleoid was measured by taking the KDE smoothed fluorescence intensity along the major cell axis and fitting by maximum likelihood a piecewise constant function, so as to determine the approximate mean location of the boundary between the nucleoid and the poles.

We note that both methods of nucleoid segmentation are invariant to fluorescence intensity, and thus avoid possible biases due to (small) differences in signal intensity between conditions.

Finally, we analyzed the intracellular dynamics of aggregates. Such analysis was performed solely during the period of time when only one nucleoid and only one aggregate were detected in the cell. For these, displacement vectors along the major cell axis were calculated for the aggregates between each consecutive frame as in (21).

4. Nucleoid Classifier

Prior to this, during the image analysis, the few cells containing more than two nucleoids were excluded from further analysis.

In the remaining cells, the classification of whether a cell contains one or two nucleoids was performed using the local maximum and minimum values of the KDE (Supplementary Figure S7). A mean of the local minima that fall within an experimentally determined midcell region (±0.3) and a mean of all local maxima were calculated. The cell was then classified to have 2 nucleoids if the ratio of the mean of the minima per that of the maxima was lower than an experimentally determined threshold value of 0.7.

The performance of the classifier was evaluated with a set of 6898 manually classified samples, 65.2% of the sample cells having a single nucleoid, which is a good representative of the mean of measured populations. When compared with using only the result from nucleoid detection, the total classification accuracy improved from 91.7% to 94.3% using this classifier. More importantly, the percentage of double nucleoid cells falsely labeled as having a single nucleoid decreased from 23.2% to 9.6%. However, the percentage of single nucleoid samples being falsely labeled as double nucleoid samples increased from 0.02% to 3.7%.

5. Example images from the microscope

In the example images below (S8-S10), nucleoids are visible in red (tagged with HupA-mCherry), while protein aggregates are visible in green. Cell borders were detected from Phase Contrast images (not shown). The example images result from merging the simultaneously obtained images from the red and green channels.

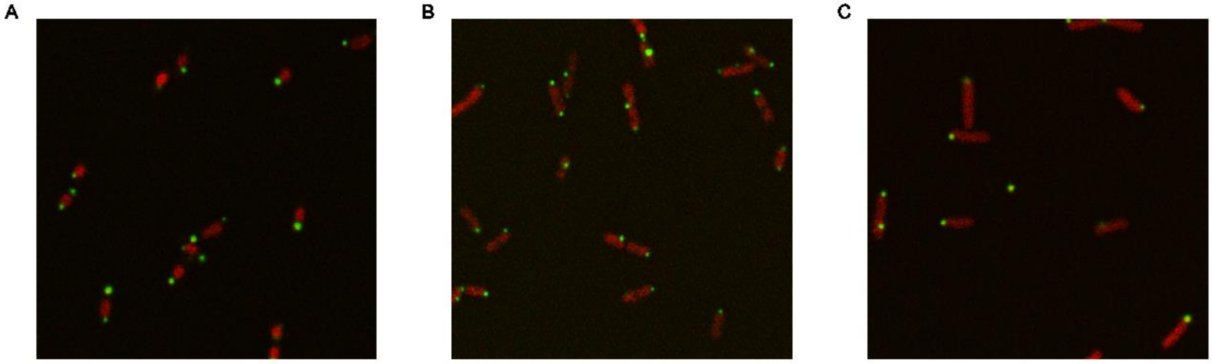

Figure S7: LB media: A – chloramphenicol, B – No antibiotic, C - rifampicin

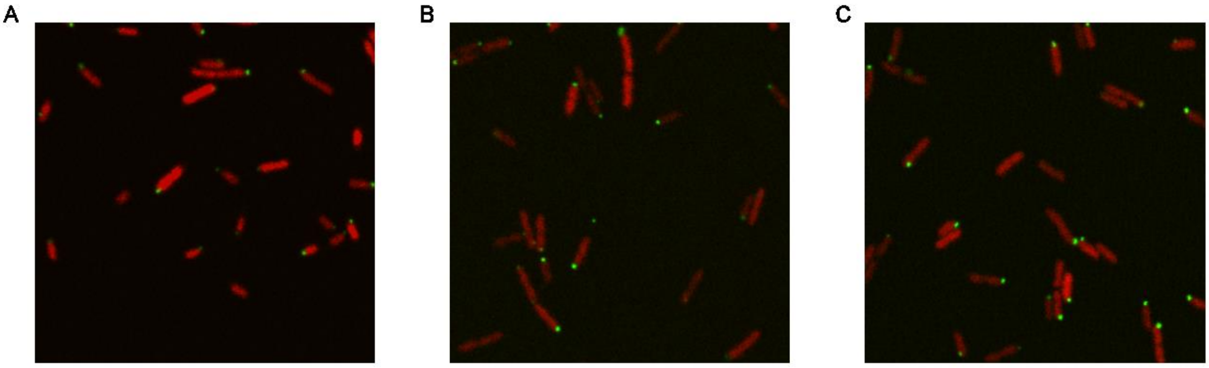

Figure S8: M63 media: A – chloramphenicol, B – No antibiotic, C - rifampicin

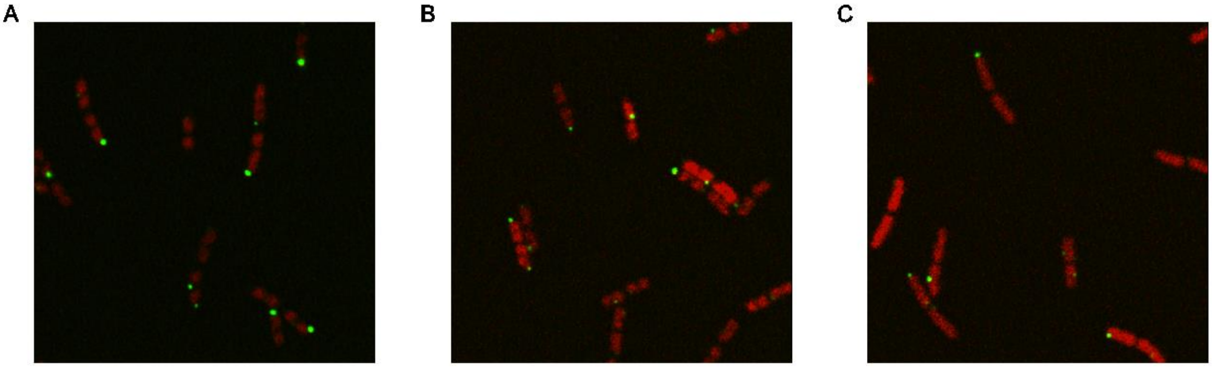

Figure S9: TB media: A – chloramphenicol, B – No antibiotic, C - rifampicin

Publication III

S.M.D. Oliveira, R. Neeli-Venkata, N. Goncalves, J. A. Santinha, L. Martins, H. Tran, J. Mäkelä, A. Gupta, M. Barandas, A. Häkkinen, J. Lloyd-Price, J.M. Fonseca, and A.S. Ribeiro, "Increased cytoplasm viscosity hampers aggregate polar segregation in *Escherichia coli*", *Molecular Microbiology*, 99(4), 686–699, 2016.

Molecular Microbiology (2016) **99**(4), 686–699

doi: 10.1111/mmi.13257

Increased cytoplasm viscosity hampers aggregate polar segregation in *Escherichia coli*

Samuel M. D. Oliveira,[1] Ramakanth Neeli-Venkata,[1] Nadia S. M. Goncalves,[1] João A. Santinha,[2] Leonardo Martins,[2] Huy Tran,[1] Jarno Mäkelä,[1] Abhishekh Gupta,[1] Marilia Barandas,[2] Antti Häkkinen,[1] Jason Lloyd-Price,[1] José M. Fonseca[2] and Andre S. Ribeiro[1]*

[1] *Laboratory of Biosystem Dynamics, Department of Signal Processing, Tampere University of Technology, 33101 Tampere, Finland.*

[2] *UNINOVA, Instituto de Desenvolvimento de Novas Tecnologias, Campus FCT-UNL, 2829-516 Caparica, Portugal.*

Summary

In *Escherichia coli*, under optimal conditions, protein aggregates associated with cellular aging are excluded from midcell by the nucleoid. We study the functionality of this process under sub-optimal temperatures from population and time lapse images of individual cells and aggregates and nucleoids within. We show that, as temperature decreases, aggregates become homogeneously distributed and uncorrelated with nucleoid size and location. We present evidence that this is due to increased cytoplasm viscosity, which weakens the anisotropy in aggregate displacements at the nucleoid borders that is responsible for their preference for polar localisation. Next, we show that in plasmolysed cells, which have increased cytoplasm viscosity, aggregates are also not preferentially located at the poles. Finally, we show that the inability of cells with increased viscosity to exclude aggregates from midcell results in enhanced aggregate concentration in between the nucleoids in cells close to dividing. This weakens the asymmetries in aggregate numbers between sister cells of subsequent generations required for rejuvenating cell lineages. We conclude that the process of exclusion of protein aggregates from midcell is not immune to stress conditions affecting the cytoplasm viscosity. The findings contribute to our understanding of *E. coli*'s internal organisation and functioning, and its fragility to stressful conditions.

Accepted 25 October, 2015. *For correspondence. E-mail andre.ribeiro@tut.fi; Tel. +358408490736; Fax +358331154989.

Introduction

Unicellular organisms, such as *Escherichia coli*, particularly when in optimal environments, can continuously divide into genetically identical cells although, similarly to multicellular organisms, they are not free from errors, e.g. in protein production (Miot and Betton, 2004), that result in malfunctional proteins that can hamper the functioning of cellular processes (Maisonneuve *et al.*, 2008).

Escherichia coli has evolved a complex machinery responsible for ensuring protein functionality that is able to catalyse proper protein folding and assist in the rescue of misfolded ones (Deuerling *et al.*, 1999; Wickner *et al.*, 1999), and can target misfolded proteins for degradation (Viaplana *et al.*, 1997), which allows both error correction and renewal of protein numbers (Willetts, 1967; Goldberg, 1972). When this fails, *E. coli* can resort to protein aggregation (Sabate *et al.*, 2010; Tyedmers *et al.*, 2010; Winkler *et al.*, 2010), which likely reduces potentially harmful effects by rendering some of the malfunctional proteins inert (Bednarska *et al.*, 2013). Recent evidence suggests that the aggregation is not an energy-free process (Govers *et al.*, 2014), which is consistent with being of importance for proper cellular functioning.

Unfavourable growth conditions or continued stress can enhance protein aggregation (Lindner *et al.*, 2008; Maisonneuve *et al.*, 2008; Winkler *et al.*, 2010; Govers *et al.*, 2014). This can lead to excessive aggregate accumulation (Bednarska *et al.*, 2013) that interferes with cellular functioning (Goldberg, 2003; Lindner *et al.*, 2008; Maisonneuve *et al.*, 2008). Recent studies showed that these aggregates are segregated to the cell poles (Winkler *et al.*, 2010; Coquel *et al.*, 2013), due to a volume exclusion effect caused by the presence of the nucleoid at midcell, similar to how plasmids are partitioned (Vecchiarelli *et al.*, 2012; Reyes-Lamothe *et al.*, 2014) and to how other large complexes (Straight *et al.*, 2007) are segregated to the poles. Provided that the segregation process is successful (evidence suggests that it is not entirely successful, even in optimal conditions; Gupta *et al.*, 2014), when the cell divides, it generates an asymmetry, in that both daughter cells will receive one new pole that is free of aggregates (Lindner *et al.*, 2008; Govers *et al.*, 2014). Consequently, as cells continue to divide, this segregation process results in the rejuvenation of several cells of the lineage (freeing them from aggregates), at the cost of a few cells with reduced reproductive vitality, due to inheriting the oldest poles containing several aggregates (Lindner *et al.*, 2008).

Several observations support the conclusion that the exclusion of aggregates from midcell is an energy-free process, caused by nucleoid exclusion (Gupta *et al.*, 2014) (first hypothesised in Winkler *et al.*, 2010). First, the exclusion effect is visible in a strong anisotropy in aggregate kinetics, located at the nucleoid borders, which favours aggregates accumulation at the poles (Gupta *et al.*, 2014). Also, while in cells where the nucleoid is centred the choice of pole is symmetric, in cells with off-centred nucleoids, a higher-than-by-chance fraction of aggregates preferentially locates at the larger pole (Gupta *et al.*, 2014). Finally, the aggregate kinetics, while affected by the nucleoid (Stylianidou *et al.*, 2014), is diffusive-like (Coquel *et al.*, 2013), even when at the pole (in agreement with the absence of transport or anchoring mechanisms).

Consequently, the efficiency with which aggregates are excluded from midcell should depend on factors such as nucleoid size as well as aggregate size and mobility within the cytoplasm, etc (Kuwada *et al.*, 2015). As these properties are likely affected by environmental conditions, e.g. temperature, it is reasonable to hypothesise that this process might lack robustness to some environmental stresses (Jeon *et al.*, 2013; Cherstvy and Metzler, 2015), particularly since, in those conditions, other functions are likely to be more critical (Clegg *et al.*, 2014).

Here, we study the robustness to non-optimal temperatures of the processes of segregation and retention of aggregates at the cell poles in *E. coli*. We address the following questions: To what extent are aggregate intracellular distributions temperature dependent? What are the causes for the temperature dependence? Finally, what are the long-term consequences of sub-optimal temperatures to aggregates numbers in cell lineages? To address these questions, we observed fluorescently tagged natural aggregates as well as synthetic fluorescent aggregates, along with inclusion bodies and nucleoids in individual cells subject to a wide range of temperatures.

Results

To study the temperature dependence of aggregate segregation and polar retention in *E. coli*, we observe aggregates by tracking IbpA-YFP proteins, which are accurate identifiers of the *in vivo* localisation of natural protein aggregates (Lindner *et al.*, 2008; Coquel *et al.*, 2013) (unlike e.g. Clp proteases and other proteins, whose tagging can alter their localisation and, possibly, aggregation; Landgraf *et al.*, 2012). Importantly, these tagged aggregates co-localise with inclusion bodies (Allen *et al.*, 1992). As such, we refer to the aggregates tagged by IbpA-YFP as 'natural' aggregates, even though, in the measurements here conducted, their emergence in the cells is externally enhanced by the addition of streptomycin to the media (Lindner *et al.*, 2008). We also observe aggregates consisting of RNA sequences bound by multiple MS2-GFP proteins (Golding *et al.*, 2005), as previous studies suggest that they behave similarly to natural aggregates (Gupta *et al.*, 2014), have long lifetimes (Gupta *et al.*, 2014), do not vary significantly in size, do not aggregate and can be tracked individually (Golding *et al.*, 2005; Muthukrishnan *et al.*, 2012; Gupta *et al.*, 2014; Häkkinen *et al.*, 2014). As their composition differs from natural aggregates, we refer to these as 'synthetic' aggregates. Finally, since the segregation of aggregates to the poles is caused by nucleoid exclusion (Gupta *et al.*, 2014), we measure nucleoids' size (measured by the relative length along the major cell axis, given the invariance in width with temperature) and location (position of the nucleoid centre along the major cell axis). For this, we performed *4′*,*6*-diamidino-*2*-phenylindole (DAPI) staining of the nucleoid and, for validation, HupA-mCherry tagging.

We first assessed which range of temperatures is not lethal to the strain used (DH5α-PRO). Results in Fig. S1 show that between 10°C and 43°C, conditions are not lethal (although at 10°C no growth is visible). Given this, microscopy measurements were performed for temperatures ranging from 10 to 43°C. Prior to image acquisition, cells were kept at the appropriate temperature for 60 minutes (e.g. Fig. S2) since, at this stage, aggregates and nucleoids already exhibit long-term behaviours (see below).

Behaviour of the synthetic MS2-GFP-tagged RNA aggregates

The MS2-GFP-tagged RNA synthetic aggregates are used since previous studies have shown that they behave similarly to the natural aggregates (at least, in optimal growth conditions), such as exhibiting preference for polar localisation (Gupta *et al.*, 2014). Also, they are visible for periods of time significantly longer than cell division (Muthukrishnan *et al.*, 2012). Further, their fluorescence intensity, which is determined by the number of MS2-GFP molecules bound to the target RNA (Golding *et al.*, 2005), has been reported to very stable over time (Muthukrishnan *et al.*, 2012; Gupta *et al.*, 2014; Häkkinen *et al.*, 2014). Finally, these properties do not appear to be significantly affected by temperature (for temperatures ranging from at least 10 to 43°C), suggesting that the number of bound MS2-GFP proteins is also not significantly temperature dependent (provided sufficient number of MS2-GFP proteins in the cytoplasm).

We performed additional tests to verify the robustness in time of their fluorescence intensity, which is a valuable property for purposes of quantification and tracking, and to verify the similarly in behaviour with natural aggregates. For this, first, we studied the temporal fluorescence intensity of MS2d-GFP-tagged RNA molecules. Namely, we observed the fluorescence intensity of 40 individual, MS2-GFP-tagged RNAs over time (1 min^{-1}) in independent cells at 37°C. By inspection, we verified that each cell contained only one tagged RNA, to facilitate tracking. From the time lapse images, we obtained the fluorescence intensity of each of the 40 individual tagged RNAs for 30 minutes, since first detected. We fitted the intensity of each spot over time with a decaying exponential function and inferred the first-order, degradation rate constant of the spot intensity. We obtained a mean decay rate of $\sim 8.1 \times 10^{-5}\ \text{s}^{-1}$, corresponding to a mean half-life of ~ 144 min, which is longer than our observation window (60 min). As such, we conclude that, during the microscopy measurement period, the fluorescence of synthetic aggregates does not decrease significantly over time (gradually or abruptly), in agreement with previous reports (Golding *et al.*, 2005; Muthukrishnan *et al.*, 2012). These results are expected given previous studies of the coat protein of bacteriophage MS2 that show that MS2 binding sites are constantly occupied by MS2d proteins (Talbot *et al.*, 1999; Fusco *et al.*, 2003), which results in the 'immortalisation' of the target RNA due to isolation from RNA-degrading enzymes.

Next, we verified whether the synthetic aggregates, similar to IbpA-YFP, also co-localise with inclusion bodies. For this, we observed 85 cells at 37°C for 1 hour. At that moment, we counted in each cell the number of inclusion bodies (visible by Phase Contrast) and the number of synthetic aggregates (visible by fluorescence microscopy). Then, we counted how many times an aggregate is co-localised with an inclusion body. We also counted how many inclusion bodies 'contained' at least one aggregate, provided that the cell contained at least one aggregate (Fig. S3). We observed that 83% of the synthetic aggregates were co-localised with an inclusion body and that 91% of the inclusion bodies had a fluorescent synthetic aggregate co-localised with it. We conclude that the synthetic aggregates can be used to accurately inform on the *in vivo* presence and localisation of protein aggregates, similar to IbpA-YFP (Lindner *et al.*, 2008).

Positioning of IbpA-YFP-tagged aggregates as a function of aggregate size

The IbpA-YFP-tagged aggregates (of sufficient size to allow detection) exhibit significant variance in size (as measured by their fluorescence intensity). As such, we investigated whether their size (within the range of detection) significantly affected their behaviour, such as the degree of exclusion from midcell. For this, we investigated the location of IbpA-YFP-tagged aggregates along the major cell axis as a function of their size, from cells at 37°C. We then extracted the 10% and the 25% smallest aggregates and their location along the major cell axis. From there, we obtained the fraction of aggregates excluded from midcell. Also, we calculated the fraction of aggregates that would be expected to be excluded from midcell if they distributed uniformly along the major cell axis, and accounting for the relative size of the nucleoid. This fraction equals 0.41 (assuming a uniform distribution along the major axis).

We found that 86% of all aggregates were located at the poles. Meanwhile, 85% of the 25% smallest aggregates were found at the poles. Finally, 88% of the 10% smallest aggregates were found at the poles. Thus, the distributions of aggregates along the major cell axis do not differ significantly with aggregate size. We conclude that, for the range of aggregate sizes that we can detect, their size does not influence the degree of exclusion from midcell.

Adaptation time of the relative nucleoid size and aggregate distributions to temperature shifts

We performed multi-modal microscopy at 10, 24, 37 and 43°C of DH5α-PRO cells expressing MS2-GFP proteins along with the RNA target that form the synthetic aggregates (*Methods*). First, cells were grown at 37°C and then kept at the appropriate temperature for 15, 45, or 60 minutes. At these points in time, we performed DAPI staining and imaged cells once. From the images, we extracted the distributions of location and fluorescence intensity from synthetic aggregates and from stained nucleoids along the major and minor axes of each cell. We then determined whether a cell has one or two nucleoids and the nucleoid(s) borders along the cell axes (*Methods*). We define the region along the major axis containing the nucleoid(s) as 'midcell', while 'poles' are the two regions between these borders and the cell extremities.

Next, we compared the distribution of fluorescence intensity of aggregates along the major cell axis of cells with one nucleoid, when kept at the appropriate temperature for 15, 45 and 60 minutes. Results in Fig. S4 show that, for all temperatures, there are no significant differences between aggregate distributions at 15 and 45 min. We also compared the normalised distances of the nucleoid borders to the cell centre at 15 and 45 min. Again, we found no significant differences (Fig. S4). The same result was obtained when comparing distributions at 45 and 60 min after placing cells at the appropriate temperature.

We conclude that, for both aggregates and nucleoids, the distributions of fluorescence intensity at each temperature beyond 15 min. of adaptation time are representative of the long-term distributions in those conditions. Given this, from here onwards, we analyse

Table 1. Relative concentration of synthetic aggregates at the poles in cells with 1 nucleoid.

T (°C)	No. cells	Mean (standard) relative nucleoid length (μm)	Mean fraction of aggregates at poles	*P* value of the *t*-test	Mean relative 3-D concentration of aggregate numbers at poles	*P* value of the KS test
10	147	0.63 (0.12)	0.44		1.32	
24	604	0.56 (0.11)	0.39	0.21	1.09	0.11 (10 vs 24)
37	300	0.53 (0.11)	0.69	< 0.01	1.86	< 0.01 (24 vs 37)
43	204	0.47 (0.13)	0.81	< 0.01	1.79	0.05 (37 vs 43)

For each temperature condition, it is shown the number of cells analysed along with the mean and standard deviation of the relative nucleoid length. Also shown is the mean fraction of synthetic aggregates' numbers at the poles along with the *p* values of a *t*-test of statistical significance. Next, it is shown the relative 3-D concentration of synthetic aggregates at the poles (as measured by the ratio between the fraction of synthetic aggregate numbers at the poles and the normalised pole volume in individual cells), and the *p* values of a KS-test of statistical significance. In both statistical tests, for *p* values smaller than 0.01, the null hypothesis that the two sets of data are from the same distribution is rejected.

data collected from cells kept at the appropriate temperature for 60 min, unless otherwise stated.

Temperature dependence of relative nucleoid lengths and aggregate spatial distributions

From images of cells expressing synthetic aggregates, we obtained the mean relative nucleoid length along the major cell axis by DAPI staining and the mean fraction of synthetic aggregates at the poles, for each condition. Results in Table 1 show that the mean relative nucleoid length decreases slowly with increasing temperature. This decrease is significant according to Kolmogorov–Smirnov (KS) tests between all pairs of conditions (*p* values smaller than 0.01).

Nucleoid size assessment by HupA-mCherry tagging (Table S1) matched the results from DAPI staining for temperatures between 24 and 43°C (showing only slightly larger nucleoids in all cases). We attempted measurements at 10°C, but the HupA-mCherry signal was too weak.

Also from Table 1, in accordance with a *t*-test of statistical significance, the mean fraction of aggregates at the poles increases significantly with temperature, except between 10 and 24°C. This increase appears to be much larger than what would be expected from the small decrease in relative nucleoid length.

To analyse whether the increase in the mean fraction of aggregates at the poles with temperature can be explained by the decrease in relative nucleoid length, for each condition, we obtained the relative 3-D concentration of aggregate numbers at the poles in each cell, accounting for the nucleoid length and the capped cylindrical shape of the cells (*Methods*). Also, we performed KS tests to compare the distributions of concentrations in individual cells from different conditions. Note that, if the aggregates tend to be excluded from midcell, their relative concentration at the poles will be larger than 1. Else, in the absence of nucleoid exclusion, this concentration should equal 1. In addition, if the degree of exclusion of aggregates from midcell is temperature dependent, we expect their relative concentration at the poles to change with temperature.

Results in Table 1 show that the mean relative concentration of aggregates at the poles is much higher than 1 at 37 and 43°C, but close to 1 at 10 and 24°C. The KS tests confirm that there is a significant change between 24 and 37°C (*p* value < 0.01). This difference in aggregate behavior is also visible when plotting the distances to the cell centre of aggregates and mean nucleoid border (Fig. 1),

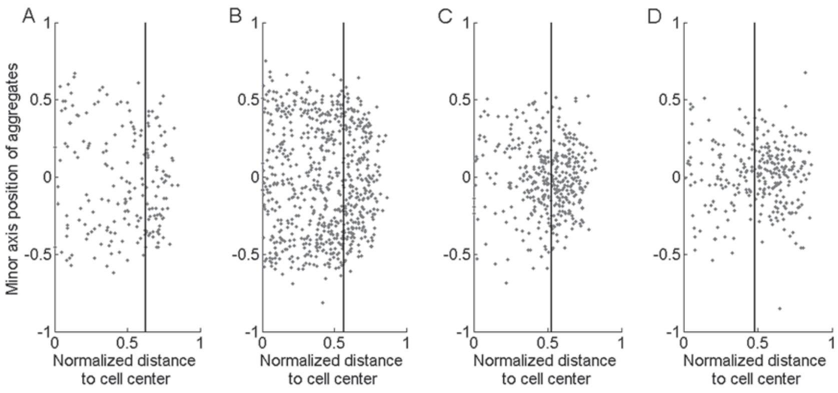

Fig. 1. Relative position versus normalised distance to cell centre of each aggregate, for various temperatures. Images were taken 1 hour after placing the cells at the specific temperature. Also shown, by the black solid line, is the mean relative nucleoid length. Measurements are from (A) 195 aggregates at 10°C (206 cells), (B) 707 aggregates at 24°C (1036 cells), (C) 398 aggregates at 37°C (367 cells) and (D) 288 aggregates at 43°C (306 cells).

Table 2. Correlations between synthetic aggregates positioning and nucleoid size and positioning in cells with one nucleoid.

T (°C)	No. cells	No. aggregates	Correlation between relative distance of aggregates to cell extreme and relative nucleoid length	t-Test	Correlation between the locations of nucleoid centre and aggregates along major cell axis	t-Test	$\mu_{nucleoid}$
10	147	195	–0.01	0.84	–0.03	0.64	0.18
24	604	707	–0.14	< 0.01	–0.09	0.02	0.14
37	300	398	–0.25	< 0.01	–0.2	< 0.01	0.16
43	204	288	–0.25	< 0.01	–0.25	< 0.01	0.19

For each temperature condition, it is shown the number of cells and of synthetic aggregates analysed, along with the correlation between the relative distance of aggregates to the closest cell extreme and the relative nucleoid length and the P values of a t-test of statistical significance. Also shown is the correlation between the locations (i.e. distance to midcell) of the nucleoid centre and of each synthetic aggregate, followed by a t-test of statistical significance. For values < 0.01, it is accepted that the correlation is significant. Finally, the mean distance of the nucleoid centre to the cell centre ($\mu_{nucleoid}$) is presented.

which shows an increase in aggregate density at the poles with increasing temperature. We conclude that the aggregate exclusion from midcell is much weaker at sub-optimal temperatures.

We performed the same measurements in cells expressing IbpA-YFP (Lindner *et al.*, 2008). Results in Table S2 show identical changes with temperature in the relative nucleoid length as well as in the mean fraction of IbpA-YFP aggregates at the poles. This allows concluding that the similarity in behaviour between synthetic and IbpA-YFP-tagged aggregates is maintained in the entire range of temperatures studied here. Further, we conclude that the spatial distributions of natural and synthetic aggregates change with temperature. Namely, the mean fraction of aggregates at the poles is significantly lower at the two lowest temperatures tested, and this cannot be explained by changes in the relative nucleoid length along the major cell axis.

Correlations of aggregate positioning with nucleoid size and positioning in individual cells

Next, we studied how temperature affects the correlation between aggregate positioning and nucleoid size and positioning. We first calculated the correlation between aggregate distance from the closest cell extreme and relative nucleoid length. Also, we performed t-tests of statistical significance of the correlation for each condition. Results in Table 2 show a negative correlation in all conditions that weakens with decreasing temperature, becoming not statistically significant at 10°C.

Next, we calculated the correlation between nucleoid centre and aggregate positioning's along the major cell axis (Fig. S5), and performed t-tests of statistical significance of the correlation for each condition. Since this correlation depends on the degree of 'off centring' of the nucleoid (Gupta *et al.*, 2014), we also compare the mean distance between nucleoid and cell centre ($\mu_{nucleoid}$) between conditions. From Table 2, first, $\mu_{nucleoid}$ shows no significant temperature dependence. Second, there are statistically significant negative correlations between the positioning of nucleoid centre and aggregates at 37 and 43°C, while at 10 and 24°C, this correlation is weak and not statistically significant.

We conclude that the aggregates positioning becomes less correlated with the nucleoids size and location for decreasing temperature, i.e., there is a reduction in the degree with which nucleoids affect aggregate positioning.

Anisotropies in aggregate dynamics

A previous study (Gupta *et al.*, 2014) showed that the correlations between aggregates and nucleoid, when existing, are generated by multiple encounters over time between them (rather than by a single event, such as a transport process). These encounters generate anisotropies in the aggregate dynamics at the nucleoid borders (Gupta *et al.*, 2014) (Fig. 2). A similar anisotropy, opposite in direction, occurs at the cell extremes, as the aggregates collide with the cell walls (Gupta *et al.*, 2014) (Fig. 2). The combination of anisotropies of opposite directions at the nucleoid borders and at the cell walls explains the long-term spatial distribution of the aggregates, namely, their preference for polar location (Gupta *et al.*, 2014).

To assess how these anisotropies are affected by temperature, we performed time lapse microscopy at 10, 24, 37 and 43°C for 45 minutes long, with images taken every minute, from which we obtained the displacement vectors of individual aggregates between consecutive frames and, from there, the 'anisotropy curve' for each condition (*Methods*), shown in Fig. 2.

From the distributions in Fig. 2, we quantified the 'degree of anisotropy', for each condition, from the area under the curve in the region of positive anisotropy (responsible for retaining aggregates at the poles; Gupta *et al.*, 2014). The sizes of these areas are shown in the insets in Fig. 2, and inform that, on average, the area has

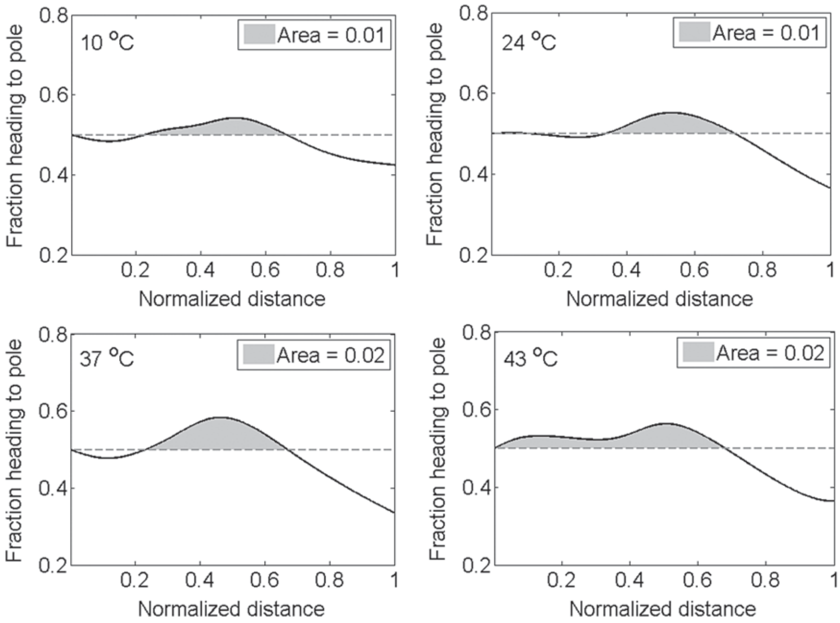

Fig. 2. Anisotropy curves of synthetic aggregates at different temperatures from time lapse images. Kernel Density Estimate (bandwidth of 0.1 normalised cell lengths) of the fraction of displacement vectors oriented towards the cell pole as a function of the distance towards midcell along the major cell axis. Measurements are at 10°C (43 cells), at 24°C (66 cells), at 37°C (184 cells) and at 43°C (41 cells).

half the size in the two lowest temperature conditions, indicating much weaker anisotropy. A similar reduction in the 'negative' areas (at the cell extremes) is also visible in these conditions. These reductions in the degree of anisotropies explain the loss of heterogeneity in the aggregate spatial distribution with decreasing temperature.

Further, we find no changes in nucleoid morphology with temperature changes that could explain this change in aggregate behaviour. Note that the mean positioning of the positive peak of anisotropy along the major cell axis is not significantly affected by temperature. This indicates that the nucleoid relative size only changes mildly with temperature (in accordance with the nucleoid relative size measurements reported in Table 1). In addition, we measured the absolute nucleoid length and width and found no significant changes with temperature (Table S3). From this lack of change in absolute nucleoid size, it is reasonable to assume that the nucleoid density does not change significantly in the range of temperatures tested, and thus is also not likely to be responsible for changes in aggregate spatial distributions with temperature. This is confirmed by inspection of the microscopy images, where it is visible that in no condition do aggregates exhibit a behaviour consistent with, e.g., 'entering' the nucleoid region. Rather, in all conditions, when at midcell, the aggregates locate near the cell inner-membrane.

Aside from this, it is noted that changes in cell morphology also cannot explain the observed changes in aggregate dynamics. First, we found no significant changes in the absolute cell width with temperature (Table S3). Second, while the absolute cell length increases with temperature (Table S3), it cannot explain the changes in aggregate relative concentrations at the poles given the definition of 'pole region' (*Methods*). Given this, we next investigated the short-term dynamics of the aggregates as a function of temperature.

Spatial dynamics of the aggregates as a function of temperature

We speculated that the reduction in anisotropies with decreasing temperature is caused by a decrease in aggregate mobility. This is supported by the fact that both the area of positive anisotropy at the nucleoid borders and the area of the 'negative anisotropy' at the cell extremes are reduced with decreasing temperature, which is consistent with a general decrease in aggregate mobility throughout the cytoplasm, rather than a change in the properties of nucleoid or cell walls (while the nucleoid's ability to exclude aggregates could be affected by temperature, e.g. due to changes in density, no such changes are expected to occur to the cell walls, for the range of temperatures tested).

We thus performed time-lapsed, multi-modal microscopy at 10, 24, 37 and 43°C to measure the degree of diffusion of synthetic aggregates in each condition (as measured by the Diffusion coefficient, D) at the single cell level (*Methods*). Results in Table 3 show that D changes widely with temperature, being much smaller at lower temperatures.

We next assessed whether these differences in D between conditions could be explained by the differences in temperature alone (i.e. by the differences in free energy). For that, we calculated the relative dynamic vis-

Table 3. Relative dynamic viscosity of the cytoplasm and displacements bias at midcell.

T (°C)	No. cells	D (μm^2 min^{-1})	Relative dynamic viscosity (relative to 37°C)	Γ (μm^2 min^{-1})
10	43	0.005	1.67	5.4×10^{-6}
24	110	0.007	1.37	4.6×10^{-5}
37	184	0.01	1	1.6×10^{-4}
43	41	0.015	0.67	2.7×10^{-4}

For each condition, it is shown the number of cells studied along with the synthetic aggregates' diffusion coefficient, D, the relative dynamic viscosity of the cytoplasm relative to 37°C, and the bias in the displacement of aggregates located at midcell, Γ. Cells were kept at 37°C for 1 hour under the microscope and then kept at the appropriate temperature for 1 hour, after which we collected images for 45 minutes, with 1 minute interval.

cosity in each condition (relative to 37°C). This quantity should equal 1, if the differences in D with temperature between conditions are caused solely by differences in free energy.

Results in Table 3 show that the relative dynamic viscosity changes widely with temperature, being much higher at lower temperatures. Thus, we conclude that the differences in D with changing temperature are not caused solely by the differences in free energy, but also by changes in the thermophysical properties of the cytoplasm.

Finally, we verified that D, and thus the relative dynamic viscosity, is not biased by the cell growth rates (which differ between conditions). For that, we calculated the bias in the displacements of aggregates at midcell, Γ (Table 3). Since the values of this quantity are much smaller than the values of D in all conditions, we conclude that this bias is not significant.

Given this, and considering also the results on the correlations between the aggregates positioning and the nucleoids size and location (Table 2), as well as the measurements of local anisotropies along the major cell axis, we conclude that, at lower temperatures, the aggregates and nucleoid interact much less frequently during the measurement period. This, along with the stochasticity in diffusion, explains the observed near-uniform distribution of aggregates along the major cell axis at the two lower temperature conditions.

Finally, we considered another possibility, namely, that the lower fraction of aggregates at the poles at the lower temperature conditions could be explained by the fact that the aggregates do not have sufficient time to reach the poles prior to image acquisition. However, if this, rather than the reduced interactions between nucleoid and aggregates, was the cause, one would not observe the decrease with decreasing temperature in the area of the regions of positive anisotropy that is visible in the plots of the fraction of aggregates heading towards the poles along the major cell axis (Fig. 2), since this quantity is independent of the number of aggregates studied.

Spatial distribution and dynamics of aggregates following osmotic stress

Given the above, it is reasonable to expect that different means to increase the cytoplasm viscosity will cause similar changes on the short- and long-term aggregate behaviours.

It is known that, under osmotic stress, cells (when plasmolysed) exhibit enhanced cytoplasmic viscosity (van den Bogaart *et al.*, 2007; Konopka *et al.*, 2009; Mika *et al.*, 2010; Jin *et al.*, 2013). We placed cells under osmotic stress, and then assessed the consequences to the short-term dynamics and long-term spatial distribution of the synthetic aggregates within. We studied plasmolysed and adapted cells, which we compared with control cells (in optimal growth conditions).

We first assessed the spatial distributions of aggregates in control, plasmolysed and adapted cells for population images obtained by DAPI staining, following the application of osmotic stress (*Methods*). Results in Table S4 show that the relative 3-D concentration of aggregate numbers at the poles is much lower in plasmolysed cells than in the control (P value much smaller than 1). Further, it is close to 1, similar to low temperature conditions (Table 1). We conclude that the phenomenon of aggregate exclusion from midcell is absent in plasmolysed cells. Further, from Table 1, in adapted cells, this quantity is not statistically different from the control, from which we conclude that these cells recovered the ability to exclude aggregates from midcell.

To determine if the change in aggregates spatial distribution in plasmolysed cells has the same cause as in cells in low temperatures, we conducted 1-hour long, time-lapsed microscopy measurements with the perfusion of osmotic stress-inducing agent, to measure the diffusion coefficient of the aggregates and, thus, the cytoplasm's relative viscosity. From Table S5, the relative dynamic viscosity of plasmolysed cells is much higher than of control or adapted cells. Also, the bias in the displacements of aggregates at midcell, Γ, is not significant. We

Table 4. Mean relative concentration of synthetic aggregate numbers in between nucleoids in cells with two nucleoids.

T (°C)	No. cells	Mean relative length of midcell (two nucleoids and space in between) (μm)	Mean relative 1-D concentration of aggregate numbers in the gap	*P* value of permutation test
10	38	0.75	0.85	
24	154	0.68	0.78	< 0.01 (10°C vs 24°C)
37	46	0.72	0.69	< 0.01 (24°C vs 37°C)
43	93	0.7	0.68	< 0.01 (37°C vs 43°C)

For each temperature condition, it is shown the number of cells studied, the mean relative length along the major cell axis of the midcell region (which includes the two nucleoids and the space in between), the relative 1-D concentration of synthetic aggregate numbers in the space in between nucleoids (gap) (as measured by dividing the fraction of aggregate numbers in the gap by the distance between the inner borders of the nucleoids in individual cells) and the results of a test of statistical significance between differences in concentration (permutation test between pairs of conditions). For *P* values smaller than 0.01, the null hypothesis that the two sets of data are from the same distribution is rejected.

conclude that the changes in aggregate spatial distribution in plasmolysed cells and in cells subject to low temperatures are both due to increased cytoplasm viscosity.

Long-term consequences of the effects of temperature changes on the degree of exclusion of aggregates from midcell

Finally, we assessed whether the loss of effectiveness in excluding aggregates from midcell at lower temperatures causes tangible, long-term effects in cells of subsequent generations. These are expected to emerge, provided that the fraction of aggregates in between nucleoids in cells close to division increases significantly (see for example Fig. S6) (Stewart *et al*., 2005; Lindner *et al*., 2008; Govers *et al*., 2014; Gupta *et al*., 2014).

We thus investigated the distribution of synthetic aggregates along the major cell axis in cells with two nucleoids as a function of temperature. From each cell, we extracted the mean relative length along the major axis of each nucleoid (in general, the two nucleoids are of nearly identical size) and of the space in between the inner borders of the nucleoids (named here as the ‘gap’). Also, we obtained the mean relative 1-D concentration of aggregate numbers in the gap for each cell and performed a permutation test to compare the mean concentration between pairs of conditions.

Results in Table 4 first show that the mean relative length of the midcell region does not exhibit a consistent, significant change with temperature. Meanwhile, the mean relative 1-D concentration of synthetic aggregates in the gap region increases significantly with decreasing temperature. We conclude that, at lower temperatures, a larger fraction of aggregates will be randomly partitioned in division and then located at the new pole of the daughter cells, thus hampering the generation of asymmetries in aggregate numbers between the cells of a lineage.

Finally, we performed the same measurements in cells expressing IbpA-YFP. Results in Table 5 show no change in the mean relative length of the midcell region but a very significant increase in mean relative concentration of IbpA-YFP aggregate numbers in the gap. Thus, we conclude that, for both the natural and synthetic aggregates studied here, the relative concentration of aggregates in between nucleoids in cells near division is significantly

Table 5. Mean relative concentration of natural aggregate numbers in between nucleoids in cells with two nucleoids.

T (°C)	No. cells	Mean relative length of midcell (two nucleoids and space in between) (μm)	Mean relative 1-D concentration of aggregate numbers in the gap	*P* value of permutation test
10	195	0.72	0.53	
24	346	0.75	0.36	< 0.01 (10°C vs 24°C)
37	66	0.76	0.23	< 0.01 (24°C vs 37°C)
43	209	0.71	0.13	< 0.01 (37°C vs 43°C)

For each temperature condition, it is shown the number of cells studied, the mean relative length along the major cell axis of the midcell region (which includes the two nucleoids and the space in between), the relative 1-D concentration of natural IbpA-YFP aggregate numbers in the space in between nucleoids (gap) (as measured by dividing the fraction of aggregate numbers in the gap by the distance between the inner borders of the nucleoids in individual cells) and the results of a test of statistical significance between differences in concentration (permutation test between pairs of conditions). For *P* values smaller than 0.01, the null hypothesis that the two sets of data are from the same distribution is rejected.

higher at lower temperatures and that this is not due to changes in the relative nucleoid length along the major cell axis but rather due to the homogenous distribution of the aggregates in the cytoplasm.

Discussion

In optimal conditions, *E. coli* cells segregate large protein aggregates to the poles via nucleoid exclusion (Gupta *et al.*, 2014). Following cell divisions, this will result in the renewal of some cells of a lineage, which will be void of aggregates, at the expense of others that will contain several aggregates and exhibit accelerated aging (Lindner *et al.*, 2008). We observed live cells within the range of temperatures where they exhibit replication and found that, at low temperatures, the aggregate segregation and retention processes become nonfunctional in that, on average, aggregates no longer preferentially locate at the poles. Also, at the single cell level, their positioning no longer correlates with nucleoid size or positioning.

This non-functionality is shown to be due to an alteration in the aggregates' short-term behaviour. Namely, their displacements distribution no longer exhibits strong anisotropies at the nucleoid borders and cell extremes, due to a much enhanced cytoplasm viscosity that renders the interactions between nucleoid and aggregates too infrequent and weak to generate significant heterogeneities in the aggregate spatial distribution. To validate these findings, we subjected cells to osmotic stress. We observed that plasmolysed cells were also unable to segregate aggregates to the poles, due to their much enhanced cytoplasmic viscosity (Konopka *et al.*, 2009) (here verified).

The similarity in aggregate behaviour at low temperatures and under osmotic stress suggests that, in any conditions where cytoplasm viscosity is increased, one should expect loss of aggregate preference for polar localisation. Relevantly, increases in cytoplasm viscosity are known to occur under common stresses, such as carbon starvation and energy depletion, as well as during the stationary growth phase (Parry *et al.*, 2014). Further, we expect that, aside from large aggregates, other large cellular components such as plasmids, enzyme complexes, micro-compartments (Kerfeld *et al.*, 2010) and other macromolecules will be subject to nucleoid exclusion under optimal conditions. As such, we expect their spatial localisation in the cytoplasm to be similarly affected by increases in cytoplasm viscosity.

What is the origin of the increase in relative viscosity with decreasing temperature? Given the size of the aggregates studied here, in accordance to (Parry *et al.*, 2014), this is likely caused by the decrease in cellular metabolism rates responsible for 'fluidising' the cytoplasm (which is in a 'near-glass' transition state when in optimal temperature; Parry *et al.*, 2014). Meanwhile, in the case of plasmolysed cells, it may be that the increased viscosity results from increased macromolecular crowding rather than reduced metabolism.

Our findings complement recent findings on how the bacterial cytoplasm functions. In Parry *et al.* (2014), the cytoplasm viscosity was shown to be 'metabolism dependent'. Conditions imposing poor metabolic rates cause increased cytoplasmic viscosity, which decreases the diffusion rate of macromolecules and other large cell components. We found that this has long-term consequences, namely, it renders nucleoid exclusion of protein aggregates far less effective, which perturbs the internal organisation of these components in the cell.

The negative effects of hampered aggregate preference for polar localisation should increase with prolonged exposure to stressful conditions. However, the consequences of failures in segregation and polar retention are likely to be rapidly dealt with (i.e. in a few generations), once conditions return to optimal, particularly in *E. coli*, which is capable of rapid division rates. This may explain its lack of energy-dependent 'repair' mechanisms (Clegg *et al.*, 2014). It might be that other bacteria, with much lower division rates (e.g. extremophiles), cannot employ the same strategy. In that scenario, compartmentalisation (Kerfeld *et al.*, 2010; Cornejo *et al.*, 2014) or transport mechanisms (in the case of eukaryotes) might be the adopted solutions.

Experimental procedures

Briefly, we used *E. coli* strain DH5α-PRO, generously provided by I. Golding (Baylor College of Medicine, Houston, TX) to study synthetic aggregates, and *E. coli* strain MGAY (kind gift from Ariel Lindner, Paris Descartes University, France) to study tagged natural aggregates. Bacterial cell cultures were grown in lysogeny broth (LB). Synthetic aggregates were induced with 100 ng ml^{-1} of anhydrotetracycline (aTc) and 0.1% L-arabinose for 50 min. After, 1 mM IPTG is added for 10 min. Natural aggregate production is induced by adding streptomycin (10 μg.ml^{-1}) for 30 min. Nucleoids were visualised by either DAPI staining or HupA-mCherry tagging. Live single-cell, single-molecule experiments were performed using Nikon Eclipse (Ti-E, Nikon) inverted microscope equipped with C2+ (Nikon) confocal laser-scanning system, and a thermal imaging chamber (CFCS2, Bioptechs, USA). Also, a peristaltic pump was used to provide continuous flow of fresh media to the cells. Example movies of time-lapse microscopy at 10°C (Movie S1) and 43°C (Movie S2) are provided. Cells were segmented from phase contrast images using software 'MAMLE' (Chowdhury *et al.*, 2013). Fluorescent aggregates were segmented as in Gupta *et al.* (2014) and Häkkinen *et al.* (2014). Nucleoids were detected and quantified as in Mora *et al.* (2011). Lineages were constructed by the software 'CellAging' (Häkkinen *et al.*, 2013). For additional information, see below.

Cells and plasmids

Experiments using synthetic aggregates were conducted in *E. coli* strain DH5α-PRO, generously provided by I. Golding (Baylor College of Medicine). The strain information is: deoR, endA1, gyrA96, hsdR17(r_K^- m_K^+), recA1, relA1, supE44, thi-1, Δ(*lacZYA-argF*)U169, Φ80δ*lacZ*ΔM15, F-, λ-, P_{N25}/*tetR*, $P_{lacI}{}^q$/*lacI* and SpR. This strain contains two constructs: (i) PROTET-K133 carrying $P_{LtetO\text{-}1}$-MS2d-GFP and (ii) a pIG-BAC vector carrying $P_{lac/ara\text{-}1}$-mRFP1-MS2-96bs (MS2-96bs stands for 96 MS2 binding site array) (Golding *et al.*, 2005). Dimeric-fused proteins MS2d-GFP are produced from the medium-copy vector, controlled by $P_{LtetO\text{-}1}$, regulated by tetracycline repressor and aTc inducer. RNA targets for multiple MS2d-GFP are produced from a single-copy F-plasmid, controlled by $P_{lac/ara\text{-}1}$ (Lutz and Bujard, 1997), regulated by LacI and AraC repressors and IPTG and L-arabinose inducers. Further, to validate the results from DAPI measurements of nucleoid size and location, we inserted the plasmid pAB332 carrying hupA-mcherry (Fisher *et al.*, 2013). Expression of HupA-mCherry is controlled by a constitutive promoter (hupA).

Experiments to study natural aggregates were conducted using the *E. coli* MG1655 (MGAY) strain carrying the ibpA-yfp sequence in the chromosome under the control of the endogenous chromosomal IbpA promoter (kind gift from Ariel Lindner, Paris Descartes University, France).

Media and chemicals

Bacterial cell cultures were grown in LB media. The chemical components of LB (Tryptone, Yeast extract and NaCl) were purchased from LabM (Topley House, Bury, Lancashire, UK) and the antibiotics from Sigma-Aldrich (St. Louis, MO). Isopropyl *b-D-1*-thiogalactopyranoside (IPTG) and aTc used for induction of the target genes are from Sigma-Aldrich. Agarose (Sigma-Aldrich) was used for microscope slide gel preparation. Finally, DAPI from Sigma-Aldrich was used to stain nucleoids.

Induction of production of fluorescent synthetic and natural aggregates

Pre-cultures were diluted from the overnight culture to OD_{600} of 0.1 in fresh LB media, supplemented with appropriate antibiotics and kept at 37°C at 250 r.p.m. in a shaker until reaching $OD_{600} \approx 0.3$.

Next, to produce synthetic aggregates, we proceeded as follows. After the DH5α-PRO cells reached an $OD_{600} \approx 0.3$, they were induced with 100 ng ml^{-1} of aTc and 0.1% L-arabinose for 50 minutes until $OD_{600} \approx 0.5$. At that stage, cells contain sufficient MS2d-GFP to detect target RNAs, and induction of $P_{lac/ara\text{-}1}$ was completed by adding 1 mM IPTG. After 10 more minutes, cells were placed the appropriate temperature (10, 24, 37 or 43°C) for 1 hour.

To induce the production of natural aggregates, first, after MGAY cells reached an $OD_{600} \approx 0.3$, they were placed at the appropriate temperature (10, 24, 37 or 43°C) for 1 hour. Then, they were incubated with streptomycin (10 μg ml^{-1}) for 30 min.

Nucleoid visualisation by DAPI nucleoid staining

For nucleoid staining, cells were kept at a specific temperature for 60 min, and then fixed with 3.7% formaldehyde for 30 min. Next, cells were re-suspended in PBS, and DAPI (2 mg ml^{-1}) was added and cells were incubated for 20 min at room temperature. Finally, cells were washed twice with PBS (to remove DAPI in excess), and placed on a 1% agarose gel pad prepared with the appropriate media for microscopy (Chazotte, 2011).

Nucleoid visualisation by hupA-mCherry nucleoid tagging

The dimeric histone-like protein HU is one of the most abundant nucleoid-associated proteins that participates in the DNA structural organisation (Claret and Rouviere-Yaniv, 1997; Azam *et al.*, 1999). A version of this protein (HupA) has been tagged with the red fluorescent protein (mCherry) to study nucleoids in live *E. coli* cells (Maisonneuve *et al.*, 2008). This study showed that hupA-mCherry allows a proper assessment of the location and size of nucleoids *in vivo.* Expression of this synthetic protein was placed under the control of a constitutive promoter (hupA).

Osmotic stress

In van den Bogaart *et al.* (2007), it was reported that increasing sodium chloride (NaCl) concentration in the media results in a rapid osmotic upshift (from 0.15 to 0.6 Osm). This causes cytoplasm plasmolysis of *E. coli* cells (the water in the cytoplasm is expelled to the environment in a few seconds). Subsequently, cells undergo an adaptation process that allows recovering the ability to divide. As the adaptation time differs from cell to cell, when observing a population shortly after imposing osmotic stress conditions, one usually finds two distinct populations: adapted and non-adapted (Jin *et al.*, 2013), which differ in cell and nucleoid morphology, as well as in division rate (Jin *et al.*, 2013). Namely, plasmolysed (non-adapted) cells exhibit longer length and elliptic shape, contain only one condensed nucleoid and do not divide (Konopka *et al.*, 2009; Mika *et al.*, 2010; Jin *et al.*, 2013). Relevantly, in these cells, the high osmolality (> 0.15 Osm) causes the Diffusion coefficient of GFP to be heavily reduced (van den Bogaart *et al.*, 2007; Konopka *et al.*, 2009).

To expose cells to osmotic stress during time-lapse microscopy, 300 mM of NaCl was added to the growth media and pumped into the thermal chamber (set to 37°C) for 1 hour. For population microscopy imaging, the cells were kept under osmotic stress for 30 minutes (osmotic stress-inducing media with 300 mM of NaCl). In both cases, approximately ~ 0.68 Osm was reached (Konopka *et al.*, 2009).

Cells were considered to be plasmolysed when exhibiting filamentous and elliptical morphology (Konopka *et al.*, 2009), not dividing during the measurement period (1 hour), and if containing only one, condensed nucleoid (Mika *et al.*, 2010; Jin *et al.*, 2013).

Microscopy

Cells were visualised using a Nikon Eclipse (Ti-E, Nikon) inverted microscope equipped with a 100× Apo TIRF (1.49

NA, oil) objective. The software for image acquisition was NIS-Elements (Nikon). Confocal images were taken by a C2+ (Nikon) confocal laser-scanning system. The pinhole size was set to 1.2 AU. For confocal images, the size of a pixel corresponds to 0.124 μm using a scan area resolution of 1024 × 1024 pixels. To visualise MS2-GFP-RNA 'spots', we used a 488 nm laser (Melles-Griot) and an emission filter (HQ514/30, Nikon). To visualise HupA-mCherry-tagged nucleoids, we used a 543 nm HeNe laser (Melles-Griot) and an emission filter (HQ585/65, Nikon). Phase contrast images of cells were captured using an external setup using a CCD camera (DS-Fi2, Nikon). Size of the images was 2560 × 1920 pixels, in which a pixel corresponds to 0.049 μm. Epifluorescence images, for visualisation of DAPI-stained nucleoids, were taken by a mercury lamp excitation and a DAPI filter cube (EX 340-380, DM 400, BA 435-485, Nikon).

For fixed and live cell measurements, we placed 5 μl of culture on, respectively, 1% and 2% agarose gel pads of LB media between a microscope slide and a cover slip. Fixed cells were imaged once, while for time lapse microscopy the fluorescence images were taken once per minute for 45 minutes. In the latter, the desired temperature was kept from start to end of the session by a cooling/heating microfluidic system that provides continuous flow of deionised water at stable temperature (which does not enter in contact with the cells) into a thermal imaging chamber (CFCS2, Bioptechs, USA). Meanwhile, a peristaltic pump provided continuous flow of fresh media to the cells, at the rate of 0.3 ml min^{-1}, through the thermal chamber. In the case of cells with synthetic aggregates, we added to the media the inducers of fluorescent synthetic aggregate production in the appropriate concentrations.

Spot detection

Fluorescent 'spots' are automatically segmented inside each cell using the kernel density estimation method for detecting fluorescently labelled subcellular objects in microscope images. This method measures the local smoothness of the image and determines spot locations by designating areas with low smoothness as a fluorescent spot. The spot intensity is then corrected by subtracting the mean cell background intensity multiplied by the area of the spot from the total fluorescence intensity of the spot (Gupta *et al.*, 2014).

Spot tracking

Spot tracking was performed using a semi-automatic method. First, we perform spot segmentation in each frame using the method above. An ID number is provided to the spot (automatically and then manually adjusted if needed) to identify it in each frame. Next, we manually correct for possible errors in the detection of the location of the spot. Afterwards, a displacement vector is automatically inserted, based on the shortest distance between the locations of the spot in consecutive frames. When the cell contains more than one spot, spots locations are determined as before but making use of the ID numbers so as to not misidentify spots between consecutive frames. Displacement vectors are then placed as before, based on the ID numbers of the spots. If, at any time point of the measurements, there are any doubts on the ID of the spots in a cell, that cell is discarded from the analysis.

Nucleoid detection and segmentation

Nucleoid detection and segmentation was done in each cell (in time series it was done at each frame). The nucleoid detection is performed using the Gradient Path Labelling algorithm (Mora *et al.*, 2011). This method starts by labelling each pixel based on its gradient azimuth and propagating these labels according to its gradient paths. The reduction of labels is obtained by applying equivalences (two labels are tagged as equivalents when both belong to the same maximum). Afterwards, a segmented image is obtained with the number of labels equaling the number of nucleoids. The Levenberg-Marquardt Least-Squares optimisation algorithm (More, 1978) is then used to obtain the parameters of 3D modified Gaussian functions that, in the case of two nucleoids, is described by $F(x,y) = G_1(x,y) + G_2(x,y) + z_0$, which fits each of the detected maximums. If only one nucleoid is present, G_2 is set to zero. In general:

$$G_i(x,y) = A_i \cdot \exp\left(-\left(a_i(x-x_{0i})^2 + 2b_i(x-x_{0i})(y-y_{0i}) + c(y-y_{0i})^2\right)^{(2/d)}\right)$$

where:

$$a = \cos^2\theta/2\sigma_x{}^2 + \sin^2\theta/2\sigma_x{}^2$$

$$b = -\sin 2\theta/4\sigma_x{}^2 + \sin 2\theta/4\sigma_x{}^2$$

$$c = \sin^2\theta/2\sigma_x{}^2 + \cos^2\theta/2\sigma_x{}^2$$

These functions allow translation in the xyz axes (x_0, y_0, z_0), amplitude scaling (A), rotation (θ), width in x-plane (σ_x), width in y-plane (σ_y) and amplitude profiling between square shape, bell shape and thin shape (d). The nucleoid fitting is done using a predefined value for d of 10, which was empirically selected to allow using the value z_0 as a threshold, in order to obtain the segmented nucleoid masks.

After nucleoid detection and segmentation, principal component analysis was used to obtain the position, dimension and orientation of the nucleoid in each cell. The polar region of a cell was defined as the area between the nucleoid and the major axis extremities (Fig. S7).

Example microscope images of cells along with the results of the segmentation process are shown in Fig. S2.

Estimation of the 3-D concentration of aggregates at the cell poles

The estimation of the concentration of aggregates at the poles accounts for the measured nucleoid size and the capped cylindrical shape of the cells. Fig. S7 shows a 2-D representation of a cell with a nucleoid within.

Let x be the absolute length of the nucleoid, w be the width of the cell along the minor axis and l be the length of the cell along the major axis. Then, the volume of the bacteria equals, approximately:

$$\text{Volume} = \pi\left(\frac{w}{2}\right)^2(1-w) + \frac{4}{3}\pi\left(\frac{w}{2}\right)^3$$

To attain the volume of the midcell region, for simplicity, we assume that: $x < 1 - w$. Given this:

$$\text{Midcell volume} = \pi\left(\frac{w}{2}\right)^2 x$$

From this, one can derive the normalised fraction of midcell and poles volumes. These equal respectively:

$$\text{Normalized Fraction of midcell volume} = \frac{x/l}{1 - w/(3\times l)}$$

$$\text{Normalized Fraction of poles volume} = 1 - \frac{x/l}{1 - w/(3\times l)}$$

Note that the latter quantity is also the expected fraction of aggregates at the poles, assuming uniform intracellular distribution and accounting for the capped cylindrical shape of the cells.

To obtain the measured mean 3-D concentration of aggregate numbers at poles, we divide the mean fraction of aggregate numbers at the poles (Table 1) by the normalised volume of that region:

$$\text{Mean 3D concentration of aggregate numbers at poles} \cong \frac{\text{Mean fraction of aggregate numbers at poles}}{1 - \frac{x/l}{1 - w/(3\times l)}}$$

Results of this estimation are presented in Table 1, for each condition. The values for *x, l* and *w* are shown in Table S3.

The above definitions and formulas are applied also to cells with two nucleoids, where the midcell region is defined as the region between the outer borders of the two nucleoids. Note that these formulas apply to all temperature conditions tested, even though as temperature increases the cells become, on average, longer.

Mean square displacement of the aggregates and relative viscosity of the medium

To measure the diffusion coefficient of the aggregates, we use the Mean Squared Displacement (MSD) of the aggregates after a time lag τ:

$$MSD(\tau) = \mathrm{E}\|\mathbf{p}(t) - \mathbf{p}(t-\tau)\|^2 + \xi^2 = 2D\tau + \xi^2$$

where $\mathbf{p}(t)$ is the position of a spot at time t, E is the expectation over all spots and over all t, and ξ^2 is the measurement noise. To extract D discounting ξ^2, we use the slope of the line taken from the first two points, i.e. $D = (MSD(2) - MSD(1))/2$. As seen in Fig. S8, the MSD is approximately linear for the first few τ. That is, for all measurements, MSD(3) lies immediately beneath the line going through MSD(1) and MSD(2), justifying the assumption of approximately diffusive motion at this timescale.

From D, and assuming that the aggregates are spherical, the dynamic viscosity η of the medium in which the diffusive particle is moving is (the Stokes-Einstein equation):

$$\eta = \frac{k_B T}{6\pi r D}$$

where k_B is Boltzmann's constant and r is the particle radius. If the changes in temperature alone suffice to explain the changes in D, the relative dynamic viscosity between conditions should be approximately 1. The relative dynamic viscosity η_1/η_2 between two temperatures T_1 and T_2 with diffusion coefficients D_1 and D_2 can be quantified as:

$$\frac{\eta_1}{\eta_2} = \frac{T_1 D_2}{T_2 D_1}$$

Anisotropy distributions

From the time lapse images, we obtained their displacement vectors along the major cell axis between consecutive frames. These inform on the directionality of an aggregate between consecutive images (assessed by the sign of the displacement vector). Also, they inform on the degree of diffusion of the aggregates along the major cell axis during the intervals between consecutive images (assessed by the magnitude of the displacement vector).

As in Gupta *et al*. (2014), we extracted the displacement vectors going toward a pole and towards the cell centre, as a function of their point of origin. Next, we defined a sliding window with a width of 0.1 cell lengths and determined which displacement vectors originated within that window and their direction. We then analysed the directionality of the displacement vectors by counting the number of displacement vectors originated in the window, which were directed towards the midcell and towards the poles. Finally, we calculated the fraction of synthetic aggregates moving towards the poles in each window, as a function of the normalised distance to the cell centre. Cell growth between consecutive frames was accounted for by projecting the origin of each displacement vector into the cell space in the following frame, before calculating the magnitude and direction. The 'anisotropy curves' obtained for each condition are shown in Fig. 2.

Possible biases in the mean square displacement of aggregates due to cell growth

Escherichia coli cells grow by increasing the walls' length via incorporating new components at the midcell region (Laloux and Jacobs-Wagner, 2014). This is likely accompanied by the absorption of materials from the environment, which maintains the cytoplasm density nearly constant (90% of the cells in exponentially growing populations exhibit densities differing less than 0.75% from the mean) (Martinez-Sala *et al.*, 1981). Consequently, the process of cell walls growth is likely heterogeneous. However, this does not affect our calculations of MSD, since, during growth, the increase in cytoplasm volume is approximately homogenous along the major cell axis, as extracellular materials (e.g. water) do not enter the cell through a particular cell region. Given this and that the position of aggregates is not determined by the cell walls, as they float in the cytoplasm, our calculation of aggregate displacement vectors between consecutive frames does not need to be compensated for the heterogeneity of the cell walls growth process.

In any case, we can assume the extreme scenario of new materials entering the cell solely at the midcell region (which can bias our estimations of displacement vectors in cells with fast growth relative to aggregate movement), and estimate the upper bound of this bias. Let $x(t)$ be the un-normalised position of an aggregate along the major cell axis at time t and let the cell length at time t be $l(t)$. In the extreme case, the position of the aggregate at time $t+\tau$ is:

$$x(t+\tau) = x(t) + N(0, D) + \frac{l_{t+\tau} - l_t}{2}$$

where N is a Gaussian distribution with a mean of 0 and a variance of D. The displacement vectors are calculated as:

$$x(t+\tau) - \frac{l_{t+\tau}}{l_t} x(t) = (l_{t+\tau} - l_t)\left(\frac{1}{2} - \frac{x(t)}{l_t}\right) + N(0, D)$$

Given the above formula, and assuming the 'worst case' scenario of all aggregates being located at midcell, the bias in the measurement of D equals:

$$\Gamma = \left(\frac{1}{2}(l_{t+\tau} - l_t)\right)^2$$

We obtained this quantity for each temperature condition and compared with the measured diffusion coefficient, D. Results in Table 3 show that even in this extreme case, the values of D are much larger than those of Γ, which can thus be ignored.

Acknowledgements

Work supported by Academy of Finland (257603, ASR), Portuguese Foundation for Science and Technology (PTDC/BBB-MET/1084/2012, JMF and ASR), Jenny and Antti Wihuri Foundation (AH), TUT President's grant (JLP and JM) and Finnish Cultural Foundation (AG). The funders had no role in study design, data collection and analysis, decision to publish, or preparation of the manuscript.

Conflict of interests

The authors declare that they have no competing interests.

References

Allen, S.P., Polazzi, J.O., Gierse, J.K., and Easton, A.M. (1992) Two novel heat shock genes encoding proteins produced in response to heterologous protein expression in *Escherichia coli*. *J Bacteriol* **174:** 6938–6947.

Azam, T.A., Iwata, A., Nishimura, A., and Ueda, S. (1999) Growth phase-dependent variation in protein composition of the *Escherichia coli* nucleoid. *J Bacteriol* **181:** 6361–6370.

Bednarska, N.G., Schymkowitz, J., Rousseau, F., and Van Eldere, J. (2013) Protein aggregation in bacteria: the thin boundary between functionality and toxicity. *Microbiology* **159:** 1795–1806.

van den Bogaart, G., Hermans, N., Krasnikov, V., and Poolman, B. (2007) Protein mobility and diffusive barriers in *Escherichia coli*: consequences of osmotic stress. *Mol Microbiol* **64:** 858–871.

Chazotte, B. (2011) Labeling nuclear DNA using DAPI. *Cold Spring Harb Protoc* **1:** pdb prot5556.

Cherstvy, A., and Metzler, R. (2015) Ergodicity breaking and particle spreading in noisy heterogeneous diffusion processes. *J Chem Phys* **142:** 144105.

Chowdhury, S., Kandhavelu, M., Yli-harja, O., and Ribeiro, A.S. (2013) Cell segmentation by multi-resolution analysis and maximum likelihood estimation (MAMLE). *BMC Bioinformatics* **14:** 1–13.

Claret, L., and Rouviere-Yaniv, J. (1997) Variation in HU composition during growth of *Escherichia coli*: the heterodimer is required for long term survival. *J Mol Biol* **273:** 93–104.

Clegg, R.J., Dyson, R.J., and Kreft, J.-U. (2014) Repair rather than segregation of damage is the optimal unicellular aging strategy. *BMC Biol* **12:** 52.

Coquel, A.-S., Jacob, J.-P., Primet, M., Demarez, A., Dimiccoli, M., Julou, T., *et al*. (2013) Localization of protein aggregation in *Escherichia coli* is governed by diffusion and nucleoid macromolecular crowding effect. *PLoS Comput Biol* **9:** e1003038.

Cornejo, E., Abreu, N., and Komeili, A. (2014) Compartmentalization and organelle formation in bacteria. *Curr Opin Cell Biol* **26:** 132–138.

Deuerling, E., Schulze-Specking, A., Tomoyasu, T., Mogk, A., and Bukau, B. (1999) Trigger factor and DnaK cooperate in folding of newly synthesized proteins. *Nature* **400:** 693–696.

Fisher, J.K., Bourniquel, A., Witz, G., Weiner, B., Prentiss, M., and Kleckner, N. (2013) Four-dimensional imaging of *E. coli* nucleoid organization and dynamics in living cells. *Cell* **153:** 882–895.

Fusco, D., Accornero, N., Lavoie, B., Shenoy, S.M., Blanchard, J.M., Singer, R.H., and Bertrand, E. (2003) Single mRNA molecules demonstrate probabilistic movement in living mammalian cells. *Curr Biol* **13:** 161–167.

Goldberg, A. (1972) Degradation of abnormal proteins in *Escherichia coli*. *Proc Natl Acad Sci USA* **69:** 422–426.

Goldberg, A.L. (2003) Protein degradation and protection against misfolded or damaged proteins. *Nature* **426:** 895–899.

Golding, I., Paulsson, J., Zawilski, S.M., and Cox, E.C. (2005) Real-time kinetics of gene activity in individual bacteria. *Cell* **123:** 1025–1036.

Govers, S.K., Dutré, P., and Aertsen, A. (2014) *In vivo* disassembly and reassembly of protein aggregates in *Escherichia coli*. *J Bacteriol* **196:** 2325–2332.

Gupta, A., Lloyd-Price, J., and Ribeiro, A.S. (2014) *In silico* analysis of division times of *Escherichia coli* populations as a function of the partitioning scheme of non-functional proteins. *In Silico Biol* **12:** 9–21.

Gupta, A., Lloyd-Price, J., Neeli-Venkata, R., Oliveira, S.M.D., and Ribeiro, A.S. (2014) *In vivo* kinetics of segregation and polar retention of MS2-GFP-RNA complexes in *Escherichia coli*. *Biophys J* **106:** 1928–1937.

Gupta, A., Lloyd-Price, J., Oliveira, S.M.D., Yli-Harja, O., Muthukrishnan, A.-B., and Ribeiro, A.S. (2014) Robustness of the division symmetry in *Escherichia coli* and functional consequences of symmetry breaking. *Phys Biol* **11:** 066005.

Häkkinen, A., Muthukrishnan, A.-B., Mora, A., Fonseca, J.M., and Ribeiro, A.S. (2013) CellAging: a tool to study segregation and partitioning in division in cell lineages of *Escherichia coli*. *Bioinformatics* **29:** 1708–1709.

Häkkinen, A., Kandhavelu, M., Garasto, S., and Ribeiro, A.S. (2014) Estimation of fluorescence-tagged RNA numbers from spot intensities. *Bioinformatics* **30:** 1146–1153.

Jeon, J.-H., Barkai, E., and Metzler, R. (2013) Noisy continuous time random walks. *J Chem Phys* **139:** 121916.

Jin, D.J., Cagliero, C., and Zhou, Y.N. (2013) Role of RNA polymerase in the organization of the bacterial nucleoid. *Chem Rev* **113:** 8662–8682.

Kerfeld, C.A., Heinhorst, S., and Cannon, G.C. (2010) Bacterial microcompartments. *Annu Rev Microbiol* **64:** 391–408.

Konopka, M.C., Sochacki, K.A., Bratton, B.P., Shkel, I.A., Record, M.T., and Weisshaar, J.C. (2009) Cytoplasmic protein mobility in Osmotically stressed *Escherichia coli*. *J Bacteriol* **01:** 231–237.

Kuwada, N., Traxler, B., and Wiggins, P.A. (2015) Genome-scale quantitative characterization of bacterial protein localization dynamics throughout the cell cycle. *Mol Microbiol* **95:** 64–79.

Laloux, G., and Jacobs-Wagner, C. (2014) How do bacteria localize proteins to the cell pole? *J Cell Sci* **127:** 11–19.

Landgraf, D., Okumus, B., Chien, P., Baker, T.A., and Paulsson, J. (2012) Segregation of molecules at cell division reveals native protein localization. *Nat Methods* **9:** 480–482.

Lindner, A.B., Madden, R., Demarez, A., Stewart, E.J., and Taddei, F. (2008) Asymmetric segregation of protein aggregates is associated with cellular aging and rejuvenation. *Proc Natl Acad Sci USA* **105:** 3076–3081.

Lutz, R., and Bujard, H. (1997) Independent and tight regulation of transcriptional units in *Escherichia coli* via the LacR/O, the TetR/O and AraC/I1-I2 regulatory elements. *Nucleic Acids Res* **25:** 1203–1210.

Maisonneuve, E., Ezraty, B., and Dukan, S. (2008) Protein Aggregates: an Aging factor involved in cell death. *J Bacteriol* **190:** 6070–6075.

Martinez-Sala, E., Martin, J.A., and Vicente, M. (1981) Relationship of *Escherichia coli* density to growth rate and cell age. *J Bacteriol* **147:** 97–100.

Mika, J.T., van den Bogaart, G., Veenholf, L., Krasnikov, V., and Poolman, B. (2010) Molecular sieving properties of the cytoplasm of *Escherichia coli* and consequences of osmotic stress. *Mol Microbiol* **77:** 200–207.

Miot, M., and Betton, J.M. (2004) Protein quality control in the bacterial periplasm. *Microb Cell Fact* **3:** 4.

Mora, A.D., Vieira, P.M., Manivannan, A., and Fonseca, J.M. (2011) Automated drusen detection in retinal images using analytical modelling algorithms. *Biomed Eng Online* **10:** 1–15.

More, J.J. (1978) The Levenberg-Marquardt algorithm: implementation and theory. In *Numerical Analysis*. Watson, G.A. (ed.). Heidelberg: Springer-Verlag, pp. 105–116.

Muthukrishnan, A.-B., Kandhavelu, M., Lloyd-Price, J., Kudasov, F., Chowdhury, S., Yli-Harja, O., and Ribeiro, A.S. (2012) Dynamics of transcription driven by the tetA promoter, one event at a time, in live *Escherichia coli* cells. *Nucleic Acids Res* **40:** 8472–8483.

Parry, B.R., Surovtsev, I.V., Cabeen, M.T., O'Hern, C.S., Dufresne, E.R., and Jacobs-Wagner, C. (2014) The bacterial cytoplasm has glass-like properties and is fluidized by metabolic activity. *Cell* **156:** 1–12.

Reyes-Lamothe, R., Tran, T., Meas, D., Lee, L., Li, A.M., Sherratt, D.J., and Tolmasky, M.E. (2014) High-copy bacterial plasmids diffuse in the nucleoid-free space, replicate stochastically and are randomly partitioned at cell division. *Nucleic Acids Res* **42:** 1042–1051.

Sabate, R., de Groot, N.S., and Ventura, S. (2010) Protein folding and aggregation in bacteria. *Cell Mol Life Sci* **67:** 2695–2715.

Stewart, E.J., Madden, R., Paul, G., and Taddei, F. (2005) Aging and death in an organism that reproduces by morphologically symmetric division. *PLoS Biol* **3:** e45.

Straight, P.D., Fischbach, M.A., Walsh, C.T., Rudner, D.Z., and Kolter, R. (2007) A singular enzymatic megacomplex from Bacillus subtilis. *Proc Natl Acad Sci USA* **104:** 305–310.

Stylianidou, S., Kuwada, N.J., and Wiggins, P.A. (2014) Cytoplasmic dynamics reveals two modes of nucleoid-dependent mobility. *Biophys J* **107:** 2684–2692.

Talbot, S., Goodman, S., Bates, S., and Fishwick, C. (1999) Stockley P. Use of synthetic oligoribonucleotides to probe RNA-protein interactions in the MS2 translational operator complex. *Nucleic Acids Res* **18:** 3521–3528.

Tyedmers, J., Mogk, A., and Bukau, B. (2010) Cellular strategies for controlling protein aggregation. *Nat Rev Mol Cell Biol* **11:** 777–788.

Vecchiarelli, A.G., Mizuuchi, K., and Funnell, B.E. (2012) Surfing biological surfaces: exploiting the nucleoid for partition and transport in bacteria. *Mol Microbiol* **86:** 513–523.

Viaplana, E., Feliu, J.X., Corchero, J., and Villaverde, A. (1997) Reversible activation of a cryptic cleavage site within *E. coli* ß-galactosidase in ß-galactosidase fusion proteins. *Biochim Biophys Acta* **1343:** 221–226.

Wickner, S., Maurizi, M.R., and Gottesman, S. (1999) Post-translational quality control: folding, refolding, and degrading proteins. *Science* **286:** 1888–1893.

Willetts, N.S. (1967) Intracellular protein breakdown in non-growing cells of *Escherichia coli*. *Biochem J* **103:** 453–461.

Winkler, J., Seybert, A., König, L., Pruggnaller, S., Hasselmann, U., Sourjik, V., *et al*. (2010) Quantitative and spatio-temporal features of protein aggregation in *Escherichia coli* and consequences on protein quality control and cellular aging. *EMBO J* **29:** 910–923.

Supporting information

Additional supporting information may be found in the online version of this article at the publisher's web-site.

Supporting Information for: “Increased cytoplasm viscosity hampers aggregate polar segregation in *Escherichia coli*”

Samuel M.D. Oliveira[1], Ramakanth Neeli-Venkata[1], Nadia S.M. Goncalves[1], João A. Santinha[2], Leonardo Martins[2], Huy Tran[1], Jarno Mäkelä[1], Abhishekh Gupta[1], Marilia Barandas[2], Antti Häkkinen[1], Jason Lloyd-Price[1], José M. Fonseca[2], and Andre S. Ribeiro[1,*]

[1] Laboratory of Biosystem Dynamics, Department of Signal Processing, Tampere University of Technology, 33101 Tampere, Finland

[2] UNINOVA, Instituto de Desenvolvimento de Novas Tecnologias, Campus FCT-UNL, 2829-516 Caparica, Portugal.

[*] Corresponding author: Tel: +358408490736, Fax: +358331154989, Email: andre.ribeiro@tut.fi
Office TC336, Department of Signal Processing, Tampere University of Technology
P.O Box 553, 33101 Tampere, Finland

Supplementary Figures

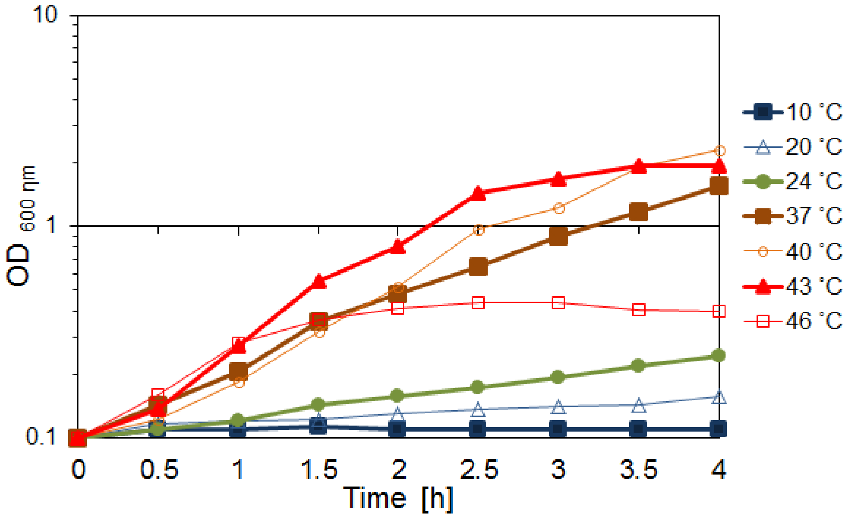

Fig. S1. Cell growth rate analysis. OD curves at 10°C, 20°C, 24°C, 37°C, 40°C, 43°C and 46°C. DH5α-PRO cells were grown in liquid LB media and the culture absorbance (OD at 600 nm) was measured every 30 minutes for 4 hours at 10 °C, 20 °C, 24 °C, 37 °C, 40 °C, 43 °C and 46 °C. The Y-axis is presented in the log scale.

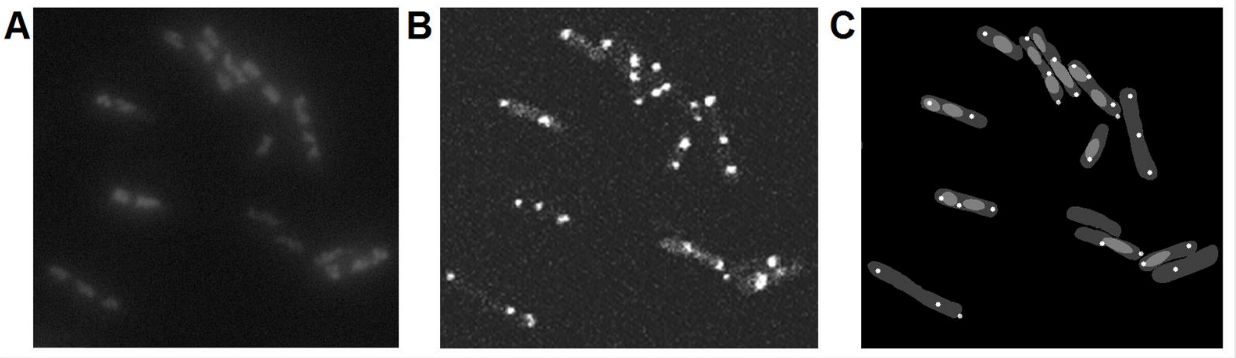

Fig. S2. Example microscopy images prior and after segmentation. (A) DAPI-stained nucleoids in cells, (B) cells with visible cytoplasm (filled with MS2-GFP proteins) along with MS2-GFP tagged RNA molecules (synthetic aggregates), visible as bright white “spots”, and (C) segmentation of the images in (A) and (B) merged into one image. Dark grey areas show segmented cells while segmented nucleoids are shown in lighter grey and synthetic aggregates are shown as small white spots.

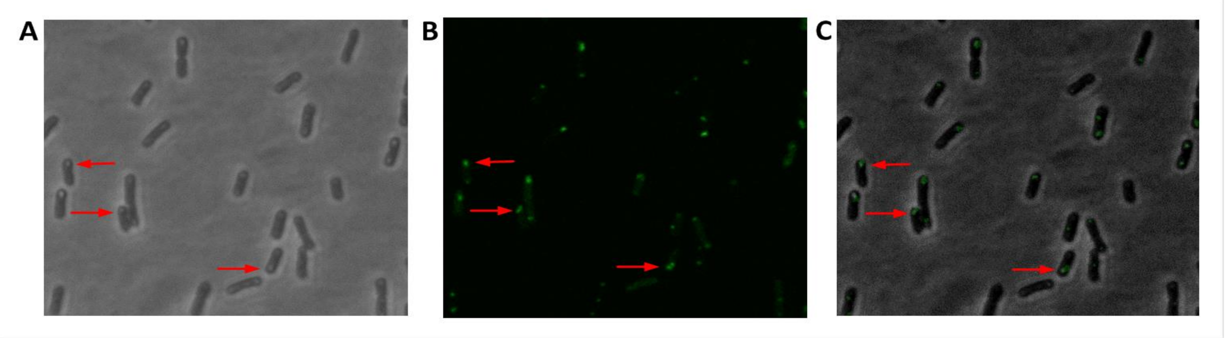

Fig. S3. Example images of cells visualized by Phase-Contrast and confocal microscopy along with merged image. (A) Example image of cells visualized by Phase-Contrast microscopy. The red arrows indicate example inclusion bodies. (B) Image by confocal microscopy of the cells with visible cytoplasm (filled with MS2-GFP proteins) along with MS2-GFP tagged RNA molecules (synthetic aggregates), visible as bright “spots”. The red arrows indicate example synthetic aggregates. (C) Images in (A) and (B) merged into one image. The red arrows indicate examples of co-localization between synthetic aggregates and inclusion bodies.

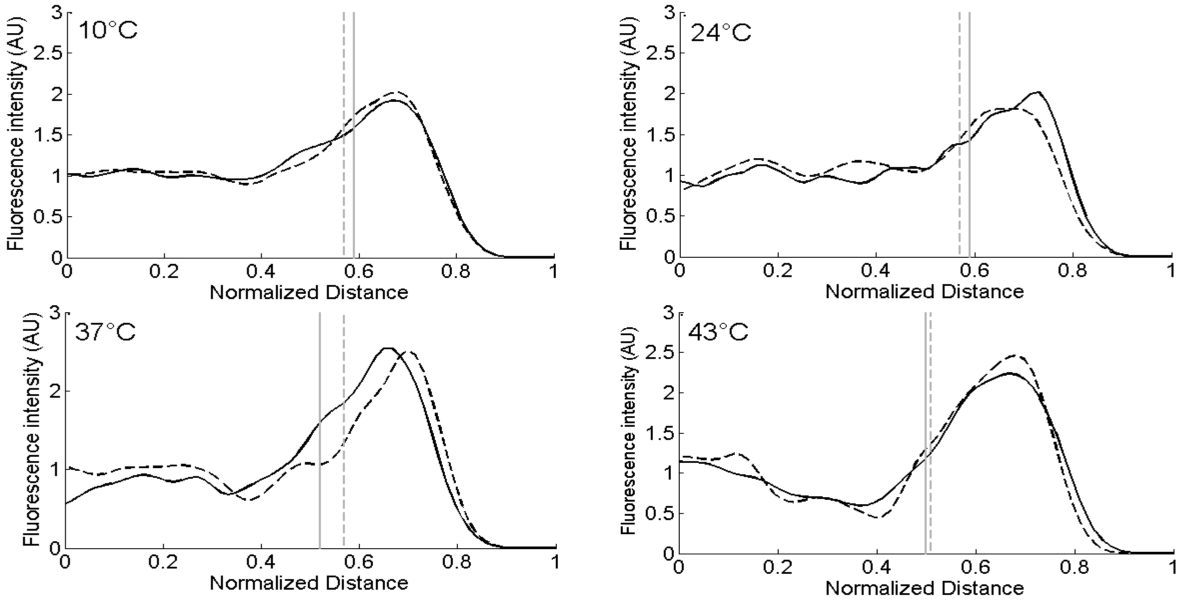

Fig. S4. Kernel density estimation of distribution of fluorescence intensity of aggregates and mean nucleoid border positioning. Kernel density estimation (KDE) of the spatial distribution of fluorescence intensity (in arbitrary units) of aggregates (black lines) and mean positioning of the nucleoid borders (vertical lines) relative to the cell center, 15 minutes (dashed lines) and 45 minutes (solid lines) after maintaining the cells at the appropriate temperature. Distances are normalized by the length of the major cell axis. All cells contain only 1 nucleoid. Measurements are from more than 300 cells per condition.

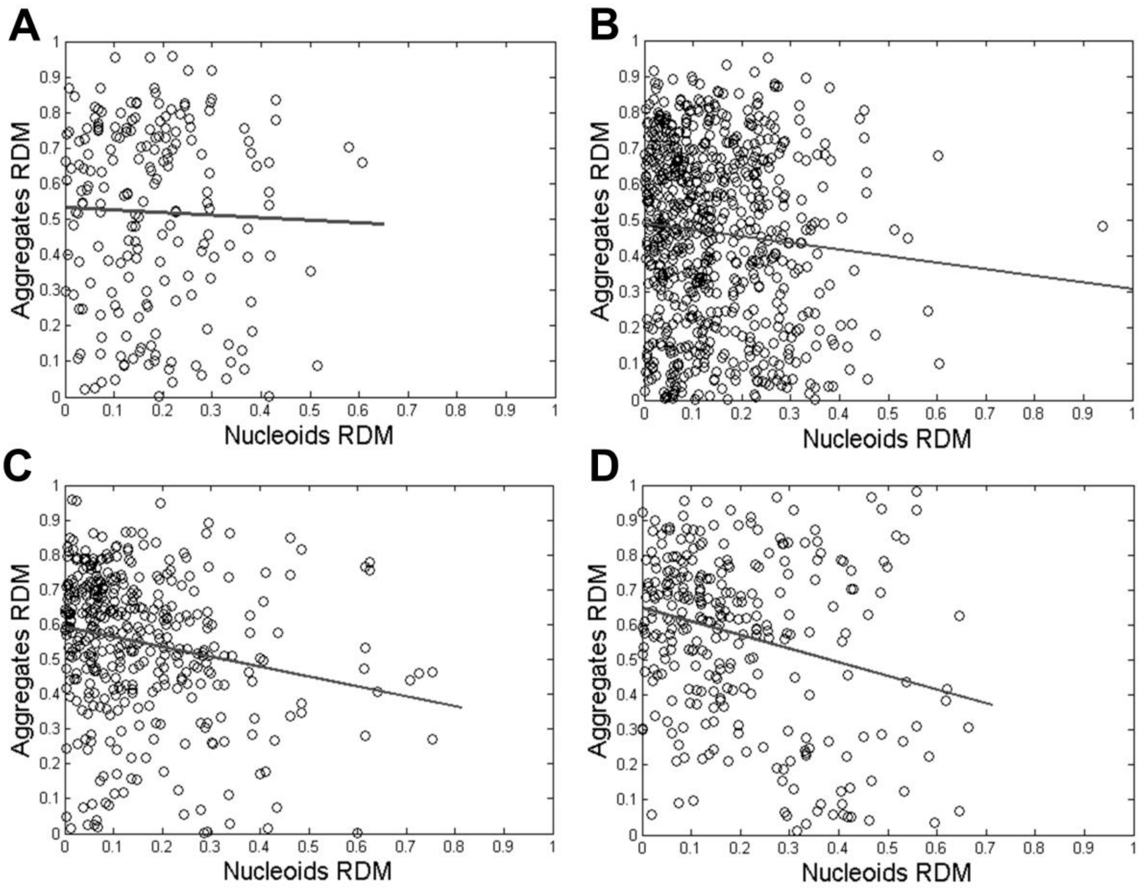

Fig. S5. Relative distance to midcell (RDM) of aggregates versus RDM of nucleoid center. RDM of individual aggregates versus RDM of the nucleoid center (along the major cell axis) measured from: (A) 195 aggregates at 10 °C, (B) 707 aggregates at 24 °C, (C) 398 aggregates at 37 °C, and (D) 288 aggregates at 43 °C. All cells contain only 1 nucleoid. The black solid line is the linear fit to the aggregates' RDM along the major cell axis as a function of the RDM of the nucleoid center. The negative inclination of the lines shows that, on average, if the nucleoid is off-centre, the aggregates will be located on the opposite side of the cell and closer to the cell center.

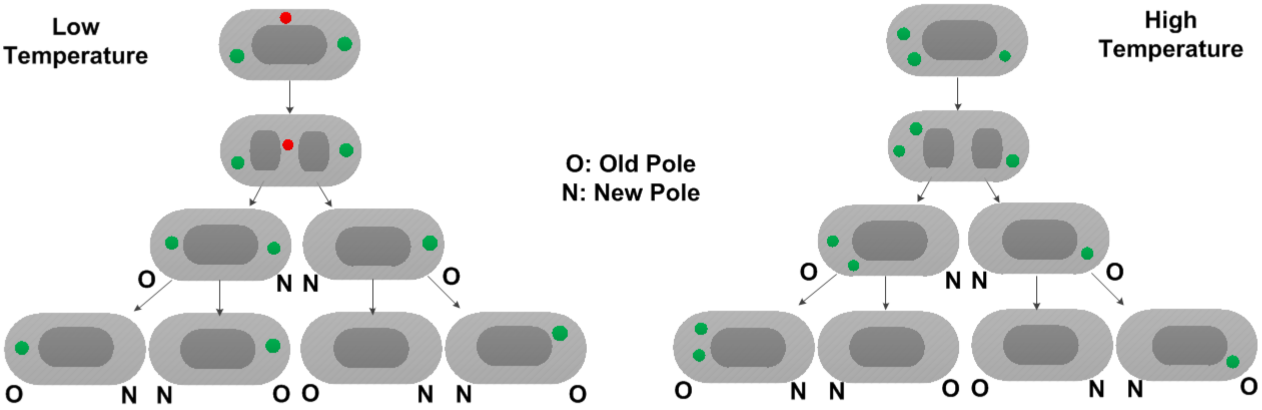

Fig. S6. Schematic representation of long-term effects of aggregates in between nucleoids prior to cell division. Cells are represented in light grey while nucleoids are represented in dark grey. (Left) Aggregates present at midcell (red balls), unlike segregated ones (green balls), will likely be located at the new poles of the cells of the next generation (with the selection of which cell following a random unbiased partitioning scheme). Consequently, only one cell of the last generation is free of aggregates. (Right) When the segregation and retention of aggregates at the poles is efficient, in the next generation all new poles of the cells will be free of aggregates, and when these cells divide, each will produce one daughter cell free from aggregates (unless new aggregates are produced in that time period). The letters 'O' and 'N' near the cells indicate whether a pole is old or new, respectively.

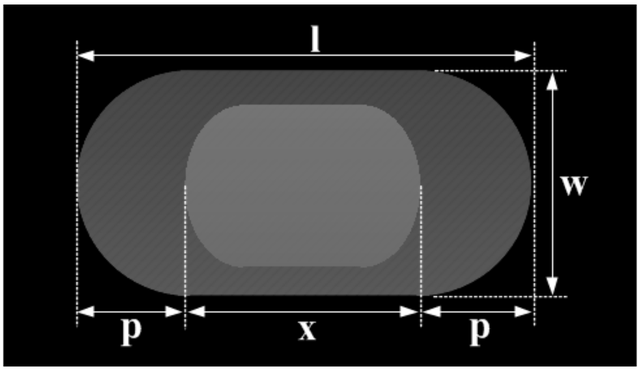

Fig. S7. Scheme of a cell with stained nucleoid. Also shown are l, the length of the cell along the major axis, w, the width of the cell along the minor axis, x, the length of the nucleoid region along the major cell axis, and p, the length of a 'polar region' of the cell.

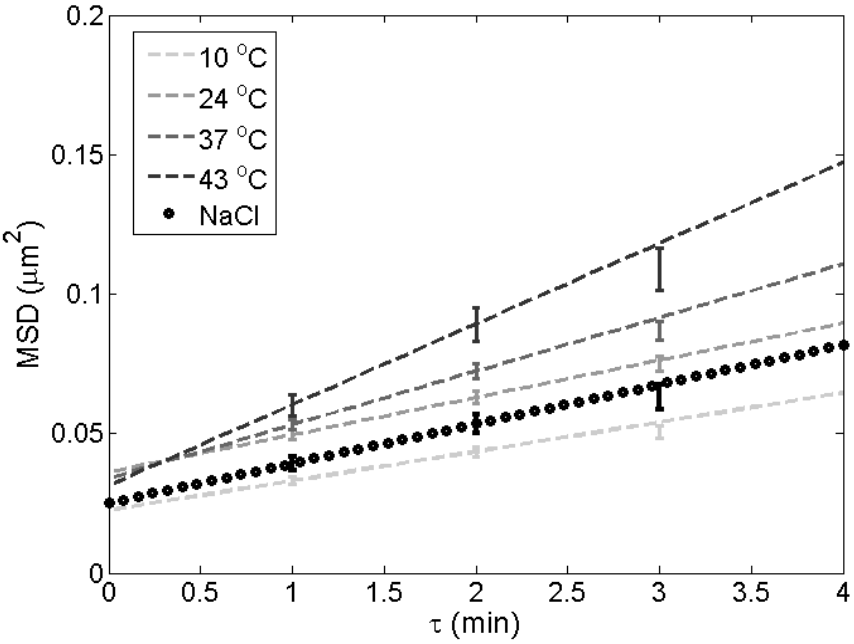

Fig. S8. Mean squared displacement of aggregates against the time lag τ. Error bars denote one standard error of the mean. The slopes of the lines represent the diffusion coefficients corresponding to the measurements presented in Table 3 in the main manuscript and in Table S5. Measurements are from 43 cells (at 10 °C), 66 cells (at 24 °C), 184 cells (at 37 °C), 41 cells (at 43 °C), and 43 plasmolyzed cells (at 37 °C and 300mM NaCl).

Supplementary Tables

Table S1. Relative nucleoid length along the major cell axis versus temperature as measured by HupA-mCherry tagging. Both mean and standard deviation (in parentheses) of each quantity are shown. Also shown is the number of cells analysed in each condition. For each condition, the mean relative length of nucleoids is shown. Visibly, as temperature is increased, this quantity decreases.

T (°C)	No. Cells	Relative Nucleoid Length (Mean and Std) in μm
24	78	0.60 (0.16)
37	53	0.57 (0.07)
43	60	0.51 (0.16)

Table S2. Relative nucleoid length along the major cell axis (mean and standard deviation), along with the fraction of IbpA-YFP aggregates at the cell poles at various temperatures, in cells with 1 nucleoid. For each condition, the mean relative length of nucleoids and the fraction of IbpA-YFP tagged aggregates at the poles are shown. Visibly, as temperature is increased, the former quantity decreases while the latter increases.

T (°C)	No. Cells	Mean (std) Relative Nucleoid Length (μm)	Mean Fraction of IbpA-YFP Aggregates at Poles
10	166	0.65 (0.07)	0.56
24	122	0.62 (0.12)	0.64
37	306	0.59 (0.10)	0.73
43	409	0.54 (0.09)	0.78

Table S3. Changes in absolute cell and nucleoid length and width along the major and minor cell axes with temperature as measured by DAPI staining. Both mean and standard deviation (in parentheses) of each quantity are shown. For each condition, width and length of cells and nucleoids within are shown. Note that, of these quantities, only the absolute cell length differs significantly with temperature.

T (°C)	Absolute Cell Length (Mean and Std) in μm	Absolute Cell Width (Mean and Std) in μm	Absolute Nucleoid Length (Mean and Std) in μm	Absolute Nucleoid Width (Mean and Std) in μm

10	2.69 (0.86)	1.05 (0.12)	1.66 (0.56)	0.66 (0.11)
24	2.40 (0.67)	1.06 (0.11)	1.33 (0.39)	0.74 (0.11)
37	2.80 (0.67)	1.06 (0.12)	1.46 (0.43)	0.67 (0.11)
43	3.77 (1.18)	1.07 (0.12)	1.76 (0.57)	0.74 (0.11)

Table S4. Mean relative 3-D concentration of synthetic aggregate numbers at the poles, in cells under osmotic stress, containing 1 nucleoid. For each condition, it is shown the number of cells studied in the microscopy measurements, along with the relative 3-D concentration of synthetic aggregate numbers at the poles at 37°C in control (LB media), plasmolyzed and adapted cells. Cells were subject to osmotic stress (300 mM NaCl) for 30 min. prior to imaging. A permutation test was applied to test for statistical differences between the concentrations between the stress conditions and the control. For p-values smaller than 0.01, the null hypothesis that the two sets of data are from the same distribution is rejected.

Condition	Cells Analyzed (No. Cells)	Mean Relative 3-D Concentration of Aggregate Numbers at Poles	P-value of a permutation test (vs. Control)
Control	300	1.86	
Plasmolyzed (NaCl)	19 (from 222)	1.07	< 0.01
Adapted (NaCl)	203 (from 222)	1.55	0.06

Table S5. *In vivo* diffusion coefficient, *D*, relative dynamic viscosity (relative to Control), η, and bias in the displacement of aggregates located at midcell, Γ, for cells under osmotic stress (plasmolyzed and adapted) along with control cells, containing 1 nucleoid. For each condition, it is shown the number of cells studied in the time-lapsed microscopy measurements, the diffusion coefficient, *D*, the relative dynamic viscosity at 37°C in control (LB media), and the bias in the displacement of aggregates located at midcell, Γ, in plasmolyzed and adapted cells as well as in control cells. Cells were subject to osmotic stress (300mM NaCl) during the 1-hour imaging procedure. A permutation test was applied to test for statistical differences between the concentrations between the stress conditions and the control. For p-values smaller than 0.01, the null hypothesis that the two sets of data are from the same distribution is rejected.

Condition	No. Cells	D (μm^{2} min^{-1})	Relative Dynamic Viscosity (η, relative to Control)	Γ (μm^{2} min^{-1})
Control	184	0.01	1	1.6 x 10^{-4}

Plasmolyzed (NaCl)	43	0.007	1.35	1.5×10^{-4}
Adapted (NaCl)	61	0.015	0.62	0.8×10^{-4}

Publication IV

R. Neeli-Venkata, S. Startceva, T. Annila, and A.S. Ribeiro, “Polar Localization of the Serine Chemoreceptor of *Escherichia coli* is Nucleoid Exclusion-Dependent”, *Biophysical Journal*, 111(11), 2512–2522, 2016.

Biophysical *Journal*
Article

Biophysical Society

Polar Localization of the Serine Chemoreceptor of *Escherichia coli* Is Nucleoid Exclusion-Dependent

Ramakanth Neeli-Venkata,[1] Sofia Startceva,[1] Teppo Annila,[1] and Andre S. Ribeiro[1,*]
[1]Laboratory of Biosystem Dynamics, Department of Signal Processing, Tampere University of Technology, Tampere, Finland

ABSTRACT We studied whether nucleoid exclusion contributes to the segregation and retention of Tsr chemoreceptor clusters at the cell poles. Using live time-lapse, single-cell microscopy measurements, we show that the single-cell spatial distributions of Tsr clusters have heterogeneities and asymmetries that are consistent with nucleoid exclusion and cannot be explained by the diffusion-and-capture mechanism supported by Tol-Pal complexes at the poles. Also, in cells subjected to ampicillin, which enhances relative nucleoid lengths, Tsr clusters locate relatively closer to the cell extremities, whereas in anucleated cells (deletion mutants for mukB), the Tsr clusters are closer to midcell. In addition, we find that the fraction of Tsr clusters at the poles is smaller in deletion mutants for Tol-Pal than in wild-type cells, although it is still larger than would be expected by chance. Also in deletion mutants, the distribution of Tsr clusters differs widely between cells with relatively small and large nucleoids, in a manner consistent with nucleoid exclusion from midcell. This comparison further showed that diffusion-and-capture by Tol-Pal complexes and nucleoid exclusion from the midcell have complementary effects. Subsequently, we subjected deletion mutants to suboptimal temperatures that are known to enhance cytoplasm viscosity, which hampers nucleoid exclusion effects. As the temperature was lowered, the fraction of clusters at the poles decreased linearly. Finally, a stochastic model including nucleoid exclusion at midcell and diffusion-and-capture due to Tol-Pal at the poles is shown to exhibit a cluster dynamics that is consistent with the empirical data. We conclude that nucleoid exclusion also contributes to the preference of Tsr clusters for polar localization.

INTRODUCTION

Escherichia coli chemoreceptor proteins perform multiple tasks, including assessing chemical gradients (1), thermosensing (2), and aerotaxis (3). These proteins are organized in trimer-of- dimers that form large clusters whose structure is further stabilized by the adaptor protein CheW and the histidine kinase CheA (1,4,5). The purpose of clustering is likely signal-processing enhancement of the receptor system (6–9). The clustering process is robust, as receptors can assemble via their cytoplasmic domains even in the absence of some chemotaxis-associated proteins, such as CheW (10). Most studies agree that cluster formation occurs via an energy-free, self-assembly process known as stochastic nucleation (11–14).

Chemotaxis-associated clusters preferentially locate at the cell poles (15–17), but the means by which this occurs remain unclear, given the lack of evidence for active transport mechanisms. Studies have suggested various mechanisms by which this may occur. For example, it has been suggested that the clusters first form at midcell and then attach to the cell membranes, and are dragged to the poles by cell growth after a few rounds of cell division (11,12). It has also been suggested that the clusters diffuse freely in the cell membranes and that polar accumulation is caused by the curved shape of the poles and the ability of the clusters to match this curvature (7,18).

Recent studies suggested that instead a diffusion-and-capture process (19) is responsible for the spatial distribution of this and several other polar proteins (20–23). One study in particular (24) identified the trans-envelope Tol-Pal complex, a widely conserved component of the cell envelope of Gram-negative bacteria (25), as being responsible for capturing the clusters at the poles, since in deletion mutants for Tol-Pal this process is impaired. The existence of a diffusion-and-capture mechanism is further supported by the observation that a fairly constant fraction (~7%) of Tsr proteins exhibit free diffusion over the entire cell surface at any given time (26).

Tsr, one of the methyl-accepting chemoreceptor proteins of the *E. coli* chemotaxis system (2), is a serine chemotaxis receptor protein that preferentially forms heterotrimeric membrane complexes at the poles. The mobility of Tsr

Submitted June 6, 2016, and accepted for publication October 19, 2016.

*Correspondence: andre.ribeiro@tut.fi

Editor: Zemer Gitai.

http://dx.doi.org/10.1016/j.bpj.2016.10.024

labeled with fluorescent Venus proteins was recently investigated and found to be similar to that of the natural system (26). These proteins can diffuse over the entire cell surface but usually exhibit restricted diffusion, particularly at the poles, where they appear to move freely except for being restricted to the same pole for several generations (12). When the cytoskeletal protein MreB is disrupted and the cell becomes rounded, Tsr clusters at the poles tend to fragment and the fraction of mobile Tsr increases (26). This suggests that, aside from the diffusion-and-capture process made possible by Tol-Pal complexes (24), one or more additional mechanisms may contribute to the preference of the chemoreceptor clusters for a polar location.

In *E. coli*, the nucleoid is usually at midcell and confined within the cell cylinder. Among other components, it contains most of the DNA, RNA, and nucleoid-associated proteins of the cell. Major nucleoid-associated proteins include H-NS, HU, Fis, IHF, and StpA. The dimeric histone-like protein HU in particular is highly abundant and involved in DNA compaction, and thus can be used to assess the nucleoid's morphology and positioning in vivo when fused with fluorescent proteins such as mCherry (27). The partitioning of replicated nucleoids in cell division involves the structural maintenance of chromosome complex MukBEF (28). The deletion of mukB causes a temperature-sensitive lethal phenotype that fails to partition the chromosome, resulting in the formation of anucleate cells.

Recent studies have reported that in addition to Tsr clusters, other types of large biomolecules in *E. coli* are segregated to and then retained at the poles. This is due to an energy-free volume exclusion caused by the presence of the nucleoid at midcell (29,30) that affects plasmids (31,32) and other large complexes (33,34). A possible contribution of nucleoid exclusion to the distribution of chemoreceptor clusters associated with chemotaxis has not yet been considered.

Here, we explored whether nucleoid exclusion contributes to the segregation and retention of Tsr chemoreceptor clusters at the cell poles. In addition, we evaluated the contribution from other, previously proposed mechanisms, namely, Tol-Pal diffusion-and-capture and dragging by cell elongation. We used *E. coli* cells expressing Tsr-Venus and harboring a plasmid that expresses the nucleoid-tagging protein HupA-mCherry, and performed live single-cell studies of the spatiotemporal distribution of Tsr clusters and nucleoids. The Venus protein is a YFP variant that is derived from GFP and has a fast maturation time (35) that allows real-time imaging by fluorescence microscopy. The tagging of Tsr with Venus does not affect its spatial distribution and is not toxic to cells (35). Measurements were conducted in wild-type (WT) and isogenic mutant cells lacking the Tol-Pal complex (Δ*tolpal*). We further studied the Tsr cluster spatial distribution in anucleoid cells (Δ*mukB*). Finally, we performed stochastic simulations of dynamic models and compared the long-term behaviors of the clusters, as indicated by in silico and in vivo data, to assess whether the proposed volume-exclusion mechanism could explain the empirical observations.

MATERIALS AND METHODS

Chemicals

For routine cultures, M9-glucose media components, isopropyl β-D-1-thiogalactopyranoside (IPTG), 4′,6-diamidino-2-phenylindole (DAPI), formaldehyde, agarose for microscopic slide gel preparation, and antibiotics were purchased from Sigma-Aldrich (St. Louis, MO). Amino acids and vitamins were purchased from GIBCO/BRL (Grand Island, NY). SYTOX Orange and a Live/Dead BacLight Viability Kit (L7007) were purchased from Thermo Fisher Scientific/Molecular Probes (Waltham, MA).

Strains and plasmids

We used *E. coli* strain (SX4) expressing the chimeric gene *tsr-venus* under the control of the P_{lac} promoter, which is incorporated into the chromosome (35) (a kind gift from Sunny Xie, Harvard University). We transformed this strain with a pBR322 derivative plasmid expressing HupA-mCherry (a nucleoid-tagging protein) under the control of a constitutive promoter with ampicillin resistance (36) (a kind gift from Nancy Kleckner, Harvard University). The host *E. coli* K-12 strain has a genotype of (*lacI*p4000 *hsd*R514 DE(*ara*BAD)567 DE(*rha*BAD)568 rph-1).

We also used *E. coli* strain MG1655 and its isogenic derivative strain lacking Tol-Pal components (MG1655 Δ*tolpal*) (27) (a kind gift from Douglas Weibel, University of Wisconsin-Madison). These were transformed with a pBR322 derivative plasmid expressing the gene *tsr-venus* under the control of the P_{lac} promoter. The *E. coli* strain MG1655 has a genotype of (F^- λ^- rph-1). The SX4 and MG1655 strains served as the WT for our studies.

The mutant strain AZ5372 lacking mukB (*trpC9941* Δ*mukB*::*kan*), referred to as Δ*mukB*, was obtained from the Keio single-gene knockout collection (36) and transformed with a pBR322 derivative plasmid expressing the gene *tsr-venus* under the control of the P_{lac} promoter.

All overnight liquid cultures were grown in M9-glucose medium for 14 h at 37°C with shaking (250 rpm), except for Δ*mukB*, which was incubated at 22°C. The M9-glucose (0.4%) medium was supplemented with amino acids and vitamins, along with kanamycin (35 μg mL^{-1}) and ampicillin (50 μg mL^{-1}).

We subsequently made subcultures by diluting the overnight culture into fresh M9 glucose medium containing the appropriate antibiotics. We opted for M9-glucose medium to maintain a well-defined cell culture condition and achieve low cellular autofluorescence. In addition, previous studies have shown that cells have a higher propensity to form arrays in minimal media than in richer media such as Terrific broth and Luria broth, suggesting that the arrays' functionality is enhanced (18).

Induction of production of Tsr-Venus

Strains from overnight cultures were diluted into fresh media with the appropriate antibiotics (as described above) at an initial OD_{600} of 0.02 and grown until they reached an OD_{600} of ~0.3, at 37°C with shaking (250 rpm). In the SX4 strain, Tsr-Venus production, controlled by P_{lac}, was induced by IPTG at the appropriate concentrations. In the MG1655 strain and its derivative, containing the plasmid expressing Tsr-Venus, induction was performed with final concentrations of 50 μM mL^{-1} IPTG for 1 h at 37°C. In both cases, cells were then left in the shaker to grow until they reached an OD_{600} of ~0.45–0.5 before microscopy was performed. In addition to microscopy, we also measured Tsr-Venus expression as a function of induction with a microplate fluorometer at 37°C (Fig. S3 in the Supporting Material).

Nucleoid visualization by HupA-mCherry tagging

To observe Tsr-Venus clusters and nucleoids in individual cells simultaneously over time, we used cells containing the plasmid from which HupA-mCherry is constitutively expressed (SX4-HupA-mCherry strain). These were induced with 200 μM mL^{-1} IPTG for 1 h at 37°C and then centrifuged, and the supernatant discarded. Then, 4 μL of cells was placed on a 1% agarose gel pad prepared in M9-glucose medium for image acquisition.

Nucleoid visualization by DAPI and SYTOX Orange staining

DAPI stains nucleoids specifically with little or no cytoplasmic labeling. Cells at an OD$_{600}$ of ~0.3 were induced with 200 μM mL^{-1} IPTG (SX4 strain) or 50 μM mL^{-1} IPTG (MG1655 and MG1655 Δ*tolpal* strain) and left in the shaker incubator at 37°C until they reached an OD$_{600}$ of ~0.5. The cells were then fixed with 3.7% formaldehyde in phosphate-buffered saline (PBS) for 30 min and washed with PBS to remove excess formaldehyde. The pellets were suspended in PBS, and DAPI (2 μg mL^{-1}) was added to this suspension (37). After incubation for 20 min in the dark, the cells were centrifuged and washed twice with PBS to remove excess DAPI. The cells were then resuspended in PBS and 8 μL of these samples was placed on a 1% agarose gel pad prepared in M9-glucose medium for microscopy observation.

To observe the nucleoids of Δ*mukB* cells, we used SYTOX Orange dye instead of DAPI, since we found that DAPI staining does not allow one to distinguish easily between cells with and without nucleoid, due to strong background autofluorescence and image blurring (38). Δ*mukB* cells containing the plasmid expressing Tsr-Venus were grown overnight in Luria broth medium at 22°C. Subsequently, they were subcultured and allowed to grow exponentially in M9-glucose medium at 22°C, followed by activation of Tsr-Venus (to a final concentration of 50 μM mL^{-1} IPTG) for 1 h at 37°C. To this culture, a SYTOX Orange solution (50μM stock concentration) was added to a final concentration of 500 nM and incubated for 10 min in the dark (38). The cells were then centrifuged twice and resuspended in fresh M9-glucose medium, and 8 μL of these samples was placed on a 1% agarose gel pad prepared in M9-glucose medium along with inducer IPTG for microscopy observation in a temperature-controlled chamber (see the "Microscopy" section below).

Measurements with ampicillin

For measurements with ampicillin, we used SX4 cells (35). Cells were grown as described in the previous section. Next, the cells were induced with IPTG (200 μM) to activate Tsr-Venus expression. Simultaneously, we introduced freshly prepared ampicillin (100 μg mL^{-1}) in the media and left the cells in the incubator for 30 min. The nucleoid was observed by DAPI staining.

To assess the proportion of viable cells after ampicillin treatment, we performed live/dead staining according to the protocol for the Live/Dead BacLight Viability Kit. Equal volumes of SYTO 9 (reagent A) and propidium iodide (PI; reagent B) from the kit were mixed and added to the cells suspended in 0.85% (w/v) NaCl (3 μL mL^{-1}of cells). After mixing and incubation at room temperature in the dark for 15 min, the cells were visualized by epifluorescence microscopy with the standard fluorescent long-pass filter set for simultaneous visualization of live and dead cells. The green fluorescent dye SYTO 9 permeates both intact and damaged cell membranes, whereas red PI only enters cells with significant membrane damage (39). Thus, upon ampicillin treatment, cells with damaged membranes take up the red PI dye, which saturates the green SYTO 9 dye that is taken up by all cells. The presence of red color is therefore indicative of cell death, and green indicates live cells.

Measurements at suboptimal temperatures

Tol-Pal deletion mutant cells (MG1655 Δ*tolpal*) with a Tsr-Venus-expressing plasmid were grown as described above. Tsr-Venus expression was induced by adding 50 μM mL^{-1} of IPTG to the culture. The cells were then left in the incubator at the appropriate temperatures (10°C, 15°C, and 24°C) for 1 h and fixed with 3.7% formaldehyde, followed by DAPI staining and microscopy image acquisition.

Microscopy

We performed single-time-point imaging of cells with Tsr-Venus and DAPI (or) SYTOX Orange-stained nucleoids (SX4, MG1655, and MG1655 Δ*tolpal* and Δ*mukB* strains), and time-lapse imaging of cells with Tsr-Venus and HupA-mCherry-tagged nucleoids (SX4-HupA-mCherry strain). With both imaging methods, phase-contrast images were acquired for cell segmentation and, in time series, for lineage construction.

In single-time-point microscopy, Tsr-Venus was induced by adding 200 μM mL^{-1} IPTG (SX4 strain) or 50 μM mL^{-1} IPTG (MG1655, MG1655 Δ*tolpal* and Δ*mukB* strains) to the liquid culture. The cells were then left in the shaker incubator at 37°C for 1 h before image acquisition. For this purpose, 8 μL of cells was placed on a 1% agarose gel pad prepared in M9-glucose medium. Images were taken after the cells were placed under observation.

For time-lapse microscopy measurements, noninduced cells (SX4 strain) were placed on a microscope slide between a coverslip and M9-glucose agarose gel pad containing IPTG (200 μM mL^{-1}). During image acquisition, the cells were constantly supplied with fresh media containing IPTG, at the same concentration, by a microperfusion peristaltic pump (Bioptechs, Butler, PA) at 1 mL min^{-1}. Images were captured every 3 min for 1 h by confocal microscopy.

Imaging was performed using a Nikon Eclipse inverted microscope (Ti-E, Nikon, Tokyo, Japan) with a C2+ point scanning confocal system and a 100× Apo total internal reflection fluorescence objective (1.49 NA, oil). For population imaging, Tsr-Venus fluorescence was measured using a 488 nm argon laser (Melles-Griot, Rochester, NY) and HQ514/30 filter. HupA-mCherry fluorescence was measured using a 543 nm He-Ne laser (Melles-Griot) and HQ585/65 filter (Nikon). For time-lapse microscopy measurements of Tsr-Venus- and mCherry-tagged nucleoid(s) (SX4-HupA-mCherry strain), we performed highly inclined and laminated optical sheet microscopy (40) using an EMCCD camera (iXon3 897, Andor Technology, Belfast, UK) and the same lasers, along with an HQ515/30 filter and Texas Red filter (Nikon). DAPI-stained nucleoids were observed by epifluorescence microscopy using a mercury lamp with a DAPI filter (Nikon), and SYTOX Orange-stained nucleoids were observed with the EMCCD camera. SYTOX Orange was visualized using 543-nm laser excitation and a Texas Red filter (Nikon). Phase-contrast images were captured simultaneously by a CCD color camera (DS-Fi2, Nikon). Finally, for the Live/Dead BacLight viability assay, we used the CCD color camera and an LF488/LP-B-NTE filter cube (Semrock, Rochester, NY) for simultaneous visualization of SYTO 9- and PI-stained cells.

Images were acquired with the use of NIS-Elements software (Nikon). Slides were kept in a temperature-controlled chamber (FCS2, Bioptechs) at a stable temperature (37°C unless stated otherwise).

Image analysis

The image analysis procedure included cell segmentation, lineage construction, detection and characterization of fluorescent spots (Tsr clusters) and nucleoids, and characterization of the spatial distributions of clusters and nucleoids. The various steps were performed using custom-made software that integrates components from the software MAMLE (41) and CellAging (42), along with the cluster-detection method proposed in (43).

Cell segmentation was performed from phase-contrast images by MAMLE (41), followed by manual correction. Next, confocal images were aligned to the phase-contrast images as described in (44). Lineage construction, when needed, was automatically performed by CellAging (42) and then manually corrected. Detection and characterization of the size and intensity of fluorescent Tsr clusters were performed as described in (43), by defining a cluster as a connected component, with each pixel having a light intensity above a threshold. For this purpose, we assume that the background pixel intensities follow a Gaussian distribution with the same median and upper quartile as the pixels in the cell. The threshold is selected by visual inspection of the outcome. From the segmented image, the number of clusters is calculated. The area of each cluster is calculated by counting the number of pixels within.

For nucleoids, we used the same method as described above. For each cell, we determined the fluorescence levels along the major cell axis of a background-corrected cell and summed the fluorescence intensities along the minor axis. For a given cell population, we normalized the cell lengths and averaged the fluorescence intensities over all cells. This method is used for images of DAPI-stained and HupA-mCherry-tagged nucleoids. To detect the boundaries of the nucleoid in each cell, we fitted a piecewise constant probability density function with three pieces to its fluorescence intensity distribution along the major cell axis by maximum likelihood. Given the two separation points obtained from the fit, we determined the center of the nucleoid as the middle point between them.

To examine Tsr-Venus spatial distributions, we first obtained background-corrected cells by subtracting the median cell intensity from each cell pixel intensity, and summed the fluorescence intensities along the minor axis. Finally, to distinguish between midcell and poles, we defined a boundary at 0.5 (with 0 being midcell and 1 being the cell extreme) as in (24). The overall image-analysis procedure is illustrated in Fig. S1.

Stochastic modeling

We implemented stochastic models of the two mechanisms responsible for the preference for a polar localization of the Tsr clusters considered here (diffusion-and-capture by Tol-Pal complexes at the poles and nucleoid exclusion from midcell; see Fig. S2). The dynamics of the models was driven by the stochastic chemical kinetics simulator SGNS2 (45), which can implement transient compartments. We used this feature to model, among other things, the diffusion-and-capture mechanism and the volume-exclusion mechanism caused by the nucleoid. It also allowed us to obtain a spatial location for each cluster in the cell (via cell compartmentalization into blocks).

The models are two-dimensional and were used to compare the dynamics of the Tsr clusters in the presence of relatively small and large nucleoids, and in the presence and absence of Tol-Pal. A description of the models, reactions, and parameters is provided in Supporting Materials and Methods.

RESULTS

To visualize chemoreceptors in vivo, we used 1) the SX4 strain with a chimeric *tsr-venus* gene inserted into the chromosome (35), 2) the MG1655 strain (WT and deletion mutant for Tol-Pal, Δ*tolpal*), and 3) the mukB deletion mutant strain (Δ*mukB*). The latter two strains contain a low-copy plasmid coding for Tsr-Venus proteins (see Materials and Methods) under the control of a *lac* promoter. SX4 cells further contain a plasmid expressing a nucleoid-tagging protein, HupA-mCherry (Materials and Methods). We found no significant difference in the spatial distribution and kinetics of Tsr clusters between SX4 and MG1655 cells. Also, we found no significant difference in nucleoid lengths when measured by DAPI/SYTOX Orange staining and by HupA-mCherry tagging, and we saw no difference in the Tsr spatial distributions when we visualized the nucleoids with either method (Fig. S9). Further, it is worth noting that, since under normal conditions the *tsr* gene is highly expressed (46), small amounts of exogenous Tsr-Venus are expected to cause minimal perturbations to normal cell functioning. Finally, unless stated otherwise, the results refer to measurements obtained using the MG1655 strain.

Spatial distributions of nucleoids and Tsr protein clusters

First, in SX4 cells, we assessed whether the spatial distributions of Tsr clusters and nucleoids are consistent with a nucleoid-exclusion phenomenon affecting the clusters' location. To do so, from images taken 1 h after induction of Tsr-Venus expression, we compared the spatial distributions of nucleoids (DAPI stained) and Tsr clusters in cells with relatively large and relatively small nucleoids.

Based on the data from 1195 cells, we selected the 10% of cells with relatively larger and relatively smaller nucleoid(s) (along the major cell axis). Cells at the thresholds of nucleoid length were included in the analysis. Also, we did not exclude cells with two nucleoids, and thus we expected that at least some of the cells with larger nucleoid(s) would have two nucleoids. The results (Fig. 1, *thin black line*) support this expectation, as in the 10% of cells with larger nucleoid(s), the fluorescence intensity from nucleoid(s) exhibits a local minimum at midcell (as the two nucleoids are at the focal points).

As is visible in Fig. 1, the center of mass of the DAPI intensity distribution is significantly closer (in a statistical sense) to the cell center in cells with relatively small nucleoids (0.37 ± 0.01) than in those with relatively large nucleoids (0.42 ± 0.00; Kolmogorov-Smirnov (KS) test, $p <$ 0.01). Also, the Tsr protein clusters are significantly farther away from midcell in cells with relatively larger nucleoid-occupied regions (KS test, $p < 0.01$), as would be expected if nucleoid exclusion affects their location. In particular, the center of mass of the Tsr fluorescent intensities is 0.72 ± 0.02 in cells with relatively larger nucleoids and 0.66 ± 0.02 in cells with relatively smaller nucleoids. The same phenomenon was observed in cells of the MG1655 strain (data not shown).

As these results could be affected by the normalization of the cell lengths (provided, e.g., that most cells with relatively larger nucleoids also had larger absolute lengths, which can be expected), we performed the same analysis on a subset of cells that exhibited similar absolute lengths (all within 2.8 ± 0.5 μm). From this subset, we again

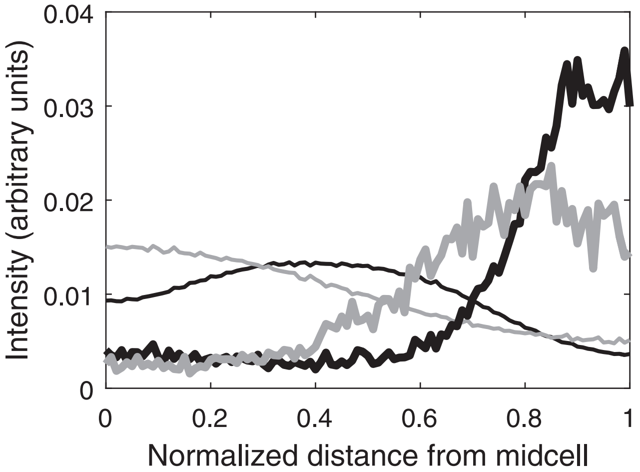

FIGURE 1 Averaged spatial distributions of fluorescence intensity (in arbitrary units (a.u.)) of Tsr-Venus and nucleoids along the major cell axis (collapsed axis, from midcell to cell extreme). The thin black line is the average nucleoid fluorescence intensity distribution from the 10% of cells with the largest relative nucleoid(s) (due to the existence of two nucleoids; 155 cells), and the thin gray line is the same distribution from the 10% of cells with the smallest relative nucleoid lengths (126 cells). The bold black and gray lines are the average spatial distributions along the major cell axis of Tsr-Venus fluorescence intensity in cells with relatively larger and smaller nucleoids, respectively.

selected the 10% of cells with larger (70 cells) and smaller (70 cells) nucleoids. We then confirmed that the cell lengths of these two subsets of cells did not differ significantly (KS test, $p = 0.73$). Finally, we performed the same test as above and found that in the cells with larger nucleoids, the Tsr clusters were closer to the cell extremities, i.e., the center of mass of the DAPI intensity distribution was significantly closer (in a statistical sense) to the cell center in cells with relatively small nucleoids (0.34 ± 0.01) than in those with relatively large nucleoids (0.42 ± 0.01; KS test, $p < 0.01$). Also, the Tsr molecules were farther away from midcell in cells with relatively larger nucleoid-occupied regions (KS test, $p \approx 0.02$), as would be expected if nucleoid exclusion affects the location of the clusters. The center of mass of the Tsr fluorescent intensities was 0.65 ± 0.02 in cells with relatively smaller nucleoids and 0.72 ± 0.02 in cells with relatively larger nucleoids.

The above results do not rule out the (unlikely) possibility that cells with larger nucleoids (e.g., close to dividing) also possess more Tol-Pal, indirectly causing the Tsr clusters to be located closer (on average) to the cell extremities. To investigate this possibility, from the data above, we selected cells with the same absolute nucleoid length (within a small range). Note that these cells differ in total cell length. If Tol-Pal levels are nucleoid-length dependent, these cells should all exhibit similar Tol-Pal levels. As such, if nucleoid exclusion is not relevant to the Tsr clusters' location, these cells should not exhibit a tangible correlation between the absolute cell length and absolute distance of Tsr clusters to the nearest cell extremity. We obtained that correlation and found it to be equal to 0.73 ($p < 0.01$), showing that in cells with similar nucleoid lengths but different cell lengths, the clusters behave differently and in accordance with a nucleoid-exclusion phenomenon.

In addition to the tests above, we also performed microscopy time-series measurements (see Materials and Methods) in which the expression of Tsr-Venus was only activated after we started observations. From these data, we assessed the location of the Tsr clusters when they first appeared. The data in Fig. S6 show that the clusters usually first appeared (i.e., became detectable) when they were already at the poles, where they tended to remain thereafter. From this, one can conclude that most clusters remain at the poles for most, if not all, of their lifetime.

Asymmetries in the spatial distributions of nucleoids and Tsr protein clusters

Finally, in search of additional evidence of nucleoid exclusion from the midcell of Tsr clusters, we assessed whether, at the single-cell level, asymmetries in the position of the nucleoid center along the major cell axis (34,47,48) are correlated with asymmetries in the Tsr clusters location. From the set of SX4 cells mentioned above (1195 cells), for each cell, we obtained the fluorescence intensity from Tsr clusters at each pole (using the definition of "pole" in Materials and Methods) and the normalized location of the nucleoid center relative to the cell center along the major axis, and calculated the Pearson correlation between these variables. As would be expected if there is nucleoid exclusion of the Tsr clusters from midcell, we found a significant ($p \ll 0.01$) correlation of -0.52 with a 95% confidence interval (CI) of $[-0.57, -0.48]$.

It is possible that this result is associated with the age of the poles, since the older pole of a cell would contain more Tol-Pal complexes and, simultaneously, off-centered nucleoids would preferentially locate closer to the older pole (although no evidence for either phenomenon has been reported so far).

To assess whether the position of the nucleoid(s), when off-centered, is biased toward the newer (or older) pole (34,49,50), we localized the nucleoid center along the major axis at each moment during the cell's lifetime (tracked from birth to division). Then, we obtained the fraction of times a nucleoid was located at the newer side of the cell. Next, we assessed whether the data collected from all cells could have resulted from an unbiased binomial distribution. We obtained a p-value of 0.148, consistent with the data being extracted from an unbiased binomial. We conclude that the asymmetries in nucleoid(s) positioning are not biased toward the newer (or older) pole, and thus differences in pole age are not a source of the anticorrelation in the positioning of the nucleoid and Tsr clusters in individual cells.

Similarly, we assessed whether the clusters' choice of pole is correlated with the pole age (Supporting Materials and Methods). We found no evidence for a tangible correlation. In addition, we also found no difference in the curvatures of the cell poles that could explain the asymmetries, at the single-cell level, in cluster numbers at each pole.

Overall, we conclude that there are heterogeneities and asymmetries in the spatial distribution of Tsr clusters that are consistent with a nucleoid-exclusion phenomenon and cannot be explained solely by a diffusion-and-capture mechanism caused by Tol-Pal complexes at the poles (24).

Spatial distribution of Tsr clusters in cells subjected to ampicillin

Next, we subjected cells (SX4 strain) to ampicillin (these cells lack ampicillin resistance; see Materials and Methods), causing enhanced elongation while halting division (51,52). We performed this test to show that when the ratio between cell and nucleoid lengths is altered by external perturbation, the spatial distribution of Tsr-Venus clusters behaves as would be expected if it is affected both by diffusion-and-capture by Tol-Pal complexes at the cell poles and by nucleoid exclusion from midcell.

Note that although SX4 cells are sensitive to ampicillin (division is halted), most appeared to remain healthy (Fig. S4). This was verified with the Live/Dead BacLight Viability Kit, which stains viable cells but not the shells of deceased cells (Materials and Methods). Also, we observed that once the drug was removed from the medium, the cells recovered and started dividing (as observed in the microscope and by spectrophotometry). As an additional precaution, during image analysis, we manually discarded (by visual inspection) cells that exhibited inclusion bodies and spheroplasts that commonly appear after ampicillin treatment, as these could affect the Tsr cluster dynamics. The remaining cells exhibited a normal rate of accumulation of Tsr clusters (as observed by inspection).

From the images of control cells and cells subjected to ampicillin, we selected cells whose length ranged from 3.5 to 4.0 μm and compared their mean relative nucleoid length (Fig. S5) and center of mass of the Tsr fluorescence intensity distribution. As shown in Table 1, we found that as the nucleoid became longer relative to the cell length, the center of mass of the distribution of Tsr-Venus moved toward the cell extremities, as would be expected from the existence of a nucleoid-exclusion phenomenon.

Effects of Tol-Pal complex deletion on the spatial distribution of Tsr

We next assessed whether, in the absence of Tol-Pal, the Tsr clusters would no longer exhibit a preference for a polar localization. For this purpose, we compared the mean fraction of Tsr fluorescence intensity at the poles in control (WT) and Δ*tolpal* cells. The results are shown in Table 2, along with the 95% CIs and the results of a test of statistical comparison between the conditions.

Finally, we performed KS tests, which showed that the mean percentage of fluorescence intensity in the cells (in both WT and Δ*tolpal* cells) was inconsistent with a normal fluorescence intensity along the major axis, which would be expected if Tsr proteins are distributed solely by means of diffusion (p-value much smaller than 0.01 for a normal distribution with a mean fluorescence at the poles equaling 50% of the total fluorescence).

As shown in Table 2, in both WT and Δ*tolpal* cells, the mean fraction of Tsr clusters at the poles is much higher than would be expected by chance (i.e., when compared with a uniform distribution along the major cell axis). This finding and the KS tests indicate that diffusion-and-capture by Tol-Pal is not the only cause of the Tsr clusters' preference for polar localization, even though the presence of Tol-Pal does significantly increase the fraction of clusters at the poles (the p-value from a two-tailed Student's t-test of statistical significance is much smaller than 0.01), as expected from previous studies (24).

Effects of Tol-Pal deletion on the spatial distribution of Tsr as a function of nucleoid length

If Tsr clusters are preferentially located at the cell poles due to a diffusion-and-capture mechanism caused by Tol-Pal complexes and a nucleoid-exclusion phenomenon, we expect that if at least one of these mechanisms is present, the Tsr clusters will still preferentially locate at the poles, although not as pronouncedly as they would if both mechanisms were active.

Given that we expect the effects of nucleoid exclusion on the Tsr clusters' spatial distribution to be gradual as a function of the nucleoid length, to study this, from the data above, we measured in each cell the relative distance of each cluster to the nearest cell extreme as well as the relative nucleoid length. Then, for WT and Δ*tolpal* cells separately, we selected the cells with relatively smaller

TABLE 1 Mean Relative Nucleoid Length and Center of Mass of the Averaged Tsr Fluorescence Distribution of the Control and Ampicillin-Treated Cells

Condition	No. of Cells	Mean Relative Nucleoid Length with 95% CI (μm)	Center of Mass of the Averaged Tsr Fluorescence Distribution with 95% CI
Control	105	0.71 ± 0.01	0.69 ± 0.02
Ampicillin	79	0.75 ± 0.02	0.75 ± 0.03

Also shown are the 95% CIs and the number of cells examined in each condition.

TABLE 2 Mean Percentage of Fluorescence Intensity at the Cell Poles for WT and Δ*tolpal* Cells

	WT	Δ*tolpal*	Student's *t*-test (WT versus Δ*tolpal*)
Number of cells	176	138	–
Mean fluorescence intensity at poles (%)	96.2	88.8	<0.01
95% CI (%)	[95.0, 97.3]	[85.3, 92.3]	–

Shown are the number of cells observed, the percentage of total fluorescence intensity located at the poles, and the corresponding 95% CIs. Also shown is the *p*-value of the Student's *t*-test between WT and Δ*tolpal*.

(≤35% of the cell length) and larger (≥65% of the cell length) nucleoids.

From the data, we first plotted the relative distance of each cluster to the nearest cell extreme versus the normalized nucleoid length in each condition (Fig. 2, A and B, for WT and deletion mutants, respectively). Visibly, at least for cells with relatively small nucleoids, the presence/absence of Tol-Pal complexes appears to be an influencing factor (as expected (24)), since in their absence the Tsr clusters are more uniformly scattered throughout the major cell axis (Fig. 2 B). This difference in the Tsr clusters' behavior due to the presence/absence of Tol-Pal complexes is less clear in cells with relatively large nucleoids (Fig. 2, A and B), in agreement with our hypothesis that nucleoid exclusion contributes to the Tsr clusters' preference for a polar localization. These results are also in line with those shown in Fig. 1.

To quantify the differences in the Tsr clusters' behavior between conditions more precisely, we calculated the degree of correlation of the Tsr clusters' relative locations along the major cell axis between all pairs of conditions (Table S2). We expected this correlation to be significant between conditions differing solely in nucleoid length (as the Tol-Pal diffusion-and-capture mechanism is present) and between cells with large nucleoids differing in the presence/absence of Tol-Pal complexes (as nucleoid exclusion is strong). Between other pairs of conditions, we expected a weaker or no correlation. The results in Table S2 confirm these expectations, showing that for the latter, the correlations become nonsignificant.

Finally, note that the degree of the correlation between WT cells with small nucleoids and Δ*tolpal* cells with large nucleoids suggests that the two mechanisms (Tol-Pal diffusion-and-capture and nucleoid exclusion) have similar effects when they act solely. Overall, the results in Table S2 further suggest that the two mechanisms have complementary effects.

In addition, this single-cell analysis of the spatial distribution of individual clusters as a function of relative nucleoid length allows us to conclude that the effects of the phenomenon of exclusion from midcell change gradually with changing nucleoid lengths, as expected (Figs. S7 and S8).

Effects of mukB deletion on the spatial distribution of Tsr clusters

Next, to further test whether nucleoid exclusion contributes to the preferential polar localization of Tsr clusters, we studied their localization in cells where the nucleoid is absent. For this purpose, we made use of mutant cells lacking the mukB protein (Δ*mukB*) (Materials and Methods). A fraction of these cells lack the nucleoid (thus becoming anucleate cells) due to failures in chromosome segregation in cell division (53). We verified this spontaneous formation of anucleate cells by visually inspecting the microscope images. In Δ*mukB* cells, although the Tsr clusters will still preferentially locate at the poles due to the presence of Tol-Pal complexes (24), their fraction at midcell is expected to increase compared with control cells (see Fig. 3, where the two cells lacking nucleoid visibly have a larger fraction of Tsr clusters at midcell than the other cells in the image).

From the images, we segmented and analyzed 302 cells, 68 of which were anucleate (as determined by visual inspection of the red channel). We compared the relative positioning along the major axis of the Tsr clusters in these cells and in WT cells (1195 control cells). The results are

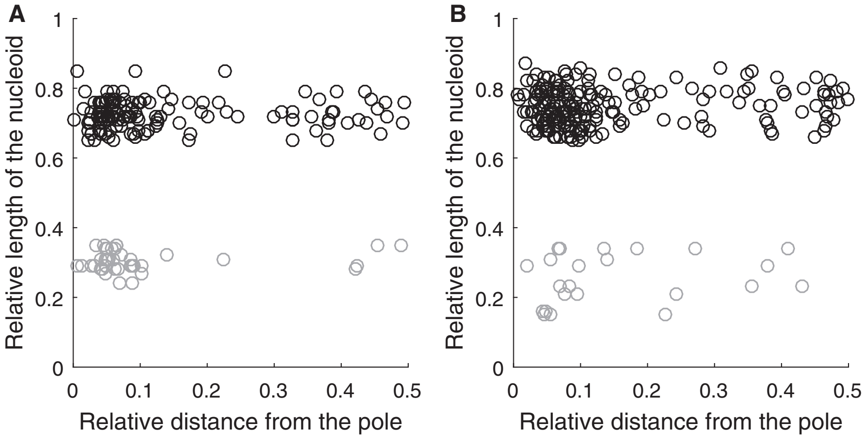

FIGURE 2 (*A*) Relative nucleoid length versus the relative distance of individual Tsr clusters from the closest cell extremity in WT cells: 133 Tsr clusters from 52 cells whose nucleoid length is ≥65% of the cell length are shown in black, and 39 Tsr clusters from 17 cells whose nucleoid length is ≤35% of the cell length are shown in gray. (*B*) Relative nucleoid length versus relative distance of individual Tsr clusters from the closest cell extremity in Δ*tolpal* cells: 198 Tsr clusters from 88 cells whose nucleoid length is ≥65% of the cell length are shown in black, and 23 Tsr clusters from eight cells whose nucleoid length is ≤ 35% of the cell length are shown in gray.

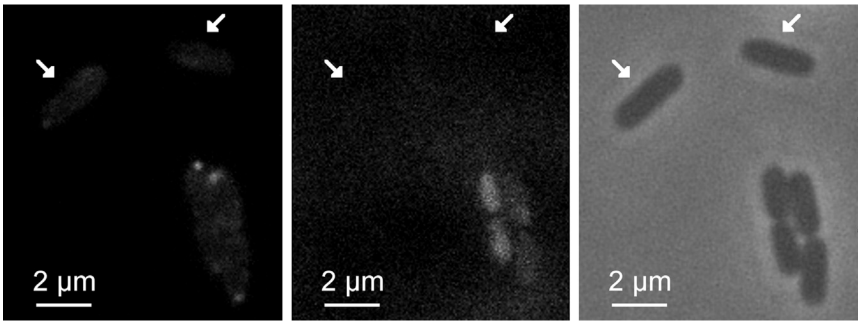

FIGURE 3 Localization of Tsr-Venus in Δ*mukB* cells at 37°C. Nucleoids were visualized by SYTOX Orange dye. The arrows indicate anucleate cells. Left: green channel showing Tsr-Venus. Middle: red channel showing nucleoids. Right: phase-contrast images showing the cell borders used for cell segmentation.

shown in Fig. 4. Whereas in Δ*mukB* cells the center of mass of the fluorescence intensity distribution of Tsr is at 0.59 ± 0.03, in control cells it is at 0.70 ± 0.01, i.e., the Tsr clusters are much closer to the cell extremities in the control cells, with the two distributions differing significantly in a statistical sense (KS test, $p << 0.01$). This supports the hypothesis that nucleoid exclusion enhances the Tsr clusters' preference for polar localization.

Effects of increased cytoplasm viscosity on the spatial distribution of Tsr clusters

We performed a final measurement to further strengthen the hypothesis that nucleoid exclusion from midcell enhances the Tsr clusters' preference for polar localization. Under reduced metabolic activity or suboptimal temperatures, the cytoplasm of *E. coli* is known to acquire glass-like features (54) that enhance its viscosity (48). This in turn greatly reduces the effects of nucleoid exclusion on the spatial distribution of large protein complexes (48).

We subjected Δ*tolpal* cells to low temperatures and assessed whether, in cells with relatively large nucleoids (i.e., occupying 65–80% of the cell length), the degree of exclusion of Tsr clusters from midcell decreases gradually as the temperature decreases. We studied Δ*tolpal* cells alone, as the effects of lower temperatures on the functionality of Tol-Pal are unknown. The results are shown in Fig. 5.

As can be seen in Fig. 5, the fraction of Tsr clusters at the poles decreases gradually with gradually decreasing temperature, as expected from the increased cytoplasm viscosity (48). As a side note, since this decrease is best fitted by a straight line (using a weighted least-square fit (55) and the Akaike information criterion (56)), we expect that in the absence of Tol-Pal, only nucleoid exclusion is involved in the segregation of clusters to the poles.

Stochastic model of nucleoid exclusion of Tsr clusters from midcell

Next, we made use of a stochastic model (for a complete description, see Supporting Materials and Methods) to test whether a nucleoid-exclusion mechanism could reproduce

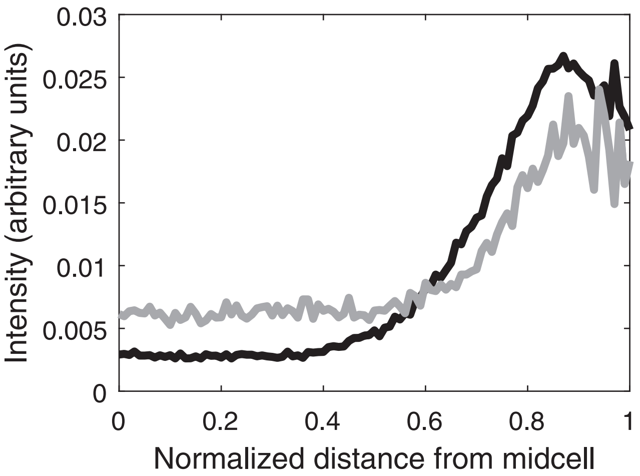

FIGURE 4 Spatial distributions of average fluorescence intensity (in a.u.) of Tsr-Venus proteins along the major cell axis (collapsed axis, from midcell to cell extremes). The black line is the fluorescence intensity distribution averaged over 1195 control cells, and the gray line is the same distribution averaged over 68 anucleate Δ*mukB* cells.

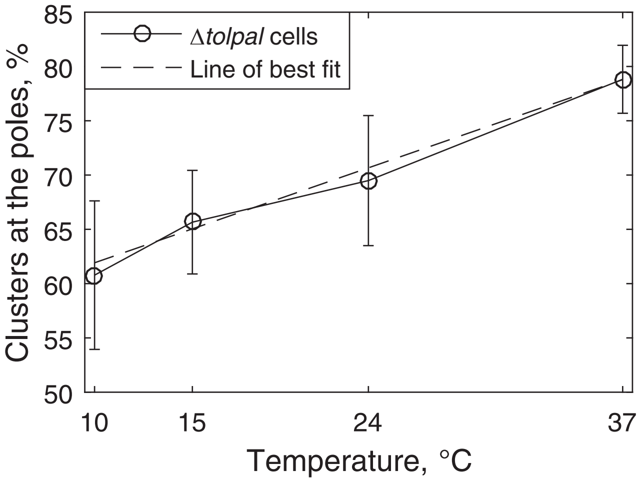

FIGURE 5 Percentage of Tsr clusters at the poles in Δ*tolpal* cells with relatively large nucleoids (occupying 65–80% of the cell length) as a function of temperature. The error bars correspond to one standard uncertainty. A line and a polynomial of second order were fitted to the data points by weighted least-square fit. The Akaike information criterion showed that the best-fitting model is a line (*dashed line*).

the empirical data. Note that in this model, the nucleoid-exclusion phenomenon acts only on Tsr proteins that are unbound to the membrane, in accordance with (26).

The model uses empirical data regarding Tsr production and degradation rates (35,57) and cell and nucleoid sizes (length and width) obtained from SX4 cells (Supporting Materials and Methods). Also, the clusters' diffusion rate and unbinding rate from Tol-Pal complexes are tuned so that the in silico spatial distributions of Tsr in cells with relatively large and relatively small nucleoids fit the empirical data (Fig. 2 A).

Using this fitted model, we first tested whether the model could reproduce the observed effect of asymmetries in nucleoid positioning on the Tsr distributions along the major cell axis at the single-cell level. We found a significant ($p \ll 0.01$) correlation of -0.65 with a 95% CI of $[-0.68, -0.62]$.

Thus, the stochastic model, assuming the existence of nucleoid exclusion and asymmetries in nucleoid positioning, reproduces the empirical observations of a strong anticorrelation between Tsr clusters and nucleoid location at the single-cell level.

Next, we assessed whether imposing differences in nucleoid length, along with assuming the presence and absence of Tol-Pal, would suffice to reproduce the observed differences in the Tsr spatial distributions observed in vivo. The results are shown in Table S3.

If we compare Tables S2 and S3, we observe a strong similarity between the model and the measurements. In short, in cases where the measurements indicate strong correlations, the model is in agreement. However, in cases where the measurements show no correlation, the model suggests much weaker correlations than in the cases where the measurements indicate strong correlations. However, the detected correlations in the simulations (Table S3, line 1, columns 2 and 3) are expected (since although smaller nucleoids should be less efficient in excluding Tsr clusters from midcell, they are not expected to be entirely ineffective). As a side note, these results also agree with the empirical data from cells subjected to ampicillin (which results in cells with relatively larger nucleoids) versus control cells.

Overall, we conclude that the dynamics of Tsr clusters of a model assuming a diffusion-and-capture mechanism caused by Tol-Pal at the poles, along with a mechanism of volume exclusion from midcell caused by the presence of the nucleoid, is in agreement with the empirical data.

DISCUSSION

Chemoreceptor proteins can assemble into large arrays, which is believed to enhance the signal-processing capabilities of the receptor system (6–9), allowing proper chemotaxis (5). In agreement with this, their ability to cluster is conserved in all known prokaryotic chemotaxis systems (58).

In *E. coli*, these clusters preferentially locate at the cell poles. This preference for polar localization may further enhance the clustering process itself and thus the signal-processing capabilities. A recent study suggested that this preference for polar localization is due to a mechanism of diffusion-and-capture made possible by Tol-Pal complexes at the cell poles (24).

Recent observations also showed that at any given time, several Tsr clusters are not in a fixed position, but rather diffuse freely within the polar region (26) (or more rarely at midcell), and that in spherical cells (when the cytoskeletal protein MreB is disrupted) the clusters are more fragmented and the fraction of freely diffusing ones increases (26). Given these observations, and the known ability of the nucleoid to exclude macromolecules such as plasmids and large protein complexes from midcell (31–34,47), we investigated the possibility that the preference of Tsr clusters for polar localization is supported by the presence of the nucleoid at midcell. For this purpose, we performed several tests while observing at the single-cell level both clusters and nucleoids.

All measurements performed here, including perturbations of the cytoplasm and cell growth, and observations in cells lacking Tol-Pal components or a nucleoid led to the same conclusion: Tsr clusters locate at the poles due to the presence of Tol-Pal at the poles along with the presence of the nucleoid at midcell. Also, these two factors have complementary effects. In addition, two observations suggest that these are likely the only two mechanisms that ensure the Tsr clusters' preference for polar localization. First, in cells lacking Tol-Pal components, the preference for polar localization decreases linearly with decreasing temperature, suggesting that only one mechanism (nucleoid exclusion) is being affected. Second, in cells lacking Tol-Pal components with relatively small nucleoids, the ability to retain Tsr clusters at the poles is much weakened.

Strikingly, a mechanism of volume exclusion from midcell is only expected to be efficient if the chemoreceptor proteins are able to form sufficiently large clusters (see, e.g., (34,59,60)). As such, we suggest that cluster formation not only enhances the signal-processing capabilities of the chemotaxis protein arrays (6–9) but also is likely essential for ensuring that the clusters are located at the cell poles. Cluster formation should greatly enhance the chances that chemoreceptor proteins will reach and remain at the poles, which is expected to enhance the efficiency of the diffusion-and-capture mechanism made possible by Tol-Pal complexes at the cell extremities.

Recent studies showed that the nucleoid plays a central role in the spatial organization of plasmids (31,32) and unwanted protein aggregates (33,34) in the cytoplasm of *E. coli*, as well as in the choice of location of the cell-division septum (61). By showing how the nucleoid contributes to the spatial organization of sensory complexes, and thus to the functional response of *E. coli* populations to various external stresses (43,62,63), our study further supports the notion that the nucleoid is critical for generating heterogeneities and asymmetries in the cytoplasm of *E. coli* that are essential for intracellular spatial organization and, combined with cell division, for cell-to-cell diversity within lineages.

SUPPORTING MATERIAL

Supporting Materials and Methods, Supporting Results, nine figures, and three tables are available at http://www.biophysj.org/biophysj/supplemental/S0006-3495(16)30951-1.

AUTHOR CONTRIBUTIONS

R.N.-V. performed experiments. S.S. and A.S.R. generated mathematical models and simulations. T.A. and S.S. performed image and data analysis. A.S.R. conceived the study. All authors contributed to the experimental design, discussion, and writing of the paper.

ACKNOWLEDGMENTS

This work was supported by the Tampere University of Technology President's Graduate Programme (R.N.-V. and S.S.), the Academy of Finland (general research grant 295027 to A.S.R.), Academy of Finland Key Project Funding (305342 to A.S.R.), and the Jane and Aatos Erkko Foundation (610536 to A.S.R.).

REFERENCES

1. Sourjik, V., and H. C. Berg. 2004. Functional interactions between receptors in bacterial chemotaxis. *Nature.* 428:437–441.
2. Lee, L., T. Mizuno, and Y. Imae. 1988. Thermosensing properties of Escherichia coli tsr mutants defective in serine chemoreception. *J. Bacteriol.* 170:4769–4774.
3. Rebbapragada, A., M. S. Johnson, …, B. L. Taylor. 1997. The Aer protein and the serine chemoreceptor Tsr independently sense intracellular energy levels and transduce oxygen, redox, and energy signals for Escherichia coli behavior. *Proc. Natl. Acad. Sci. USA.* 94:10541–10546.
4. Wadhams, G. H., and J. P. Armitage. 2004. Making sense of it all: bacterial chemotaxis. *Nat. Rev. Mol. Cell Biol.* 5:1024–1037.
5. Parkinson, J. S., P. Ames, and C. A. Studdert. 2005. Collaborative signaling by bacterial chemoreceptors. *Curr. Opin. Microbiol.* 8:116–121.
6. Kentner, D., and V. Sourjik. 2006. Spatial organization of the bacterial chemotaxis system. *Curr. Opin. Microbiol.* 9:619–624.
7. Endres, R. G. 2009. Polar chemoreceptor clustering by coupled trimers of dimers. *Biophys. J.* 96:453–463.
8. Skidmore, J. M., D. D. Ellefson, …, J. R. Maddock. 2000. Polar clustering of the chemoreceptor complex in Escherichia coli occurs in the absence of complete CheA function. *J. Bacteriol.* 182:967–973.
9. Liberman, L., H. C. Berg, and V. Sourjik. 2004. Effect of chemoreceptor modification on assembly and activity of the receptor-kinase complex in Escherichia coli. *J. Bacteriol.* 186:6643–6646.
10. Kentner, D., S. Thiem, …, V. Sourjik. 2006. Determinants of chemoreceptor cluster formation in Escherichia coli. *Mol. Microbiol.* 61:407–417.
11. Greenfield, D., A. L. McEvoy, …, J. Liphardt. 2009. Self-organization of the Escherichia coli chemotaxis network imaged with super-resolution light microscopy. *PLoS Biol.* 7:e1000137.
12. Thiem, S., D. Kentner, and V. Sourjik. 2007. Positioning of chemosensory clusters in E. coli and its relation to cell division. *EMBO J.* 26:1615–1623.
13. Thiem, S., and V. Sourjik. 2008. Stochastic assembly of chemoreceptor clusters in Escherichia coli. *Mol. Microbiol.* 68:1228–1236.
14. Wang, H., N. S. Wingreen, and R. Mukhopadhyay. 2008. Self-organized periodicity of protein clusters in growing bacteria. *Phys. Rev. Lett.* 101:218101.
15. Maddock, J. R., and L. Shapiro. 1993. Polar location of the chemoreceptor complex in the Escherichia coli cell. *Science.* 259:1717–1723.
16. Sourjik, V., and H. C. Berg. 2000. Localization of components of the chemotaxis machinery of Escherichia coli using fluorescent protein fusions. *Mol. Microbiol.* 37:740–751.
17. Zhang, P., C. M. Khursigara, …, S. Subramaniam. 2007. Direct visualization of Escherichia coli chemotaxis receptor arrays using cryo-electron microscopy. *Proc. Natl. Acad. Sci. USA.* 104:3777–3781.
18. Huang, K. C., R. Mukhopadhyay, and N. S. Wingreen. 2006. A curvature-mediated mechanism for localization of lipids to bacterial poles. *PLOS Comput. Biol.* 2:e151.
19. Rudner, D. Z., Q. Pan, and R. M. Losick. 2002. Evidence that subcellular localization of a bacterial membrane protein is achieved by diffusion and capture. *Proc. Natl. Acad. Sci. USA.* 99:8701–8706.
20. Ebersbach, G., A. Briegel, …, C. Jacobs-Wagner. 2008. A self-associating protein critical for chromosome attachment, division, and polar organization in caulobacter. *Cell.* 134:956–968.
21. Bowman, G. R., L. R. Comolli, …, L. Shapiro. 2008. A polymeric protein anchors the chromosomal origin/ParB complex at a bacterial cell pole. *Cell.* 134:945–955.
22. Ringgaard, S., K. Schirner, …, M. K. Waldor. 2011. A family of ParA-like ATPases promotes cell pole maturation by facilitating polar localization of chemotaxis proteins. *Genes Dev.* 25:1544–1555.
23. Yamaichi, Y., R. Bruckner, …, M. K. Waldor. 2012. A multidomain hub anchors the chromosome segregation and chemotactic machinery to the bacterial pole. *Genes Dev.* 26:2348–2360.
24. Santos, T. M. A., T. Y. Lin, …, D. B. Weibel. 2014. Polar localization of Escherichia coli chemoreceptors requires an intact Tol-Pal complex. *Mol. Microbiol.* 92:985–1004.
25. Sturgis, J. N. 2001. Organisation and evolution of the tol-pal gene cluster. *J. Mol. Microbiol. Biotechnol.* 3:113–122.
26. Oh, D., Y. Yu, …, K. Ritchie. 2014. Dynamics of the serine chemoreceptor in the Escherichia coli inner membrane: a high-speed single-molecule tracking study. *Biophys. J.* 106:145–153.
27. Fisher, J. K., A. Bourniquel, …, N. Kleckner. 2013. Four-dimensional imaging of E. coli nucleoid organization and dynamics in living cells. *Cell.* 153:882–895.
28. Niki, H., A. Jaffé, …, S. Hiraga. 1991. The new gene mukB codes for a 177 kd protein with coiled-coil domains involved in chromosome partitioning of E. coli. *EMBO J.* 10:183–193.
29. Winkler, J., A. Seybert, …, B. Bukau. 2010. Quantitative and spatio-temporal features of protein aggregation in Escherichia coli and consequences on protein quality control and cellular ageing. *EMBO J.* 29:910–923.
30. Coquel, A. S., J. P. Jacob, …, H. Berry. 2013. Localization of protein aggregation in Escherichia coli is governed by diffusion and nucleoid macromolecular crowding effect. *PLOS Comput. Biol.* 9:e1003038.
31. Reyes-Lamothe, R., T. Tran, …, M. E. Tolmasky. 2014. High-copy bacterial plasmids diffuse in the nucleoid-free space, replicate stochastically and are randomly partitioned at cell division. *Nucleic Acids Res.* 42:1042–1051.
32. Vecchiarelli, A. G., K. Mizuuchi, and B. E. Funnell. 2012. Surfing biological surfaces: exploiting the nucleoid for partition and transport in bacteria. *Mol. Microbiol.* 86:513–523.
33. Straight, P. D., M. A. Fischbach, …, R. Kolter. 2007. A singular enzymatic megacomplex from Bacillus subtilis. *Proc. Natl. Acad. Sci. USA.* 104:305–310.

34. Gupta, A., J. Lloyd-Price, …, A. S. Ribeiro. 2014. In vivo kinetics of segregation and polar retention of MS2-GFP-RNA complexes in Escherichia coli. *Biophys. J.* 106:1928–1937.
35. Yu, J., J. Xiao, …, X. S. Xie. 2006. Probing gene expression in live cells, one protein molecule at a time. *Science.* 311:1600–1603.
36. Baba, T., T. Ara, …, H. Mori. 2006. Construction of *Escherichia coli* K-12 in-frame, single-gene knockout mutants: the Keio collection. *Mol. Syst. Biol.* 2:2006.0008.
37. Chazotte, B. 2011. Labeling nuclear DNA using DAPI. *Cold Spring Harb. Protoc.* 2011:t5556.
38. Bakshi, S., H. Choi, …, J. C. Weisshaar. 2014. Nonperturbative imaging of nucleoid morphology in live bacterial cells during an antimicrobial peptide attack. *Appl. Environ. Microbiol.* 80:4977–4986.
39. Boulos, L., M. Prévost, …, R. Desjardins. 1999. LIVE/DEAD BacLight : application of a new rapid staining method for direct enumeration of viable and total bacteria in drinking water. *J. Microbiol. Methods.* 37:77–86.
40. Tokunaga, M., N. Imamoto, and K. Sakata-Sogawa. 2008. Highly inclined thin illumination enables clear single-molecule imaging in cells. *Nat. Methods.* 5:159–161.
41. Chowdhury, S., M. Kandhavelu, …, A. S. Ribeiro. 2013. Cell segmentation by multi-resolution analysis and maximum likelihood estimation (MAMLE). *BMC Bioinformatics.* 14 (*Suppl 10*):S8.
42. Häkkinen, A., A. B. Muthukrishnan, …, A. S. Ribeiro. 2013. CellAging: a tool to study segregation and partitioning in division in cell lineages of Escherichia coli. *Bioinformatics.* 29:1708–1709.
43. Annila, T., R. Neeli-Venkata, and A. S. Ribeiro. 2016. Robustness to sub-optimal temperatures of the processes of Tsr cluster formation and positioning in Escherichia coli. *Proc. 9th Int. Jt. Conf. Biomed. Eng. Syst. Technol*. 3:137–141.
44. Lloyd-Price, J., S. Startceva, …, A. S. Ribeiro. 2016. Dissecting the stochastic transcription initiation process in live Escherichia coli. *DNA Res.* 23:203–214.
45. Lloyd-Price, J., A. Gupta, and A. S. Ribeiro. 2012. SGNS2: a compartmentalized stochastic chemical kinetics simulator for dynamic cell populations. *Bioinformatics.* 28:3004–3005.
46. Mowbray, S. L. 1999. Bacterial chemoreceptors: recent progress in structure and function. *Mol. Cells.* 9:115–118.
47. Neeli-Venkata, R., A. Martikainen, …, A. S. Ribeiro. 2016. Robustness of the process of nucleoid exclusion of protein aggregates in Escherichia coli. *J. Bacteriol.* 198:898–906.
48. Oliveira, S. M. D., R. Neeli-Venkata, …, A. S. Ribeiro. 2016. Increased cytoplasm viscosity hampers aggregate polar segregation in Escherichia coli. *Mol. Microbiol.* 99:686–699.
49. Lindner, A. B., R. Madden, …, F. Taddei. 2008. Asymmetric segregation of protein aggregates is associated with cellular aging and rejuvenation. *Proc. Natl. Acad. Sci. USA.* 105:3076–3081.
50. Ping, L., B. Weiner, and N. Kleckner. 2008. Tsr-GFP accumulates linearly with time at cell poles, and can be used to differentiate 'old' versus 'new' poles, in Escherichia coli. *Mol. Microbiol.* 69:1427–1438.
51. Spratt, B. G. 1975. Distinct penicillin binding proteins involved in the division, elongation, and shape of Escherichia coli K12. *Proc. Natl. Acad. Sci. USA.* 72:2999–3003.
52. Yao, Z., D. Kahne, and R. Kishony. 2012. Distinct single-cell morphological dynamics under beta-lactam antibiotics. *Mol. Cell.* 48:705–712.
53. Onogi, T., M. Yamazoe, …, S. Hiraga. 2000. Null mutation of the dam or seqA gene suppresses temperature-sensitive lethality but not hypersensitivity to novobiocin of muk null mutants. *J. Bacteriol.* 182:5898–5901.
54. Parry, B. R., I. V. Surovtsev, …, C. Jacobs-Wagner. 2014. The bacterial cytoplasm has glass-like properties and is fluidized by metabolic activity. *Cell.* 156:183–194.
55. Chatterjee, S., and A. S. Hadi. 2006. Regression Analysis by Example. John Wiley & Sons, Hoboken, NJ.
56. Akaike, H. 1974. A new look at the statistical model identification. *IEEE Trans. Automat. Contr.* 19:716–723.
57. Taniguchi, Y., P. J. Choi, …, X. S. Xie. 2010. Quantifying E. coli proteome and transcriptome with single-molecule sensitivity in single cells. *Science.* 329:533–538.
58. Gestwicki, J. E., A. C. Lamanna, …, J. Adler. 2000. Evolutionary conservation of methyl-accepting chemotaxis protein location in Bacteria and Archaea. *J. Bacteriol.* 182:6499–6502.
59. Rudner, D. Z., and R. Losick. 2010. Protein subcellular localization in bacteria. *Cold Spring Harb. Perspect. Biol.* 2:a000307.
60. Thompson, S. R., G. H. Wadhams, and J. P. Armitage. 2006. The positioning of cytoplasmic protein clusters in bacteria. *Proc. Natl. Acad. Sci. USA.* 103:8209–8214.
61. Gupta, A., J. Lloyd-Price, …, A. S. Ribeiro. 2014. Robustness of the division symmetry in Escherichia coli and functional consequences of symmetry breaking. *Phys. Biol.* 11:066005.
62. Alon, U., M. G. Surette, …, S. Leibler. 1999. Robustness in bacterial chemotaxis. *Nature.* 397:168–171.
63. Oleksiuk, O., V. Jakovljevic, …, V. Sourjik. 2011. Thermal robustness of signaling in bacterial chemotaxis. *Cell.* 145:312–321.

Biophysical Journal, Volume *111*

Supplemental Information

Polar Localization of the Serine Chemoreceptor of *Escherichia coli* Is Nucleoid Exclusion-Dependent

Ramakanth Neeli-Venkata, Sofia Startceva, Teppo Annila, and Andre S. Ribeiro

Supporting Material for “Polar Localization of the Serine Chemoreceptor of *Escherichia coli* is Nucleoid Exclusion-Dependent”

Ramakanth Neeli-Venkata, Sofia Startceva, Teppo Annila, and Andre S. Ribeiro

Fluorescent microplate reading

Aside from microscopy, the fluorescence from Tsr-Venus proteins under the control of P_{lac} was also measured with a Thermo Scientific* Fluoroskan Ascent Microplate Fluorometer. Cells of the SX4 strain at OD_{600} of ~0.3 were induced with various IPTG concentrations and grown at 37 °C with shaking, until reaching an OD_{600} ~ 0.6. From this, cells were centrifuged and suspended in PBS (Phosphate Buffered Saline). 150 μl of the cells that were suspended in PBS were taken and placed on a 96 well microplate and measured for relative fluorescence levels of Venus protein with excitation (509 nm) and emission (538 nm) wavelengths (1). We performed 3 independent experiments with 3 replicates per condition.

Image analysis

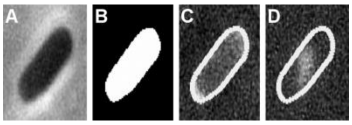

FIGURE S1 Example images used in Tsr clusters detection and nucleoid size and positioning estimation. (*A*) Phase contrast image. (*B*) Segmented cell by semi-automated segmentation from phase contrast image. (*C*) Corresponding fluorescent image for Tsr clusters detection (note the crescent shaped cluster at the lower pole) along with the detected cell border (segmented). (*D*) Example image of a cell with segmented border and fluorescence from a DAPI-stained nucleoid.

Stochastic models

Tsr is a trans-membrane protein that is not expected to be significantly affected by nucleoid exclusion when bound to the membrane. However, not all Tsr proteins are attached to the inner membrane at any given time. First, when produced, these proteins will diffuse in the cytoplasm, prior to reaching the inner membrane. Also, each Tsr is expected to be in a transient state between cytoplasmic and membrane-bound, with significant preference for the membrane-bound state. In particular, according to measurements (2), a significant fraction of Tsr proteins freely diffuse at any given moment, indicating that the rates of binding and unbinding of Tsr to the inner membrane likely do not differ by several orders of magnitude. We expect that it is when unbound from the membrane that the Tsr proteins are subject to being excluded to the poles due to the presence of the nucleoid at midcell.

We implemented a 2-dimensional (2D) model, where the cell and nucleoid are modelled as rectangles with semicircular poles, as in previous models (2–7). Cell growth and nucleoid replication are not considered. The cell membranes and nucleoid are impenetrable to the Tsr clusters and, unless stated otherwise, the nucleoid center is precisely at the cell center (Fig. S2).

A model cell is a 2-dimensional grid of square blocks, with an inner and an outer membrane. The inner membrane is one-block-wide and encloses the intracellular environment. Tsr proteins can only enter a block of the inner membrane if Tol-Pal is present ('membrane blocks' with Tol-Pal are named 'Tol-Pal blocks'). The outer membrane is a 1-block-wide layer of blocks to which Tsr proteins cannot move to. Inner blocks occupied by the nucleoid or the cytoplasm are named 'nucleoid blocks' or 'cytoplasm blocks', respectively. Model Tsr proteins can move to any passable block at a fixed rate (nucleoid, inner membrane without Tol-Pal, and outer membrane blocks are not passable). At a Tol-Pal block, the rate of passage to a neighbor passable block is smaller than at a cytoplasm block.

The Tol-Pal diffusion-and-capture mechanism is implemented in the inner membrane blocks at the poles (Fig. S2), with each block having a rate of passage that is weighted so as to represent the 'binding strength' of Tol-Pal in a 3-dimensional cell. The concentration of Tol-Pal in a block decreases linearly with the distance from the block to the cell extremity, which allows modeling the gradual decrease of Tol-Pal with the distance from the cell extremities.

We implemented a 1-step stochastic model of expression of Tsr. Nevertheless, regarding where these proteins first appear in the cell, we account for the fact that the Tsr-Venus assembly process (namely, transcription, translation, folding, and chromophore maturation) takes 7.0 ± 2.5 min (1), with most of this time being spent in the last steps. This, combined with the fast diffusion rates when not in cluster formation (8), suggests that, by the time these proteins become active, they will be virtually randomly located in any of the cytoplasm or Tol-Pal blocks. As such, the location where they first appear is randomly selected. Finally, Tsr degradation is implemented by a zero order reaction whose rate is uniform in space. Unless stated otherwise, a simulation of each model cell is conducted for 2h prior to data acquisition (as model cells are initialized without Tsr proteins).

The aspect ratio of the cell and the nucleoid size (length and width) relative to the cell size were estimated from our empirical data. The length of the model cell, L, was set to 100 blocks, which we found to provide sufficient resolution. Fig. S1 depicts model cells with large (A, C) and small (B, D) nucleoids, as well as control (A, B) and deletion mutants for Tol-Pal (C, D).

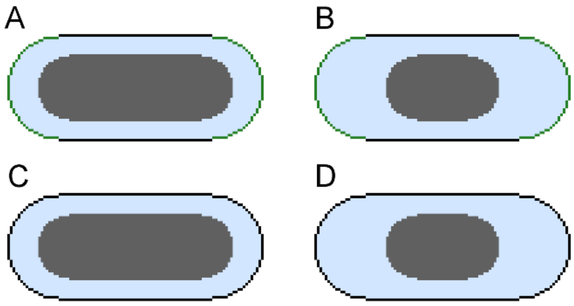

FIGURE S2. The blue area represents the cytoplasm, the grey area represents the nucleoid, the black lines represent membrane regions without Tol-Pal, and the green lines represent membrane regions with Tol-Pal (at the poles). In each model cell, the cell width is 0.42*L* and the nucleoid width is 0.26*L*. (*A*) control cell with relatively large nucleoid (0.76*L*), (*B*) Δ*tolpal* cell with relatively large nucleoid (0.76*L*), (*C*) control cell with relatively small nucleoid (0.44*L*), (*D*) Δ*tolpal* cell with relatively small nucleoid (0.44*L*). Only control cells have green lines.

Since our model is 2D, as mentioned above, we tuned the ability of each Tol-Pal block of capturing Tsr proteins as a function of its distance from the closest cell extremity, as this determines the number of Tol-Pal blocks that is expected to be at that distance in a three-dimensional (3D) model. For this, we:

1. Assume a 3D cell model, consisting of a cylinder of length 0.58*L* and radius 0.21*L* representing midcell and of two hemispheres of radius 0.21*L* each (representing the poles). Tol-Pal blocks are located along the cell inner membrane at the cell poles.

2. Split the cell into L slices along the major axis, each slice being 1 block wide.

3. Convert the 3D model into a 2D model, by setting in the 2D model, at each slice, the ability of Tol-Pal block(s) of capturing Tsr clusters as a function of the amount of Tol-Pal blocks in the corresponding slice in the 3D model (Table S1).

Supplementary Table S1 lists all reactions and events in model cells. The notation of the cell blocks is the following: c_{cyto} is a cytoplasm block, c_{TP} is a Tol-Pal block, $c_{passable}$ is a passable block (cytoplasm and Tol-Pal blocks), and $c_{neighbour}$ is an allowed destination for a moving Tsr protein (a passable block in the 4-neighbourhood of the block the protein is presently located in). A Tsr protein located in block c is denoted '$Tsr.c$'.

Reaction/event	**Parameter**	**Description and references**
$\varnothing \xrightarrow{k_{tsr}} Tsr.c_{passable}$	$k_{tsr} = \frac{1.4}{3 \cdot N_{passable}}$ sec^{-1}	Tsr production. The rate of Tsr production in each $c_{passable}$, is: $k_{tsr} = \frac{n_{burst}}{\tau_{mRNA} \cdot N_{passable}}$, with the average lifetime of mRNA, τ_{mRNA}, and the average number of Tsr proteins produced per burst, n_{burst}, being estimated from (1). $N_{passable}$ is the number of $c_{passable}$ blocks in the cell.
$Tsr.c_{passable} \xrightarrow{d_{tsr}} \varnothing$	$d_{tsr} = \frac{1}{1800}$ sec^{-1}	Tsr degradation reaction in each passable block (9).
$Tsr.c_{cyto} \xrightarrow{v_{cyto}} Tsr.c_{neighbour}$	$v_{cyto} = 1$ blocks/sec	Tsr motion reactions. Velocities v_{cyto} and v_{TP} were fit so that the spatial distributions of Tsr proteins for large and small nucleoids (after 2h of simulations) match the data from control cells. n_i is the number of Tol-Pal blocks in slice *i* of the 2D model, c_i is the circumference of the corresponding slice of the 3D model, ρ_i is the percentage of inner membrane blocks occupied with Tol-Pal, and r_i is the distance (in blocks) from the slice *i* to the cell extremity along the major cell axis. When $r_i = 0.21L$, Tol-Pal is removed from the inner membrane block.
$Tsr.c_{TP} \xrightarrow{\alpha_i \cdot v_{TP}} Tsr.c_{neighbour}$	$v_{TP} = 1$ blocks/sec $\alpha_i = \frac{n_i}{c_i \cdot \rho_i}$ $\rho_i = \frac{0.21L - r_i}{0.21L}$ $i \in [1, L]$	

TABLE S1: Reactions, parameters, and events in model cells.

Results

Expression of Tsr-Venus as a function of induction strength

We measured Tsr-Venus expression as a function of induction strength with a microplate fluorometer at 37 °C (Fig. S3 *A*). A fold change of ~110 was observed when increasing IPTG levels from 0 to 1000 µM ml^{-1}, in agreement with a previous study (1).

Next, by live cell microscopy, with cells kept at 37 °C prior and during observation, we measured the fluorescence intensity of Tsr-Venus from individual cells (Methods) when increasing IPTG levels from 0 to 500 µM ml^{-1}, 2 hours after induction of the target gene. The mean Tsr-Venus levels detected from the images show close agreement with the microplate fluorometer measurements (Fig. S3 *B*). We conclude that the quantification methods of Tsr-Venus levels from live cell imaging are accurate.

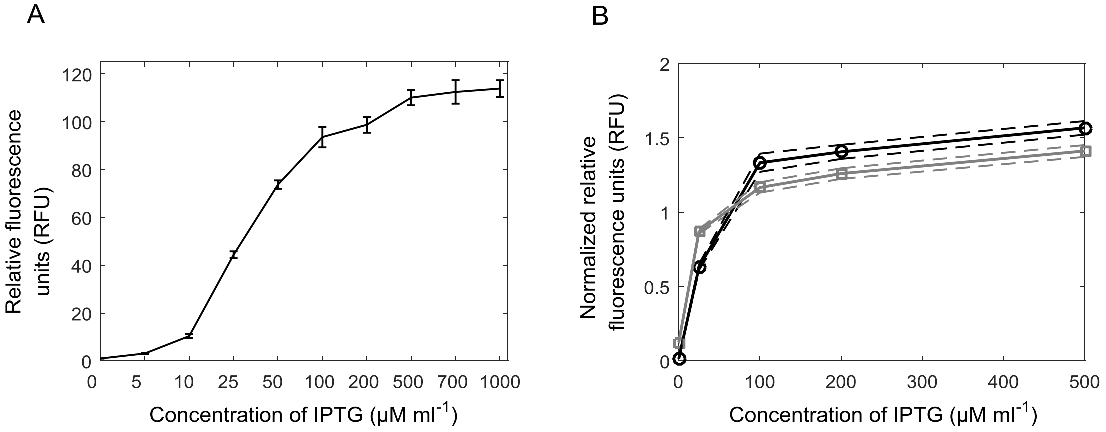

FIGURE S3. Induction curves of Tsr-Venus. (*A*) Mean expression levels of the target proteins (Tsr-Venus) estimated by microplate fluorometer as a function of the induction level by IPTG. Error bars are the standard deviation of three independent measurements. (*B*) Comparison of the induction curves (normalized by the mean, in arbitrary units) when measured by microplate fluorometer (black line) and by confocal microscopy (grey line), from live cells, 2 hours after induction by IPTG, for varying IPTG concentrations. Only the conditions observed in both the microscope and the plate reader are shown. Dashed lines are the standard deviation of the relative fluorescence units (RFU) from independent measurements, at each IPTG concentration.

Ampicillin treated cells

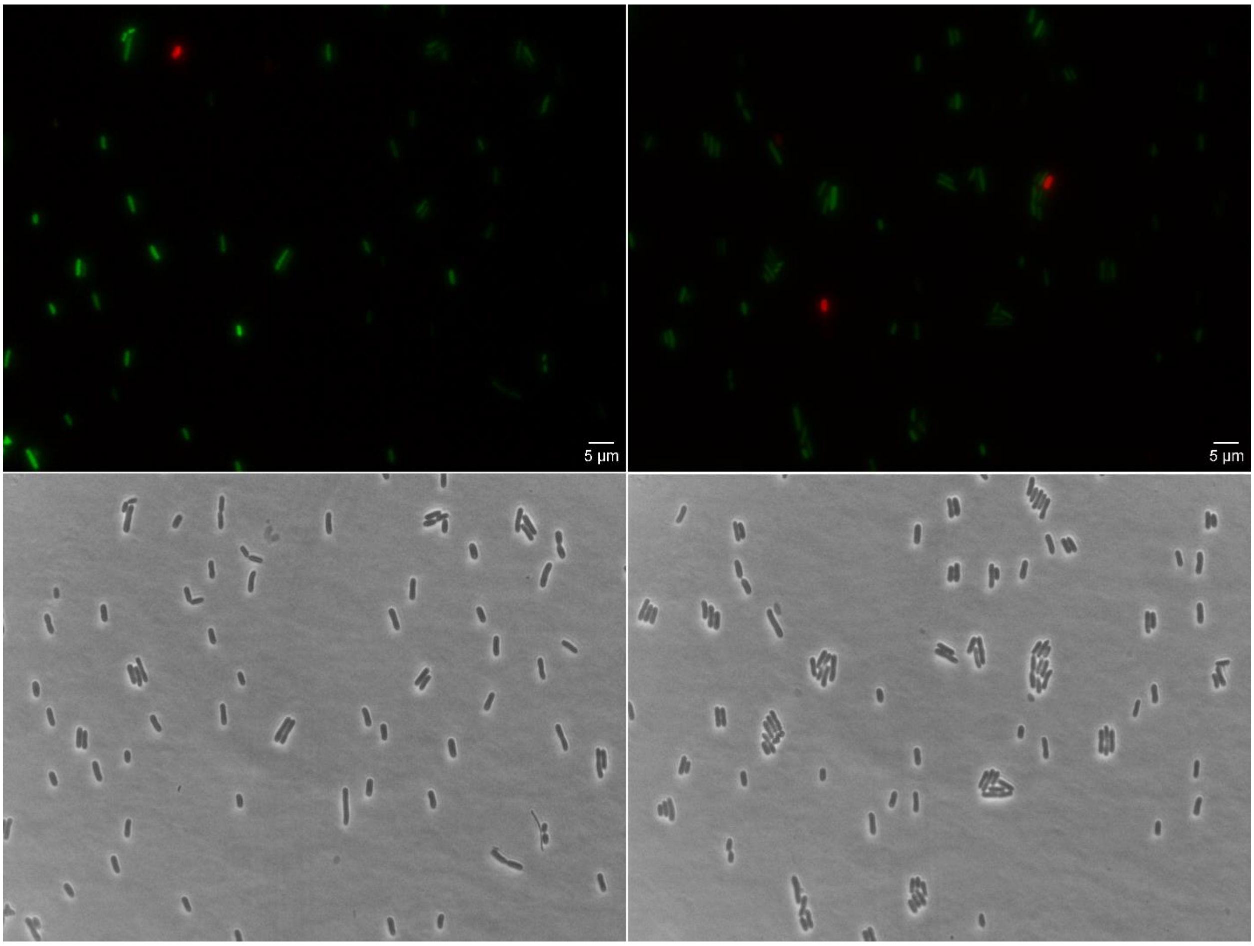

FIGURE S4. Epifluorescence microscopy images of cells treated with ampicillin (top right) and control cells (top left) subject to a BAC Live/Dead Assay. Green is indicative of viability while red is indicative of death cells. Visibly, the population subject to ampicillin contains several viable cells that were used for further analysis. In these experiments, expression of Tsr-Venus is not activated, so as to not generate 'background' fluorescence. Also shown are phase contrast images of the cells treated with ampicillin (bottom right) and control cells (bottom left).

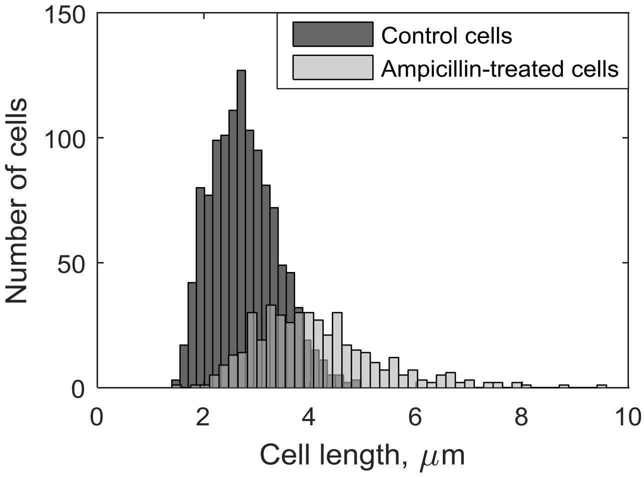

FIGURE S5. Distribution of individual cell length from 436 cells treated with ampicillin (light grey) and from 1195 control cells (dark grey). In these experiments, expression of Tsr-Venus is activated.

Degree of symmetry of the process of segregation of Tsr clusters to the poles

We quantified the degree of symmetry of the process of segregation of Tsr clusters to the poles, relative to the poles age. For this, based on data obtained from time-lapse microscopy measurements (Methods), from the fluorescence along the major cell axis of individual cells and the definition of poles and midcell (main manuscript), we determined the fraction of cells with higher fluorescence intensity at the old pole compared to the new pole, the moment prior to dividing. Then, we tested whether the measured biases could arise from sampling from an unbiased binomial distribution.

For this test, we analyzed SX4 cells (216 cells), kept at 37 °C prior and during observation. We observed that 63% of the cells contained more Tsr at the old pole (*p*-value of 0.6×10^{-5} from a binomial test that the measured distribution can be distinguished from an unbiased binomial distribution), in agreement with previous studies (10).

This statistically significant bias could result from the presence of inherited clusters (which locate solely at old poles), rather than the process of segregation to the poles (11). To assess this, to the distribution of fluorescence along the major cell axis of each cell prior to its division, we discounted the same distribution obtained when the cell was born. As such, we obtained an approximate distribution of fluorescence of proteins produced during the cells' lifetime. From these (216 cells), we obtained the numbers of cells with larger and smaller amounts of Tsr-Venus at the old pole. Next, we calculated the same p-value as before, by comparing the empirical distribution with an unbiased binomial distribution. This *p*-value is larger than 0.05, from which we conclude that the process of segregation of Tsr clusters to the poles is symmetric relative to the poles age (as reported in (10)).

From these measurements it is also possible to conclude that cell divisions introduce non-negligible biases in the numbers of Tsr-Venus between old and new poles of the cells, in agreement with (10).

Tsr clusters location when first detected

We studied, from time-lapse microscopy data, the location of Tsr clusters when first detected in control cells where the induction of Tsr-Venus was made while the cells were already under observation. From Fig. S6, most clusters are already at the poles when first observed.

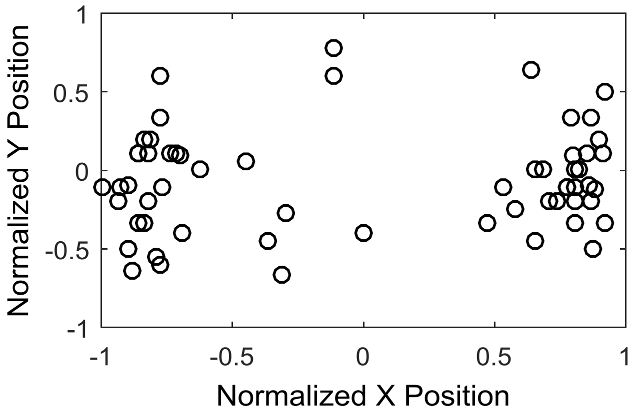

FIGURE S6. Relative positioning of Tsr-Venus clusters when first detected during a cell's lifetime (X and Y axes normalized to the interval [-1, 1]). We arbitrarily set the 'left pole' and 'top of the cell' as the negative (-1) and the 'right pole' and 'bottom of the cell' as positive (+1), with 'left', 'right', 'top' and 'bottom' being defined by the positioning of the cell in the image.

Tsr clusters location as a function of relative nucleoid length

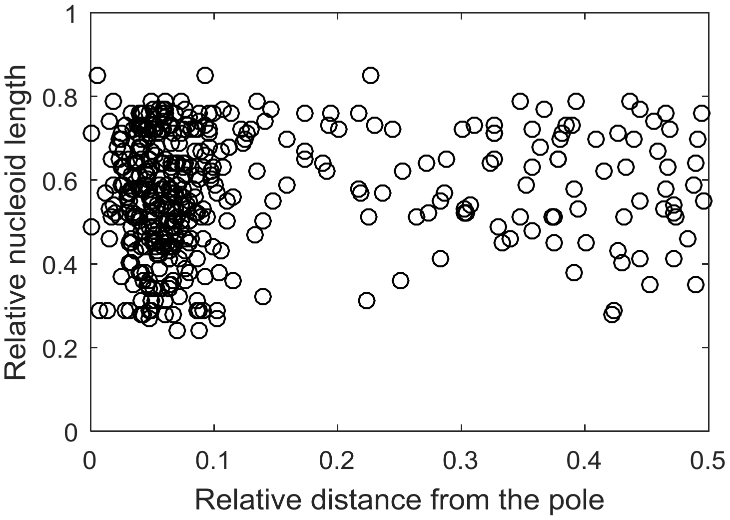

FIGURE S7: Relative nucleoid length versus relative distance of individual Tsr clusters from the closest cell extremity in WT cells.

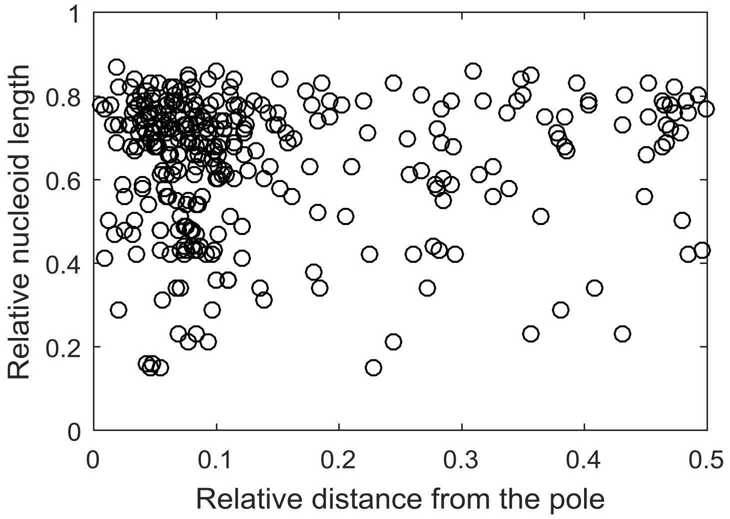

FIGURE S8: Relative nucleoid length versus relative distance of individual Tsr clusters from the closest cell extremity in Δ*tolpal* cells.

Comparison of DAPI staining and HupA-mCherry tagging

As noted in the main manuscript, Tsr-Venus distributions are identical in cells stained with DAPI and cells expressing HupA-mCherry at 37 °C (Fig. S9). As expected, they are also identically anti-correlated with the distributions of nucleoid(s) fluorescence (Pearson correlation equaled -0.87). Finally, the p-value of the *t*-test of statistical significance assuming that the data are uncorrelated was smaller than 10^{-4}, i.e. the anti-correlation is statistically significant.

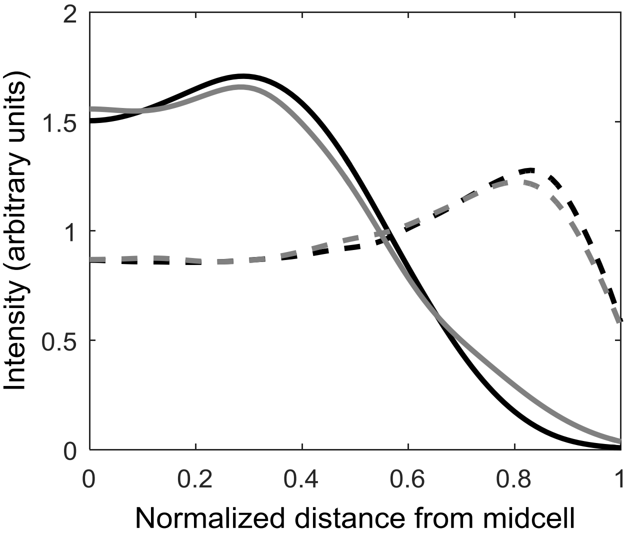

FIGURE S9. Kernel density estimates (KDEs) of the spatial distributions of the background-subtracted fluorescence of cells with the nucleoids stained by DAPI (black lines, 125 cells) and by HupA-mCherry (grey lines, 58 cells). Also shown (dashed lines) are the KDEs of fluorescence intensities (arbitrary units) of Tsr-Venus along the major cell axis (bandwidths 0.05) of the same cells.

Correlations between Tsr clusters spatial distributions as estimated from the empirical data

Strain, **Nucleoid length**	**WT,** **large**	**WT,** **small**	**Δ*tolpal*,** **large**
Δ*tolpal*, **small**	$p = 0.05$	$p = 0.17$	$p = 0.75$
Δ*tolpal*, **large**	$p < 0.01$ $r = 0.75$ $r \in [0.33, 0.92]$	$p < 0.01$ $r = 0.69$ $r \in [0.21, 0.90]$	
WT, **small**	$p < 0.01$ $r = 0.61$ $r \in [0.08, 0.87]$		

TABLE S2 p-values of the Pearson correlation between Tsr clusters spatial distributions in WT and Δ*tolpal* cells with relatively large (occupying ≥ 65% of the cell length) and small (occupying ≤ 35% of the cell length) nucleoids. When the correlation is significant ($p < 0.01$), the Pearson correlation value r, and the 95% CI of r are also shown.

Correlations between Tsr clusters spatial distributions in the stochastic models of nucleoid exclusion of Tsr clusters from midcell

Strain, **Nucleoid length**	**WT,** **large**	**WT,** **small**	**Δ*tolpal*,** **large**
Δ*tolpal*, **small**	$p = 0.19$	$p < 0.01$ $r = 0.52$ $r \in [0.29, 0.70]$	$p < 0.01$ $r = 0.44$ $r \in [0.18, 0.64]$
Δ*tolpal*, **large**	$p \ll 0.01$ $r = 0.82$ $r \in [0.71, 0.90]$	$p \ll 0.01$ $r = 0.80$ $r \in [0.67, 0.88]$	
WT, **small**	$p \ll 0.01$ $r = 0.93$ $r \in [0.87, 0.96]$		

TABLE S3 *In silico* model. *P*-values of the Pearson correlation between Tsr clusters spatial distributions in WT and Δ*tolpal* cells with relatively large and small nucleoids. When the correlation is significant ($p < 0.05$), the Pearson correlation value r, and the 95% CI of r are also shown. The data from each condition is from 1000 cells.

SUPPORTING REFERENCES

1. Yu, J., J. Xiao, X. Ren, K. Lao, and X.S. Xie. 2006. Probing gene expression in live cells, one protein molecule at a time. Science. 311: 1600–3.
2. Oh, D., Y. Yu, H. Lee, B.L. Wanner, and K. Ritchie. 2014. Dynamics of the serine chemoreceptor in the escherichia coli inner membrane: A high-speed single-molecule tracking study. Biophys. J. 106: 145–153.
3. Koch, A.L., and J. V. Holtje. 1995. A physical basis for the precise location of the division site of rod-shaped bacteria: The Central Stress Model. Microbiology. 141: 3171–3180.
4. Helgesen, E., S. Fossum-Raunehaug, and K. Skarstad. 2016. Lack of the H-NS protein results in extended and aberrantly positioned DNA during chromosome replication and segregation in Escherichia coli. J. Bacteriol. 198: 1305–1316.
5. Fisher, J.K., A. Bourniquel, G. Witz, B. Weiner, M. Prentiss, and N. Kleckner. 2013. Four-Dimensional Imaging of E . coli Nucleoid Organization and Dynamics in Living Cells. Cell. 153: 882–895.
6. Zimmerman, S.B. 2006. Shape and compaction of Escherichia coli nucleoids. J. Struct. Biol. 156: 255–61.
7. Fritsche, M., S. Li, D.W. Heermann, and P.A. Wiggins. 2012. A model for Escherichia coli chromosome packaging supports transcription factor-induced DNA domain formation. Nucleic Acids Res. 40: 972–980.
8. Elowitz, M.B., M.G. Surette, P. Wolf, J.B. Stock, and S. Leibler. 1999. Protein Mobility in the Cytoplasm of. 181: 197–203.
9. Taniguchi, Y., P.J. Choi, G.W. Li, H. Chen, M. Babu, J. Hearn, A. Emili, and X.S. Xie. 2010. Quantifying E. coli Proteome and Transcriptome with Single-Molecule Sensitivity in Single Cells. Sci. (New York, NY). 329: 533–538.
10. Ping, L., B. Weiner, and N. Kleckner. 2008. Tsr-GFP accumulates linearly with time at cell poles, and can be used to differentiate “old” versus “new” poles, in Escherichia coli. Mol. Microbiol. 69: 1427–38.
11. Gupta, A., J. Lloyd-Price, R. Neeli-Venkata, S.M.D. Oliveira, and A.S. Ribeiro. 2014. In vivo kinetics of segregation and polar retention of MS2-GFP-RNA complexes in Escherichia coli. Biophys. J. 106: 1928–37.

Tampereen teknillinen yliopisto
PL 527
33101 Tampere

Tampere University of Technology
P.O.B. 527
FI-33101 Tampere, Finland

ISBN 978-952-15-3990-9
ISSN 1459-2045